UNIVERSITÀ DEGLI STUDI DI PALERMO

Dottorato di Ricerca in Ingegneria Civile e Ambientale – Indirizzo Materiali
Dipartimento di Ingegneria Civile, Ambientale, Aerospaziale e dei Materiali - DICAM
ING-IND/22 - Scienza e tecnologia dei materiali

PREPARATION AND CHARACTERIZATION OF BIOPOLYMERIC POROUS STRUCTURES FOR ADVANCED APPLICATIONS

IL DOTTORE
Francesco Lopresti

IL COORDINATORE
Prof. Mario Di Paola

IL TUTOR
Prof. Roberto Scaffaro

CICLO XXIX
ANNO CONSEGUIMENTO TITOLO 2017

PhD Thesis:

Preparation and characterization of biopolymeric porous structures for advanced applications

Francesco Lopresti*

Università degli Studi di Palermo

Dipartimento di Ingegneria Civile, Ambientale, Aerospaziale, dei Materiali

*Phone: +39 3297966208
*E-mail: francesco.lopresti01@unipa.it
*E-mail: francesco_lopresti@hotmail.it

Preface

This PhD thesis represent the requirement fulfillment of the doctoral program in Material Engineering, XXIX cycle. The activities were mainly carried out at the Department of Civil, Environmental, Aerospace and Materials (DICAM) of the University of Palermo during the period between January 2014 and December 2016. The work was supervised by Prof. Roberto Scaffaro, Full Professor at the University of Palermo.

I would like to express my sincere gratitude to Prof. Roberto Scaffaro, for his invaluable and constructive supervision of the work and for his encouragement. Furthermore, I would like to thank the entire working team and in particular Prof. Luigi Botta for his highly qualified help.

Part of this work was conducted at the Italian National Council of Research, at the *Istituto per lo Studio dei Materiali Nanostrutturati* (ISMN), under the supervision of Dr. Maria Luisa Bondì that I want to sincerely thank for her qualified scientific contribution.

Abstract

Porous biopolymers received an increasing academic and industrial interest finding application in several fields such as tissue engineering, bioprocess intensification and waste removal.

Tissue engineering combines the knowledge of materials science and bioengineering in order to develop structures able to substitute and restore the normal function of injured or diseased tissues. In this context, polymeric 3D or 2D scaffolds are widely investigated as temporary cell guidance during the tissue restore.

Porous biomaterials can offer a versatile and cost effective way for immobilization of filamentous microorganisms in submerged fermentation processes for the production of biologically active compounds. Engineered biopolymeric membranes can lead to an increment of cell densities, improved gas–liquid mass transfer, stimulate microbial metabolism, protect cell from unfavorable agents, and preserve their physiological activity thus resulting in a net increment of bio-productivity.

Finally, in the recent years, much effort has been dedicated to the development of sustainable and inexpensive sorbent materials for oil/water separation based on natural fibers, which combine attractive properties such as renewability, biodegradability, high specific strength and modulus, low density and environmental friendliness. In this context, porous bio-materials can act as a multifunctional devices able a combining

the properties of sorbents materials and that of the organic carrier able to enhance the activity and viability of oil-degrading cells for bioremediation.

Table of Content

Abbreviations

Ac	**Acetone**
ACT	Actinorhodin
ANOVA	Analysis of Variance
AO	Acridine orange
ATR-FT-IR	Attenuated total reflectance Fourier transform infrared
BET	Brunauer–emmett–teller
BH	Bushnell–Haas mineral medium
BLS	Bi-layered scaffolds
BPO	Benzophenone
CAM	Computer-aided manufacturing
CDI	1,1'-carbonyldiimidazole
CFSE	Carboxyfluorescein succinimidyl ester
CFU	Colony forming units
CNT	Carbon nanotubes
COL	Collagen
CS	Chitosan
DAPI	4',6-diamidino-2-phenylindole
DCM	Dichloromethane
DMEM	Dulbecco modify eagle medium
DOE	Design of experiment
DPBS	Dulbecco's phosphate buffered saline
ECM	Extracellular matrix
EDC	N-(3-dimethylaminopropyl-N'-ethylcarbodiimide) hydrochloride
EtOH	Ethanol
FBS	Fetal bovine serum
FGS	Functionally graded scaffolds
GnP	Graphene nanoplatelets
GO	Graphene oxide
GPA	Pegylated-GO aerogel
HA	Hyaluronic acid
HAp	Hydroxyapatite
HC	Hydrocarbon
IP	Image processing
ITE	For interface tissue engineering
K3-EDTA	Tripotassium ethylenediaminetetraacetate
LSCM	Acridine orange
Micro-CT	Microcomputed tomography
MW	Microwave
OA	Orthogonal arrays
ORS	Oil removal sponge

PA 6	Polyamide 6
PAD	Pores area distribution
PCL	Polycaprolactone
PDMS	Poly(dimethylsiloxane)
PE	Polyethylene
PEG	Poly(ethylene glycol)
PEO	Polyethylene oxide
PES	Polyethersulfone
PGA	Polyglycolic acid
PHBV	Poly(3-hydroxybutyrate-co-3-hydroxyvalerate)
PI	Propidium iodide
PL	Particulate leaching
PLA	Polylactic acid
PLGA	Poly (lactide-co-glycolide)
PP	Polypropylene
PSD	Pore size distribution
PSF	Polysulfone
PTES	Perfluorooctyltriethoxysilane
PU	Polyurethane
PVA	Polyvinyl alcohol
PVDF	Poly(vinylidene fluoride)
RGO	Reduced graphene oxide
RP	Rapid prototyping
SAMs	Self-assembled monolayers
SC	Solvent casting
SE	Surface energy
SEM	Scanning electron microscopy
SFF	Solid free-form
SLA	Stereolithography
TE	Tissue engineering
TS	Tensile strength
XPS	X-ray photoelectron spectroscopy

Introduction

1.1 Overview

Polymeric materials obtained by renewable sources and with potential biodegradability and/or bioactivity are becoming more and more interesting both from an academicals and an industrial point of view [1–10]. In particular, porous biopolymers received an increasing interest thus finding application in several technologically advanced fields such as biomedical devices [11,12], bioprocess intensification [13,14] and waste removal [15]. The success of porous biopolymers, can be ascribed to several factors such as the relative easy processability if compared with other materials. In fact, they can be produced melt in a 3D molded monolithic form [11] or in thin films [16] thus providing significant advantages in many practical applications. Furthermore, the diversity of synthetic routes for biopolymers facilitates the design and/or modification of structures capable of incorporating multiple chemical functionalities into the porous framework or at the pore surface [17]. Moreover, biopolymers can easily be filled with nanoparticles thus enhancing certain properties or adding new, in the prospective of multifunctional porous materials [16].

1.2 Biopolymers and their Bulk and Surface Modification

Porous biomaterials for advanced applications can be either natural or synthetic. However, synthetic biopolymers offer several advantages over natural materials since they are more available in the market, they usually exhibit higher mechanical performance and they can be tailored to give a wide range of more predictable properties. In this context, the most common biodegradable synthetic polymers being used or studied for advanced applications include polylactic acid (PLA), polyglycolic acid (PGA) and polycaprolactones (PCL) [16,18,19]. On the other hand, natural biopolymer such as collagen (COL), hyaluronic acid (HA) and chitosan (CS) are widely used in the preparation of scaffold for biomedical applications [20–30] or as oily waste removal in the case of cellulosic porous structures [15,31,32].

On the basis of the final application, surface chemistry of biopolymers could be not adequate and needs modifications able to preserve the favorable bulk characteristics of the biomaterial, such as strength and degradation ability [33]. For instance, the surface of most synthetic polymers is hydrophobic and exhibit a low surface energy (SE) value thus negatively affecting the polymer-cell interactions [34].

Among the several approaches proposed for the surface modification of polymers, low-pressure plasma has gained great scientific and industrial importance [34,35]. Plasma can be described as an energetic medium composed of radicals, atoms, electrons, positively and negatively charged ions, and molecules, which are obtained by using outer energetic source [36]. It is often used to improve adhesion of coatings, wettability, printability, bio-compatibility and other surface related properties of polymers [34,35]. On the other hand, in order to improve oil/water selectivity in biopolymeric sorbent for oily waste removal, superhydrofobic surfaces are required [15,37–40].

1.3 Functionally Graded Porous Biopolymers

Functionally graded porous biopolymers are usually developed in tissue engineering field. Tissue engineering combines the knowledge of materials science and bioengineering in order to develop structures able to substitute and restore the normal function of injured or diseased tissues. In this context, polymeric three-dimensional scaffolds are widely investigated as temporary cell guidance during the tissue restore [41–43].

It is well known that living tissues are characterized by a gradient of different cell type, extracellular matrix (ECM) morphology, mineral amount and composition as well as mechanical response. Designing functionally graded scaffolds (FGS) requires the examination of the hierarchical structure of native tissues from the microbiological level up to the tissue structure in order to recognize and exploit the relationships between structure and function. The main challenge of this strategy lays in finding methods able to customize, as much as possible, each region of the scaffolds in order to achieve the best regenerative performance taking into account both the tissue and the patient requirements [44]. Bilayer structures are usually intended for scaffolds

designed for osteochondral repairs. In fact, osteochondral defects involve both bone and cartilage as well as their interface. Thus, the possibility to tune specific tailored properties in different regions of the scaffold just integrating two layers with different chemo-physical properties is a key challenge that can led to a superior osteochondral repair, compared with monolayered scaffolds.

Multilayer systems are characterized by assembling three or more layers in a single structure in order to achieve a gradient of properties such as pore size [44–51], pore shape [52], mineral content [26,53,54] or chemical cues [38,50,55–61]. Multilayer scaffolds are usually designed for osteochondral repairs [45,46,50,51,54,60] but they were also developed for cranial [61], vascular [62], human dermis [48] and tendon-bone interface [56] regeneration. The principal alternative to bilayer and multilayer scaffolds are the continuous gradient scaffolds. These scaffolds may overcome the problem of inefficient binding between different layers while displaying a continuous change in terms of material composition, pore architecture or growth factors type [63–66].

1.4 Main Applications of Porous Biopolymeric Structures

1.4.1 Tissue engineering

Tissue engineering (TE) is a rapidly growing, interdisciplinary field within the health sciences that is devoted to the manufacture of intact tissue and organ constructs by imitating natural biological development [67]. The field aims to regenerate whole biological components outside the body for eventual replacement therapy (i.e. implantation) via the manipulation of cells, natural or synthetic cell-supporting scaffold materials, and bioactive molecules. TE holds promise in addressing the urgent need of all surgical subspecialties requiring viable, transplantable body parts for the reconstruction of a myriad of anatomic structures. For instance, TE has shown potential to address major problems in transplantation, such as donor organ shortage and the need for lifelong immunosuppression, by (1) serving as a potentially inexhaustible source of tissues and organs and (2) circumventing the need for

immunosuppression by growing tissue via the expansion of autologous cells [68]. To date, the main technology used for the biofabrication and subsequent implantation of hollow organs (i.e. trachea) involves the seeding of cellular material onto supporting scaffold material. Cell-scaffold technology relies on the principle that cells require a supporting structure to proliferate and exert function [45].

The ideal TE scaffold is a transient structure that degrades over time while allowing regenerated tissue to take its place. These scaffolds are often constructed from biomaterials which, in addition to providing a suitable 3D or 2D porous structure, can lend biological and mechanical signals to induce cell growth and differentiation [69,70]. In this sense, the ideal biomaterial should recapitulate the form and activity of the ECM that supports the seeded cells in vivo.

The importance of imitating ECM should not be understated. In the past decade, it has become increasingly apparent that it plays a fundamental role in the viability and functionality of cells, tissues, and organs. Thus, a deeper understanding of the relationship between ECM and cells will facilitate the manufacturing of better scaffolds [71].

In designing the next generation of advanced biomaterials, it must be taken into consideration that body tissues and organs are highly specialized in structure and function. Variations in ECM are likely to parallel the specializations of their corresponding tissues. Thus the design of a single, all-encompassing biomaterial is not a practical design goal [72].

The most widely used natural polymers to fabricate tissue engineering scaffolds include fibrin, collagen, gelatin, chitosan, alginate, and hyaluronic acid [22,73–76]. Fibrin is a non-globular fibrous protein, and plays a critical role in blood clotting by polymerizing into a mesh over a wound site. It forms a tight complex with thrombin and it has been used in mixtures with thrombin to produce an in situ forming gel. Type I COL, which is the most abundant collagen of the human body is found in tendons, skin, artery walls, and fibrocartilage, and can be extracted from animal tissues. COL and gelatin, which is a denatured form of collagen, can form porous gel matrices, are also used to functionalize the surface of synthetic polymers to enable cellular attachment [69]. CS is a cationic polysaccharide with hydrophilic properties, which is used as a scaffolding material to support cell adhesion and differentiation, and owing

to its osteoconductive nature, it is particularly applied for bone tissue engineering [75]. Alginate is an anionic polysaccharide, which is widely derived from cell walls of brown algae. In the presence of divalent cations such as Ca^{2+} it is capable of forming gels with a high swelling degree [25]. HA is an anionic nonsulfated glycosaminoglycan, which is mainly found in connective, epithelial, and neural tissues. It forms crosslinkable hydrogels with various modifications and is highly cell repellent [77].

The synthetic polymers used for fabricating tissue engineering scaffolds can be grouped into synthetic and natural polymers. Biodegradable synthetic polymers commonly used for this purpose include poly(a-hydroxyester)s, polyanhydrides, and polyorthoesters [68]. The poly(a-hydroxyester)s such as PLA, PGA and its copolymers, used in the form of a solid foam, are the most extensively applied as biodegradable scaffolds [11]. Biodegradable polymers, which are approved by the Food and Drug Administration (FDA), can easily be processed into various structures of 3D matrices, and thus are preferred for scaffold engineering over non-biodegradable polymers. Most notably, poly (lactide-co-glycolide) (PLGA) copolymers are advantageous biodegradable materials for fabricating tissue engineering scaffolds, due to the tunability of degradation behavior and mechanical properties through changing the combination ratios of constituents to match the specific requirements for the tissue to be regenerated. By carefully optimizing the degradation behavior of the polymer, it is possible to engineer scaffolding materials with comparable degradation rates to the rate of tissue formation and ECM production, which would ultimately result in a successful regeneration of the damaged tissue. It should be noted that biodegradable polymers degrade into acidic products, which might hinder cell adhesion and growth. This problem can be overcome by using biocompatible hydrophilic polymers such as poly(ethylene glycol) (PEG) functionalized with cell-adhesive groups [45,46].

1.4.2 Bioprocess Intensification

Most of industrially relevant bioproducts are produced by means of submerged cultivations of microorganisms. In this context, actinomycetes, Gram-positive mycelial bacteria, are very prolific producers of naturally occurring bioactive

molecules, including most of clinically relevant antibiotics as well as a wide range of enzymes of industrial interest [78,79]. In these bacteria, the biosynthesis of bioactive molecule is coupled with a complex physiological developmental program as demonstrated in *Streptomyces coelicolor*, a model strain producing various bioactive metabolites, including the blue colored polyketide antibiotic actinorhodin (ACT) [13,80,81].

The production of enzymes and bioactive molecules from actinomycete strains take place mostly by means of submerged (i.e. in a liquid growth medium) fermentations in bioreactors, including industrial processes. However, submerged fermentations is far away from reproducing the real life-style of terrestrial actinomycetes, like streptomycete species which are characterized by a saprophytic growth of mycelia cells on solid organic substrates from plants and fungi [82]. Therefore, actinomycete submerged fermentations usually require an optimization of bacterial growth parameters for the development of a robust and economically feasible production process.

During actinomycete submerged fermentations, one of the most frequent factors negatively affecting bio-production deals with the formation of mycelial cell pellets [83,84]. In this way, inner mycelium usually suffers starvation and/or hypoxia due to a bad diffusion of nutrients and oxygen [84,85].

Immobilization of filamentous microorganisms in submerged fermentation processes for the production of biologically active compounds has become more and more attractive. More in detail this strategy offers some peculiar advantages over free mycelial cells, such as augmented cell densities, improved gas–liquid mass transfer, stimulate microbial metabolism, protect cell from unfavorable agents, preserve their physiological activity and the possibility of increase cultivation life, which result in a net increment of bio-productivity [13,14,86–90].

In this context, porous biomaterials can offer a versatile and cost effective way to improve the bioprocess of submerged bacterial fermentation.

1.4.3 Oily Waste Recovery: Sorbent Materials and Bioremediation

Oil pollution is one of the environmental concerns that are currently becoming a major issue in the petroleum industry. The importance of oil pollution issues becomes correspondingly significant with the increase of petroleum activities. Sources of oil pollution may arise from the run-off of oil from onshore facilities and from oil tanker spills during transportation. Annually, the amount of oil that is transported across the international sea, are about five millions tones [91].

The current methods of controlling oil spills include using booms [92], skimming [93], and burning the oil on the surface of the water [94]. These techniques are time consuming and energy inefficient, and they create pollution and require excessive energy for recovery of the oil. Offshore, where turbulent conditions exist, the use of booms and the skimming method might not be feasible due to the propensity for oil to disperse in sea water. Burning is the most economical method to eliminate the oil, but the time required to burn the oil can lead to its dispersion, depending on the wind direction, and even worst, burning the oil causes high CO_2 emissions into the environment [95].

Therefore, it is preferable to use sorbents to recover the spilled oils because of their peculiar properties such as uptake capacity, uptake rate, buoyancy, oil retention, durability, reusability and recoverability of the oil that has been absorbed by the sorbent. In the recent years, much effort has been dedicated to the development of sustainable and inexpensive sorbent materials based on natural fibers, which combine attractive properties such as renewability, biodegradability, high specific strength and modulus, low density, and environmental friendliness [96]. Cotton [97,98] wooden chips [99], kapok [100,101], rice straw [100,102], banana fibers [103] and kenaf [97] have been considered as oil sorbents, but the lack of oil/ water selectivity and the poor toughness of these materials have driven the research community to look for better alternatives such as cellulosic aerogels [15] or synthetic biomaterials [104].

In this context, bioremediation is a promising non-invasive and cost-effective technology that could help a more effective and sustainable recovery of contaminated water and sediment. Successful delivery of bioremediation requires a combination of expertise from such diverse fields as engineering, biology, and biotechnology. In the

last few years, the application of biotechnological processes that involves microorganisms with the objective of solving environmental pollution problems, is rapidly growing. One of the key points for bioremediation is maintaining high biomass of bacterial populations. To improve the survival and retention of the bioremediation agents in the contaminated sites, bacterial cells must be immobilized.

Immobilized cells have been extensively used in the production of useful chemicals, treatment of wastewaters and bioremediation of pollution cause of its longer operating lifetime and enhanced stability and survival of the cells [105,106]. Ideally, the carrier material would be biodegradable, available in large quantities, low cost, and have the appropriate physical properties to allow for sufficient aggregation of specific microorganisms useful for bioremediation [107]. The carrier materials that have been studied include sawdust, wheat bran, calcium alginate, potato starch fiber, Styrofoam and polyurethane foams [107–114] but be applied in an oil-polluted marine environment, the carrier material should float. A floatable formulation makes it easier for degraders to have contact with the oil pollutant [115,116].

The type of support media used for anoxic biomass immobilization can affect the efficiency of a bioreactor as well as the number of cells adhering to the support. In this context, porous bio-materials can act as a multifunctional devices able a combining the properties of sorbents materials and that of the organic carrier able to enhance the activity and viability of the cells.

2 State of the Art and Aim of this Work

2.1 Strategy for Fabricating Porous Biopolymers

Particulate Leaching

Particulate leaching (PL) is one of the popular techniques that are widely used to fabricate porous biopolymers, in which a porogen agent is used to create the pores or channels in the 3D polymeric structure.

Polymer and porogen agents can be combined by melt mixing by heating the system above the polymer's glass transition temperature. After solidification, the composite is subjected to leaching to obtain the final porous structure. The principal advantages of this method lay in the absence of organic solvent during the preparation.

Scaffaro et al. prepared by melt mixing PCL and PLA based scaffold for osteochondral defects using NaCl as porogen agent and PEG as co-porogen agent. The authors demonstrated the high control and predictability of the pore size distribution by tuning the NaCl crystals size (from 20μm to 500 μm) and the porosity of the biopolymeric structures simply changing the amount of NaCl particles [11,13,19,43,46,117].

Oh et al., prepared hydrophilic porous scaffold in PLGA/polyvinyl alcohol **(PVA**) by melt molding and particulate leaching. The scaffolds exhibited highly porous and open-cellular pore structures with pore size in the range 200–300 μm and porosity about 90% [118].

Reignier and Huneault prepared interconnected PCL porous scaffolds by a combination of polymer and salt particulate leaching. In the first step of this technique, a co-continuous blend of two biodegradable polymers, PCL and polyethylene oxide (PEO) and a certain amount of NaCl particles are melt blended using a twin screw extruder. Subsequently, extraction of the continuous PEO and mineral salts using water yields a highly porous PCL scaffold with fully interconnected pores [119].

On the other hand, particulate leaching is used with solvent techniques. In particular, they involve casting the dissolved polymer around a suitable porogen,

drying and solidifying the system. After, the porogen agent is removed by using a selective solvent.

Tang et al. prepared PLGA based scaffold by using this method and a gelatin-microsphere template as porogen [49]. Liao et al. used NaCl as porogen agent for PLGA obtaining a highly porous three-dimensional scaffold (>85 vol %) with a well interconnected porous structure [120].

Wu et al. used a "room-temperature" injection molding/particulate leaching approach for fabrication of biodegradable three-dimensional porous scaffolds made in PLGA. In this approach, a "wet" composite of particulate/polymer/solvent was used in processing, and thus the injection was not performed at melting state. Appropriate viscosity and flowability were obtained at a certain solvent content so that the composite was able to be injected into a mold under low pressure at room temperature thus avoiding thermal degradation of polyesters [121].

Sin et al. reported an enhanced solvent casting/particulate leaching (SC/PL) method developed for preparing three-dimensional porous polyurethane (PU) scaffolds for cardiac tissue engineering. The enhanced method involved the combination of a conventional SC/PL method and a step of centrifugation, with the centrifugation being employed to improve the pore uniformity and the pore interconnectivity of scaffolds [122].

Hou et al. proposed a technique for the preparation of porous polymeric structures involving coagulation, compression molding and particulate leaching. The technique combines the advantages of thermal processing methods and particulate leaching. A high molecular weight polymer solution in an organic solvent containing dispersed water-soluble salt particles is precipitated into an excess of non-solvent. The polymer–salt composite is then processed by thermal processing methods into devices of varying shapes and sizes, which can subsequently be extracted to give the desired porous structures. The porosities of the scaffolds could be varied between 70% and 95% by adjusting the polymer to salt ratio and the pore size could be controlled independently by varying the leachable particle size [123].

Particulate-leaching is a simple technique to fabricate porous polymeric scaffolds with a controlled degree of porosity and pore size, which is achieved by controlling the amount of salt added and the size of the salt particles respectively. The porogen

agent are usually hydrosoluble solid particles such as NaCl or sucrose but often, hydrosoluble polymers such as PEG were used in order to improve the porous interconnections [11,45,46,124].

Electrospinning

Electrospinning is a versatile, simple and cost-effective technique that produce polymer fibers employing electrostatic forces. Nanofibers are basically fibers with diameters on the order of a few hundreds of nanometers. These nanofibers possess high surface area which is favorable for many applications such as tissue engineering, waste removal or controlled release [125–127].

The basic configuration of electrospinning consists of three major components: (i) a high-voltage power system, (ii) a fiber collector, and (iii) a spinneret. The spinneret is directly connected to a syringe, which acts as a reservoir for the polymer solution to be electrospun. This polymer solution can be fed through the spinneret with the help of a syringe pump at a steady and controllable feed rate. The fiber-collecting device is positioned in front of the spinneret, with an appropriate gap (usually a few centimeters). A high-voltage/low-current power system is required for the conversion of polymer solution to a charged polymer jet. The electric voltage (usually up to 30 kV) is applied across the spinneret and the grounded metallic counter electrode (fiber collector) to facilitate the charged jet to eject from the spinneret tip toward the surface of the fiber collector.

In order to be able to perform electrospinning experiments with the aim of achieving fibers with a target diameter, a predetermined surface topology, is needed controlling various parameters characteristic of electrospinning. Following list and range of the most relevant parameters governing electrospinning technology:

Electric and material parameters and ranges [128]:

- Molecular weight of selected polymer species 10^4 – 10^7 g/mol
- Applied voltage 5 – 100 kV
- Solution flow rate 0.01 – 1 ml/min
- Polymer concentration 1 – 40 wt%

- Electrode distance 1 – 100 cm

System parameters characteristic of the spinning solutions:

- Surface tension 20 – 75 mN/m
- Electric conductivity 0.05 – 30 mS/m
- Dielectric permittivity 15 – 90
- Shear viscosity 20 – 300 000 cP
- Viscoelastic relaxation time 2 – 500 ms

Charge characteristics affecting the jet deformation:

- Current 1 – 10 000 nA
- Surface charge density 10^{-8} – 10^{-6} C/cm

Control of Nanofiber Diameters

The diameter of the nanofibers produced by electrospinning is a key parameter for most of the applications envisioned for such fibers and the nonwovens composed of them. The diameter of the nanofibers controls structural features such as pore sizes and specific surface areas in nonwovens that, in turn, affect the selectivity of filters, the permeability of filters, and catalytic activities in systems using nanofibers to immobilize catalysts or the cell proliferation in tissue engineering relying on nanofiber-based scaffolds. A feature unique for electrospinning is that fiber diameters down to just a few nanometers can be produced particularly from polymer solutions. However, the diameter can also be extended up to more than 10 μm if required. So, the task is to find out first of all which spinning parameters have the strongest impact on the fiber diameter, and secondly how to adjust these parameters to obtain specified fiber diameters consistently and reproducibly. Spinning solution and its polymer concentration are key parameters.

One key factor controlling the diameter of the nanofibers produced in electrospinning is the stretching to which the fluid jet is subjected during the course of the spinning process with the major stretching taking place in the bending instability regime–the higher the stretching of the jet the smaller the diameter of the final fibers.

A further powerful approach towards modifying fiber diameters over a broad range consists in varying the polymer concentration within the spinning solution keeping the

feeding rate about constant. A low polymer concentration will cause, first of all, a strong shrinkage of the fiber diameter due to solvent evaporation. However, the effect of polymer concentrations can cause a fiber diameter variations amounting to a factor of 100 and more. A major effect of a variation of the polymer concentration on resulting fiber diameters comes obviously also from the corresponding strong variation of the viscosity and the viscoelastic response of the fluid jet to deformations. In fact, it is well known that, usually, an increasing viscosity lead to an increase in fiber diameter.

A further approach towards controlling the fiber diameter consists in adding components that vary the electric conductivity of the solvent. An increased conductivity tends to increase the charge density at the surface of the jets, thus decreasing the tendency of droplet formation during electrospinning.

Another factor affecting the fiber diameter is the variation of the distance between the spinning die and the counter electrode. Various effects may contribute to fiber - diameter variations as the distance is decreased among them an increase in the electric field, a suppression of later stages of elongational processes induced by the bending instability or the suppression of the complete evaporation of the solvent. It is for this reason that again the induced fiber-diameter variations vary strongly with the polymer system under consideration.

An approach that has more recently come into the focus of electrospinning is to use a mixture of a solvent selected for the polymer under considerations, adding a certain amount of a nonsolvent in order to obtain more stable electrospinning processes and a more reproducible preparation of fibers with a given diameter. The best-known example is electrospinning of polyamides, in particular polyamide 6 (PA 6), in mixtures of the solvent formic acid with the nonsolvent acetic acid. A rather broad range of solvent/nonsolvent concentrations can in principle be exploited to induce a stable spinning process. It is well known that this approach can be used also for other polymer/solvent systems. Yet, so far no real explanation has been offered for the underlying effects. It seem possible that a major effect comes from the induction of heterogeneous regions in the spinning solution.

Electrospinning permit to produce core–shell fibers composed of polymer shells and cores or of low molar mass materials as core and a polymer shell, or even to

produce hollow fibers by using coaxial needles. In coaxial electrospinning two dies arranged in a concentric configuration are connected to two reservoirs containing different spinning solutions in this approach.

A variety of materials including biodegradable polymers such as PLA and PCL, as well as water-soluble materials such as (PEO), (PVA), and natural polymer such as COL, silk protein, and other peptides have been electrospun [129–134].

Gas Foaming

The gas foaming fabrication of biopolymers is widely exploited for the fabrication of highly porous scaffolds for tissue engineering. This process involves saturating a polymer solution with carbon dioxide at a high pressure (800 psi) which results in the phase separation of clustered carbon dioxide molecules and the creation of pore nucleation, a process called "foaming" [135].

Upon the completion of the foaming process, the polymeric scaffold turns into a 3D porous structure with expanded polymeric volume and a decrease in polymeric density. The amount of carbon dioxide dissolved in the polymer solution determines the porosity and porous structure of the scaffolds. However, the porous structure fabricated using this technique often lack the suitable pore interconnectivity, and thus are too compact for the use in tissue engineering. By combining gas foaming with salt leaching the porosity of the scaffolds is controlled by the use of salts [136]. Using this method, the polymer to be expanded in the foaming process comes together around salt particles to create a well-connected polymeric network.

Phase Separation

The phase separation scaffold fabrication technique involves demixing of a homogeneous polymer solution by using either another solvent or lowering the temperature to the point below the bimodal solubility curve [137]. This technique separates the polymeric solution into polymer-lean and polymer-rich phases. Polymer is dissolved in phenol or naphthalene, followed by the dispersion of biologically active molecule in these solutions. By lowering the temperature a liquid-liquid phase is separated, and quenching the mixture below the freezing point of the solvent forms a two phase solid, which is subsequently freeze dried to produce porous scaffolds with

bioactive molecules integrated into that structure [138]. The porous structure achieved by the phase separation technique can be finely tuned by adjusting the various thermodynamic and kinetic parameters such as the selection of solvent phase separation temperatures. An advantage of the phase separation technique is that it can easily combine with other fabrication technology (particulate leaching) to design three dimensional structures with control pore morphology. However, the drawback of using this technique is the lack of pore interconnectivity in the resultant scaffold [139]. The coarsening process and the use of surfactants can be applied to improve the uniformity of the pore size and pore morphology of the scaffold [137].

Freeze-drying

The freeze drying technique provides a rapid method for fabricating 3D porous biopolymers [140,141]. This technique involves creating pores by freezing the polymer solution and removing the solvent crystals by lyophilization under high vacuum. The polymeric solution can either contain water (i.e., emulsion-based freeze drying) or be devoid of water (i.e., non-emulsion-based freeze drying). The polymer solution is cast in a metal mold, followed by freezing under high vacuum, which causes the removal of solvent from the polymer and the creation of interconnected pores in the resultant device [142].

A variety of biocompatible polymers have been utilized to fabricate biopolymeric porous structures using the freeze drying technique. Representative polymers include silk proteins [143], PGA, PLA [144] and PLGA. Parameters such as freezing rate, temperature, and pH influence the pore size; for example, a fast freezing rate results in smaller pores. Main advantages of this technique are that it eliminates a salt-leaching step which could have compromised the purity of the scaffold by the trace amount of salt remaining in the scaffold and the possibility to achieve high porosity (higher than 90%). However, this technique often requires organic solvents, potentially dangerous for biomedical application and a long processing time [145].

Rapid Prototyping

Rapid prototyping (RP), also referred to as solid free-form (SFF) technique, is comprised of a group of mechanical processes technologies that fabricate a 3D object

in a layer-by-layer fashion. The RP applies computer-aided design (CAD) and computer-aided manufacturing (CAM) programs to build highly complex structures by layering a series of thin 2D slices (i.e., cross sections) with defined properties [146,147]. The cross sections are designed by CAD programs, and corresponding to each cross section, the RP machine fabricates layers of materials which are laid down one at a time, moving from the bottom to the top to build the porous structure with predefined properties such as porosity, interconnectivity, and pore size. Those characteristics are very important for tissue engineering because enable this technique to fabricate anatomically shaped scaffolds. The RP methodologies include stereolithography (SLA), selective laser sintering, ballistic particle manufacturing, and 3D printing. SLA, which is one of the most common types of RP, operates by patterning a photopolymer using a laser beam. RP is an efficient technique for generating the porous structures with defined properties such as size, shape, pore size/interconnectivity, etc. Major advantages of this technique include high reproducibility of the porous architecture and composition, the ability to control mechanical properties and degradation kinetics of the final product, which can result in fabrication of biomimetic scaffolds, with a variety of designs and material compositions for particular applications or for various tissue engineering purposes [147–150]. However, the main drawback of this technique currently is its low resolution and limitation in the choice of polymeric materials that can be applied for this technique [68].

Phase inversion method

Phase inversion process is an effective and convenient method and has been investigated well. A majority of polymeric membranes applied in oil/water emulsion separation have been prepared by phase inversion process [151,152]. In this process, a homogeneous polymer and solvent mixture are cast as a thin film or a hollow fiber shape, and then immersed into a nonsolvent coagulation bath. The film with a symmetric or asymmetric structure is formed by the diffusional interchange of solvents and nonsolvents across the interface between casting solution and non-solvent coagulant [153]. By means of phase inversion process, blending two or more specific substances with hydrophilic and hydrophobic structures and properties with

engineering polymers for instance poly(vinylidene fluoride) (PVDF), polysulfone (PSF) and polyethersulfone (PES) on account of their eminent chemical resistance, thermal stability and mechanical strength [154,155], which has the advantages of easy preparation for anticipatory properties and well-controlled porosity, is an efficient way to develop potential polymeric membranes applied in oil/water emulsion separation. A superhydrophobic-superoleophilic PVDF membrane was fabricated by Jiang and coworkers via an inert solvent-induced phase-inversion process [156]. The obtained PVDF membranes, for the first time, were able to efficiently separate both micrometer and nanometer-size surfactant-free and surfactant stabilized water-in-oil emulsions solely driven by gravity, with high flux and separation efficiency (oil purity in filtrate after separation > 99.95wt%).

2.2 Strategy for Fabricating Functionally Graded Porous Biopolymers

Porous biopolymeric devices with engineered chemical, physical and mechanical properties can play a crucial role in several fields, such as biomedical but also waste treatment and bioprocess intensification [19,46,157,158].

The development of porous laminates composed by different kinds of biopolymer allow controlling several parameters by tuning the properties of each single layer and by eventually assembling them into a single device [41,62,159]. For instance, this feature is of main concern for interface tissue engineering (ITE), a rapidly developing field that aims to the production of structures designed either to repair or to regenerate diseased or damaged zones at the interface of different types of tissue. Interface tissues are more complex than the homogeneous ones because of the presence of multi-phasic and/or anisotropic structures that gradually change from one tissue to another [41,157,159]. The desire to mimic these natural structures has driven biomechanical engineers to develop custom-made bio-inspired materials with mechanical properties similar to natural tissues [53,62,66]. Usually, porous multiphasic laminates are developed by 3D printing, suturing, glue or press fitting two/three layers, even if the best challenge is achieving a well joint monolith presenting functionally graded properties [25,41,55,160–166].

In general, functionally graded scaffolds fabrication strategies can be categorized in i) bi-layered or ii) multilayered depending on the number of layers composing the whole structure. In other cases, scaffolds are characterized by a continuous gradient of one or more specific properties that cannot be related to the presence of well distinguishable layers. Furthermore, FGS can be multiphasic [11,60,167] or monophasic [45,46,157] since a single material can also be used to produce multilayered scaffolds if a significant variations in physical properties among the layers (i.e. porosity, pore size or pore shape) is present.

Bilayer structures are usually intended for scaffolds designed for osteochondral repairs. In fact, osteochondral defects involve both bone and cartilage as well as their interface. Thus, the possibility to tune specific tailored properties in different regions of the scaffold just integrating two layers with different chemo-physical properties is a key challenge that can led to a superior osteochondral repair, compared with monolayered scaffolds.

Multilayer systems are characterized by assembling three or more layers in a single structure in order to achieve a gradient of properties such as pore size [44–51], pore shape [52], mineral content [26,53,54] or chemical cues [38,50,55–61]. Multilayer scaffolds are usually designed for osteochondral repairs [45,46,50,51,54,60] but they were also developed for cranial [61], vascular [62], human dermis [48] and tendon-bone interface [56] regeneration.

The principal alternative to bilayer and multilayer scaffolds are the continuous gradient scaffolds. These scaffolds may overcome the problem of inefficient binding between different layers while displaying a continuous change in terms of material composition, pore architecture or growth factors type [63,64,139,168–171].

Particulate Leaching

Several researchers fabricated bilayer or trilayer scaffolds by particulate leaching. The FGS system can be prepared by solution casting of the biopolymer in a mold containing hydrosoluble particles with two or more different size distribution [172–174]. When biopolymer/porogen composites are prepared by melt, the multilayer structure is usually prepared by an iterative compression molding. This procedure enable the preparation of FGS presenting different pore size distribution [19,46,117],

chemical composition [11,167] or both [11]. Furthermore, this strategy enable achieving a gradient of nanofillers such as hydroxyapatite (HAp) likely able to enhance the biomimetic properties of the scaffold [175]. Particulate leaching allows tuning the porosity and pore size by simply tailoring the size and concentration of porogen agents. On the other hands, the pore shape is strongly affected by the porogen geometry that is difficult to control.

Freeze drying

The versatility of freeze-drying lays in the possibility to obtain multilayer constructs via an iterative technique that allows the material composition and scaffold microarchitecture to be specifically tailored in each region of the scaffold.

Levingstone et al., adopted this method to prepare threelayered scaffold mimicking the native composition of subchondral bone ECM. The articular cartilage-mimicking layer, was composed by a rich glycosaminoglycan content and type II collagen. The cartilage-mimicking layer of the scaffold was made by type I collagen, type II collagen and HA. Finally, the bone-mimicking layer was prepared with type I collagen and HA [55]. Zhu et al. used a similar approach to fabricate a CS based fourlayered scaffold presenting a porous structure able to mimic the cartilage ECM. The Collagen/CS–PCL/CS scaffolds presented hierarchically distributed average pore-size and porosity as well as interconnected porous structure [51].

Kon et al., Yusong et al., and Algul et al. prepared threelayered scaffolds made by CH, gel and collagen, respectively, by overlapping layers with increasing amount of mineral phases. The assembled layers were then freeze-dried obtaining a biomimetic interconnected porous structure [53,54,176]. The main advantage of freeze-drying lays in the possibility to obtain highly porous, multilayer constructs through an iterative technique that can be adopted for a wide range of polymers. On the other hand, the method is not easy to be scalable at an industrial level, and it is usually adopted for small prototypes.

Electrospinning

Multi-layer electrospun scaffolds are usually developed by consecutively electrospinning different materials.

Wang et al. used this technique to prepare a threelayer scaffold for cranial defects. The inner PLA layer was designed to reduce tissue adhesion on brain. The middle layer, made by PLA/PCL blend, was designed to avoid water infiltration. Finally, the collagen-based outer layer was designed to promote cell adhesion. The mechanical and *in vivo* biological test demonstrated that the multilayer scaffold has a sufficient mechanical strength and adequate biochemical properties to be potentially used for cranial repairs [61].

Bye et al. used the same approach to prepare poly(3-hydroxybutyrate-co-3-hydroxyvalerate) (PHBV)/PCL or PLA multilayer scaffolds demonstrating the reliability of these systems as bio-barriers for preventing cell penetration [58].

Electrospinning is a versatile technique for fabricating nano/microscale fibers, which has a great potential for mimicking the microenvironment of natural ECM by controlling a large number of parameters such as flow rate, potential, distance between syringe and collector and so on. Moreover, this approach allows preparing scaffolds constituted by different layers in an easier way with respect to other technique. On the other hand, the intrinsic morphology of the porous structures is often difficult to be permeated by cells, without specific precautions.

2.3 Porous Biopolymer-based Nanocomposites

Several biopolymers often shows relative low mechanical properties and an intrinsic poor hydrophilicity and, consequently, a low cellular affinity [177]. For these reasons, several scientific researches focused on the development of high performance porous biopolymers such as post-process surface modifications [17], blends with other biopolymers [178] and/or the use of nanofillers [179–181]. More in detail, the scientific literature reports a wide number of nanofillers used for improve their mechanical performance such as multiwalled carbon nanotubes [180], biopolymeric nanoparticles [181], nanoclays [182] and nano-hydroxyapatite [183]. Among these, graphene and its derivatives are now considered the most promising fillers for the development of high performance materials [184,185]. In particular, the use of graphene oxide (GO) as a precursor provides the possibility to exploit the variegated oxygen moieties useful to covalently attach several specific compounds, thus

extending and diversifying its application fields [186]. Graphene is the name given to a flat monolayer of carbon atoms tightly packed into a honeycomb-like carbon lattice where the sp^2 hybridized carbon atoms are arranged in a regular hexagonal pattern in a 2D layer [187]. Although having been studied for over sixty years and widely used for describing the properties of various carbon-based materials, graphene was believed to be unstable with respect to the formation of curved structures such as fullerenes or nanotubes. Unexpectedly, Geim and Novoselov proved in 2004 that free-standing graphene was possible [188]. Graphene and graphene-derived materials have aroused a great deal of interest because monolayer graphene has been shown to be about 100 times stronger than steel with a theoretical modulus around 1 TPa and strength of 150 GPa [189], to conduct electricity better than copper in the in-plane direction and to show improved barrier properties due to its platelet-like morphology. Also, owing to its atomic thickness, graphene presents a high specific surface area with high possibility of interaction with other substrates [187]. Nevertheless, as happens with other nanosized graphitic structures, single layer graphene synthesis is still challenging, especially in terms of attaining considerable quantities for industrial implementation. Two main types of graphene-derived materials have been gaining ground in terms of possible large-scale production: reduced graphene oxide (RGO) and graphene nanoplatelets (GnP). RGO may be obtained by the chemical or thermal reduction of GO, usually synthesized through the oxidation of graphite by means of the Hummers method [186,190,191]. Nonetheless, reduction of GO generates structural defects in the carbon lattice, considerably reducing the electrical properties when compared to pristine graphene [187]. GnP, which are unique nanoparticles consisting of short stacks of graphene sheets obtained by the previous intercalation of small molecules between graphite layers and later mechanical/thermal exfoliation [192], have surged as a possible alternative to RGO.

2.4 Surface Modification of Biopolymeric Porous Structures

Bulk modification is a strategy whereby surface properties are changed by modifying the bulk of the polymer matrix. Polymer blending or the use of nanofillers are widely studied in order to change surface properties such as wettability roughness.

For instance, cell-signaling peptides are incorporated into the biomaterials, and the resulting recognition sites are not only present on the surface but also in the bulk of the materials [193]. This is mostly beneficial for applications focusing on injectable biomimetic materials. The encapsulation of cells within these materials is desirable for localized delivery by injection, thus avoiding a surgical procedure.

Surface modification differs from bulk modification in this respect that an object/film is fabricated from a bulk material and subsequently only the surface is modified. It is possible to categorize the different available surface modification strategies in several ways. For example, some processes are single-step processes; others consist of two or more subsequent steps in order to achieve the desired modification. A surface can be changed chemically by introduction of functional groups or by covalent coupling of molecules onto the surface. Another approach is the physical adsorption of a polymer onto the surface. This is, for example, the case for dip-coating processes [194], but we will not include all of these physical surface modifications except for self-assembled monolayers (SAMs), which are also based on physical interactions.

The most common industrial techniques for direct surface modification include flame treatment, metal deposition, irradiation techniques, and corona-discharge techniques.

The modification of a surface by grafting polymers onto the surfaces can also be achieved in a variety of manners. Graft polymerization can be achieved by an ionic mechanism, a coordination mechanism, coupling mechanism or free-radical mechanism. The free-radical mechanism can be subdivided in chemical grafting, mechano-chemical grafting and radiation induced-grafting. Radiation-induced grafting can be achieved by using different kinds of radiation. High-energy radiation such as γ-rays, X-rays and electron beams are known as ionizing radiation. Midenergy radiation, mostly UV rays, laser or plasma sources and low energy radiation (infrared, ultrasonic, microwave (MW) and visible sources) can bring about desired changes in the polymer backbone depending upon the irradiation time and energy of radiation.

Wet Chemical Surface Modification

A first class of methods includes the wet-chemical methods. This involves the reaction between a chemical compound in solution and a surface. Classic examples include aminolysis and alkaline or acidic hydrolysis. Treatment with hydrogen peroxide is considered a wet chemical method. The hydroperoxides, which are thus introduced on the surface, serve as initiation sites for the subsequent grafting of vinyl monomers.

Hydroxyl and carboxyl end-groups are generated when a polyester is hydrolyzed via autocatalytic cleavage of main-chain ester-bonds [195]. Normally roughness and hydrophilicity of the surface increase [196]. In some cases, both enhanced cell attachment and spreading are reported. In general, subsequent immobilization of natural proteins tends to increase cell adhesion and viability [197,198]. As for hydrolysis, this also is a surface degradation reaction, roughness also tends to increase, and thus wettability increases. Characterization of surfaces is a rather specific field with specific complications and limitations. It is challenging to evaluate to what extend the change in wettability is due to the introduction of amine groups on the surface, and to what extend the increased wettability can be attributed to the increased roughness.

Recently, the surface modification of commercial polymer sponges, such as polyurethane and melamine sponges, have tuned the surface properties of the sponges from hydrophilicity to superhyphobicity, which has attracted considerable attention [199–206]. Due to their low density, high porosity, three-dimensional skeleton structure, good elasticity, and flexibility, polymer sponges have exhibited excellent sorption of both water and oil, making them impractical for highly efficient and selective removal of oils from water [199]. However, the modification of sponges through coating hydrophobic materials on their surfaces can tune the surface property of a sponge from hydrophilicity to superhydrophobicity, resulting in great improvement of the sorption selectivity. Thus, far, several materials have been used to modify the surface properties of commercial sponges, such as hydrophobic polymers [201,203], superhydrophobic activated carbon [205], carbon nanotubes (CNTs) [206] and graphene [200,202]. Zhu et al. modified polyurethane sponges by initially coating sponge skeletons with a film of copper via electroless deposition and subsequently modifying the skeletons with superhydrophobic and superoleophilic coatings through a solution-immersion process [199]. The obtained superhydrophobic sponges

exhibited selective sorption of various oils up to 13 times their weight and sorption capacity retention of about 50–90% after nine cycles. In another study, Zhou et al. impregnated polyurethane sponges with ferric chloride and perfluorooctyltriethoxysilane (PTES) and subsequently vapor-phase-polymerized pyrrole to produce superhydrophobic coatings of PTES–polypyrrole [201]. The as-prepared sponge selectively absorbed oil from water with high uptake capacity, as much as 20 times its own weight and the sorption capacity retention of about 85% after 5 cycles. Wang and Lin recently reported a method to modify the surface properties of polyurethane sponges by repeatedly dip-coating them in a CNT/poly(dimethylsiloxane) (PDMS) solution, drying them, and finally curing them at 120 °C for 6 h.(30) The obtained superhydrophobic CNT–PDMS-coated sponges exhibited good oil sorption capacity, up to 25 times their own weight.

Dip coating is a simple old way of depositing onto a substrate, especially a uniform thin film of liquid for solidification into a coating. The basic flow is steady, and in it film thickness is set by the competition among viscous force, capillary (surface tension) force and gravity. Thickness and uniformity can be sensitive to flow conditions in the liquid bath and gas overhead. The faster the substrate is withdrawn, the thicker the film deposited [194].

In general, these wet chemical methods are very useful, but some drawbacks should be noted. The most important disadvantage is that these reactions are nonspecific, introducing a range of functional groups. The degree of surface modification may not be repeatable comparing polymers of different molecular weight, crystallinity, or tacticity.95 Irregular surface etching as indeed been reported [207]. As this surface degradation affects the outer shell of the device a loss of mechanical properties93 or faster degradation might be the case. Surface modification of surfaces treated with hydrogen peroxide has also been reported. Hydrogen peroxide decomposes to hydroxyl radicals, which are more reactive than other oxidative chemicals by applying ultraviolet radiation [208]. This technique is used to create hydroperoxide groups on polymers by immersing samples in hydrogen peroxide solution and simultaneous irradiation with UV-light [209]. This is called photooxidization.

Dry Surface Modification

Ozone treatment

Ozone can be used as such, but it was found that a combination of ozone and UV irradiation increased the kinetics of the process significantly. This observation could be attributed to different pathways for both methods [210]. UV-ozone treatment of different materials such as polyethylene (PE), poly(etheretherketone), poly(vinyl fluoride), and PS were studied [211–213]. As for wet-chemical treatment, it can be stated that this is a nonspecific technique. Furthermore, the surface composition will depend on the cleaning procedure. In addition, reorientation at the surface seems to occur [212]. Another concern is the degradation of polymers, which is known to be enhanced by ozone [214].

UV-Treatment and Photografting

UV treatment has been extensively used for surface graft polymerization of polymers in the presence of a photoinitiator or photosensitizer [215,216]. Depending on the chemical structure of the grafted polymer, different functionalities are introduced to the surface. UV can be applied while the sample is kept under vacuum conditions, or submerged in an inert gas such as argon, or covered with monomer solution. Often, the photoinitiator, mostly benzophenone (BPO), is either precoated on the substrate or present in solution. UV light excites the BPO, which can abstract hydrogen atoms from the polymer film when it relaxes, thus creating free radicals on the surface. Some authors have reported the introduction of polymers with amine-side-chains. The photoinduced graft polymerization of acrylamide on polypropylene (PP) membranes for the improvement of the antifouling properties was reported [217].

High-Energy Radiation

The most common radiation types, used in industry, include γ-radiation and e-beam radiation [218]. Ion beams are used in order to achieve ion implantation in the outer surface layer or to deposit coatings. Many different ions have been employed for irradiating polymers such as hydrogen and helium atoms, as well as ions of gold or uranium [218]. Ion implantation does not directly introduce functional groups onto the surface but the surface chemistry, and thus the surface properties, are changed.

For the treatment of polymers, it should be noted that high-energy irradiation can cause additional chemical effects. Free radicals can recombine, leading to cross-linking. Chains can be cleaved, leading to degradation of the polymer [219,220]. These processes occur mostly simultaneously. Higher-energy radiation is considered not a viable route for the modification of most biodegradable polymers [221,222].

Non-thermal Plasma treatment

Plasma treatment can be used to directly or indirectly introduce different functionalities on inert surfaces. Direct modification includes the reactive NH_3 plasma, which is known to introduce, among others, amines, where O_2 plasmas introduces a mixture of mainly COOH and OH functionalities. Argon plasmas are typically used to introduce free radicals. Indirect modification is based on the grafting of polymers bearing the desired functionalities onto the surface. Both strategies and recent advancements in the field will be discussed extensively in the next paragraph.

The use of plasma modification techniques has some major advantages. First of all, some techniques will influence the mechanical properties of the outer layer of an implant. It is clear that wet chemical treatment of a surface will cause a partial degradation and scissions of the polymers at the surface, leading to a decrease of mechanical strength and leading to a faster degradation. A comparative study demonstrated that the structural and chemical integrity of PLGA 3D scaffolds was adversely affected by wet chemical methods [223]. Another advantage is that plasma enables to uniformly change surfaces, regardless of the geometry. The technique can be used on complex objects such as 3D components for tissue engineering or artificial organs [224], nanoparticles and films [225]. Another major advantage is that the use of hazardous solvents can be avoided, as plasma is a solvent-free technique.

In plasma technology, nonthermal plasmas are generated by an electrical gas discharge. The application of a strong electric field to a neutral gas ensures ionization in the gas volume and the created charged particles are accelerated in the applied electrical field. Especially the electrons are affected by the field due to their light mass and gain most energy. They achieve high temperatures (105-106 K), while the heavy ions efficiently exchange their energy by collisions with the background gas and thus remain cold. The gas temperature is below 473 K. On collision between energetic

electrons and neutral molecules, radicals are created. These radicals play an important role in the chemical activity of the plasma. As a result of the low gas temperature, plasma surface treatment is applicable to heat-sensitive materials, such as biopolymers [226]. Typical for surface modification developed plasma sources is that they operate at low pressures (10^{-3}-1000 Pa). At low pressure the discharge is more stable, and it is easier to control the plasma reactions. A long mean free path of the gas particles guarantees only few collisions and thus only a small reduction in the number of chemically active species.

The application field of plasma technology is growing very fast. Moreover, increasing demands from industry encourage the continuous development of more efficient and more flexible plasma techniques. Therefore, it can be noticed that in recent plasma technology research, large efforts are made to develop atmospheric pressure technology-based plasma reactors to overcome the disadvantages of low pressure. Because there is no need for vacuum devices, the investment costs are much lower, and atmospheric plasma technology can easily be scaled up to industrial dimensions and integrated in in-line processes [227].

2.5 Aim of this Work

Porous biopolymeric structures are rapidly developing for different advanced applications such as biomedical, bioprocess intensification and oily waste recovery.

Porous structures properties such as pore morphology, porosity, mechanical performance and wettability can be tuned in several ways, involving both processing and post-processing parameters.

Since it cannot be identified an optimum for each final application, each device has to be engineered in order to achieve the best performance in the required field of application. For instance, the pore size distribution can drive the cell migration and differentiation for tissue engineering while the development of functionally graded porous structures can support different cell lines. The use of nanofillers can lead to

increase the mechanical performance of the material and, at the same time, enhance its surface property for the final application.

In this work several biopolymeric porous structures were prepared by using two main approaches: particulate leaching and electrospinning. The devices were designed and prepared for three main applications: tissue engineering, bioprocess intensification and oily waste removal.

The processing-morphology-properties relationships were evaluated by considering both processing and post-processing parameters such as pore size distribution, the use of nanofillers and surface chemical treatments.

3 Experimental

3.1 Materials and Processing

This section of PhD thesis deals with the description of the materials used in this work.

3.1.1 Materials

PLA and PCL were chosen as polymeric matrix of the porous structure developed in this PhD thesis.

The PLA used in the frame of this work was a sample purchased by Natureworks (PLA 2002D, density 1.24 g/cm3) while PCL, Mw=80000 Da, was purchased by Sigma Aldrich, as well as NaCl (purity > 99%, d = 2.17 g/cm3), calcium chloride ($CaCl_2$, purity>93%, ρ=2.15 g/cm3) and PEG, Mw = 2000 Da.

For the solution of PCL dichloromethane (DCM) and ethanol (EtOH) were used, while for PLA solutions, chloroform and acetone (Ac) were used

For the GO-g-PEG synthesis, neat graphite (grade Ma 399, 45 μm) was purchased by NGS Naturgraphit (Germany). Phosphoric acid, sulfuric acid, hydrochloric acid, potassium permanganate, hydrogen peroxide solution, ethanol, diethyl-ether, 1,1′-carbonyldiimidazole (CDI), ethylenediamine, sodium sulfate, chloroform, N-(3-dimethylaminopropyl-N′-ethylcarbodiimide) hydrochloride (EDC), Dulbecco's Phosphate Buffered Saline (DPBS), Triton X-100 and tripotassium ethylenediaminetetraacetate (K3-EDTA) were purchased by Sigma Aldrich.

Collagen used in this work was a Rat Tail Collagen (purchased by Corning). Dulbecco Modify Eagle Medium (DMEM) was purchased by Sigma Aldrich as well as the 4′,6-diamidino-2-phenylindole (DAPI). The Fetal Bovine Serum (FBS) by Euro Clone while the carboxyfluorescein succinimidyl ester (CFSE) was purchased by CellTrace™ CFSE, Life Technologies. The AlamarBlue Cell Viability Reagent was purchased by Invitrogen.

Water of double distilled quality was obtained from MilliQ Plus systems (Millipore, Germany).

3.1.2 Melt Mixing and Particulate Leaching

3D Porous structures were prepared by combining melt mixing, compression molding and particulate leaching as schematically presented in Figure 1.

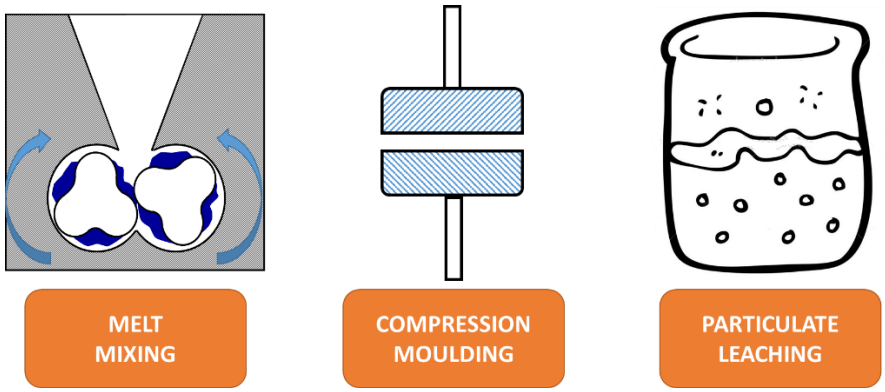

Figure 1 - Schematic representation of the fabrication rout of 3D porous structures

Before melt mixing, dried NaCl (45 grams at time) was put in an automatic sieving machine (Figure 2A) for 30 minutes at the highest available frequency without occurring in resonance. NaCl was collect in several fractions, ranging from 1000 to salt particles size smaller than 45 µm as schematized in Figure 2B.

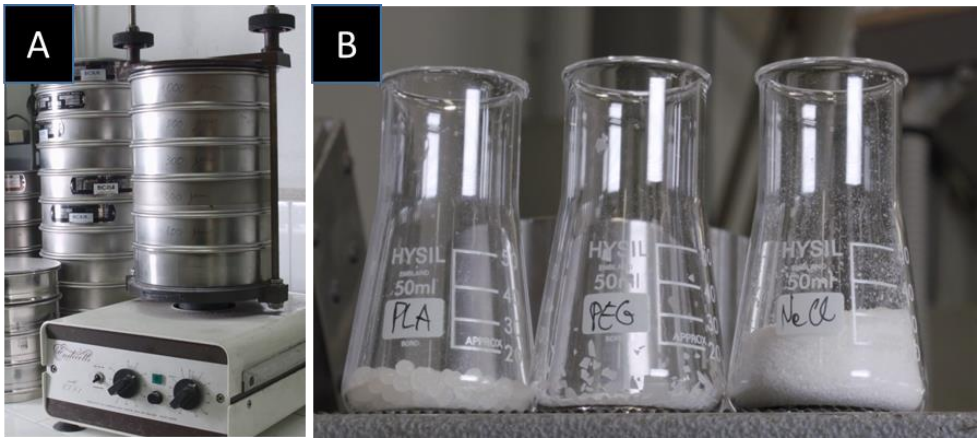

Figure 2 - A) Automatic sieving machine used for NaCl; B) Picture of the materials used for the preparation of 3D PLA porous structures.

PLA (or PCL), PEG and NaCl, with weight percentage composition of respectively 20/5/75, were fed to a batch mixer (Plasticorder PLE-330 Brabender, Germany, Figure

3). The temperature was set to 190°C in the case of PLA and to 100 °C for PCL, the rotor speed was 64 rpm, the mixing time was around 10 minutes, in order to ensure achieving a constant value of torque.

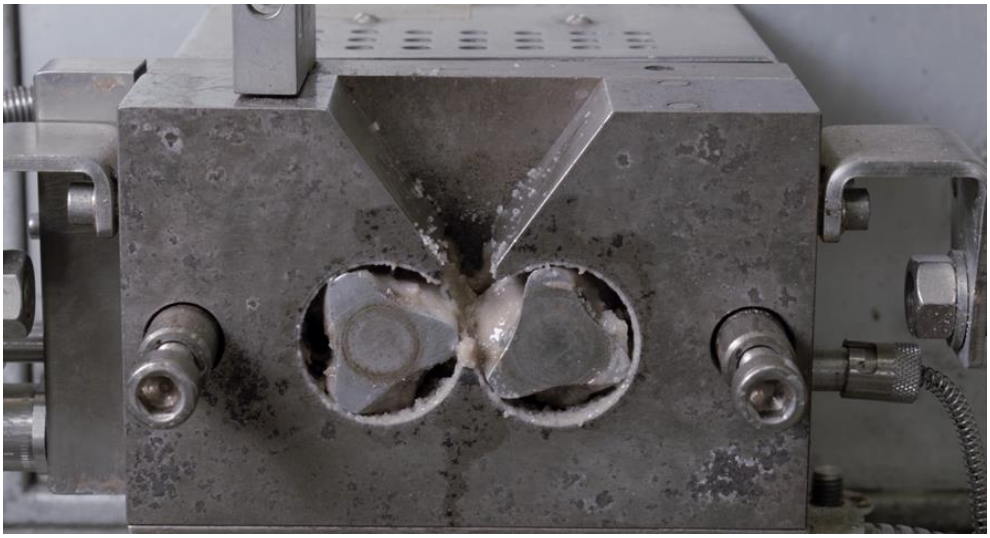

Figure 3 – Laboratory batch mixer (Plasticorder PLE-330 Brabender, Germany)

Thereafter, the samples were fed out and rapidly cooled in liquid nitrogen. The materials collected were ground and compression-molded in a laboratory press (Carver, USA, Figure 4) at 190 °C for PLA and 100°C for PCL at 180 bar in appropriate cylindrical molds with a diameter of 10 mm and different widths.

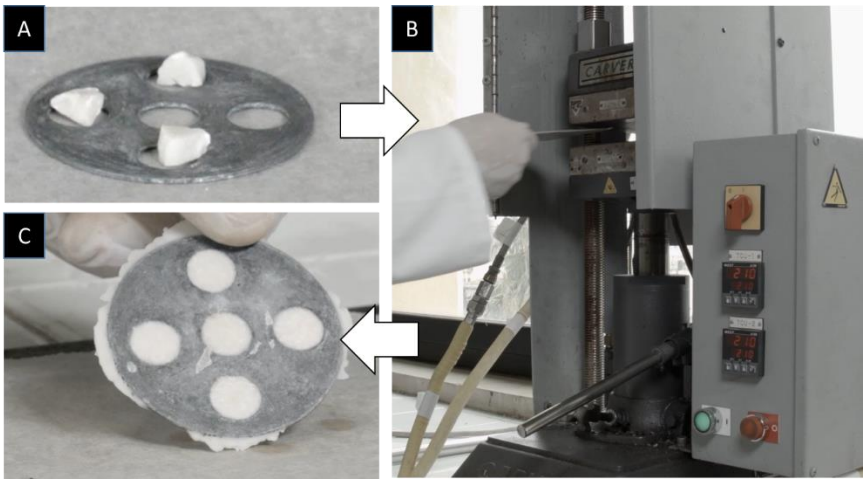

Figure 4 - A) Mold and blend before compression molding; B) Laboratory press (Carver, USA); C) Mold and blend after compression molding

The pre-compressed monolayers were eventually assembled by further compression molding in order to obtain functionally graded porous structures.

Finally, the porogen part of the blends (NaCl and PEG) was removed by selective leaching in demineralized water for 5 hours Figure 5A,B. The resulting structure were then allowed to dry for 12 hours at room temperature Figure 5C.

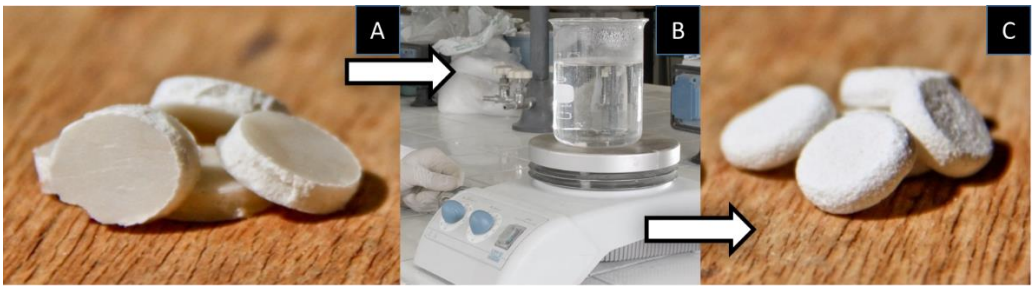

Figure 5 - A) Blend before leaching; B) Leaching step in demineralized water; C) 3D porous structures after leaching and drying in fume hood.

A sterilization step was needed in order to use the scaffold as biological support. The polymeric devices were sterilized for 24 h with ethanol (EtOH) 70% under vacuum to allow the pores filling; porous structures were then thoroughly washed with complete PBS. Thereafter, in order to prevent cells to drop on the culture plate and to encourage a fast cell adhesion in the scaffold, the polymeric supports were treated with collagen at 100 μg ml^{-1}.

3.1.3 Electrospinning

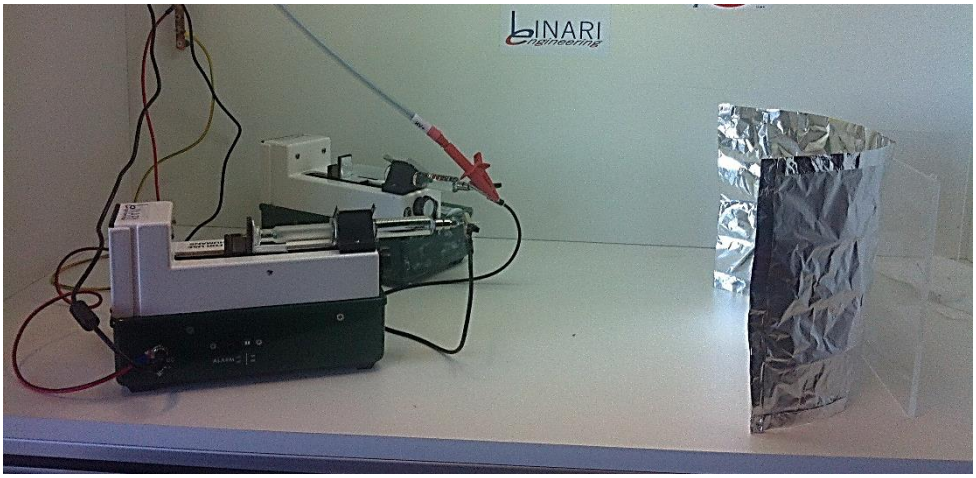

Figure 6 - Electrospinning equipment (Linari Engineering-Biomedical Division, Italy).

A conventional electrospinning equipment (Linari Engineering-Biomedical Division, Italy) was used to prepare nanofibrous mats in PCL and PLA, as shown in Figure 6. The polymeric solutions were prepared as follows:

- 10 wt% of PCL was dissolved in DCM:EtOH (8:2 vol)
- 10 wt% of PLA was dissolved in $CHCl_3$:Ac (2:1 vol)

For both system the presence of the non-solvent was chosen in order to obtain smooth fibres morphology, as discussed above.

Typically, the solution was filled in a 10-ml glass syringe fitted with a 19-gauge stainless steel needle, and then the electrospinning was performed at a series of constant parameters: flow rate, 1 ml/h; distance between the needle tip and the collector, 15 cm; supplied high voltage, 15 kV; temperature, 25 °C and relative humidity, 40%. The obtained nanofibers were collected on a grounded rotary drum (diameter = 100 mm) and collected on an aluminium foil.

The speed of the rotary drum could be changed from 5 rpm up to 200 rpm thus controlling the orientation of the fibres. Usually the collecting time was 90 min. The collected scaffolds were subsequently dried for at least 2 days under fume hood in order to remove any residual solvents.

3.1.4 Plasma treatments

PLA electrospun membrane was treated in a plasma reactor (Tucano, Gambetti, Italy, Figure 7) with polarized anode at radio frequency (13.56 MHz).

Figure 7 - Plasma reactor (Tucano, Gambetti, Italy)

The process was carried out in four steps: i) reaction chamber from ambient pressure to 0.2 mbar; ii) stabilization of the inner pressure (5 s); iii) air inlet and plasma

reaction (see below for further details); iv) venting to ambient pressure (about 100-150 s). The initial pressure in the chamber was 0.2 mbar. After air inlet (P = 0.3 mbar) and during plasma treatment the total pressure was 0.5 mbar. The airflow mass rate was kept at 10 sccm by using two mass flow controllers. For the modification of PLA, the power was set at 50 W and the reaction time was 30 s. The treatment was repeated twice in order to expose both surfaces of the PLA film to the electrode. The plasma modified electrospun PLA mats will be denominated PLA-plasma.

3.1.5 Amino-terminated-PEG synthesis

Amino-terminated-PEG was obtained as described in the scientific literature by Ranucci et al. [228]. Briefly, a mixture of PEG (6 g, 3 mmol) and CDI (2.5 g, 15 mmol) in anhydrous chloroform (30 ml) was stirred for 30 min at room temperature, diluted with further chloroform (100 ml) and washed with water (3 × 50 ml). The organic phase was collected, dried on Na_2SO_4 and filtrated. A solution of ethylenediamine (3.5 g, 60 mmol) in chloroform (30 ml) was added and the resulting mixture was stirred for 2 h at room temperature. The product was washed with 10% aqueous potassium nitrate solution (3 × 50 mL) and water (50 ml), dried over Na_2SO_4 and evaporated in vacuo. The colorless solid obtained was used without further purification for the reaction of coupling with GO.

3.1.6 PEGylation of GO

GO *Figure 8* aqueous suspension (1 mg/mL) was sonicated for 1 h to give a clear solution. The amino-PEG (*Figure 8*A) above described (10 mg/mL) and EDC (10 mg/mL) were added and the resulting mixture allowed to react overnight (*Figure 8*B).

The final product (GO-PEG, *Figure 8*C) was obtained by centrifugation at 4000 rpm for 1 h. The viscous, brownish slurry was dialyzed (Spectra/Por® Standard RC tubing; MWCO 12–14 kDa) against demineralized water for 24 h (*Figure 8*D) and then freeze-dried under the following conditions: −30 °C and 600 μbar overnight to achieve the corresponding PEGylated-GO aerogel (GPA, *Figure 8*E).

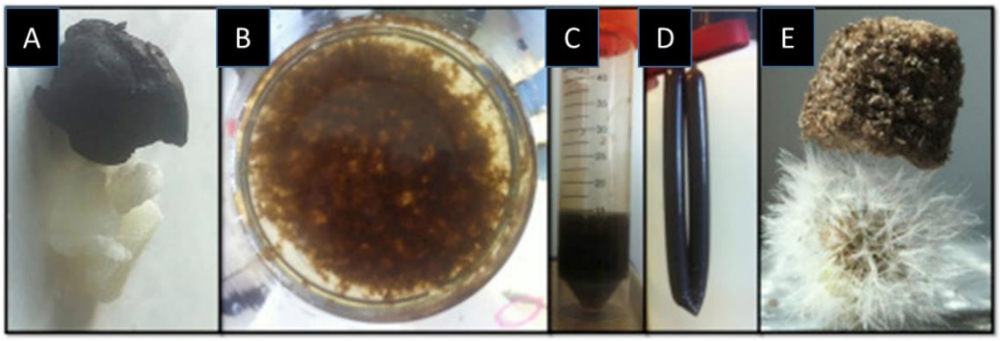

Figure 8 - A) GO (black) and PEG-NH3 (white); B) GO and amino-PEG reacting; C) GO-PEG slurry; D) Slurry dialysis; E) PEGylated GO standing on Taraxacum officinalis.

3.1.7 Cells Lines And Culture Conditions

For the biomedical applications of the porous structures, the following cell lines were utilized: MC3T3-E1, osteoblastic from mouse C57BL/6 calvaria and NIH3T3, fibroblastic from Mouse Swiss NIH embryo (ECACC, European Collection of Cells Cultures). Each cell line was grown in DMEM added with 1% glutamine; 1% antibiotics and 10% of FBS. These cell lines were chosen as models due to their different size, with the aim to investigate the influences of different pore size on their migration and proliferation inside the functionally graded porous scaffold.

For the bioprocess intensification, *Streptomyces coelicolor* A3(2) (ATCC BAA-471) spore suspensions were prepared in aqueous glycerol solution (20% v/v) according to Kieser et al. [229]. The spore amount was quantified by counting the colony forming units (CFU) by seeding serial dilutions of spore suspension aliquots on growth medium agar plates incubated at 30°C for at least two days.

For both free- and immobilized-cell cultivations, *S. coelicolor* spores (10^8/mL) were inoculated into 50 ml sterile flasks containing 10 ml R5A liquid medium [229] and incubated at 30°C on orbital shaker (200 rpm). Three independent series of cultures were prepared and processed as biological replicates. All the procedures were carried out in sterile conditions.

In order to evaluate the usability of 3D porous structure for bioremediation, two high potential degrading bacterial strains were cultured. *Nocardia cyriacigeorgica* SoB, belonging to Actinobacteria class [230] and *Alcanivorax borkumensis* SK2

belonging to Gammaproteobacteria [231]. The strains were selected for ability to degrade a wide range n-alkanes (C8-C36 SOB strain, C5-C32 and alkane branched SK2 strain). Nocardia SoB was grown in the Bushnell–Haas mineral medium (BH; Difco) with 1% (v/v) hexadecane (C16) as the sole carbon source at 30°C for 7 days with continuous shaking at 200 rpm. Alcanivorax borkumensis SK2 was inoculated in Onr7a mineral medium supplementing with 1% (v/v) of hexadecane C16 and cultivated under the same condition. Control culture on BH and ONR7a medium without the hydrocarbon (HC) were also inoculated. The strain was cultivated also in mineral medium agar plates, the HC source was supplied by placing a filter paper on the lid of the Petri dish with 100µl of C16. Control plates on medium without the HC were also inoculated. The resulting pure culture of each degrading bacterial strains was used in subsequent experiments.

The hydrocarbons-degrading strains, were inoculated in 3 ml of mineral medium (ONR7a and BH respectively) with 3D polycaprolactone scaffolds containing hexadecane as the sole carbon source (1% v/v). The cultures were incubated at 30°C with shaking at 200 rpm for 48h. Control culture on BH and ONR7a medium containing scaffold saturated with hexadecane without the HC were also inoculated. Before treatment all the 3D scaffolds were sterilized by exposure to UV for 30 minutes.

3.2 Characterizations and Numerical Analysis

The following section deals with the description of the characterization methods herein adopted. Results will be presented and discussed in the following chapters.

3.2.1 Design of Experiments Using the Taguchi Approach

Taguchi has given the discipline and the structure of design of experiment (DOE), so that experimenters that work in different parts of the world employ similar design and obtain similar results [232]. First, he has established a set of orthogonal arrays (OAs), each of which can be used to describe a large number of experimental situations; second, he has devised a standard method for the analysis of the results.

The symbolic designation for the arrays carries the key information on the size of the experiment; in the L_8 orthogonal array, the number 8 indicates 8 runs are required. One basis property of the OAs is that each parameter is tested at each level the same number of times; so, the values of the parameters are tested in a fair and balanced manner [233]. Experiments design by OAs are attractive thanks to experimental efficiency, but there are some potential tradeoffs. OAs work well when the interaction between factors are minimal, that is the effect of one factor does not change with the level of another factor [234]. Moreover, the best combination of the factors could not be in the runs performed because the OAs only represents a portion, which includes all the independent combinations of the factors chosen, of all the possible experiments [234]. Nevertheless, the combination of standard experimental design techniques and analysis methods, in Taguchi approach, has produced consistency and reproducibility rarely found in any other statistical method.

The Taguchi's technique includes several steps. After the problem identification, it follows:

1. Brainstorming to identify all influencing factors to be included in the study; setting of their levels.
2. Design of experiments by selecting the appropriate Taguchi's orthogonal array.
3. Running of the experiments.
4. Analysis of the results to determine the optimum conditions.

5. Confirmation experiment.

These steps are in contrasts with the traditional techniques in which some initial ideas are tested, followed by other ideas and tests and so on. Before beginning the experimental runs, Taguchi's approach decides the entire process, i.e. the factors, the levels, how run the tests, how analyse the results. Taguchi's approach can be employed to obtain the optimal values of parameters for the configuration design with the minimum number of investigation.

3.2.2 Analysis of Variance

The analysis of variance (ANOVA) is the most common statistical method applied to results, in a factorial design of experiments, to determine which factors examined have most influence on the property of interest. The effect of one factor represents the variation of the response of interest of the process varying the levels of the same factor.

ANOVA computes quantity called sum of squares, degree of freedom, variance and variance ratio and organizes in standard tabular format [232]. ANOVA uses a F-test to determine the statistically significant factors within the confidence interval examined. To better understand the analysis applied in this study, we first explain how to apply ANOVA to a L_8 matrix with seven factors each at two levels (our case study).

Table 1 - L_8 Taguchi orthogonal array for a seven parameters and two-levels experiment. The additional column on the right is related to the values obtained for the generic property studied.

Expt. no.	A	B	C	D	E	F	G	Property y
1	1	1	1	1	1	1	1	**y_1**
2	1	1	1	2	2	2	2	**y_2**
3	1	2	2	1	1	2	2	**y_3**
4	1	2	2	2	2	1	1	**y_4**
5	2	1	2	2	1	1	2	**y_5**
6	2	1	2	1	2	2	1	**y_6**
7	2	2	1	2	1	2	1	**y_7**
8	2	2	1	1	2	1	2	**y_8**

Table 1 displays the L_8 OA with an additional column related to the values obtained for the generic property to be maximized. The A-G letters refer the seven factors investigated, each at level 1 or 2, while "y_1" represents the mean value of the property obtained from the experiment no. 1, "y_2" represents the mean value of the property obtained from the experiment no. 2, and so on.

ANOVA partitions total variation of one property into its appropriate components [235]: the variation due to each factor, the variation due to the interaction between factors and the variation due to error. Taguchi methodology only takes into account the variation due to each factor and not the interactions between factors and the error. The equation of the total variation can be defined as

Eqn. 1: $SS_T = SS_A + SS_B + SS_C + SS_D + SS_E + SS_F + SS_G$

where SS_T = total sum of squares, SS_i = sum of squares due to *i*-factor (*i*=A,B,…G)

SS_T is the measure of the total variation of the property, while SS_i is the measure of the variation of the property due to the individual factor. The sum of squares for the factor A, column 1, is

Eqn. 2: $SS_A = \frac{(A_1 - A_2)^2}{N}$

where N is the number of observations (equal to 8 for L_8 array), A_1 and A_2 are the sum of the values y_i related with the level 1 and the level 2, respectively, of the factor A. That is

Eqn. 3: $A_1 = y_1 + y_2 + y_3 + y_4$

Eqn. 4: $A_2 = y_5 + y_6 + y_7 + y_8$

In the same way are calculated the sum of squares related to the other factors SS_B, SS_C, SS_D, SS_E, SS_F, SS_G. While performing ANOVA, the degrees of freedom (DOF) have also to be considered together with each sum of squares. The total degrees of freedom DOF_T are calculated:

Eqn. 5: $DOF_T = N - 1 = 8 - 1 = 7$

The degrees of freedom of the factor A are:

Eqn. 6: $DOF_A = k_A - 1 = 2 - 1 = 1$

where k_A is the number of levels of factor A. At the same way, the degrees of freedom of the other factors are equal to 1. The next step calculates the variance (*V)* due to *i*-factor, as the sum of squares of the factor divided its degrees of freedom:

Eqn. 7: $V_i = \frac{SS_i}{DOF_i}$

where *i*= A, B, …G.

In ANOVA studies, error variance determination is very important. Since Taguchi's matrices do not assign columns for error evaluation, the column factor with the

smallest effect is considered assigned to the error and used to evaluate the error variance V_e [234]:

$$Eqn.\ 8:\ V_e = \frac{SS_e}{DOF_e}$$

where SS_e is the sum of the squares due to the error (variation due to the error), coincident with the smallest value among SS_i values, and DOF_e indicates the degrees of freedom of the error; by definition $DOF_e = DOF_T - \Sigma\ DOF_i$.

The tool to see which design parameters are statistically significant on the quality characteristic is called *F*-test. Obtained data are used to estimate F value:

$$Eqn.\ 9:\ F = \frac{V_i}{V_e}$$

This value of F calculated, F_{calc}, is compared with the value F_{crit} obtained by proper tables (*F*-tables) as a function of confidence level, degrees of freedom of the numerator and degrees of freedom of the denominator (namely error). Each combination of this three information is related to one F_{crit} value. The confidence levels generally taken into account are 99%, 95% or 90%. A factor is statistically significant when the condition $F_{calc} > F_{crit}$ is verified, otherwise the factor is not statistically significant.

When there are not statistically significant effects, a better evaluation of error variance can be carried out by merging the effects of more columns. This combination of the effects is called pooling. There are two strategies of pooling, the pooling up and the pooling down [234]. The strategy of pooling up, applied in this study, involves the *F*-test execution on the column effect immediately larger than the smaller effect (taken as error). If the new effect is also not statistically significant, the two effects are gathered together and assumed as error to test the effect of the next larger column. This iterative process goes on until there is statistical significance. Since the effect of the error increases, it may occur that no effect is significant.

3.2.3 Morphological Analysis

Morphology of the porous structures was evaluated by scanning electron microscopy (SEM), (Phenom ProX, Phenom-World, Figure 9A).

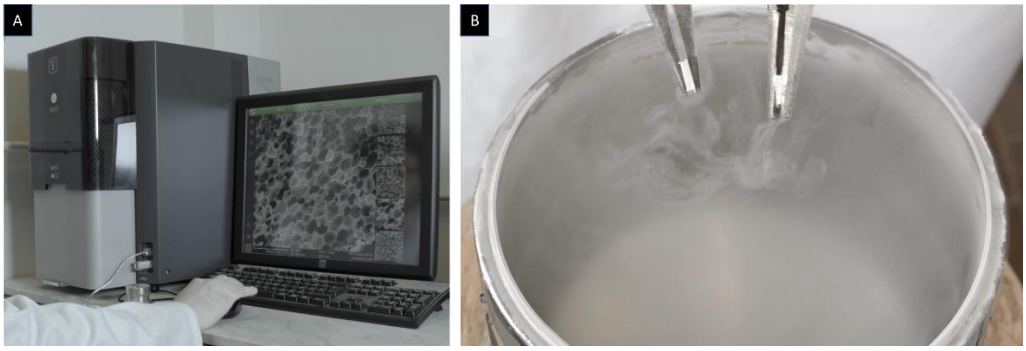

Figure 9 – A) Scanning electron microscopy, (Phenom ProX, Phenom-World); B) Sample broken under liquid nitrogen

The samples, broken under liquid nitrogen (Figure 9B), were attached on an aluminum stub using an adhesive carbon tape and then sputter coated with gold (Sputtering Scancoat Six, Edwards) for 90 s under argon atmosphere before imaging to avoid electrostatic discharge during the test.

3.2.4 Image Processing

Total porosity is usually measured by gravimetry [236,237]. Mercury intrusion porosimeter allows measuring both the open porosity (i.e. of the pores that are reachable by the mercury) [236,237] and the pores dimension [238], by using the Washburn equation [238]. Moreover the open porosity can be calculated also by liquid displacement method [239]. In this case, a specimen of the porous material is immersed in a known volume of liquid that, on increasing pressure, gives information on its empty volume.

However, biomaterials are often very soft and can be significantly deformed or damaged under strong pressures thus modifying the actual pore size. Moreover, if the pores are interconnected by channels much smaller than the pore itself, the intrusion methods do not allow getting the correct pores distribution. In latter case, methods based on image processing (IP) are definitely more effective. IP was developed in the past decades to characterize several different structures: devices for tissue engineering [43], water treatment [240] and other applications such as soil characterization [241] and pitting corrosion [242].

More in detail, by SEM, the images can be analyzed using appropriate software that are able to measure the porosity and, above all, the dimension of pores sections, visible

on the 2D fracture surface [11,117]. The IP processing on images acquired by SEM allows a direct evaluation of the thickness of the walls of the structure, of the pores diameter, of the interconnection level and of the eventual anisotropy. Moreover, the recent developments of microcomputed tomography (micro-CT) allowed determining porosity and PSD on a 3D basis [243,244].

One of the most delicate phases of the IP characterization of porous structure is the so-called image segmentation, i.e. the set of procedures able to determine the interesting regions of the image that, in the examined case, are those occupied by pores. The non-automatic application of the segmentation operations implies a large waste of time and can be particularly difficult or even impossible for complex systems. In order to overcome this problem, over the past years there have been developed some software-assisted procedures.

Typically, for instance in polymer based porous materials, in the images obtained by SEM, the regions occupied by pores have a brightness intensity level lower than those occupied by the polymeric phase. In the ideal case, it is sufficient to determine a pixel intensity threshold value to easily distinguish the portions of images belonging to polymer and those belonging to the pores. Once this threshold level is determined, it is possible to obtain a binary image, having pixel intensity set to 1 in the regions corresponding to pores and to 0 in the background, and therefore the pore size distribution (PSD**)** can be evaluated very easily by analyzing its properties. However, in many practical cases, the irregularity of the inner morphology of the porous devices makes the threshold level very variable in the different regions of the same image, so that an effective segmentation requires the application of complex and/or specifically developed procedures.

Pore Size distribution

In the frame of this work, pore size analyses were carried out using a MATLAB (MathWorks Inc., MA, USA) based software. The custom-made software is able to accomplish the segmentation of images containing pores of any geometry in a semi-automatic way. It converts the digital images into binary form and then calculates the pores area distribution (PAD). The software reports the percentage of the total area occupied by the pores having diameters in a given interval. The different colors were

assigned to three increasing intervals of the size of the pores. PAD were calculated in different seven region of the scaffolds. The showed histograms are representative data.

Fibers Diameter Analysis

Fiber diameter distribution was determined by using Diameter J. It is a plugin, created for ImageJ, able to analyze an image and find the diameter of nanofibers at every pixel along a fibers axis. The software produces a histogram of these diameters and summary statistics such as mean fiber diameter [245].

3.2.5 Porosity, Fluid Uptake, Connectivity

The parameters related to porous properties of the structures were obtained by gravimetric measurement. Theoretical porosity, porosity and connectivity were calculated according to the following expression [46]:

Eqn. 10: $Porosity_{th}(\%) = \frac{V_{porogen}}{V_{total}} \times 100\ \%$

Eqn. 11: $Porosity\ (\%) = \left(1 - \frac{\rho_{scaffold}}{\rho_{matrix}}\right) \times 100$

Eqn. 12: $Connectivity = \frac{(m_0 - m_{dry})}{m_{NaCl} + m_{PEG}} \times 100\ \%$

m_{NaCl} and m_{PEG} are respectively the theoretical mass of NaCl and PEG, by assuming homogeneous blends. m_0 is the weight of scaffold before leaching and m_{dry} the weight of the device dried after leaching. The density (ρ) of NaCl, PEG, PLA and PCL are respectively 2.16 g/cm^3, 1.12 g/cm^3, 1.24 g/cm^3 and 1.14 g/cm^3 . $\rho_{scaffold}$ is the apparent density of the scaffold.

The theoretical porosity was calculated by assuming the complete solvation of all the porogen agents (PEG and NaCl). The real porosity was calculated as the reciprocal of the ratio between the apparent density of the scaffold and the non-porous polymeric material density by using expression (2). It expresses the ratio between the empty volume of the scaffold and its full volume (empty + full). Connectivity is a parameter

that give information about the continuity of the porogen phases and was evaluated using Eq. (3). It was determined by evaluating the variation of weight of the scaffold before and after the porogen agent extraction.

The bulk water absorption (water uptake) was evaluated as the difference between the weight of the humid devices (m_{wet}) and the weight of the dry sample according to

$$Eqn.\ 13:\ Water\ uptake\ (\%) = \left(\frac{m_{wet} - m_{dry}}{m_{dry}}\right) \times 100\ \%$$

The percentage of pores filled by water was evaluated as the ratio between the volume of water into the scaffold and the empty volume given by the real porosity. The volume of water filled by the devices was evaluated as the weight difference between the dry and wet sample.

3.2.6 Surface Area

Surface area and pore size measurements were performed by using a Sorptomatic 1900 Carlo Erba Instrument. Before measurement, each sample was outgassed under vacuum at 120 °C for 3 h. Surface area was determined by physical adsorption of N_2 at the liquid nitrogen temperature, using the Brunauer–Emmett–Teller (BET) equation [26]. Pore size distributions were obtained from the desorption curve of the isotherm, by using the procedure developed by Dollimore and Heal [246].

3.2.7 Oil Uptake and Membrane Reusability

The oil uptake of oil removal sponge (ORS) was evaluated by immersing the samples in a backer containing the oily waste. In particular, the mass-based and volume-based oil absorption capacity (oil uptake) were calculated according to

$$Eqn.\ 14:\ Mass - based\ oily\ uptake\ (\%) = \left(\frac{m_{wet} - m_{dry}}{m_{dry}}\right) \times 100\ \%$$

Eqn. 15: $Volume - based\ oily\ uptake\ (\%) = \left(\frac{V_{wet} - V_{dry}}{V_{dry}}\right) \times 100\ \%$

where m_{wet}, V_{wet}, m_{dry}, V_{dry} respectively indicate the weights and the volumes of the sponge before and after oil absorption. For this measurement a precision balance (Sartorius AX224) with a resolution of ± 0.1 mg was used.

The reusability of the ORS was evaluated by removing the pollutant from the device by two methods depending on the boiling point of pollutant. High boiling point pollutants (motor oil and olive oil) were removed by rinsing ORS two times with 75 mL of diethyl ether for 30 min, in a soxhlet apparatus, in order to assess the possibility to recycle the ORS in a close system thus avoiding solvent loss. Thereafter, the ORS were dried for 6 hours in a fume hood to remove the diethyl ether.

In the case of volatile waste (gasoline), the pollutant was removed from ORS by direct evaporation. The vapors were then collected and condensed for recycling. In particular, ORS were dried in a fume hood overnight. The minimum time necessary to totally remove the gasoline by simple evaporation was experimental determined.

3.2.8 X-Ray Diffraction Analysis

The microstructure of nanocomposites and nanoparticles were investigated by X-ray Diffraction (XRD) using an Empyrean PANalytical II diffractometer with a Cu Kα radiation source (λ = 1.5406 Å). The XRD patterns were recorded in the 2θ range 5–30 at a scanning speed of 1 θ /min at ambient temperature.

3.2.9 Differential Scanning Calorimeter Analysis

Differential scanning calorimetry (DSC) (DSC131 evo, SETARAM Instrumentation, France) was performed in a temperature range of 0–100 °C at a heating rate of 5 °C/min to evaluate the thermal properties of the scaffolds. Dried samples with a weight of approximately 10 mg were loaded in an aluminum pan.

The crystallinity of electrospun materials were then evaluated using the following equation:

Eqn. 16: $\chi_c\,(\%) = \frac{\Delta H_m}{\Delta H^0{}_{PCL} \times X_{PCL}} \times 100$

Where $\chi_c\,(\%)$ is the percent crystallinity of PCL, X_{PCL} is the weight fraction of PCL, and $\Delta H^0{}_{PCL} = 135.44\ J/g$ stands for the enthalpy of fusion of 100% crystalline PCL [247].

3.2.10 Complex Viscosity Determination

Rheological characterization tests were performed using a plate–plate rotational rheometer Mars (Thermofisher). A 25-mm parallel-plate geometry was used and all tests were performed at 25 °C. Oscillatory frequency sweep tests were performed at a constant stress of 1 Pa with an increase of angular frequency from 1 to 100 rad/s.

3.2.11 Mechanical Properties

The 3D porous structures were mechanically tested under compression using an Instron 3365 mechanical testing machine (UK). The cylindrical specimens (3:10 height to diameter ratio) were tested in compression mode until failure with an uniform crosshead speed of 1 mm min^{-1}.

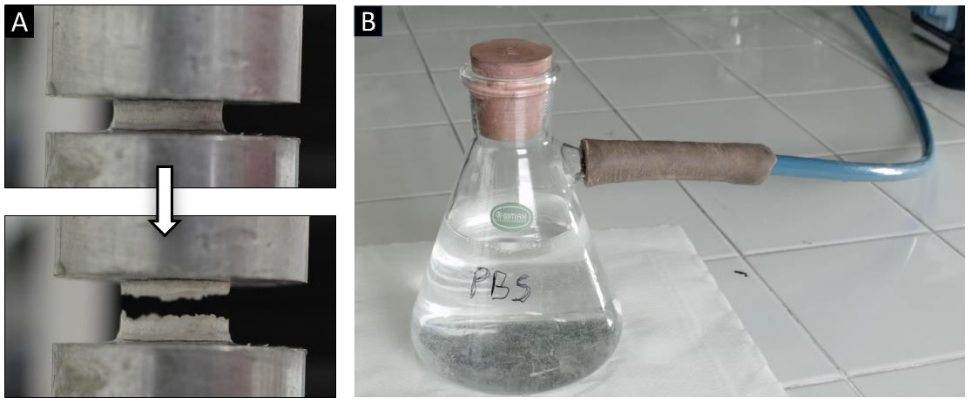

Figure 10 – A) Custom-designed interfacial strength test equipment; B) Vacuum flask used for fill 3D porous structures with PBS before mechanical tests.

The tensile stress-strain curves of the 3D porous structures were obtained using a custom-designed interfacial strength test equipment fitted to an Instron 3365 (UK)

testing machine (Figure 10A), following a method described in the scientific literature [19,55]. The rig design allows the secure fixation of the scaffold during testing while ensuring the correct alignment of the sample between the machine's load cell and base platen. Samples were adhered to aluminum test stubs of the equipment using a high viscosity adhesive (Patter Power Epoxy).

The tests were performed both in PBS, (pH=7.4) at 37 °C (wet condition) and in air at room temperature (dry condition). In order to prepare samples to measurements in BioPuls Bath, they were filled by PBS in a vacuum flask for 5 min to let PBS to fill all the pores as shown in Figure 10B. Subsequently scaffolds were left in PBS at 37 °C for 15 min to achieve the test temperature (Figure 11A,B).

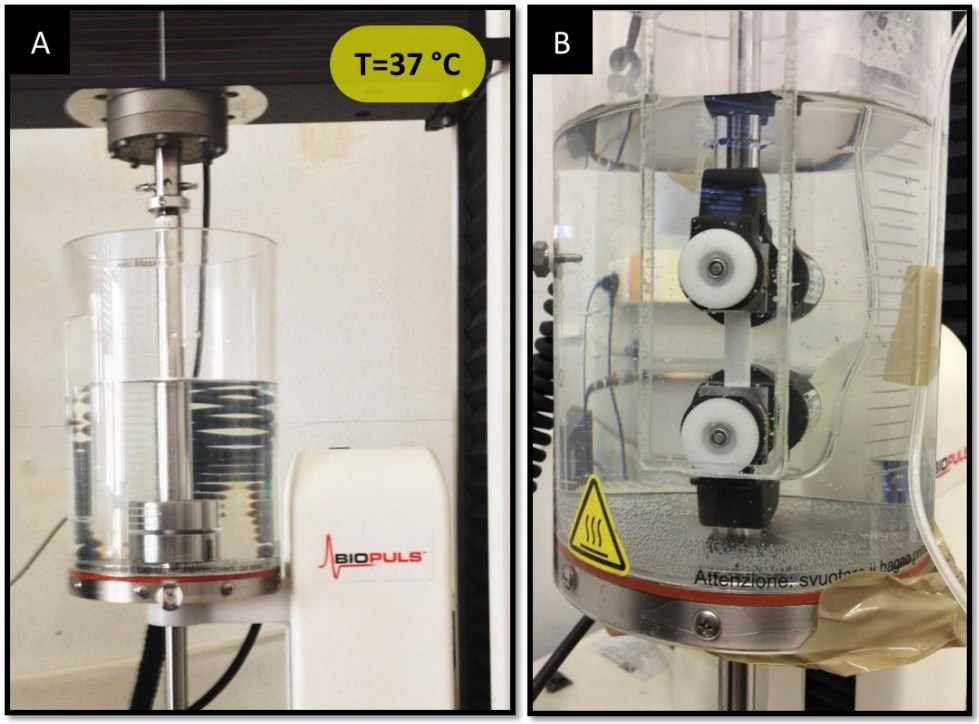

Figure 11 - Pictures of the mechanical experimental setup immersed in PBS at 37 °C. A) Compressive test; B) Tensile test.

A 1 kN load cell was used under a tensile load applied at a crosshead speed of 1 mm min^{-1}. Failure was expected to occur either at the ultimate tensile strength (TS) of one of the component layers of the scaffold or as a result of delamination at the layer interfaces. The interfacial adhesion strength was evaluated as the maximum strength of the stress strain curve. Seven specimens were measured for each material. The mechanical analyses were performed before and after the collagen treatment but not

significant differences were found. For sake of brevity, the data obtained after the collagen treatment were shown.

2D porous structures were mechanically tested only in tensile mode.

3.2.12 Wettability and Surface Properties

Static Contact Angles

Static contact angles were measured on all the samples using an FTA 1000 (First Ten Ångstroms, UK) instrument. More in detail, 4 μL of fluid were dropped on the fiber mats with an automatic liquid drop dosing system. Images of the drop on the surface were taken after 20 seconds. Tests were performed on PLA and PLA-plasma films obtained by solvent casting and on PLA and PLA-plasma nanofibrous membranes. The angle measurements were taken 1 hour after the sample modification. At least 7 spots of each composite nanofiber mat were tested and the average value was taken.

In order to evaluate the SE of the materials, water (polar liquid) and diiodomethane (Sigma Aldrich, dispersion liquid) were chosen as fluids.

It is assumed that the SE (γ_S) has two components: dispersive (γ_S^d) and polar (γ_S^p) [248]. In such case:

Eqn. 17: $\gamma_S = \gamma_S^p + \gamma_S^d$

Considering the two components of SE Owens and Wendt proposed the equation:

Eqn. 18: $\gamma_{SL} = \gamma_S + \gamma_L - 2\left(\gamma_S^d + \gamma_L^d\right)^{0.5} - 2(\gamma_S^p + \gamma_S^p)^{0.5}$

From the Eqns. (17) and (18):

Eqn. 19: $\gamma_L \frac{1+cos\theta}{2} = (\gamma_S^d \gamma_L^d)^{0.5} + (\gamma_S^p \gamma_L^p)^{0.5}$

To determine γ_S from the equation (17), contact angles (θ) measurements must be made for two different liquids with known values of γ_L^d and γ_L^p. For this purpose water (γ_L^d = 21.8 mJ/m^2, γ_L^p = 51 mJ/m^2) and diiodomethane (γ_L^d = 48.5 mJ/m^2, γ_L^p = 2.3 mJ/m^2) were used. Using these two liquids, SE is calculated from the set of equations [35]:

Eqn. 20: $$\begin{cases} \left(\gamma_S^d\right)^{0.5} + 1.53\left(\gamma_S^p\right)^{0.5} = 7.80\ (1 + cos\theta_W) \\ \left(\gamma_S^d\right)^{0.5} + 0.22\left(\gamma_S^p\right)^{0.5} = 3.65\ (1 + cos\theta_D) \end{cases}$$

Where θ_W and θ_D are the contact angles obtained from water and diiodomethane drops respectively.

X-ray photoelectron spectroscopy

X-ray photoelectron spectroscopy (XPS) spectra were recorded with a PHI 5000 VersaProbe II scanning XPS Microprobe using monochromatic Al-Kα radiation (hν = 1486.6 eV) from an X-ray source operating at 200 μm spot size, 30 W power, and 15 kV acceleration voltage. The (iterative) Shirley background subtraction and the peak fitting with Gaussian–Lorentzian-shaped profiles were performed for the high-resolution XPS spectra analysis using Multipak software version 9.6.0.15 (ULVAC-PHI). The detected spectra were shifted to coincide with the C 1s hydrocarbon peak at 285 eV. To resolve and analyze the chemical bonding states of the carbon atoms, a Shirley type background was subtracted and Gaussian–Lorentzian peak components were fitted to the C 1s high-resolution spectra.

Attenuated Total Reflectance Fourier Transform Infrared

The attenuated total reflectance Fourier transform infrared (ATR-FT-IR) spectrometry was performed using a Perkin-Elmer spectrum one spectrometer in the 4000–400 cm^{-1} wavenumber range at room temperature. 16 scans with a resolution of 4 cm^{-1} were performed on samples for each spectrum. The use of ATR-FT-IR allowed the direct analysis of the surface of the samples.

3.2.13 Biological essays

Biocompatibility Evaluation Porous Structures

To evaluate the absence of cytotoxicity from scaffold on the cells, we carried out the Acridine Orange (AO) essay. Each scaffold and the positive control were stained with [100 μg/ml] of AO solution (Sigma) for 10″; thoroughly washed with Phosphate Buffer Saline (PBS; EuroClone) and immediately examined by fluorescence

microscopy (490–530 nm). The apoptotic cells were identified on the basis of well documented morphological criteria, most obviously by their characteristically condensed chromatin stained by the acridine orange.

Laser Scanning Confocal Microscopy

Laser Scanning Confocal Microscopy (LSCM) analysis of cell in co-culture grown on the scaffold

Co-culture of MC3T3-E1 and NIH3T3 cell lines were carried out on the device in order to evaluate a differential cell permeability in the multi-layered devices. The MC3T3-E1 cells and the NIH3T3 cells were seeded on different layers of the same multi-layer scaffold. Cells in co-culture were grown in DMEM for six days; the culture medium was changed three times. For the confocal analysis preparation the samples were fixed with acetic acid/methanol (1:1/v:v) solution on ice for 15 min, washed with PBS and stained by propidium iodide (PI) (1:3000) for 30 min.

Bacterial Cultivation Profile Analyses

Protein extraction from biomass samples, collected from free and immobilized mycelium at different growth times, was performed by sonication according to Puglia et al [249]. Protein concentration was determined using the Bradford reagent [250].

Actinorhodin from samples was collected at different growth times from either free or immobilized mycelium cultivations. It was extracted by using KOH (1N) and spectrophotometrically quantified at 640 nm according to Kieser [229].

4 Results and Discussion

4.1 Development of a facile method to determine pore size distribution in porous scaffold by using image processing

Herein it will be described a digital imaging procedure able to accomplish the segmentation of images containing pores of any geometry and able to measure the PSD in a semi-automatic way. In order to test the effectiveness of the procedure, we carried out an analysis of the complex structure of a homemade polymer-based scaffold for bone cartilage regeneration and of a similar structure prepared by other authors.

Image Processing

The procedure for the segmentation of the images has been developed using the Matlab® programming language; it consists in four steps that are represented in the flow chart of Figure 12:

1) pre-processing of the image,

2) assisted procedure for threshold determination,

3) binarization and morphological analysis,

4) verification procedure.

In order to simplify the analysis, the matrices of grey levels I_0 are scaled to assume values in the range 0 (black) and 1 (white).

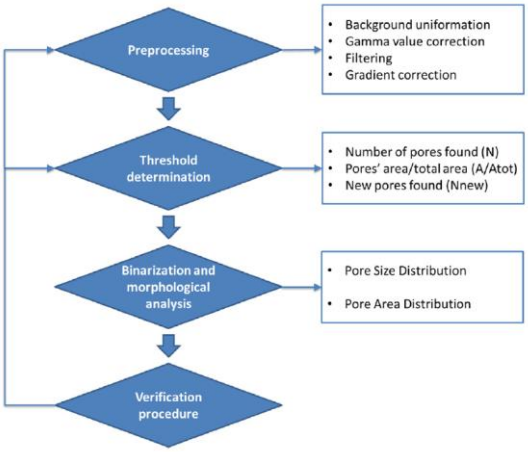

Figure 12 - Schematic flow chart of the image-processing algorithm.

Pre-processing

In the pre-processing step, the original acquired image is modified in order to eliminate disturbing elements from the image, to maximize the contrast between walls an pores and to even the threshold value that allows identifying the pores on varying the spatial coordinates of the image. In this phase, both classical procedures of contrast e*nhancement* of the digital images [251,252] and two procedure specially developed for the analysis of the pores are applied, according to the choices made by the operator.

The classical procedures used in the pre-processing step are the application of a median filter and the so called *gamma correction* of the image [251].

The application of a median filter with an appropriate dimension of the filtering window is carried out in order to eliminate both the electronic noise and alien elements having dimension smaller than the pores and not useful for the elaboration [251,252]. The median filtering is always carried out and the length of the side of the pixel windows is usually chosen of 3 or 5 pixels.

The gamma correction [251] consists in elevating the grey levels matrix I_0 to an exponent γ as

Eqn. 21: $$I(i,j) = I_0^{\gamma}(i,j)$$

with the aim to increase the contrast between the darker parts of the images, related to the pores, and the brighter ones, related to the background. Values of the exponent in the field $0<\gamma<1$ increase the contrast in the regions of the image having lower values of intensity, while values in the field $\gamma>1$ [251] increase the contrast in the regions with higher values. The operator has to decide if the gamma correction has to be applied and to select the value of the γ exponent that, in the analysis of pores, is suggested to be in the range [0.2, 2.0].

As regards the two procedures specially developed, the first one increases the contrast between the regions of the image occupied by the pores and those occupied by the walls using the gradient of the intensity in the pixels, while the second one corrects the non-uniformity of the brightness intensity on varying the spatial coordinates of the image to even the threshold value that allows identifying the pores. The two procedures will be referred to as *procedure to increase contrast* and *procedure to correct uniformity*.

The procedure to increase contrast can be effectively applied when the pores are characterized by a surface roughness much lower than that of the walls, as shown by the SEM micrograph reported in Figure 13A. In these cases the region of the image occupied by the pores are characterized by a local intensity gradient lower than that in the neighbour zones. In the procedure to increase contrast, the value of the brightness gradient for each pixel is initially determined simply as [251,252]

Eqn. 22:
$$G'(i,j)=\sqrt{\left[I(i,j+1)-I(i,j)\right]^2+\left[I(i+1,j)-I(i,j)\right]^2} \quad (2)$$

then the resulting values are linearly scaled in order to make them vary in the same intensity range of the image, i.e. [0,1],

Eqn. 23:
$$G(i,j)=\frac{G'(i,j)}{\max_{i,j}\left\{G'(i,j)\right\}} \quad (3)$$

Finally, the values of intensity and gradient are summed

Eqn. 24:
$$I'_G(i,j)=I(i,j)+G(i,j) \quad (4)$$

and linearly scaled in the field [0,1]

Eqn. 25:
$$I_G(i,j)=\frac{I'_G(i,j)}{\max_{i,j}\left\{I'_G(i,j)\right\}} \quad (5)$$

In Figure 13B the effect of applying this technique to the image of Figure 13a is shown.

The procedure to correct uniformity is carried out to correct the non-homogeneous illumination of the material surface during the acquisition of the image. This effect is clearly visible in Figure 13A,B where the regions of the images close to the low-left edge are darker than the neighbour areas.

In particular, the procedure to correct uniformity consists in the four steps described in the following.

Firstly, the pores are eliminated from the image by applying a sequence of median filtering operations [251,252] using pixel windows with size increasing up to a dimension larger than that of the pores. The median filtering can be applied using conventional square shaped pixel windows, nevertheless, in the proposed procedure, more effective circularly shaped windows have been used. The image obtained is

herein referred to as *background image*, I_B. It is possible to observe that the intensity of I_B in each pixel is proportional to the illumination level on the material surface during the acquisition. The mean value of I_B is also determined as

Eqn. 26: $$I_{B_{\text{mean}}} = E\left[I_B(i,j)\right] \quad (6)$$

In the second step the intensity of the background image is subtracted to that of the original image, obtaining the *deviation matrix* I_D

Eqn. 27: $$I_D(i,j) = I(i,j) - I_B(i,j) \quad (7)$$

In the third step the intensities of the pixels of the deviation matrix are multiplied by factors related to the intensity of the background image in order to correct the non uniformity. In particular each intensity is multiplied by the ratio between the maximum value of the intensity of the background image, $I_{B\max}$, and the local intensity of the background image obtaining the *uniform deviation matrix* as:

Eqn. 28: $$I'_{DU}(i,j) = I_D(i,j)\frac{I_{B_{\max}}}{I_B(i,j)} \quad (8)$$

The values of the uniform deviation matrix are then scaled in such a way that the modulus of the its minimum value, that is a negative number, is equal to the mean value of the background intensity (6), for the reason explained in the following:

Eqn. 29: $$I_{DU}(i,j) = I'_{DU}(i,j)\frac{I_{B_{\text{mean}}}}{\min_{i,j}\left\{\left|I'_{DU}(i,j)\right|\right\}} \quad (9)$$

In the last step the mean value of the intensity of the background image (6) is added to the intensities of the uniform deviation matrix obtaining the *uniform image*

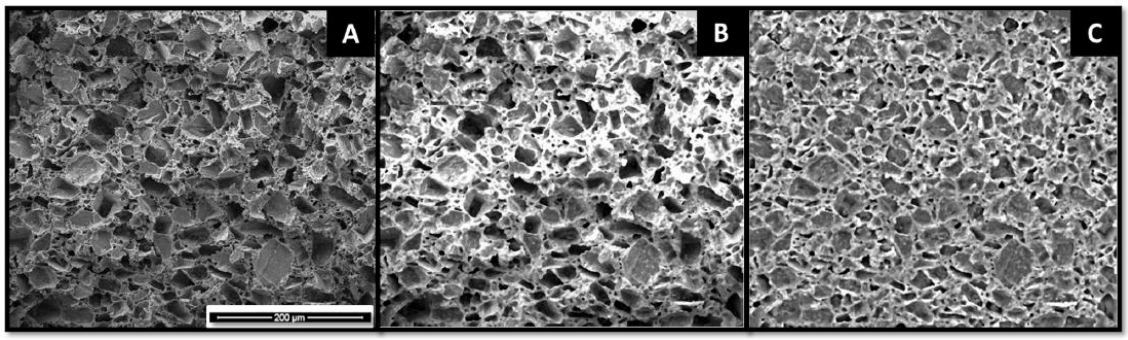

Figure 13 - Analysis of a ternary blend PLA/PEG/NaCl (45–65 µm): (A) original SEM micrograph; (B) image obtained by the application of the procedure for increasing the contrast; (C) image obtained by the application of

both the procedure for increasing the contrast and the procedure for correcting the non-uniformity of the brightness intensity.

$$I_U(i,j) = I_{DU}(i,j) + I_{B_{mean}} \qquad (10)$$

Notice that, by means of Eq.(9), the minimum intensity of the uniform image is 0.

The efficacy of the procedure can be observed by comparing the final result shown in Figure 13C with Figure 13B.

Summarizing, in Figure 13A it is possible to observe the image as acquired, in Figure 13B the sole effect of procedure to increase contrast, while in Figure 13C the combined effect of both the procedures to increase contrast and to correct uniformity. In the final image, the contrast between the walls and the pores is clearly higher than that of the original image.

Assisted procedure for threshold determination

The second step consists in determining the most appropriate threshold level to binarize the image, in order to obtain a graphical mapping of the pores distribution. The proposed procedure automatically provides the operator with information that help to find the best threshold level.

In particular, the image obtained by the pre-elaboration step is binarized by using as threshold values all the intensity levels of the image, starting with 0. For each binarization the following parameter are determined: number of pores (N), ratio between the area occupied by pores and the total area (A/Atot), number of new pores found with respect to the previous threshold value (Nnew). Such parameters are then shown as a function of the threshold value (Figure 14) to ease the operator in choosing the best level, in the way described in the following. The graphs reported in Figure 14 are hereinafter referred to as Threshold Analysis Diagrams (TADs).

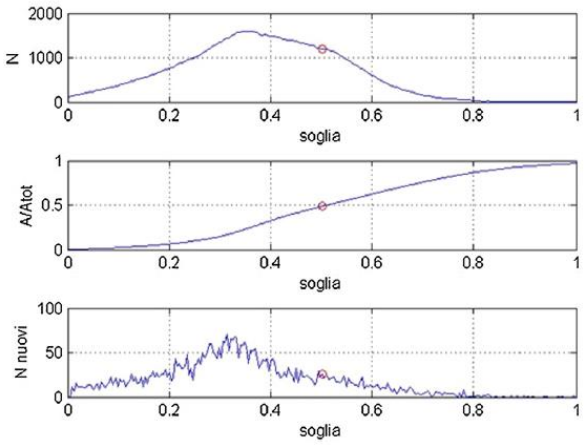

Figure 14 - The TAD: number of detected pores (N), cumulative area of pores compared to total area (A/Atot) and number of detected new pores (Nnew), as a function of the threshold level obtained by processing the micrograph of the PLA/PEG/NaCl (45–65 µm) blend.

Binarization and morphological analysis

In this step the binary image of the pores is determined using the selected threshold level and the binary image is elaborated to determinate the regions of the image occupied by each pore [51,52]. Morphological operations are also used to determinate the boundaries of the pores [52].

The areas of the pores are determined in number of pixels and converted in square micrometers, using the peak marker of the micrograph as scale factor.

The results obtained by the analysis are summarized in two histograms. The first one represents the PSD Figure 16A; it reports the number of pores having diameters in a given interval. The second histogram represents the Pores Area Distribution Figure 16B; it reports the percentage of the total area occupied by the pores having diameters in a given interval. The red, green and blue colours are assigned to three increasing intervals of the size of the pores; furthermore the intensities of the colours are made proportional to the size of the pores. This representation has been proposed to facilitate the analysis of the results.

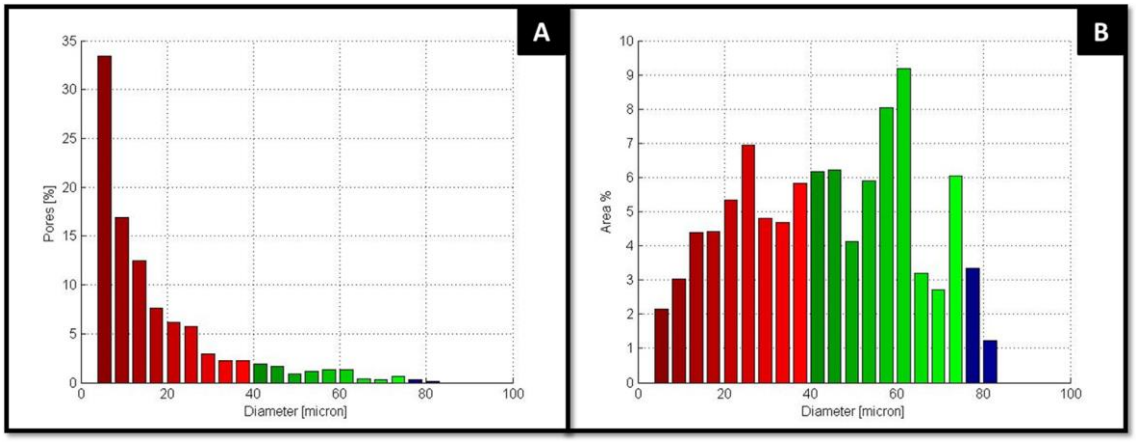

Figure 15 - (A) original image obtained by SEM microscopy; (B) boundaries of pores determined by the program; (C) map of the pores automatically determined by the program, shown in different colors according to the size range (blue: larger, green: intermediate, red: smaller) (For interpretation of the references to color in this figure legend, the reader is referred to the web version of this article).

Verification procedure

In order to verify if the parameters selected in the previous steps have leaded to a correct identification of the pores in the image, the original SEM micrograph (Figure 16A) and two images respectively with the boundaries and the areas of the pores superimposed to the original image (Figure 16B,C) are shown to carry out a visual comparison. Also in this representation, the red, green and blue colours are assigned to three increasing intervals of the size of the pores, in order facilitate the analysis of the results.

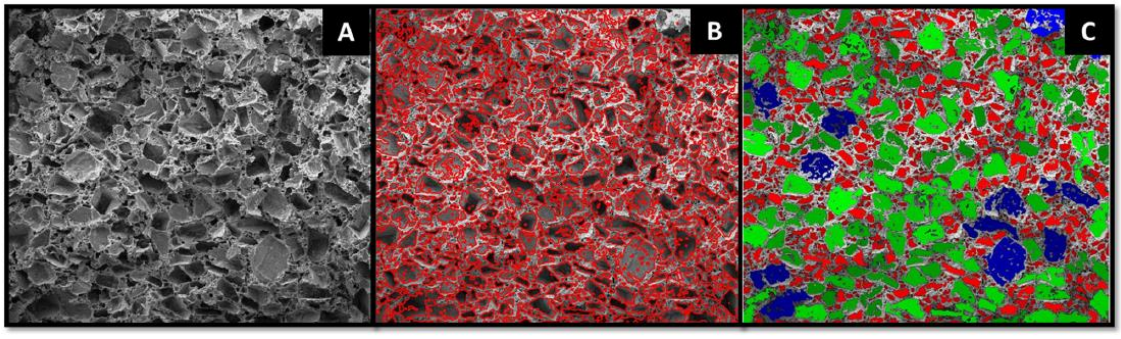

Figure 16 -(A) "Macro-pores" size distribution and (B) "Macro-pores" area distribution of PLA/PEG/NaCl (45–65 µm) blend (For interpretation of the references to color in text, the reader is referred to the web version of this article).

If the results of the verification procedure do not satisfy the operator, it is possible to modify the pre-processing parameters and/or the threshold level until the best compromise is achieved.

Results and Discussion

In order to verify the capability of the software to identify and analyze pores on structures and images with different characteristics, different SEM micrographs considering several magnifications have been used.

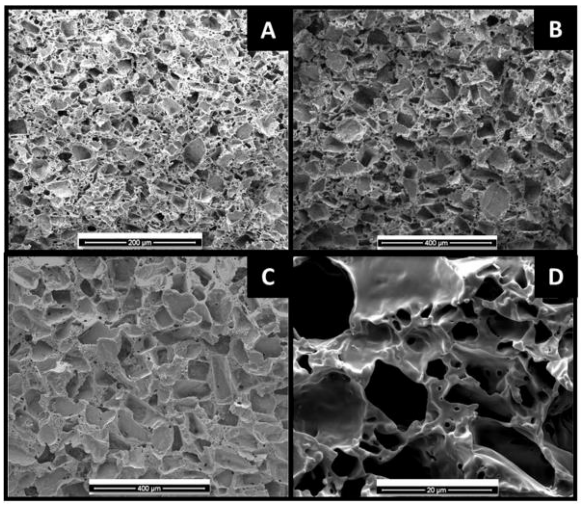

Figure 17 - Original SEM images of four different PLA scaffold morphology: (A) 90–110 µm pore size; (B) 45–65 µm pore size; (C) 0–40 µm pore size; (D) 0–80 µm pore size.

In particular, four different porous devices obtained by selective leaching of NaCl and PEG in boiling water of a PLA-PEG-NaCl blend processed in the melt. More in detail, the four sample micrographs are related to four different NaCl granulometries used to prepare the blends.

In Figure 17A it is shown a section of a PLA based device obtained by leaching the ternary system with salt particle size in the range 0-40 µm. The image shows a device architecture with very thin walls and with pores with a high density and a small dimension with respect to the whole image wideness.

In Figure 17B it is shown a micrograph similar to Figure 17A although the pores and the walls are slightly large. In this case, the particle size of the salt used to prepare the ternary blend falls in the range 45-65 µm. It can also be observed that the magnification is lower as revealed by the different pick marker.

In the third case, Figure 17C, the image is related to a ternary blend containing salt with a size in the range 45-65 mm. The magnification is the same of Figure 17B and the pores appear more regular and a lower distribution. The pores walls have a

thickness comparable with the dimension of the pores themselves that, at the magnification chosen, are fairly large compared to the whole image area.

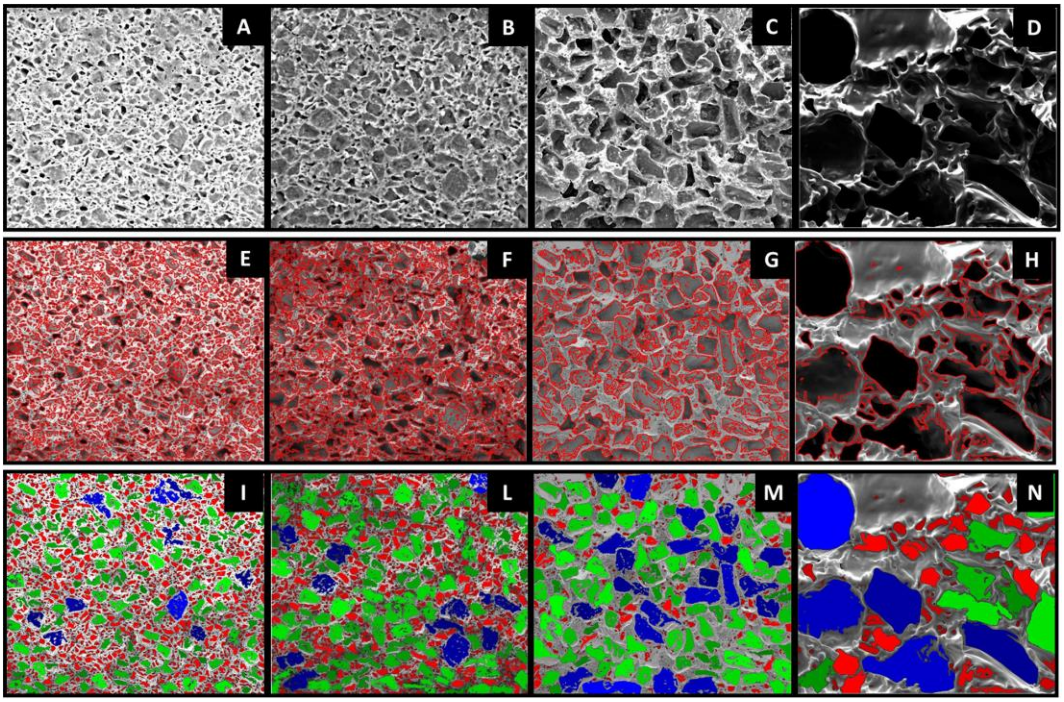

Figure 18 -A–D: images of four different scaffold morphology after the pre-processing step; E–H: boundaries of the pores determined by the program; I–N: maps of the pores determined by the program, shown in different colors according to the size range (blue: larger, green: intermediate, red: smaller)

The last image, Figure 17D, related to the ternary system containing salt with size in the range 0- 80 micron, was acquired with a higher magnification in order to better analyze pores smaller than 10 mm that can be attribute to the solubilisation of the PEG phase [253]. In this latter micrograph, the space surrounding the pores has to be attributed to a single wall of the structure that appears slightly notched.

Using the proposed procedures, an automatic segmentation of the images was carried out choosing the appropriate pre-processing parameters and threshold level.

In Figure 18A-N there are respectively reported: the images of the four scaffolds after the pre-processing step (Figure 18A-D), the boundaries of the pores determined by the program, superimposed to the original images (Figure 18E-H), and the areas attributed to the pores of the four leached system presented above, colored according to the size ranges (Figure 18I-N).

In Figure 19, the histograms analogous to those described in Figure 16 and Figure 18 and the TADs relative to the four scaffolds analyzed are shown. In particular, the

final PSDs of the blends PLA/PEG/NaCl with NaCl particle size of 50-110 µm, 45-65 µm, 0-40 µm and 0-80 µm are respectively shown in Figure 19 from a to d.

The images of Figure 18A-C have been pre-processed by both the procedures to increase contrast and to correct uniformity. The first procedure has been applied because the walls surrounding the macropores presented a high number of small pores that generate high levels of intensity gradient in the digitized image.

Figure 18D has been pre-processed by the procedure to increase contrast and that for gamma correction, using γ=2, obtaining a good definition of the pores edge with very good results in the determination of the size distribution, as shown in Figure 19.

Thus, the proposed procedure requires very few interaction with the operator and is able to recognize, with a high degree of reliability, the regions to be attributed to the pores, despite the presence of various confounding factors, such as irregularities of their geometries, low contrast, non uniformity of illumination. This is confirmed by the results shown in Figure 18E-H and Figure 18I-N, where the boundaries and the regions of the pores determined by the procedure are superimposed in the original images.

The final evaluation results allow concluding that each material presents a high number of small pores and no pores with larger dimension than the largest initial salt particle size. Nevertheless, these information, although useful, do not allow to know the distribution of the areas associated to the pores.

In Figure 19E-H the percent distribution of the areas associated to the pores are reported. It can be deduced that the most part of the area occupied by the pores is strongly influenced by the salt crystal size.

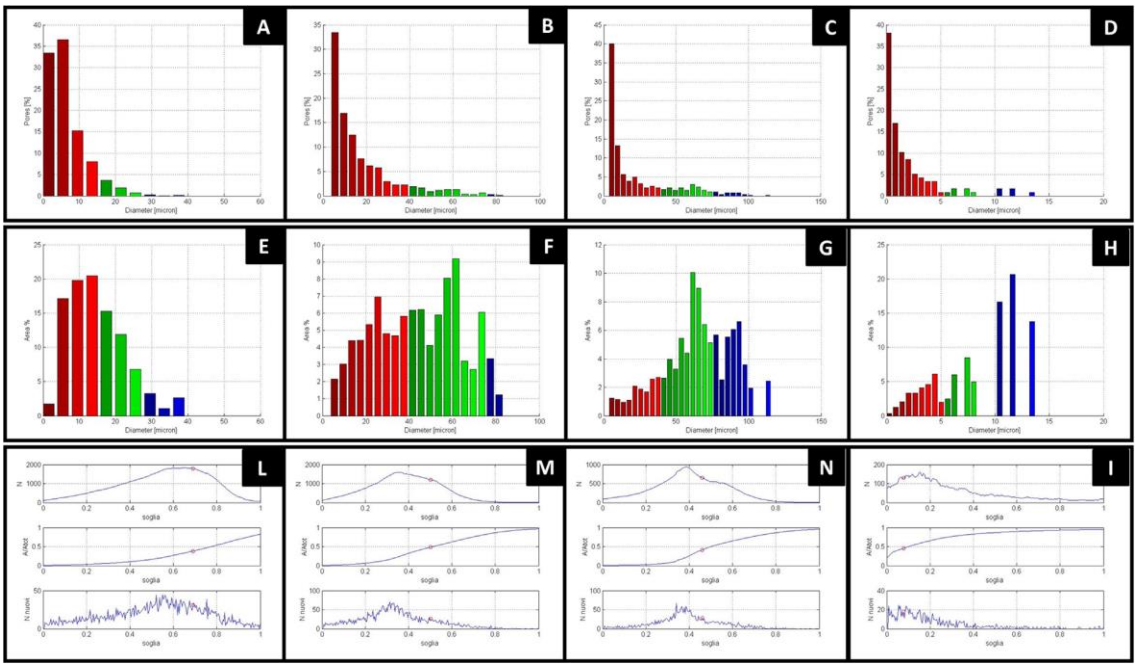

Figure 19 - A–D: histograms of the PSD of the four scaffold morphologies analyzed; E–H: histograms of the corresponding pores area distribution; L–I: corresponding TADs.

Moreover, the analysis of different images proved that the knowledge of TADs can be very useful in order to help the operator in the choice of the best threshold value.

In particular, it was observed that the best threshold level for the binarization always lies in the field where the number of detected pores N presents higher values, although it does not necessarily coincides with that corresponding to the maximum of N. Moreover, it was noted that the best threshold level almost always belongs to the field in which the curve that describes the A/Atot ratio presents a linear behaviour.

Nevertheless, these aspects require further investigation.

Table 2 - Declared pores size of scaffold from literature and pore size range obtained by the image processing.

Pore morphology	Mean pore size declared (µm)	Mean pore size by IP (µm)	References
Irregular	100–200	100–200	[173]
Irregular	100	10–60	[254]
Irregular	53±9	50–150	[255]
Elliptical	55	40–100	[255]
Spherical	200–700	200–700	[256]

Different geometric descriptors were used to analyze the pore size and shape from SEM images, including pore equivalent diameter (i.e. the diameter of a circle with the same cross sectional area), pore maximum opening, and inscribed circle diameter (i.e. diameter of the largest circle that can fit into the irregular pore shape). The 'inscribed circle diameter' parameter is evaluated as the diameter of the largest circle that would touch only two points on the pore boundary. The pore inscribed circle is particularly important since it may be directly related to membrane rejection characteristics. These pore geometric descriptors were determined at both pore top and pore mid-height to provide information on pore average size and maximum size to study the reproducibility of the technique [251,252].

The demonstration of the validity of the investigation process can be found in Table 2. In particular, in Table 2 there are summarized the results obtained by SEM analysis of porous scaffolds for tissue engineering prepared in the frame of different works, comparing the results reported in the original paper with those obtained with the analysis presented in this work.

Conclusion

In the present work a digital image processing procedure for the characterization of the porosity and pore architecture of materials have been developed.

It is based on the application of well known algorithm of image processing applied in a specially developed sequences.

The efficacy of the procedure has been verified analyzing the PSD and PAD of porous polymeric scaffold obtained by particulate leaching with different pore size and irregular pore morphology.

The software was able to recognize pores, and provide information about PSD and PAD of the porous devices with a semi-automatic procedure. Furthermore the software supply the operator with a colored maps of the different size range of the porous structure in order to simplify the analysis of the system.

Its use can be easily extended to soft materials such as hydrogels or membranes or all of those materials in which knowing the microstructure becomes crucial to ensure the functional performance required.

4.2 Optimization of Process Variables in the Manufacturing of 3D Porous PLA by Using Taguchi Method

Design of Experiments using the Taguchi approach

The experiments were conducted with seven variables (factors) and two discrete values (levels) for each variable: type of porogen salt, salt granulometry, temperature and time of melt mixing, temperature, time and pH of leaching. The factors selected during the brainstorming step and their levels are shown in Table 3.

With seven factors, each with two levels, the full factorial design would have required 27=128 experiments while the Taguchi approach reduces the experimental runs to eight. Table 4 presents the L8 Taguchi OA selected in this study with the assigned parameters. The table consists of seven columns, which were assigned the seven factors, and eight rows which define the eight trial conditions that have to be performed. Across the row it is possible to read the discrete values, at the level 1 or 2 that must be assumed during the experiment.

Table 3 - Parameters selected and their values at two different levels.

Code	Parameter	Level 1	Level 2
A	Salt granulometry [μm]	0-45	90-110
B	Mixing temperature [°C]	190	220
C	Mixing time [seconds]	300	600
D	Porogen salt	NaCl	$CaCl_2$
E	Leaching time [hours]	5	8
F	Leaching temperature [°C]	50	70
G	Leaching pH	4.74 buffer	7 no buffer

Table 4 - Taguchi orthogonal array L8 of the experimental runs.

Expt.	A	B	C	D	E	F	G
1	0-45	190	300	NaCl	5	50	4.74
2	0-45	190	300	$CaCl_2$	8	70	neutral
3	0-45	220	600	NaCl	5	70	neutral
4	0-45	220	600	$CaCl_2$	8	50	4.74
5	90-110	190	600	$CaCl_2$	5	50	neutral
6	90-110	190	600	NaCl	8	70	4.74
7	90-110	220	300	$CaCl_2$	5	70	4.74
8	90-110	220	300	NaCl	8	50	neutral

Morphological analysis of scaffolds

The morphology of the scaffolds was observed to investigate the effect of salt type and particles size on the internal porous architecture. Since the pores morphology strongly depends on the type of salt involved in the experiment, the SEM images related to NaCl salt, i.e. experiments no. 1, 3, 6, 8, and the SEM images related to $CaCl_2$ salt, i.e. experiments no. 2, 4, 5, 7, will be shown and discussed separately.

Experiments with NaCl as porogen salt (expts. no. 1, 3, 6, 8)

Figure 20a–d show the SEM images of the porous architecture of the scaffolds derived by leaching of NaCl salt.

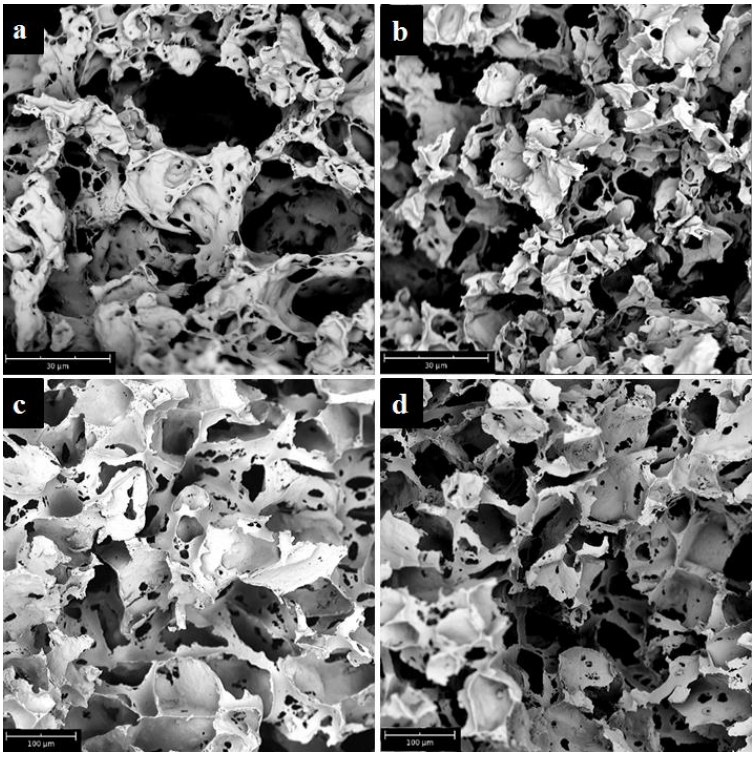

Figure 20 - SEM images of the scaffolds derived by leaching of NaCl salt: (a) experiment no. 1 and (b) expt. no. 3, scale bar 30 µm; (c) expt. no. 6 and (d) expt. no. 8, scale bar 100 µm.

In Figure 20a, the morphological structure of the scaffold manufactured under the experimental conditions no. 1 is highly porous with highly interconnected pores. Besides the pores resulting by solubilisation of NaCl, it is possible to observe micro-pores due to PEG solvation in the walls which appear rough, as reported elsewhere [257–259]. The presence of the these micro-pores in the structure is crucial because they (i) ensure the interconnection between the macro-pores, (ii) allow the water to

penetrate more deeply in the structure and then to better leach the scaffold, and (iii) allow the passage of cell nutrients after implantation.

In the picture it is possible to observe small residues of NaCl or PEG. Therefore, we might deduce that the leaching conditions of the experiment no. 1, T=50 °C and t=5h, are not optimal for the porosity but the analysis of variance proves otherwise.

Figure 20b shows the morphology of the scaffolds fabricated under the experimental condition no. 3. The wall thickness is lower than that of the expt. no. 1. This result can be explained by the higher temperature and time of mixing, 220 °C and 10 minutes versus 190 °C and 5 minutes. Since composition and salt granulometry are the same in both the experiments, the only reason for the lower thickness is the lower viscosity of the blend. The structures of this experimental run not show residual NaCl or PEG thanks to the higher temperature of leaching, 70 °C.

In Figure 20c the size range of the salt changes in 90-110 μm compared to 0-45 μm of the Figure 20a,b. The pore dimensions observed correspond to the salt granulometry, therefore the leaching technique allows the pore dimensions control through the size of salt particles. The walls of the internal structure are rough, thanks to PEG incorporation in the blend, as it was also found in the other experimental runs. However, compared to the previous cases, the pores are better enveloped by the PLA. This result can be justified by the larger dimensional range of the salt particles that produces a lower interfacial area and, as a consequence, allow the PLA to more easily cover the particles surface. It is evident the good leaching, in agree with the strong leaching conditions, T=70 °C and t=8h.

The morphological structure of the scaffolds manufactured in the run no. 8 is showed in Figure 20d. It is similar to the previous, indeed the salt granulometry is the same. The wall thickness is analogous, consistent with the torque values of the two blends.

Experiments with $CaCl_2$ as porogen salt (expts. no. 2, 4, 5, 7)

In the following experiments, the scaffolds were manufactured with $CaCl_2$ as porogen salt.

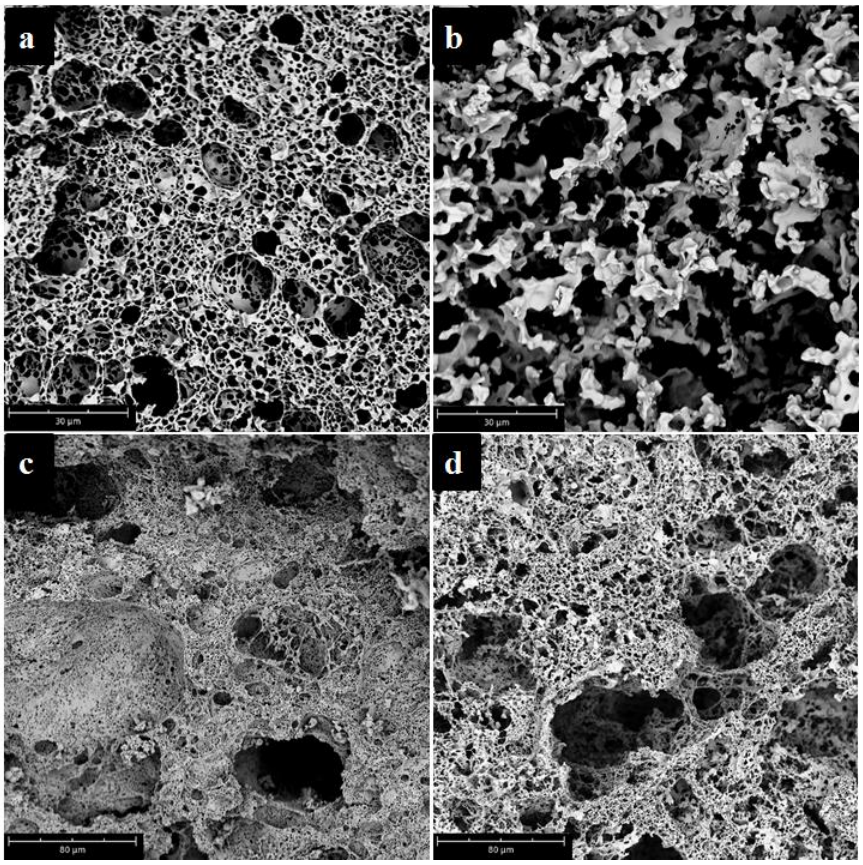

Figure 21 - SEM images of the scaffolds derived by leaching of $CaCl_2$ salt: (a) experiment no. 2 and (b) expt. no. 4, scale bar 30 µm; (c) expt. no. 5 and (d) expt. no. 7, scale bar 80 µm.

The morphologies, Figure 21a-d, are deeply different compared to those deriving from sodium chloride. In Figure 21a, the pore shape is uniform and rounded. The walls are not indented, as they were in the case of NaCl, and the small thickness allow to form a continuous structure surrounding the pores, despite the higher superficial area of the salt particles due to the smaller granulometry. These results may derive from the different shape and interplay of $CaCl_2$ crystals with the matrix, compared to NaCl crystals. The walls show micro-pores and the structure is entirely leached, as expected from the strong leaching variables (T=70 °C, t=8h). Figure 21b displays the SEM image of the scaffolds fabricated during the no. 4 experimental run. The structure is highly porous and interconnected with rough walls. In Figure 21c, the morphology of scaffolds no. 5 is similar to the previous except for pore dimensions. Finally, Figure 21d exhibits the internal structure of the scaffolds prepared during the experiment no. 5. All the structure are highly porous and interconnected. As can be seen from the Figure 21a-d, the use of $CaCl_2$ as porogen agent makes difficult the control of internal

architecture of the scaffold. Indeed, although the experiments no. 5 and no. 7 were carried out with salt granulometry in the range 90-110 µm, the resulting pores dimension is smaller. This phenomenon should be due to the breakage of the $CaCl_2$ particles during the melt mixing.

Viscosity measurements of the blends

Blends containing NaCl salt

During the mixing operation the torque values were collected versus time to indirectly monitor the variation of viscosity of the blends. The resistance offered by the blends depends both on kind and on granulometry of the salt and on mixing temperature.

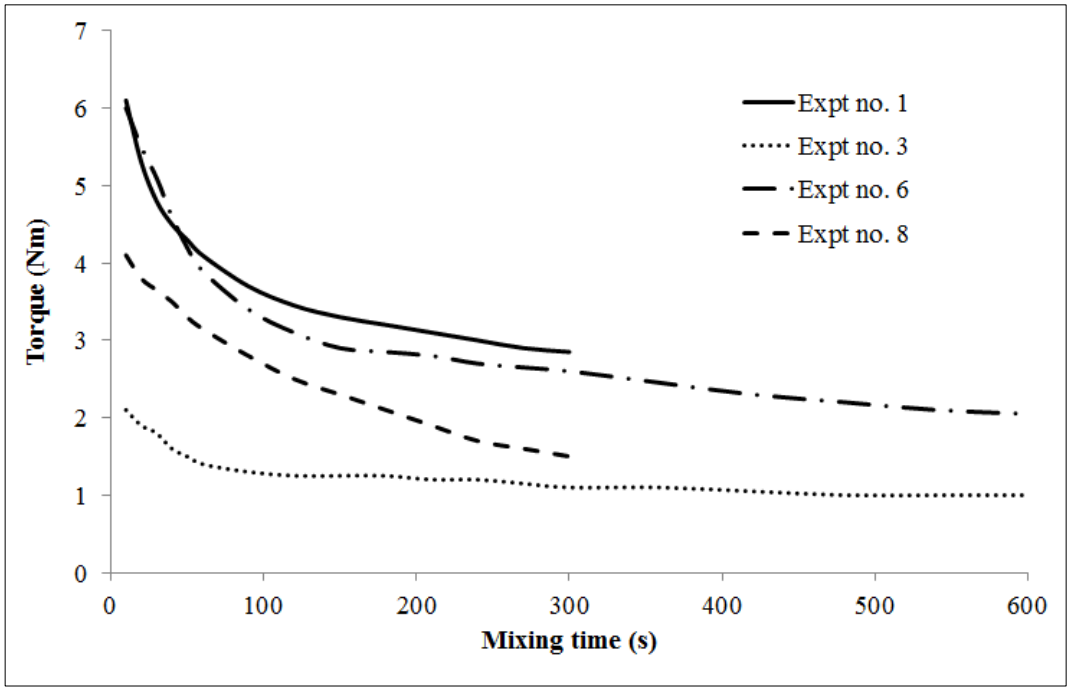

Figure 22 - Torque curves of the blends containing NaCl salt, experiments no. 1, 3, 6, 8.

In Figure 22 are reported the torque values of the blends incorporating sodium chloride as porogen salt. Comparing the curves related to the same particles size 0-45 µm, expts. no. 1 and no. 3, it is note that the torque of the blend processed at 220 °C (expt. no. 1) is, during the early seconds, three times greater than the blend processed at 190 °C (expt. no. 3). The torque values of the two blends at the stopping moment (300 s and 600 s for expts. no. 1 and no. 3, respectively) justify the difference in thickness of the walls of the two resulting scaffolds; indeed, the walls of the scaffold

no. 1 are thicker than those of the scaffold no. 3, as observed in the morphological analysis.

The same considerations can be done by comparing the torque values of the curves for the expts. no. 6 and no. 8 (Figure 22), which are characterized by the same salt granulometry equal to 90-110 µm, and different mixing time (see Table 4)

All the curves stabilize after the initial steep decrease due to the melting of the polymer matrix. This stabilization is remarkable for longer time, i.e. 600 s, and less evident for shorter time, i.e. 300 s.

Blends containing $CaCl_2$ salt

The blends containing $CaCl_2$ show torque values higher than those of the blends with NaCl, particularly in the early moments of the mixing (Figure 23). This behaviour might be due to the smaller granulometry of the crystals that produces a large superficial area. Indeed from SEM images of the expts. no. 2 and no. 4, it can be observed high concentration of the pores in the dimensional range 1-10 µm and few pores in the dimensional range 10-45 µm. Likewise, for the 90-110 µm size range, most of pores belong to a smaller dimensional range, probably due to the breakage of salt particles during the mixing.

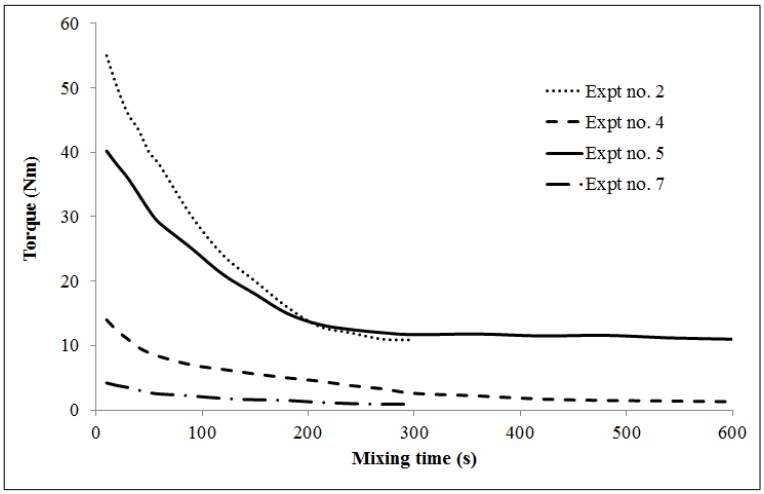

Figure 23 - Torque curves of the blends containing CaCl2 salt, experiments no. 2, 4, 5, 7.

The curves (Figure 23) display that the systems mixed at 190 °C, namely expts. no. 2 and no. 5, offer values of torque greater than the systems no. 4 and no. 7 mixed at 220 °C, in accordance with the decrease of viscosity with temperature. In the Figure

23, it can be seen that, at the same temperature, the torque of the blends no. 2 and no. 4 (size range 0-45 µm) is higher than that of the blends no. 5 and no. 7 (size range 90-110 µm), respectively. At the same temperature conditions, the torque depends by the dimensional range of the particles; with the decrease of the diameter of the particles, the torque increases because of the higher interfacial area and subsequent larger interaction between salt and polymer matrix.

As in the case of blends with NaCl, at the beginning of the mixing time, the values of torque decrease quickly because of the melting of the polymer matrix which causes the reduction of viscosity, afterwards the trend is almost constant.

Statistical analysis of the results

In this work, the properties investigated are compressive Young's modulus in air, compressive Young's modulus in PBS, and porosity. The aim of the optimization of process parameters on the quality characteristic is "bigger is better".

Effect of the process variables on mechanical properties

The compressive mechanical tests were carried out both in air at ambient temperature and in PBS at 37 °C to simulate the cellular environment in which the scaffold will work.

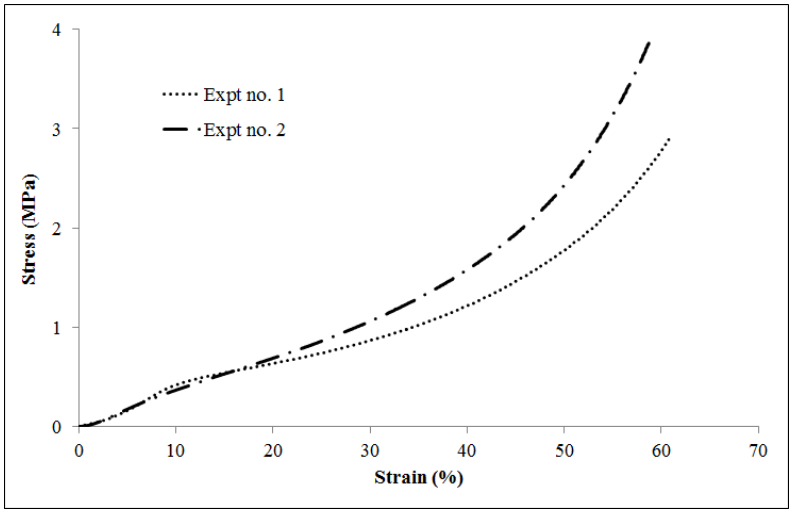

Figure 24 - Representative stress-strain curves of the scaffolds manufactured in the expt. no. 1 (with NaCl salt) and in the expt. no. 2 (with CaCl2 salt).

Figure 25 displays the stress-strain curves (σ-ε) of the scaffolds manufactured in the expts. no. 1 and no. 2, like representative curves. The curves of the samples, in all

the experiments, show an initial linear stretch indicating the elastic deformation, likely correlated with the bending of the walls of the pores [45], followed by a transition zone that indicates the beginning of the permanent plastic deformation.

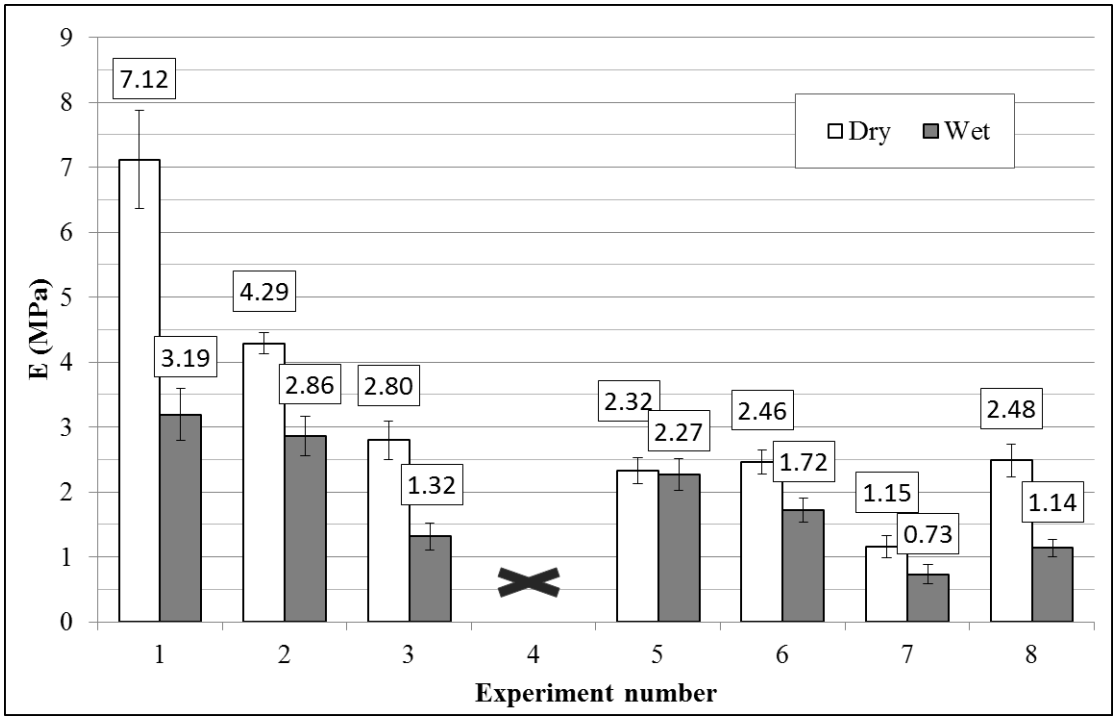

Figure 25 - Compressive Young's modulus of the scaffolds in dry and wet environment, for all the experimental runs.

The final region of the stress-strain curve monolithically increases, indicating the typical plastic deformation of the thermoplastic polymers, which may be associated with the densification of the internal architecture of the sample. The shape of the stress-strain curves of the scaffolds tested in PBS is the same.

Figure 25 reports the mean values of the compressive Young's modulus in air and in PBS, calculated as the slope of the linear stretch in the stress-strain curves, for the scaffolds of all the experimental runs. The diagram does not show the values of the expt. no. 4 because the scaffolds have crumbled during the leaching; the phenomenon might be imputed to the previous degradation of the material during the melt mixing operation under strong conditions, i.e. T=220 °C and t=600 s.

Table 5 - ANOVA for Young's modulus in air.

Source	SS	DOF	V	F_{calc}	P (%)
A	4.205	1	4.205	23.74×	13.19
B	11.907	1	11.907	67.22×	37.34
C	6.956	1	6.956	39.27×	21.82
D	6.301	1	6.301	35.58×	19.76
E	2.163	1	2.163	12.21×	6.78
F*	0.186	1	0.186		0.58
G*	0.168	1	0.168		0.53
Tot	31.887	7			
e pooled	0.354	2	0.177		

ANOVA was employed to investigate the effect of the factors on compressive Young's modulus in air and in PBS. The data in Figure 26 are used to calculate F value of F-test. Table 5 shows the results of pooled ANOVA for the dry elastic modulus. At first, the column G was associated with the estimate of the error due to its lower SS value; in these calculations, no factor was statistically significant, for any confidence level. Therefore, by the pooling up strategy and by merging G and F column effects, the value of F calculated, for all the factors A-E, was larger than F_{crit} value. F_{crit} was extrapolated by proper F-table by considering one DOF for the numerator and two DOF for the denominator, namely e-pooled. For a level of confidence of 90%, the factors A-E were statistically significant, while for higher levels of confidence (95% or 99%) no factors were statistically significant because the condition $F_{calc}>F_{crit}$ was never verified. Even with the increasing the merging of the factors up to six (the maximum possible number) in e-pooled, the factor B, which showed the higher influence, had no statistical significance. The significant factors affecting Young's modulus in air and their optimal levels are listed in Table 6, in order of contribution.

From the diagram in *Figure 25*, it can be observed that the greatest elastic modulus is observed for the of the experiment no. 1, following the expt. no. 2. These blends are been melt mixed at 190 °C for 10 minutes which are the optimal levels of the first two factors statistically significant revealed by the analysis of variance; their lower levels may be justified by the reduced degradation of the polymer matrix during melt processing, resulting in the better mechanical performance of the scaffolds. Following in significance the type of salt, the size range and the time of leaching.

Table 6 - Significant factors affecting Young's modulus in air and in PBS and their optimal values, in order of contribution.

Significant factors	Optimal level
Young's modulus in air	
B: Mixing temperature	190 °C
C: Mixing time	300 s
D: Porogen salt	NaCl
A: Salt granulometry	0-45 μm
E: Leaching time	5 h
Young's modulus in PBS	
B: Mixing temperature	190 °C
C: Mixing time	300 s
G: Leaching pH	7 no buffer
E: Leaching time	5 h
A: Salt granulometry	0-45 μm
D: Porogen salt	NaCl

The use of NaCl salt gives more uniform internal structure while the smaller pore size leads to more homogeneous mass distribution of PLA in the scaffold [260] and a greater number of points of contacts, so that the elastic modulus of the devices is higher. The level 1 of the factor E allows the scaffolds to be exposed at the thermal stress of leaching for a shorter time, however it is the least influential factor.

The tests carried out in wet condition present values of the elastic modulus lower than the corresponding in dry (*Figure 25*), therefore the elastic characteristic of the materials immersed in the physiological solution decreases, except for the expt. no. 5 that presents a values almost constant.

The analysis of variance performed for the wet elastic modulus was resulted in the values in Table 6. At 99% confidence level and by using the pooling up strategy, the factor B is the only significant factor, that is the temperature of mixing. The optimal value is 190 °C (level 1). By taking in account the 95% confidence level and by considering the factor F for the evaluation of the error, all the factors are statistically significant. In this case, the pooling up method is not necessary. Table 7 displays the significant factors, listed in order of contribution, and their optimal values. It is interesting to note that, unlike the dry elastic modulus, in this case the pH of leaching takes statistically significance overcoming the effects of time leaching and salt granulometry.

Table 7 - ANOVA for Young's modulus in PBS.

Source	SS	DOF	*V*	F_{calc}	F_{calc}	P (%)
A*	0.285	1	0.285		2533+	3.49
B	5.865	1	5.865	15.318 #	52136+	71.85
C*	0.852	1	0.852		7569+	10.43
D*	0.285	1	0.285		2533+	3.49
E*	0.401	1	0.401		3560+	4.91
F*	0.112×10^{-3}	1	0.112×10^{-3}			0.00
G*	0.475	1	0.475		4225+	5.82
Tot	8.163	7				
e pooled	2.297	6	0.383			

* Factors merged in *e pooled;* # Significant at 99% confidence level; + Significant at 95% confidence level. Percent contribution P (%) = SS_{Tot}/SS_i

Effect of the process variables on porosity

Table 8 and Table 9 show the response in porosity for the eight experimental runs and the application of ANOVA, respectively. For each confidence level (99, 95 and 90%), no factor is statistically significant, including the combination of factors through the pooling up strategy.

Therefore, for the porosity both the two levels of the selected parameters give optimal results, without statistically significant differences. However, the observation of the ANOVA values displays that the leaching temperature and the salt granulometry are the most influential factors. The greatest porosity is obtained when the temperature leaching is set at 70 °C and the salt granulometry is 90-110 μm. Indeed, the salt solubility increases with the temperature and the large pores allow better penetration of the water into the scaffold structure.

Table 8 - Results for porosity.

Expt. no.	Porosity (%)
1	79.5
2	83.5
3	81.5
4	-
5	81.8
6	84.7
7	84.5
8	83.0

Table 9 - ANOVA for porosity

Source	SS	DOF	*V*	F_{calc} *(e=E)*	F_{calc} *(e p. 2)*	F_{calc} *(e p. 3)*	F_{calc} *(e p. 4)*	F_{calc} *(e p. 5)*	F_{calc} *(e p. 6)*	P (%)
A	0.100	1	0.100	1.377	1.327	1.295	1.274	1.252		16.66
B	0.081	1	0.081	1.114	1.073					13.48
C	0.085	1	0.085	1.172	1.130	1.103	1.084			14.18
D	0.078	1	0.078	1.076						13.01
E	0.072	1	0.072							12.10
F	0.101	1	0.101	1.393	1.343	1.310	1.289	1.267	1.216	16.85
G	0.082	1	0.082	1.135	1.093	1.067				13.73
Tot	0.599	7								
e pool. 2	0.150	2	0.075							
e pool. 3	0.231	3	0.077							
e pool. 4	0.313	4	0.078							
e pool. 5	0.398	5	0.080							
e pool. 6	0.498	6	0.083							

Percent contribution P (%) = SS_{Tot}/SS_i

Conclusions

Processing parameters have a great impact on the mechanical properties of the scaffolds. The Taguchi method has been applied for investigation the effects of process parameters on the properties of porous scaffolds for tissue engineering. The target parameters have been selected during the brain-storming step taking in consideration the application requirements.

Rheological tests have been performed during the melt mixing of the blends PLA/PEG/salt. Morphological analysis and compressive mechanical tests in air and in PBS have been carried out on the scaffolds fabricated. The analysis of variance has been employed to obtain the statistically significant factors and their optimal levels. ANOVA has revealed that, in relation to the mechanical properties, the temperature of mixing is the most statistically significant variable and its optimal level is the lowest. It is due to the reduced degradation of the polymer during the melt mixing. In accordance with this assumption, it can be justified the following second significant variable, the mixing time, and its lower optimal level. For the mechanical properties, the results obtained in this study indicate that, the statistically significant factors are temperature and time of mixing, kind of porogen salt, following salt granulometry and

time of leaching, and their optimal levels are the lowest. For the porosity ANOVA results show that the all factors are no significant.

The combination of Taguchi's experimental design and ANOVA gives a simple and effective systematic approach for the determination of the optimal levels of the significant parameters.

The optimal values obtained may be adopted in future process of fabrication of porous scaffolds within the same process manufacturing and materials. Moreover, this study may be considered how preliminary investigation for further experimental investigation of the significant factors in more complicated factorial design, for instance with a full factorial design, to explore non-linear effects and interactions between parameters.

4.3 3D PCL Membranes for Oily Waste Removal

This section describe an eco-friendly technology to prepare a NaCl templated polycaprolactone biodegradable sponge for the selective absorption of oil from water. The eco-friendly process for fabricating the PCL oil removal sponge (ORS) does not require any synthesis processes and use of organic solvents and it is not environmentally hazardous, thus promoting potential in environmental applications. The proposed PCL sponge are also able to remove micrometer size oil droplets typical of emulsions, and can be clean-up in close system at least 50 times exhibiting low efficiency loss. Devices are characterized from morphological, mechanical, and oily uptake point of view by considering 3 different oily waste (olive oil, motor oil, gasoline) and considering 50 cycles of recycle.

Morphology

Typical SEM images of PCL sponges are shown in Figs. 1 a-b.

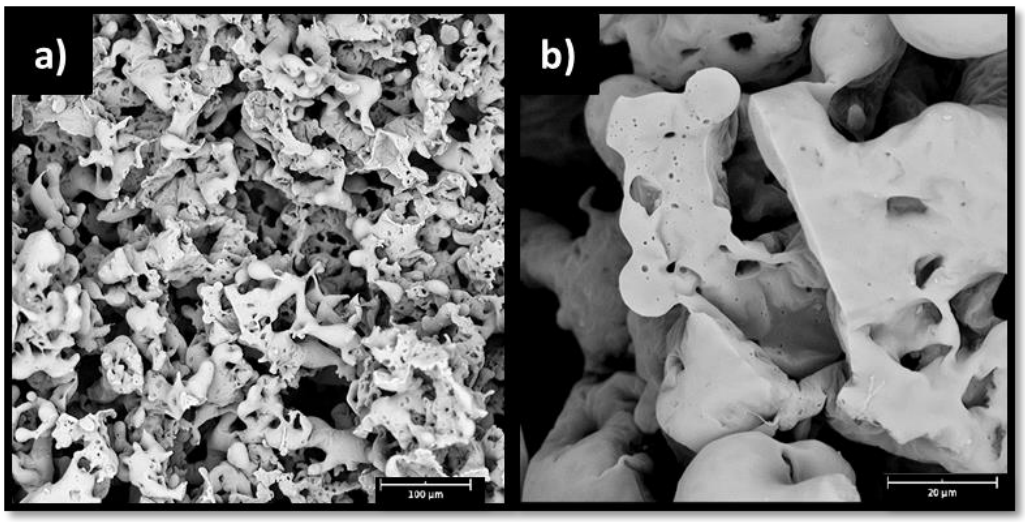

Figure 26 - SEM images of ORS at different magnifications, scale bar a) 100 µm; b) 20 µm.

The sponge morphology of ORS was characterized by a multimodal pore structure with distinct pore sizes and pore architectures. The macropores are homogeneously distributed in the polymer matrix as shown in Figure 26a. The size of these macropores varies considerably throughout the scaffold from 50 to 100 micrometers and depends on the size distribution of the salt particles added. Moreover the absence of salt crystals suggests that the dissolution of the porogen agents is complete. In addition to the

macropores resulting from the leaching of salt crystals, a micropores network was created by the extraction of the PEG porogen polymer, characterized by cylindrical pores with a maximum size of approximately 5 µm, as shown in Figure 26b. The presence of micropores is crucial for their whole interconnection and to enlarge the specific area of the device.

Oil uptake

As shown in Figure 27a, the porous and highly interconnected structure, appears to be highly hydrophobic, and shows potential interest in the removal of oily and hydrophobic pollutants. In fact, when a drop of water and a drop of olive oil were put onto the surface of the sponge, the drop of oil was immediately absorbed, while the drop of water remained stable onto the surface of the sponge with a contact angle of 130 degrees (Figure 27b).

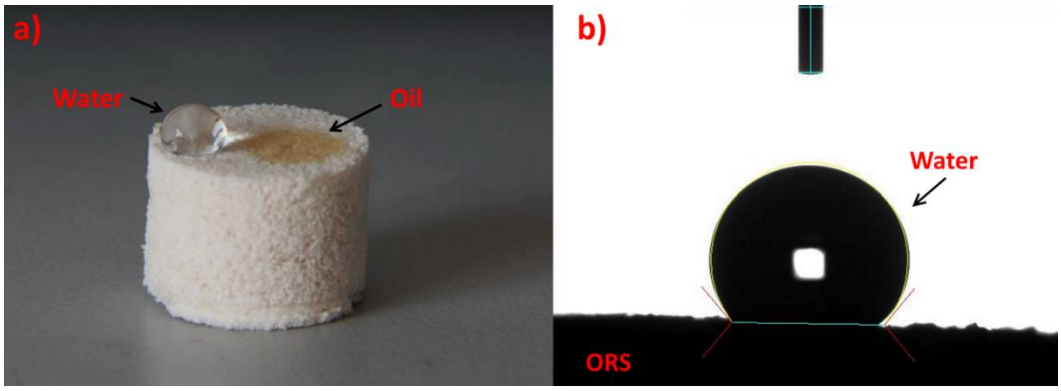

Figure 27 - Two drops of water and oil onto the surface of sponge. The drop of water remains onto the surface, while the drop of oil was immediately absorbed. In the inset, the water contact angle measurement of the virgin sponge.

Accordingly, when an ORS was placed in contact with a system simulating polluted waters, consisting of distilled water and olive oil, it was able, in a few seconds, to completely and selectively remove the organic pollutant from the water (see Figure 28). Indeed, when a sponge is placed onto the surface of a biphasic mixture (Figure 28a) it is able to be around half-filled just within 4 seconds (Figure 28b), and starts to sink after 8 seconds (Figure 28c) indicating a filling higher than 50%. After 12 (Figure 28d) and 16 seconds (Figure 28e) the sponge gradually absorb the pollutant up to completely entrap and remove it within only 20 seconds (Figure 28f). Furthermore, since density of the ORS-oil system is lower than the water one, the sponge floated on

the water surface, indicating a potential easy removal of oil spillage or any oily leakage. The selective oil uptake was evaluated by weighing the water before adding oil and the biphasic mixture after the immersion of the ORS. In particular, it was found that the water's weight after the ORS immersion and the subsequent removal was about the 99% of the initial weight. Moreover, in order to verify if the water even after the uptake contained still oil, it was evaporated and thereafter weighted finding that no residue was present. These findings suggest the selectivity of the ORS in removing the oil.

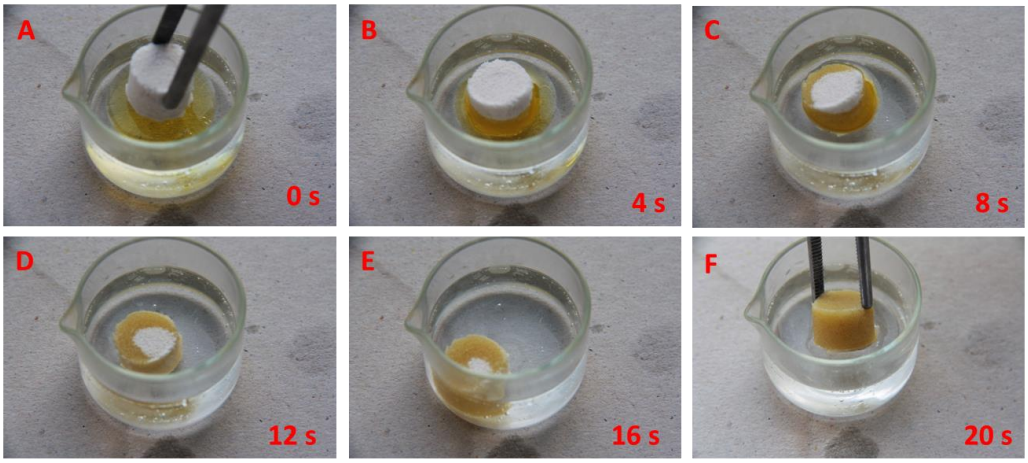

Figure 28 - Photo-frame every 4 seconds of a sponge immerse into the biphasic solution of water and olive oil. Initially the sponge float onto the surface, but while it is filling up, it starts to precipitate on the bottom of crystallizer.

With the aim to evaluate the possibility to recycle the ORS, we looked for a system able to remove the absorbed olive oil, but at the same time that do not damage the ORS. Exploiting the insolubility of polycaprolactone in different organic solvents [261] we chose diethyl ether as solvent to clean-up and recycle the ORS, since its ability to dissolve oily compounds and without damaging PCL porous architecture. SEM images reported in Figure 29a-b, show in fact that the morphology of ORS is the same of the virgin one reported in Figure 26a-b. Encouraged by these interesting results, we decided to evaluate the possibility to recycle the ORS up to fifty times and even to assess the effect of different pollutants, i.e. olive oil, motor oil and gasoline. In fact, a good system with the capability to remove organic pollutants, should be also reusable, thus permitting to recover the pollutants without affecting removal efficiency.

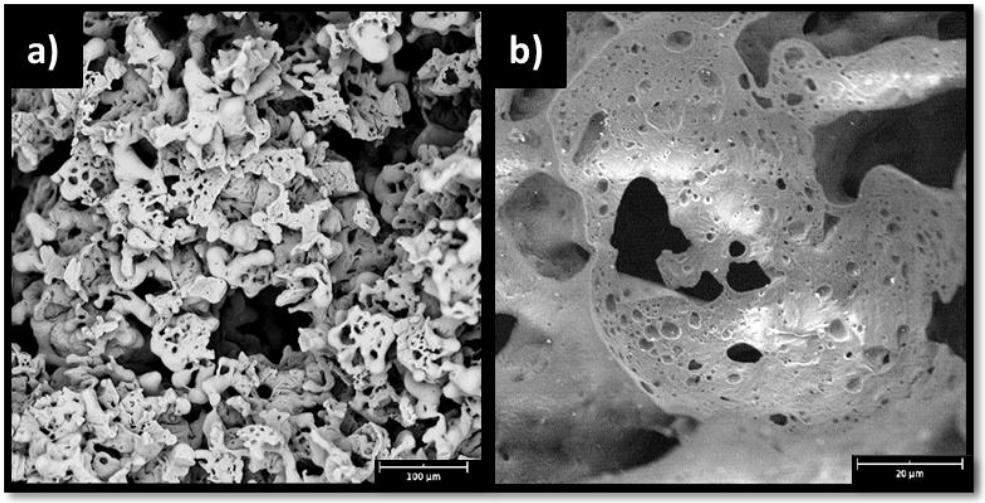

Figure 29 - SEM images of the ORS after cleaning up at different scale bar a) 100 µm; b) 20 µm

In order to characterize the absorptive capability of the ORS, we used the following parameters: mass and volume of seized pollutant, and the correlated parameters, mass and volume-based oil uptake % (accordingly respectively to Eqns. 14 and 15) that are reported as a function of the cycle number in Figure 30. In particular, the results

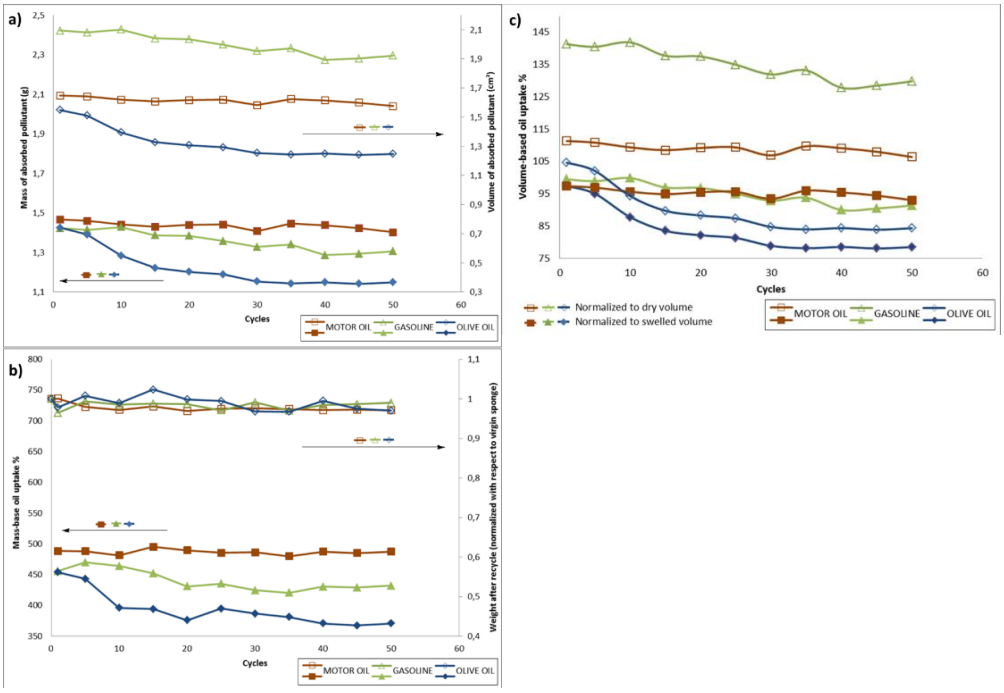

Figure 30 - a) Mass and Volume of absorbed pollutant versus number of cycles, b) the weight of sponge after each cycle and mass-base oil uptake %. c) volume-base oil uptake in relation to dry volume and swelled volume of the ORS.

reported in Figure 5a show that the ORS is able to absorb a similar amount of pollutant

for all the fifty tested cycles although when the olive oil is used, a very slight decrease of the absorbed mass of pollutant can be observed on increasing the cycle number.

To take into account the different densities of the three used pollutant, their absorbed volume was reported in the same figure (Figure 30a). It is worth noting that, considering the absorbed volume, the largest amount of seized pollutant was of gasoline. This may be likely caused by the capability of gasoline to completely fill all the pores of different diameters of the ORS, while the more viscous motor and olive oils are able to fill only the capillaries and the pores with larger diameters.

In Figure 30b it is shown the weight of the ORS after every cycle, i.e. after absorbing the pollutant and the following cleaning up, normalized with respect to the pristine one. The weight of ORS remains the same after each cycle, indicating an optimal extraction and total removal of the pollutants.

Still, in Figure 30b, when the results of oily uptake were shown in terms of mass-based oil uptake, a value up to 500% (respect to the original weight) can be observed. In particular it was higher for motor oil, gasoline and olive oil respectively.

But if the same data were reported as a function of volume-based oil uptake (Figure 30c) an unexpected result is observed. Indeed the uptake values were unreasonably higher than 100%. In order to find a possible answer, we observed, that, when the ORS were put in contact with the pollutant, an increase of the volume of the sponges occurs. The size of swelling changes depending on the analyzed systems and in particular it was of 36% for the gasoline, 13% for the motor oil and 7% for the olive oil (See Table 10). Indeed, as shown in Figure 30c, if the results were normalized with respect to the new volume of swelled sponges, the results get back under the reasonable 100%.

SEM analyses were performed on ORS used for the removal of the three standard pollutant after 10, 25 and 50 cycles, as shown in Figure 31, to analyze the effect of wastes and of the clean-up on the morphology of the reused samples.

After 10 and 25 cycles, all ORS samples showed morphology very similar to the virgin one (Figure 26), thus likely suggesting that matrix surface is inert towards both the oily wastes and the diethyl ether used for the clean-up. Indeed, the multimodal pore structure seems to remain unchanged, as neither breakages nor discontinuity of the polymeric phase were detected.

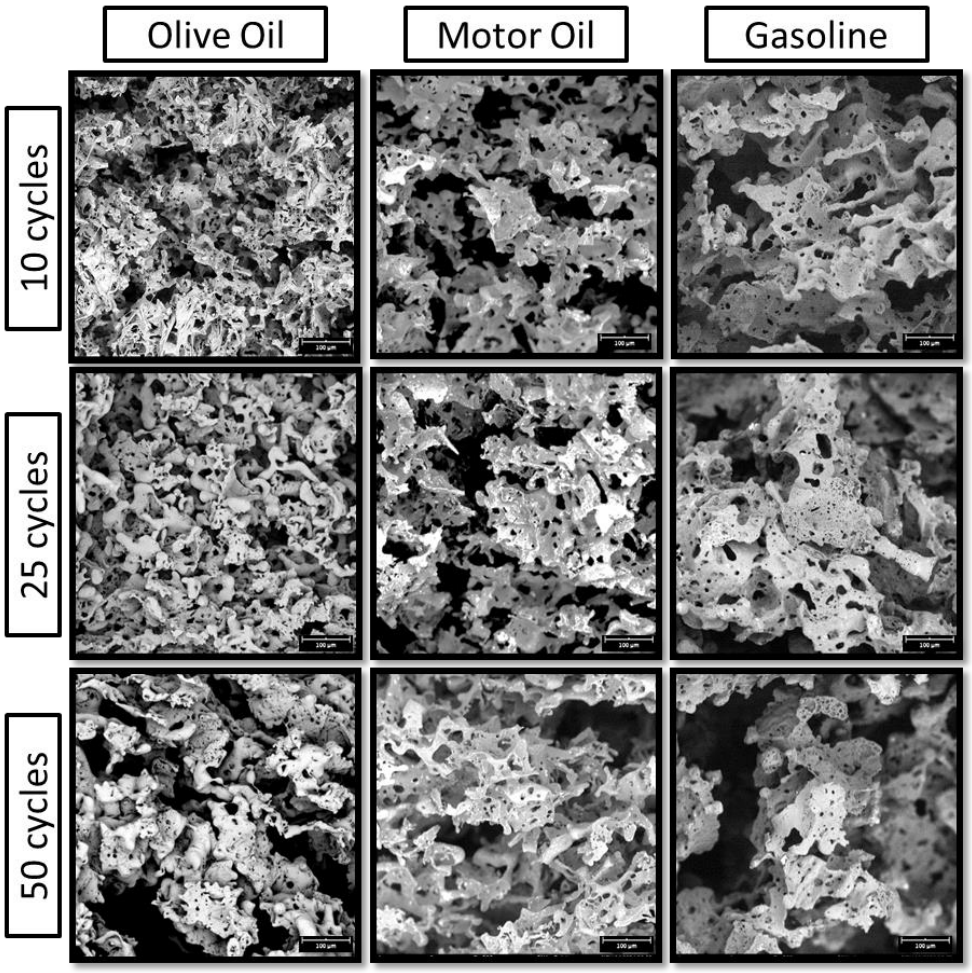

Figure 31 - SEM images of ORS morphology after 10, 25 and 50 recycles for different oily systems

After 50 cycles, a higher discontinuity of the internal structures was visible in every sample. In particular, the appearance of empty regions (around 300 μm) was clearly visible in ORS that absorbed olive oil and gasoline. On the other hand, those which absorbed motor oil after 50 cycles seemed to retain the pristine morphology, even if the pore structure seems to be partially compromised with some empty regions which size did not exceed 100 μm.

The pristine roughness of the pore architecture appear unchanged, thus confirming the absence of any waste residual after cleaning cycle.

Porosity and connectivity.

Porosity and connectivity are important parameters related to sponge-based devices. The first feature refers to the volume that could be potentially filled by fluids, the second influences the interconnection rate between pores by assuming that the porogen agents (NaCl and PEG) are removed by the fluid phase (Water) during the leaching step.

Table 10 - ORS properties

Sample Designation	Theoretical Porosity (%)	Dry Porosity (%)	Wet Porosity (%)	Swelling Volume (%)
Virgin	82	83.7 ± 0.5	-	-
Olive oil 10	82	81.9 ± 0.3	84.0 ± 0.3	7 ± 0.04
Olive oil 25	82	81.5 ± 0.4	83.8 ± 0.2	7 ± 0.08
Olive oil 50	82	81.3 ± 0.2	83.7 ± 0.4	7 ± 0.1
Motor oil 10	82	82 ± 0.3	85.0 ± 0.2	13 ± 0.07
Motor oil 25	82	81.7 ± 0.3	84.7 ± 0.3	13 ± 0.1
Motor oil 50	82	81.7 ± 0.4	84.6 ± 0.5	13 ± 0.15
Gasoline 10	82	82.1 ± 0.4	87.4 ± 0.2	36 ± 0.1
Gasoline 25	82	82 ± 0.5	87.2 ± 0.3	36 ± 0.15
Gasoline 50	82	81.8 ± 0.3	87.1 ± 0.5	36 ± 0.2

The sponges were designed with a theoretical volumetric porosity of 82%, assuming the complete extraction of porogen agents. The measurement of the real porosity of sponges, calculated according to eq. 2, was 83.7% ± 0.5%. It was found to be higher than the theoretical one, presumably due to the loss of low amounts of PCL during process and/or to small inhomogeneity of the blend itself.

The value of the real porosity did not change significantly as a function of the number of recycles and type of pollutants as shown in Table 10.

The value of the connectivity measured according to Eqn. 3 was around 99.5% for all the materials.

Wet porosity was evaluated by considering the volume of the sample filled by the oily pollutants. As already mentioned, the ORS were found to swell when filled by all the pollutants analyzed in this work.

Among the pollutants investigated in the frame of this work, gasoline induced the strongest swelling (36% volume increase), thus determining a wet porosity of about 88%. When the ORS were filled by motor oil and olive oil, the swelling observed was

only 13% and 7%, respectively. The highest volume increase displayed by the gasoline-ORS system could be ascribed to the lower viscosity of the gasoline waste.

Values of porosity and swelling volume are listed in Table 10.

Mechanical properties

The results of the compression tests were interpreted in terms of stress–strain curves for the several fabricated ORS. A typical stress-strain curve is shown in Figure 32. The plot put into evidence that ORS showed the typical behavior of polymeric foams under compression tests. It is possible to divide the plot into three different regions, i.e. linear, transition and densification region. All the samples showed an initial linear-elastic behavior associated with the bending of the pore walls. The compressive modulus (E_1) was determined as the slope of the linear region in the stress-strain curve and it is reported in Figure 33a as a function of the type of pollutant and the number of cycles. In the second region, it is possible to notice a transition attributable to the beginning of the plastic deformation [254,255].

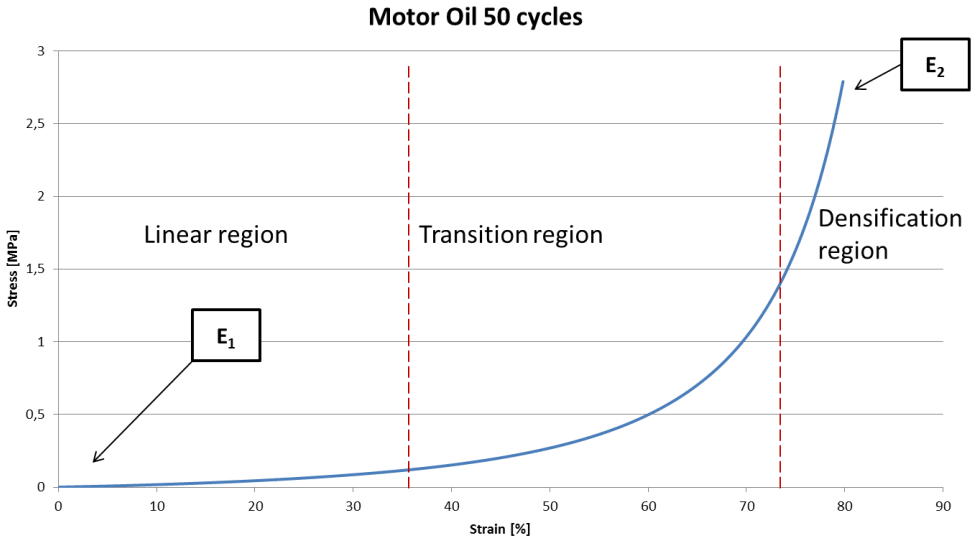

Figure 32 - Representative stress strain curve for ORS and points of evaluation of E1 and E2 parameters

In the last region of the plot, the stress was found again to vary linearly with the strain. In this latter case, the so-called plastic modulus (E2) measured was due to the densification phenomena occurring since the pore walls collapsed thus filling the voids. As consequence, a steep increasing in stress was measured. E2 as a function of

the type of pollutant and of the number of the cycles is shown in Figure 33b. The plot put into evidence that ORS showed the typical behavior of polymeric foams under compression tests. It is possible to divide the plot into three different regions, i.e. linear, transition and densification region. All the samples showed an initial linear-elastic behavior associated with the bending of the pore walls. The compressive modulus (E_1) was determined as the slope of the linear region in the stress-strain curve and it is reported in Figure 33a as a function of the type of pollutant and the number of cycles. In the second region, it is possible to notice a transition attributable to the beginning of the plastic deformation [262,263]. In the last region of the plot, the stress was found again to vary linearly with the strain. In this latter case, the so-called plastic modulus (E_2) measured was due to the densification phenomena occurring since the pore walls collapsed thus filling the voids. As consequence, a steep increasing in stress was measured. E_2 as a function of the type of pollutant and of the number of the cycles is shown in Figure 33b.

Compressive modulus was found to be almost independent on the kind of pollutants up to 25 cycles. Meanwhile a large reduction of E_1 value was visible at 50 cycles, although motor oil seems to get worse. Obviously a reduction of the E_1 value can be attributed to the degradation of polymeric matrix due to the polymer-pollutants interaction. Moreover, the high specific area of these devices accelerated the chemical degradation of the matrix, since the pollutants could act as a solvent. The behavior of the E2 as a function of the typology of pollutants and of the number of cycles was very similar to that of E1. The value was found to be 1000% higher than E1 because the porosity of the system was gradually reduced by densification phenomena but, in all the cases, a decrease with respect to the initial value was evident. The most remarkable difference can be observed at 50 cycles for motor oil and for gasoline wastes with a significant decrease of E2.

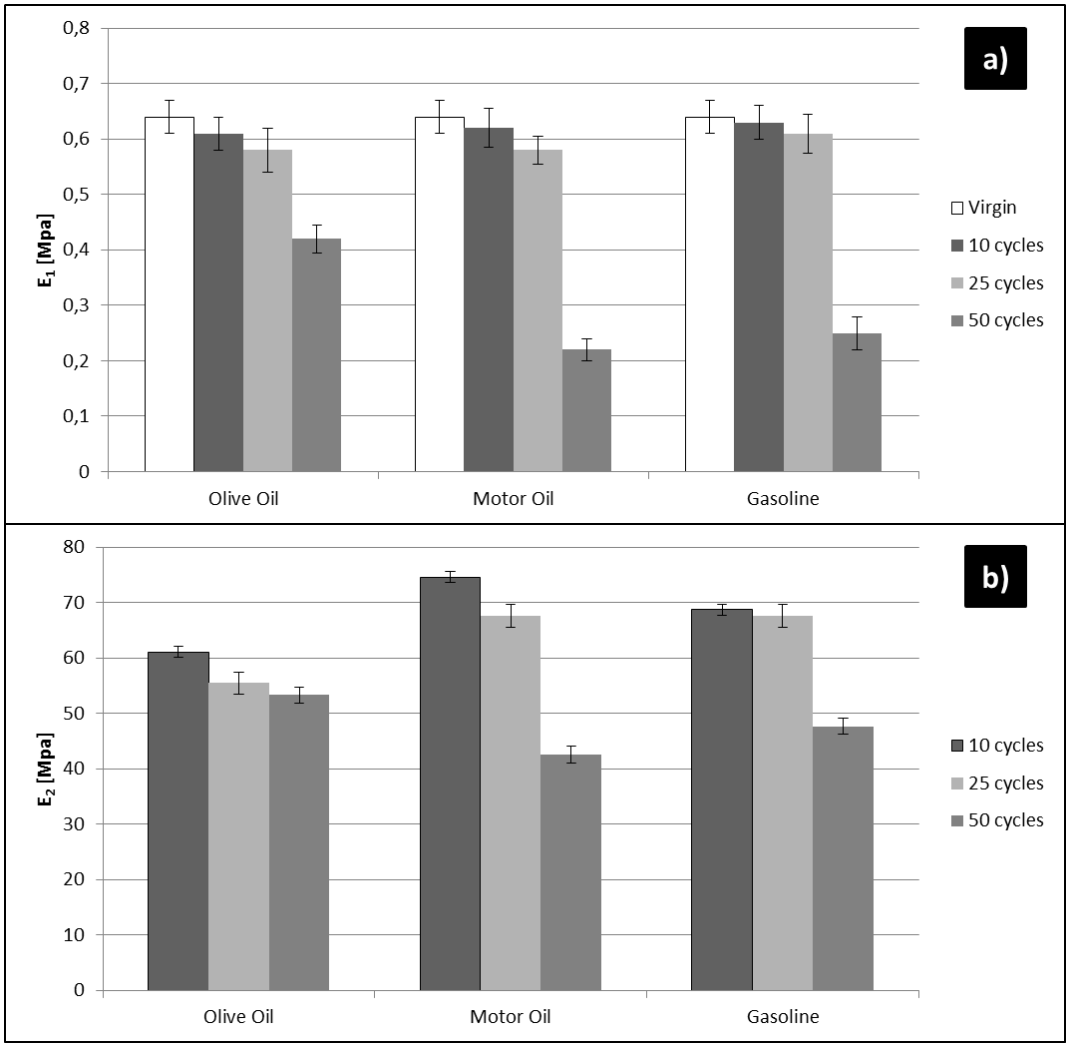

Figure 33 - Variation of E_1 (a) and E_2 (b) with the increasing of recycles for different oily systems.

4.4 3D Porous Structures Presenting Pore Size Gradient

PLA-based porous structures presenting pore size gradient

In this section is presented the preparation and characterization of PLA-based porous structures presenting pore size gradient. The aim of this work is to find a correlation between the preparation, the morphology and mechanical properties of the PLA-based three-layered scaffold. Moreover the structural characteristics of this device, similar to the spongy bone structures, prompted us to investigate about the effect of different pore size layers on cellular permeation and the possibility of using the three-layered porous PLA/PEG scaffold for bone regeneration. The samples code and the NaCl granulometry chosen for this application are listed in Table 11.

Table 11 - Materials prepared by melting PLA, PEG and NaCl in different granulometry.

Sample code	Granulometry NaCl (µm)
M 500	500–1000
M 300	300–500
M 100	100–200
M 90	90–110
M 45	45–65
M 10	<40

Morphological analysis of monolayered scaffold

The morphology of the scaffolds were analyzed to determine the effect of NaCl particles size on the porous architecture of the PLA-based scaffold. Figure 34A-F shows images obtained by SEM of the monolayered scaffold developed by leaching material filled with different size of salt. Measurement of pore size revealed a scaffold average pore size strongly controlled by the NaCl granulometry filled in the polymer matrix. In particular M 500 (Figure 34A refers to the material filled by salt grains seized from 500 to 1000 µm (M 500). From Figure 34A it is possible to note that pores have an average diameter of 500 µm, probably due to the breakage of salt particles with diameter higher than 500 µm during the melt mixing. As clearly visible from the

same figure, pore architecture is characterized by a low number of irregular pores, lowly interconnected surrounded by walls of about 10 µm. In Figure 34B it is shown the morphology of M 300.

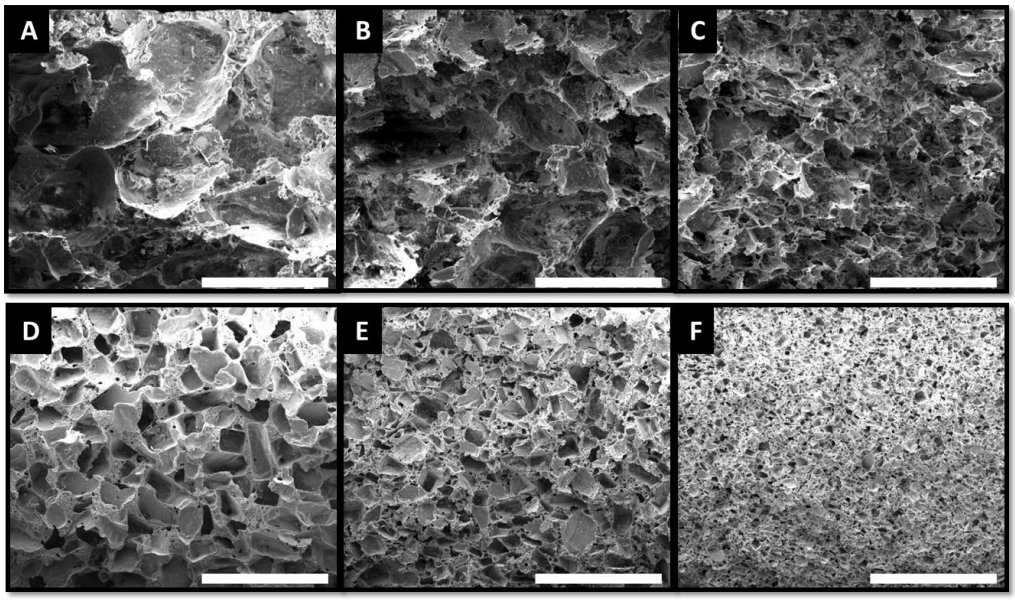

Figure 34 - SEM images of monolayered scaffold obtained by leaching melts with different salt particles size: M 500 (a), M 300 (b), M 100 (c), M 90 (d), M 45 (e) e M 10 (f), scale bar is 400 µm.

In this case the pores presented an average diameter in the same range of the salt particles filled during melt mixing (300–500 µm) so particles were not broken by process. Walls around pores, are thinner (about 5 µm) than the M 500 ones. M 100, (Figure 34C), an heterogeneous network composed by pores with higher dimension (200 µm) surrounded by little ones (100 µm). This pore architecture increases the interconnection between pores and their density for unit of volume but it drastically reduces walls thickness. M 90, (Figure 34D), morphology, shows roughly cubic pores that seems to be homogeneously distributed throughout the polymer matrix because the salt filled in this blend was seized in a range smaller than previous (90–110 µm). Micropores due to PEG solvation were present inside the walls that, in fact, appear very rough. M 45, (Figure 34E), SEM image shows a high density of pores for unit of volume with dimension ranging from 45 µm to 70 µm. M 10 materials, (Figure 34F), present the highest density of pores per unit of volume. This structure is highly interconnected and its pores have an average pore size of 20 µm with walls very thin (thickness even below than 1 µm).

Morphological analysis of three layered scaffold

Figure 35A-C is the picture of a section of the three-layer system composed by M 500, M 300 and M 100 (TL A) after the leaching process.

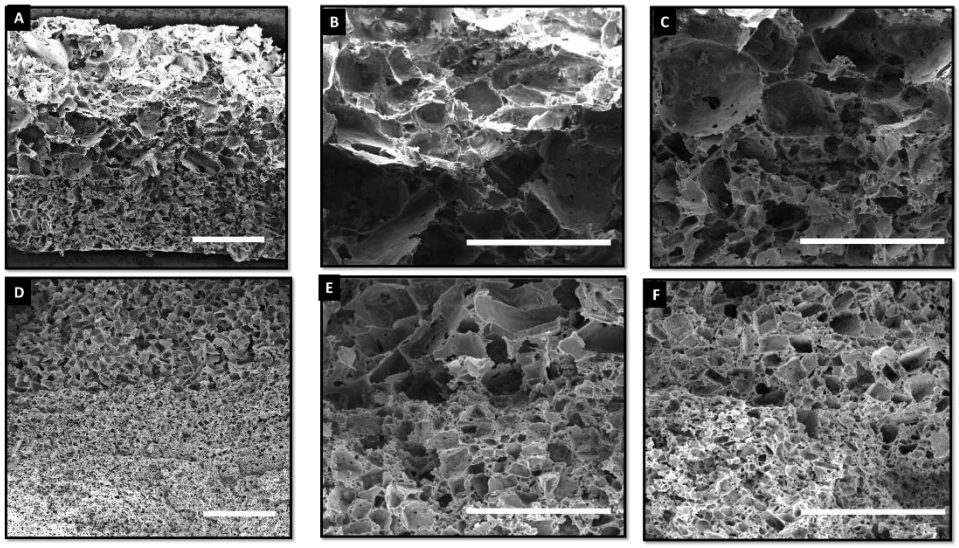

Figure 35 - (A,B,C) SEM images of three-layered scaffold type A: (A) entire cross section; (B) transition region between layers M 500 and M 300; (C) transition region between layers with pores of M 300 and M 100. (D,E,F) SEM images of three-layered scaffold type A: (D) entire cross section; (E) transition region between layers with M 90 and M 45; (F) transition region between layers M 45 and M 10. Scale bars are 500 µm.

In Figure 35A it is possible to identify clearly the three layers with the three different average pore size. The Figure 35B,C, shows at a higher magnification the transition regions between respectively (M 500–M 300) and (M 300–M 100) layers. It can be observed that the whole device do not present internal cleavages and no matrix discontinuity can be distinguished among the different layers. Figure 35D shows a SEM image of the three-layer device composed by M 90, M 45 and M 10 (TL B) after the leaching process. It demonstrate that TL B presents morphological characteristic similar to TL A. Again, as matter of fact, three layers with pores of different sizes can be easily recognize, while Figure 35E,F showing respectively the transition region (M 90–M 45) and (M 45–M 10), allows observing that the different layers constitute a single structure without flaking. Pore architecture of every single layer is, as expected, the same of the corresponding monolayer in every region.

Porosity, connectivity and water uptake analysis

In Table 12 are summarized theoretical porosity (%), porosity (%), connectivity (%), water uptake (%), pores filled by water (%) in function of scaffolds pore size and for the three-layered devices.

Table 12 - Theoretical porosity (%); porosity (%); connectivity (%); water uptake (%); pores filled by water (%) in function of scaffolds pore size.

Scaffold code	Theoretical porosity (%)	Porosity (%)	Connectivity (%)	Water uptake (%)	Pores filled by water (%)
M 500	70.84	70.12±0.62	99.70±0.08	210.5±10.1	99.63±0.22
M 300	70.84	70.04±0.46	99.58±0.12	200.4±12.5	99.1±0.35
M 100	70.84	70.08±0.65	99.65±0.10	203.8±11.4	99.75±0.15
M 90	70.84	69.94±0.32	99.42±0.15	185.8±14.7	99.26±0.41
M 45	70.84	69.87±0.57	99.54±0.09	192.8±7.1	99.08±0.13
M 10	70.84	69.91±0.71	99.46±0.13	187.65±6.5	99.57±0.18
TL A	70.84	70.05±0.76	99.35±0.10	196.3±11.7	99.23±0.31
TL B	70.84	69.65±0.82	99.40±0.11	181.5±13.3	99.48±0.24

In this work, the composition of the mixture was designed to obtain scaffolds with a theoretical porosity of 70.8%. The porosity calculated with **Eq. (2)**, is very close to the theoretical one for all the scaffold types, which makes reasonable conclude that all the charge porogen agents were extracted from devices. This hypothesis is confirmed by the value of the connectivity higher than 99% for all the materials as calculated from **Eq. (3)**. The water uptake, slightly changes for the different pore sized scaffolds but for all the samples there is a percentage of pores filled with water higher than 99%, which demonstrates the high degree of interconnection architecture porous.

Effect of pore architecture in mechanical properties and interfacial adhesion strength

Mechanical behavior of monolayer samples with different pore size are shown in Figure 36A. All the samples show an initial section characterized by a linear-elastic region, likely associated with the bending of the walls of the pores, followed by a transition that can be associated to the beginning of permanent plastic deformation [262,263]. This region of the stress–strain curve assumes different aspects depending on the average pore size. For materials M 300 and M 500 it was observed a distinct peak a of the stress to associate to the structural failure of the specimens, in other cases (M 100, M 90 and M 45) the curves show a horizontal slope therefore the effort does not change during deformation for a stretch deformation. Finally for monolayers with the smallest pore size the trend of plastic region is not associated with a plateau, but

the stress describes a monotonically increasing curve. The last region of the stress strain curve can be associated to the densification region of for all the morphologies. Here, during compression, the pore's walls touch each other causing a steep increase of the stress.

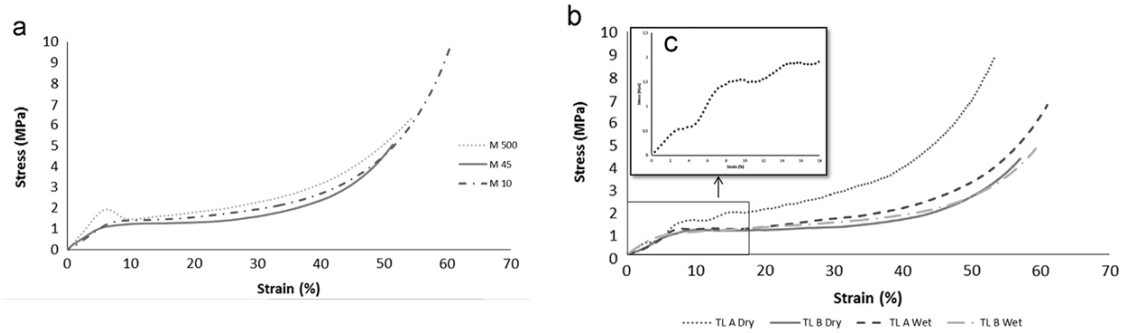

Figure 36 - (a) Stress–strain curve for monolayer scaffold type M 500; M 45 and M 10 in dry condition; (b) Stress–strain curve for three-layer scaffold type A and B in dry and wet environment; c (inset) particular of the first part of the stress strain curve referred to TL A in dry environment.

The stress–strain curves of TL A and TL B samples are shown in Figure 36B both in air and in PBS solution. The mechanical behavior of TL A is characterized by three linear regions followed by three following plateau. This behavior makes reasonable to think that the system collapses one layer at time starting with the weakest one. TL B mechanical behavior instead is very similar to that of monolayers ones because mean pore size of the layers composing it are very close each other's so the plateaus, well visible for TL A, are overlapped for TL B.

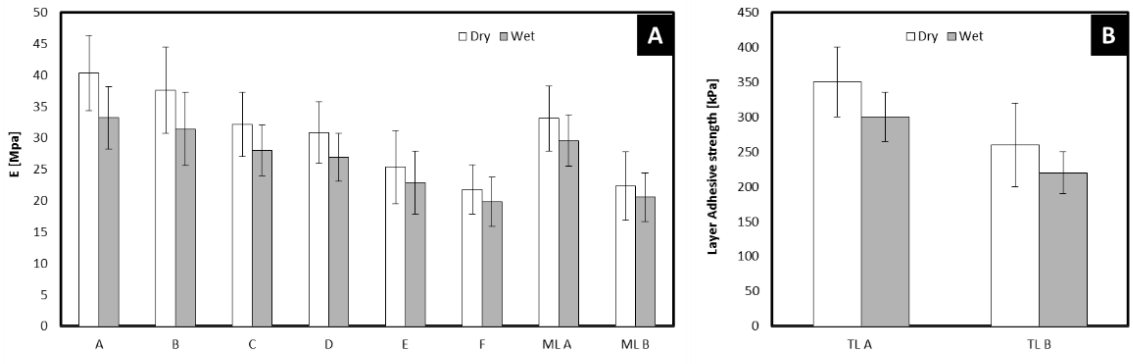

Figure 37 – A) Compressive Young modulus of mono and three-layered scaffold with different pore size in wet and dry environment; B) Layer adhesion strength test results for TL A and TL b in dry and wet condition. In all cases, delamination was not seen at the interfaces. Instead, failure occurred within the intermediate of the

weakest layer. The tensile properties were lower for the TL B than for TL A scaffold. In wet condition the adhesive strain was reduced of about 10% for all tested scaffold.

The histogram in Figure 37A reports the compression elastic modulus evaluated in air and in PBS calculated as the slope of the linear region of the stress strain curve for the monolayers and the three-layer. A trend can be found for this parameter that decrease with the decrease of mean pore size. For three-layered scaffold the *E* value is comparable to that of their respective weaker layer (i.e. M 100 for TL A and M 90 for TL B). The interfacial adhesion strength for TL A and TL B in dry and wet environment, are shown in Figure 37B. Delamination of the different layers was not observed during testing. Failure occurred around the middle part of the weakest layer of TL A (M 100) and the weakest layer of TL B (M 10). The tensile properties were lower for TL B than for TL A. Tests carried out in wet environment showed a decrease of the interfacial adhesion strength of about 10% for all the studied morphologies.

Cell viability and NIH3T3 proliferation rate

Cell viability of NIH3T3 and MC3T3-E1 cells was evaluated by Acridine Orange Assay. As is possible to observe from Figure 38a cell seeded on plate and treated with DXR [10 µM] for 3 h, showed the characteristic apoptotic morphology [69]. On the contrary, in Figure 38b,c are reported respectively NIH3T3 and MC3T3-E1 cells seeded on the device and observed after six days. The tested device do not has released cytotoxic components, in fact cells showed their physiological morphology.

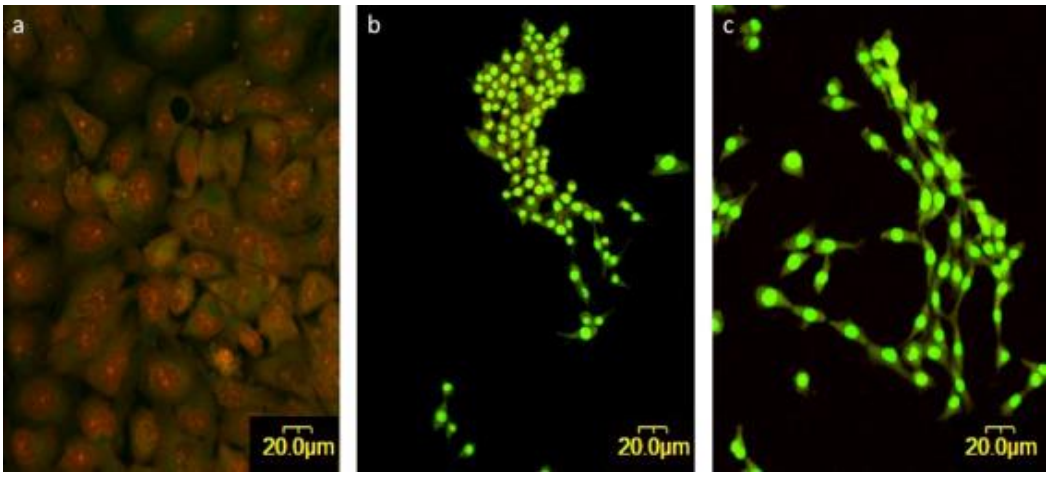

Figure 38 - Exclusion of cytotoxicity by Acridine Orange assay. (a) Positive control. (b) NIH3T3 cell grown on PLA/PEG scaffold for six days. (c) MC3T3-E1 cell grown on PLA/PEG scaffold for six days. As is possible to observe from panel (a), cell seeded on plate and treated with Doxorubicine 10 mM for 3 h, show the characteristic

apoptotic morphology. On the contrary, in panel (b) and (c), the tested device do not has released cytotoxic components, and cell show their physiological morphology.

To evaluate the ability of NIH3T3 to proliferate on and inside the three-layered scaffold, the proliferation rate of cell culture was analyzed using an ImageJ64 software. The histogram Figure 39a shows that the fibroblasts are grown in a linear way and have doubled in four days.

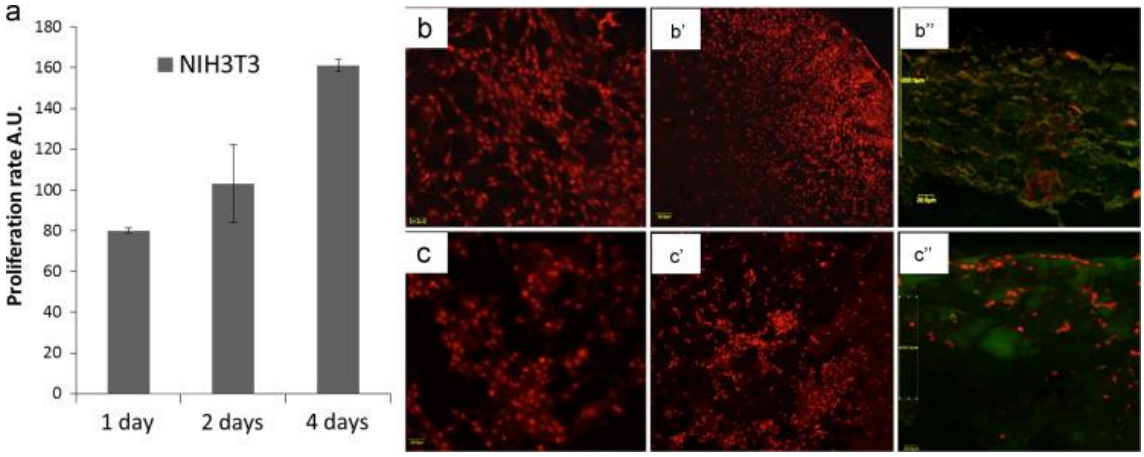

Figure 39 - (a) Analysis of the proliferation rate of fibroblast NIH3T3 cells cultured in the PLA/PEG scaffold using ImageJ 64 software; (b,b') MC3T3-E1 cells grown on surface with minor pore size of PLA/PEG scaffold for 6 day. Nuclei were labeled by PI. From analysis of confocal microscopy was possible to observe the osteoblastic cells proliferation on scaffold surface but, due to their dimension, cells cannot migrate inside it (b"). On the contrary, NIH3T3 cells fibroblastic cells, proliferate on surface with porosity 90–110 μn (c, c') and they are able to migrate inside the polymeric scaffold interconnections, as is possible to observe from the transverse section (c"). (In a and c magnification was 30× In a', b, c' and d, magnification was 10×).

Cells morphology and permeation

The cell morphology was analyzed both, by LSCM and by SEM. The LSCM analysis were carried out to observe different proliferation in co-culture of NIH3T3 and MC3T3-E1 cells. In particular, MC3T3-E1 osteoblastic cells, seeded on the surface with minor pore size (M 10), (Figure 39b,b′), grown and were able to form a layer of about 200 μm, as is described in the figure (Figure 40A,a,b, B). NIH3T3 cells, proliferated on the surface of the layer M 90 (Figure 39c,c′) and they were able to migrate inside the scaffold (Figure 39 c″).

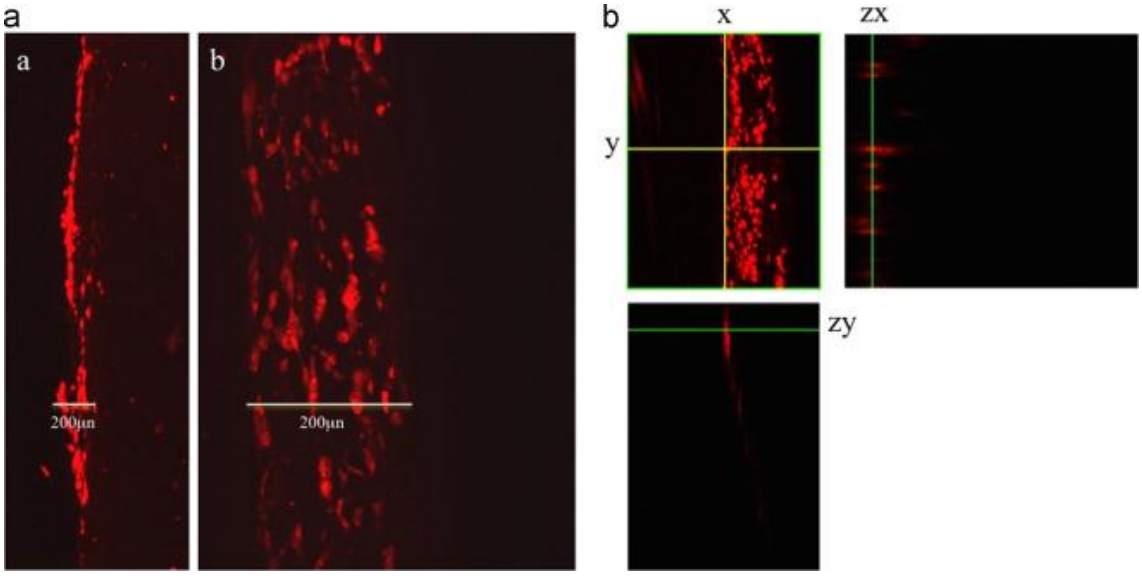

Figure 40 - Transverse sections of MC3T3-E1 grown on the surface with minor pore size of PLA/PEG scaffold; A (a; 10× magnification) The cells were able to form a layer of about 200 µn, as can be observed from the reconstruction of individual sections, obtained from the analysis of confocal microscopy. [Panel A(b; 20× magnification). [Panel B] Analysis of the fluorescence rate of the sample in the 3D using Fluoview 1000 software. As is shown, along the Z axis, the fluorescences appear on the same plane; this indicate that the cells proliferate along X and Y axis and they do not migrate along Z dimension

These results are confirmed by SEM micrographs, (Figure 41a–c). MC3T3-E1 osteoblastic cells were found on the external surface of the layer M 10 of TL B and appears about 40 µm length (Figure 41a). On the other hand NIH3T3, fibroblast cells, smaller than the osteoblast, were found both, on the upper surface of the layer M 90 and inside the layer M 45. (Figure 41b,c). To recognize the differences in dimension between the different cell lines used, it was used the 2D co-culture of MC3T3-E1 and NIH3T3 image showed in Figure 41d.

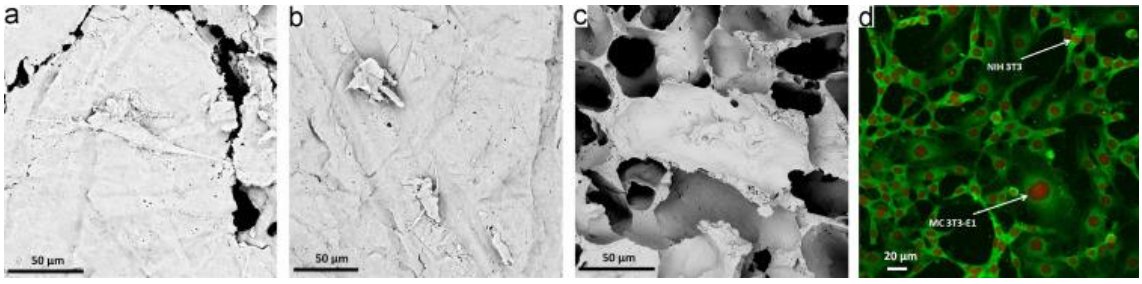

Figure 41 - (a) SEM micrographs of osteoblast on the layer M 10 of TL B. (b), and (c) SEM micrographs of fibroblast respectively on the surface of layer M 90 and on inside the layer M 45. Scale bar is 50 µm. (d) MC3T3-E1 and NIH3T3 seeded together on 2D coverglass. PI (red nuclei) and Phalloidin FITC (green cytoplasm). Is evident the different size of two cell lines in co culture.

Discussion

In our study the melt mixing-salt leaching fabrication method was used to create two three-layered scaffolds with mean pore sizes ranging from 10 to 1000 µm and high interconnected structures.

The first part of this work focused on verifying the predictability of pore size distribution of single layer scaffolds in order to prepare three-layered (or multi-layered) scaffolds with high control of pore architecture by controlling the mean pore size of each single layer composing it. NaCl was chosen as the mineral water-soluble porogen agent and it was found to be the critical factor in terms of pore structure and size. While it acts as a template, the pore structure strongly depends on the salt size and morphology. Moreover the presence of an organic water soluble porogen phase (PEG) partially miscible with PLA [43,257], during leaching step creates a microporous network able to enhance pore interconnection [43,257]. While the NaCl grain size allows control of the scaffold pore dimensions as demonstrated from morphological analysis of each single layer from 10 until 1000 µm, the amount of porogen agents in the melt permit the prediction of porosity. Scaffold porosity is a crucial parameter because it influences both biological and mechanical properties. Although high values of porosity ensure the best regenerative properties, the mechanical properties are strongly affected [264,265].

In fact by considering the complete removal of the porogen agent a theoretical porosity of 70.8% could be evaluated in our work, meanwhile real porosity evaluated by gravimetric measurements, are very close to theoretical one (69.9%), demonstrating that all of the porogen agents were removed during the leaching step. This result is confirmed by the value of the connectivity higher than 99% for all the materials as calculated from **Eq. (3).** Traces of residual PEG are present in the scaffolds enhancing their wettability as previously described [257]. The water uptake, slightly changes for the different pore sized scaffolds but for all the samples there is a percentage of pores filled with water higher than 99%, which demonstrates the high degree of pore interconnection. A highly interconnected porous structure is very important because it allows the seeded cells to theoretically reach every part of the volume of the scaffold.

After having tested the possibility of obtaining porous monolayers with a high control and predictability of pore architecture and porosity, the following step was the

preparation of a three-layer system. The morphological architecture of devices produced in this work, presents three well recognizable layer with different pore size. In particular the mean pore size of every single layer is, as expected, the same as the corresponding monolayer in every region demonstrating a high potential predictability of pore architecture of multi-layered scaffolds. This enabled control of the pore size within each region of the scaffold is crucial since it has been shown that scaffold pore size has a considerable effect both on mechanical properties and on the control of seeded cells. In particular, Levingstone et al. [265] and Murphy et al. [266] showed respectively that both mechanical properties and cells infiltration are significantly affected by scaffold mean pore size.

One of the most complex problems to overcome in the production of multi-layered devices in discontinuous gradient is to avoid any kind of detachment or cleavage between one layer and another [265]. By observing the morphology of the transition region between one layer and another, the device does not present internal cleavages and no matrix discontinuity can be distinguished among the different layers. In order to quantify the adhesion between different layers of TL A and TL B, a custom layer adhesion strength measurement technique was used. The interfacial layer strength was tested until failure with the delamination of the layers. Subsequent examination of the fracture surfaces, delamination was found to occur around the middle part of the weakest layer of TL A and TL B rather than at the interface, corroborating the high adhesion among different layers.

Once tested the predictability of the pore architecture of three-layered scaffolds, mechanical test under compression were conducted in order to analyze the effect of pore size and distribution in the mechanical behavior of the scaffolds both in air at room temperature and in PBS at 37 °C to imitate physiological work conditions.

The relationship between morphology and mechanical behavior can be explained by considering that the maximum stress occurs when the internal structure collapses. Morphological analysis showed that the pore size strongly influences the density of pores per unit of area but also the thickness of the walls around pores. In particular by considering devices with the same porosity, a device that has smaller pores (i.e. M 10) has a greater density of pores per unit of volume and thinner walls if compared with a material with a greater pore diameter (i.e. M 500). When M 500 is mechanical tested

under compression the walls collapse during the compression and the densification phenomena begins later so a peak in the stress–strain curve after the elastic region is appreciable. If the structures presents smaller pores (i. e. M 10) the densification phenomena begins almost simultaneously to the walls yield because the number of pores is much higher and are filled immediately by the material that come from the thin outer walls. This phenomena does not allow the identification of a distinct structural failure.

Observing mechanical behavior of TL A and TL B both in wet and dry conditions, it could be noted that even the mechanical behavior of multilayered scaffolds can be easily predicted by the control of pore architecture. In particular, three-layered systems present the same Young's modulus of their respective weaker layer giving us the possibility to control another crucial parameter of scaffold design. It is well known that mechanical response is crucial for the growth stem cells and differentiation so the possibility to design scaffold [267] with tunable mechanical response is a meaningful result.

The structural characteristics of the device TL B could permit to control the infiltration of different cells inside the scaffold. Pore size ranging from 10 to 100 μm can avoid osteoblast permeation (mean diameter 40 μm) while fibroblast (mean diameter 10 μm) can easily migrate inside. As is well known in literature, PLA is an highly biocompatible polymer [268], however, before starting the biological analysis we wanted to verify the non cytotoxicity of the device. As can be observed (Figure 38) the cells, grown on the scaffold surface for one week don′t show apoptotic signals. Tested the absence of cytotoxicity of the device, the first step was to analyze the ability of cells to proliferate in the TL B. Two cell types in co-culture, with different size were chosen as is shown in the Figure 40d, to mimic the heterogeneous population of bone structure, and to study their different interactions with the device.

Cell infiltration in 3D scaffold is strongly affected by surface properties and by cell–polymer interactions. It was demonstrated in scientific literature [257] that with our fabrication method, a certain amount of PEG can be found in the surface of the scaffold pores. Results of cells adhesion tests suggested that the presence of PEG on the surface is sufficient for adequate cell adhesion and infiltration in the polymeric matrix, in agreement with others studies [269,270].

As described in the results section, although our data are still preliminary and require further studies, the characteristics of the scaffold and biological responses obtained from the co-culture prototype, they suggest that the device designed by us could have major applications in the field of bone regeneration. The next step will be to use mesenchymal stem cells in place of fibroblasts, which, once migrated within the different layers of the scaffold with similar structure to that of spongy bone, and influenced by the environmental factors, [158,271] they will be induced to differentiate in bone cells.

Conclusions

In this work PLA, degradable scaffolds with a discrete pore size gradient has been developed combining melt mixing, compression molding and selective leaching. The devices present high interconnected pore structure with a porosity of 70% and high predictability of pore size by controlling the granulometry of NaCl in the melt mixing step, confirmed by SEM analysis.

Morphological analysis also showed that three-layered scaffold are characterized by well fixed layers with different pore size. Interface adhesion strength tests revealed high layer adhesion without interface fractures.

Mechanical tests showed the strong correlation between pore size and mechanical behavior of scaffold that present a distinct peak of yield stress in the case of high pore diameter (500 μm and 300 μm), a plateau in the case of smaller ones (100 μm; 90 μm and 45 μm) and it is monotonically increasing for the smallest one (20 μm). The Young modulus increases with the pore diameter without changing the total porosity of devices while compressive test in PBS at 37 °C reduces the Young modulus by 10%. Three-layered scaffold present a Young modulus comparable with that of its weaker layer. PLA/PEG based scaffold with discrete pore size gradient realized without using organic solvent presents interesting biomedical applications in particular concerning with interface tissue engineering

The characteristics of the scaffold and biological responses obtained from the co-culture prototype suggest that the device designed by us could have major applications in the field of bone regeneration.

PCL-based porous structures presenting pore size gradient

In this section is presented the preparation and characterization of PLA-based porous structures presenting pore size gradient. The aim of this work is to find a correlation between the preparation, the morphology and mechanical properties of the PLA-based three-layered scaffold. Moreover the structural characteristics of this device, similar to the spongy bone structures, prompted us to investigate about the effect of different pore size layers on cellular permeation and the possibility of using the three-layered porous PLA/PEG scaffold for bone regeneration. The sample codes of the materials as well as the composition and the NaCl granulometry, are shown in Table 13.

Table 13 - Materials prepared by melt mixing PCL, PEG, and NaCl in different granulometry

Sample code	PCL [wt%]	PEG [wt%]	NaCl [wt%]	NaCl granulometry [µm]
M 100	20	5	75	90–110
M 50	20	5	75	45–65
M 10	20	5	75	<40

Morphology

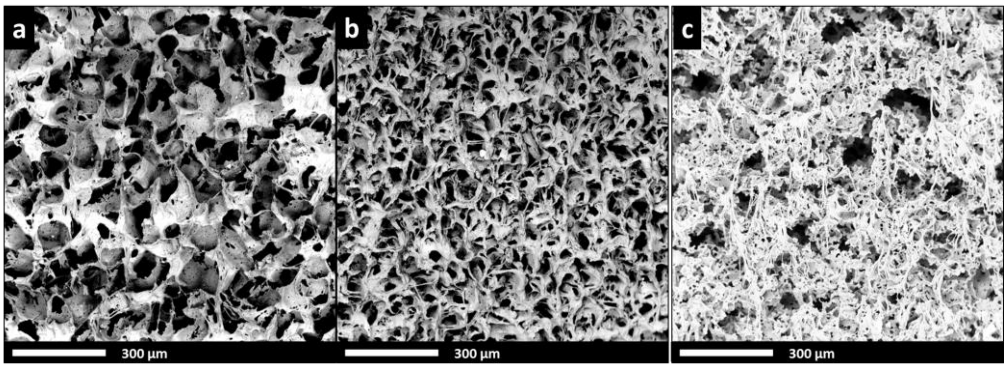

Figure 42 - SEM images of monolayered scaffold obtained by leaching melts with different salt particles size: M 100 (a), M 50 (b) and M 10 (c)

Figure 42(a-c) shows images obtained by SEM of monolayered scaffolds realized by leaching material filled with different sized salt crystals. In particular, M 100, (Figure 42a), morphology, shows roughly cubic pores that seems to be homogeneously distributed throughout the polymeric network. M 45, (Figure 42b), SEM images show a high density of pores per unit of volume with dimensions ranging from 40 µm to 60

µm. M 100 and M 50 presented a multimodal pore structure i.e. with distinct pore sizes and pore architectures. In fact, micropores network, characterized by pores ranging from 1 to 5 µm are reasonably due to PEG solvation, can be observed into the pores wall [19,43]. Finally, M 10 materials, (Figure 42c), present the highest density of pores per unit of volume. This structure in highly interconnected with an average pores size of 20 µm with walls very thin (thickness even below 1 µm). In this case it is more difficult identify the multimodal pore structure.

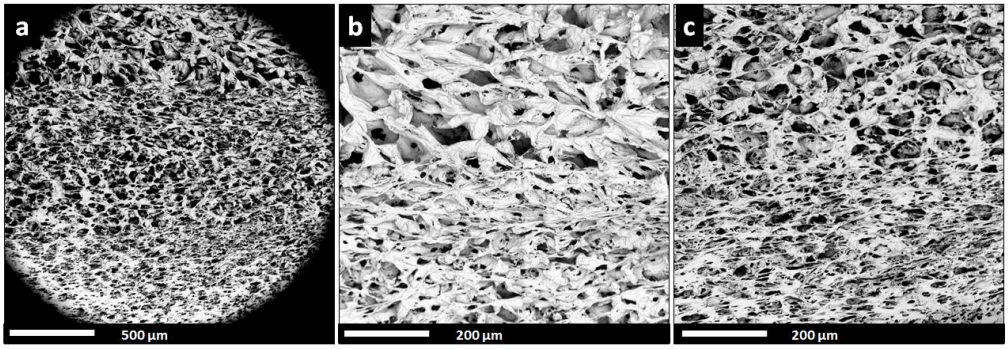

Figure 43 - SEM images of three-layered scaffold type A: a) entire cross section; b) transition region between layers with M 100 and M 50; c) transition region between layers M 50 and M 10

After having tested the possibility to obtain porous monolayers with a high control and predictability of pore architecture, the following step was the preparation of a three-layers systems as described in the experimental section. Figure 43a-c is the picture of a section of a three-layer system composed by M 100, M 50 and M 10 (TL) after the leaching process. In Figure 43a it is possible to observe clearly the three layers with the three different average pore size.

Table 14 -Theoretical porosity (%), porosity (%), connectivity (%), water uptake (%) in function of scaffolds pore size

Scaffold code	Theoretical Porosity (%)	Porosity (%)	Connectivity (%)	Water Uptake (%)
M 100	70,84	70,18 ± 0,55	99,45 ± 0,15	220,2 ± 11,4
M 50	70,84	69,84 ± 0,42	99,32 ± 0,14	270,3 ± 14,7
M 10	70,84	69,97 ± 0,47	99,54 ± 0,22	290,8 ± 7,1
TL	70,84	69,55 ± 0,72	99,60 ± 0,20	280,5 ± 13,3

In particular, it is possible to see that each layer presents the same morphology as the equivalent monolayer. The full control of the pores size within each region of the three-layered scaffold is crucial since it has been shown that scaffold pores size has a

considerable effect both on the mechanical properties and on the control of the proliferation of seeded cells. In particular, Levingstone et al. [265] and Murphy et al. [266] showed that both mechanical properties and cells infiltration are significantly affected by scaffold mean pores size.

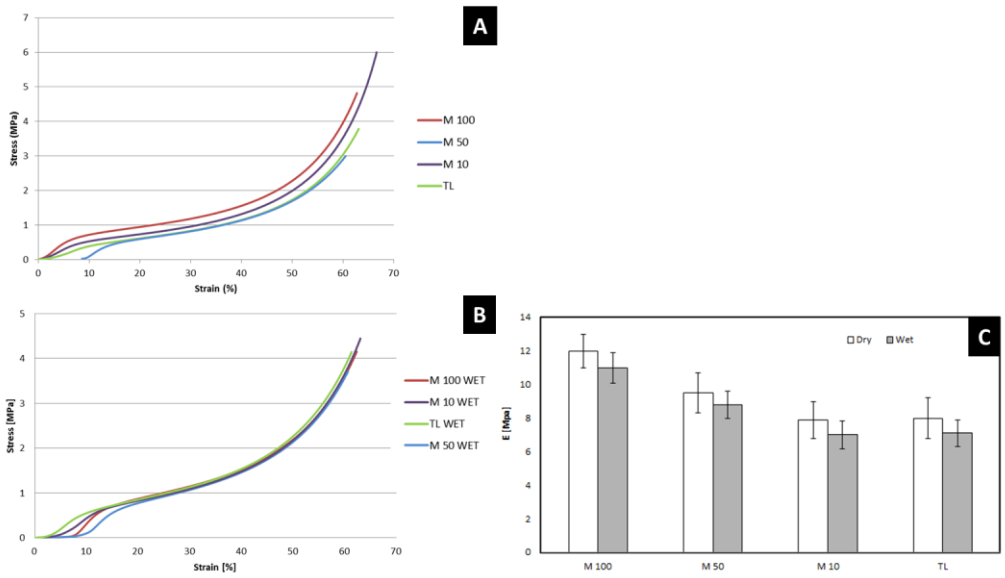

Figure 44 (A,B) Stress-strain curve for tested scaffold in dry condition (A) and in wet condition (B); (C) Compressive Young modulus of mono and three-layered scaffold with different pore size in wet and dry environment

One of the most complex problems to overcome in the production of multi-layered devices in discontinuous gradient is to avoid any kind of detachment or cleavage between one layer and another. Figure 43b-c, shows at a higher magnification the transition regions between respectively (M 100 – M 50) and (M 50 – M 10) layers. It can be observed that the whole device do not present internal cleavages and no matrix discontinuity can be noted among the different layers.

In Table 14 there are summarized the theoretical porosity (%), the porosity (%), connectivity (%), water uptake (%) as a function of scaffolds pores size for the single layers and for the whole TL device. Although high values of porosity ensure best regenerative properties, the mechanical properties can be negatively affected [38]. In this work, the composition of the mixture was designed to obtain scaffolds with a theoretical porosity of 70.8 %.

A serious problem related to leaching technology in scaffold production is the partial and not complete removal of porogen agents, because traces of mineral porogen residues could have negative effects on cells proliferation and can cause inflammation

to the surrounding tissues. The presence of another water-soluble organic phase in the mixture, PEG, had the role to increase the degree of interconnection between the pores by allowing a complete leaching of mineral filler as shown in scientific literature [19,43]. The porosity calculated by Eqn 11, is very close to the theoretical one for all the scaffold types, which makes reasonable to conclude that all the filled porogen agents were extracted from the devices.

This hypothesis is confirmed by the value of the connectivity, higher than 99% for all the materials, as calculated from Eqn 12. A highly interconnected porous structure is very important because it makes easy the seeded cells to infiltrate the scaffold even in its inner parts. The water uptake, slightly changes for the different pores sized scaffolds but for all the samples there is a percentage of pores filled with water higher than 99 %, which demonstrates the high degree of interconnection architecture porous.

It is well known that typical stress–strain curves of polymeric scaffolds exhibit qualitative characteristics similar to that of metallic or polymeric foams [43,264]. Stress-strain curves of representative monolayer samples with different pores size (M 100, M 50 and M 10) and for TL are shown for dry and wet condition in Figure 44A and Figure 44B respectively. All the samples show an initial region characterized by a linear-elastic behavior, likely associated with the elastic bending of the pores walls, followed by a transition that can be associated to the beginning of permanent plastic deformation [19,264]. The last region of the stress strain curve can be associated, for all the morphologies, to pores densification. In this region, in particular, the pores walls touch each other cells thus causing a steep increase of the stress.

The elastic modulus calculated as the slope of the first linear region depends on the pores architecture and on the environmental conditions of the mechanical tests.

In fact TL modulus, evaluated in PBS at 37 ° C ± 0,1 °C is 7,09 ± 0,85 MPa while it grew up to 8,04 ± 1,12 MPa in dry environment. An increase of about 10 % of this value was evaluated ether for TL and for each monolayer composing it when tested in dry conditions. This change of modulus can be associated with the higher testing temperature adopted and to presence of the liquid phase on testing medium.

By testing monolayer a decrease of elastic modulus of samples was observed with the decrease of the respective average pores size. M 100 showed E value of 12,04 ± 0,98 MPa in dry environment; M 50 E value is 9,53 ± 1,11 MPa and M 10 elastic

modulus is 7,91 ± 1,08 MPa as showed in the histogram in Figure 44C. With the same porosity, reducing the average pore size means increase the volumetric density of defects that cause a loss of mechanical properties of scaffold as observed by other related studies [19,264]. More in detail, TL presented an elastic modulus comparable with that of the monolayer M 10 so its weakest layer as visible from Figure 44C. This demonstrate that the elastic modulus of the multilayer device, with the gradient geometry realized in this work, is dependent from the weakest layer composing it.

The structural characteristics of this device, similar to the multilayer cartilage of the extracellular matrix (ECM), prompted us to investigate about the effect of different pore size layers on cellular permeation. MC3T3-E1 osteoblastic cell and NIH 3T3 fibroblastic cell line were chosen as a model for their different size. To be sure that the tested device was biocompatible, cell viability was evaluated by the Acridine Orange essay. NIH-3T3 and MC3T3-E1 cells seeded respectively on the device, showed their physiological morphology also after six days in culture. On the contrary, the same cells, seeded on plate and treated with DXR [10µM] for 3hr, (positive control) showed the characteristic apoptotic morphology **[41]** (Data not shown). This results confirmed that polymeric support did not release cytotoxic components, according to the manufacturing of the device.

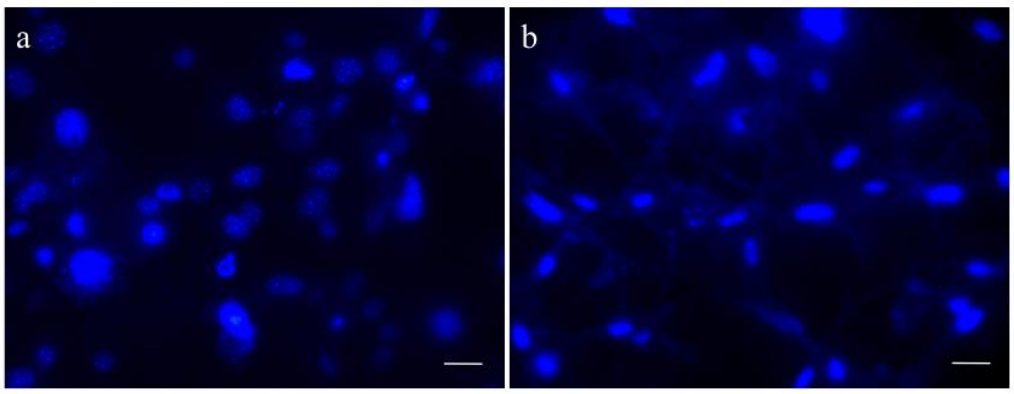

Figure 45 - The MC 3T3-E1 cells seeded on PCL, respectively after 1day (a) and 2days (b) of culture. Cells were stained with DAPI. Scale Barr was 20µn

To investigate about the effect of different pore size layers on cellular permeation and to observe as NIH 3T3 and MC3T3-E1 cells, in co-culture, interacts with the device surface and proliferate on and inside it, LSCM analysis were carried out. Data obtained suggest that: MC3T3-E1 osteoblastic cells, seeded on the surface with lowest

pore size (M 10), due to their high size cannot migrate inside the polymeric support; they have been able to grow only on the scaffold surface as is shown in Figure 45. Differently, NIH3T3 fibroblastic cells, smaller than the osteoblast, proliferate on surface of layer M 90 and they were found able to migrate inside the polymeric scaffold interconnections as demonstrated from 3D analysis with Imaris software (Figure 46).

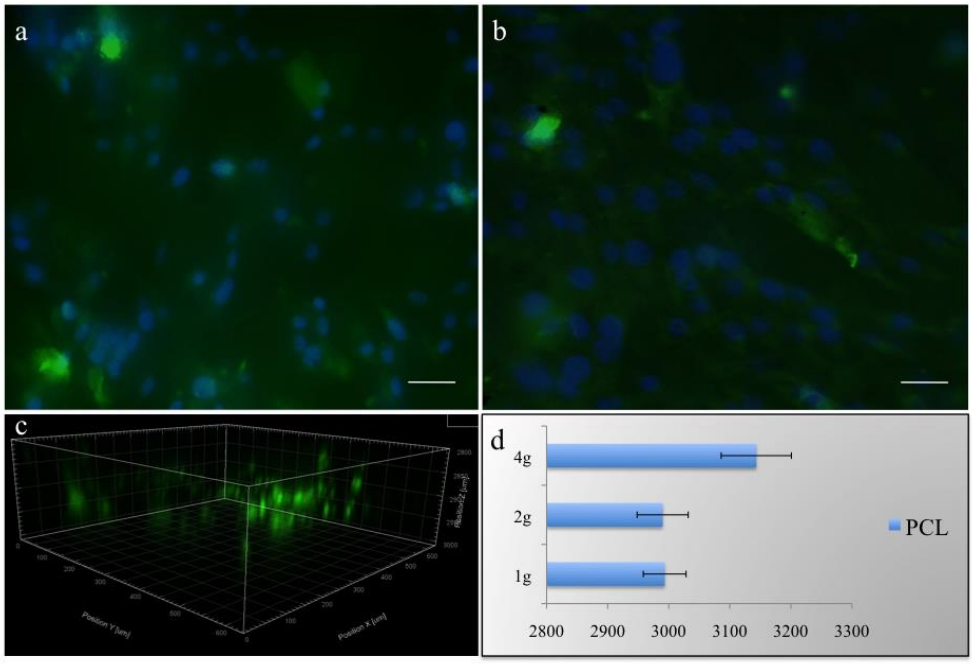

Figure 46 - The NIH 3T3 cells seeded on PCL , respectively after 2days (a) and 4days (b) of culture. (Magnification was 20X) 3D representation of cell migration inside of the scaffold interconnections using Imaris software. (c) The histogram(d) show the migration rate of NIH 3T3 inside PCL device. Data are a media of three different samples. Cells were stained by CSF FITC and DAPI.

These data were also confirmed by SEM images of scaffold after cell immobilization. From Figure 47a it is possible to observe MC3T3-E1 on the top of the layer M 10, while in Figure 47b some NIH3T3 cells on the surface of layer M 100. Figure 47c is a SEM images of a cross section of the Layer M 50 of TL, which confirmed that only NIH3T3 were found inside the porous structure.

These data, also if needing of further investigations, suggest the possibility of using the three-layered porous polycaprolactone/polyethylene glycol (PCL/PEG) scaffold for cartilage regeneration.

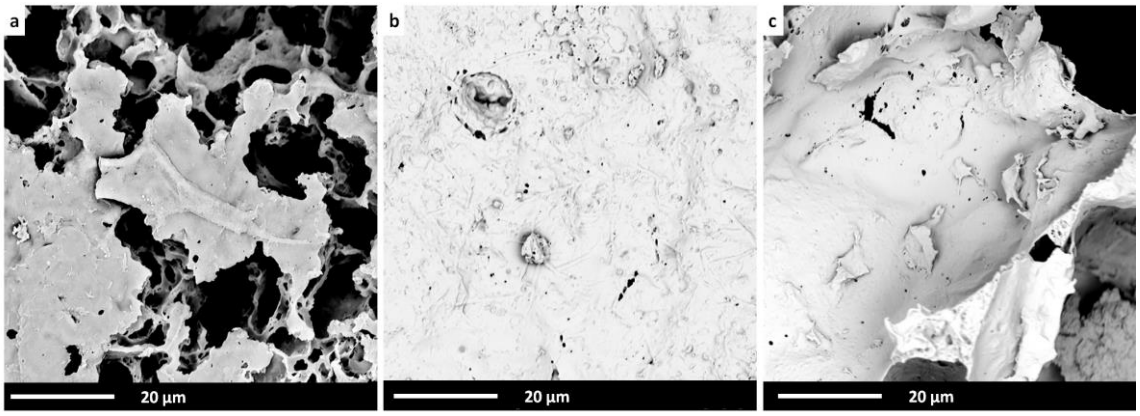

Figure 47 - a) SEM micrographs of osteoblast on the layer M 10 of TL. b), and c) SEM micrographs of fibroblast respectively on the surface of layer M 100 and on inside the layer M 50.

Conclusions

In this work PCL, degradable scaffolds with a discrete pore size gradient has been realized combining melt mixing, compression molding and selective leaching. The devices present high interconnected pore structure with a porosity of 70% and high predictability of pore size by controlling the granulometry of NaCl in melt mixing step, confirmed by SEM analysis.

Morphological analysis also showed that three-layered scaffold are characterized by well joint regions with different pore size, without loss of adhesion or interface fracture.

Mechanical test showed the strong correlation between pore size and mechanical behavior of scaffold that present a neat peak of yield stress in case of high pore diameter, and a plateau in case of little ones. Young modulus increase with the pores diameter without changing the total porosity of devices while compressive test in PBS at 37 °C reduce young modulus of 10%. Three-layered scaffold present a young modulus comparable with that of the weaker layer. PCL/PEG base scaffold with discrete pore size gradient realized without using of organic solvent present interesting biomedical application in particular concerning with interface tissue engineering

The characteristics of the scaffold and biological responses obtained from the co-culture prototype, they suggest that the device designed by us could have major applications in the field of bone regeneration.

4.5 Integration of 3D Porous PCL and PLA for Heterogeneous Devices

Mechanical behavior of Polylactic acid/Polycaprolactone porous layered functional composites

In this section, it will be discussed the preparation and characterization of a chemically graded laminate porous device composed by a PLA-based core and a PCL-based shell in form of monolith.

The novelty of this work can be principally ascribed to the preparation route of the multiphasic porous laminates, conducted by melt. In fact, the devices were fabricated by combining melt mixing, compression molding and particulate leaching.

The relative volume ratio was controlled by the thickness of each layer in order to investigate the correlation between the preparation, the morphology and mechanical properties of three-layered laminate based on PCL and PLA. In particular, the study of mechanical properties of porous bio-laminates were investigated as a function of the relative contribution of the layers to the whole laminated device.h

System fabrication

In brief, PLA (or PCL), PEG and NaCl (seized: 100-200 μm), with weight percentage composition of respectively 20/5/75, were fed to a batch mixer. In Table 15 the different size thickness of the layers.

Table 15 –Sample code and thickness of the layers of the porous laminates

Sample Code	PCL Layer (mm)	PLA Layer (mm)	PCL Layer (mm)
PCL	3	0	0
LAM_0.5	1.25	0.5	1.25
LAM_1	1	1	1
LAM_2	0.5	2	0.5
PLA	0	3	0

Morphological analysis

Figure 48a-f show SEM micrographs of monolayer and multi-phasic laminates.

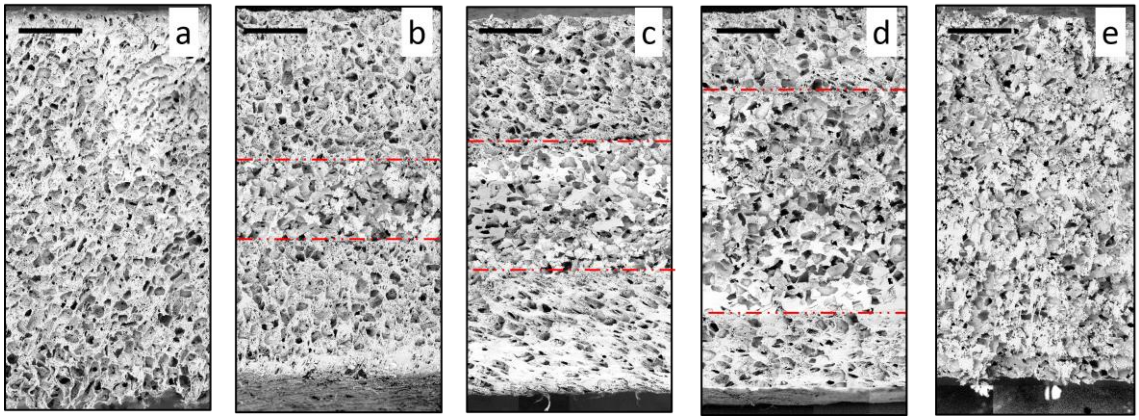

Figure 48 - SEM images of porous laminates: a) PCL sample; b) PCL laminate with PLA core 0.5 mm thick (LAM_0.5); c) PCL laminate with PLA core 1 mm thick (LAM_1); d) PCL laminate with PLA core 2 mm thick (LAM_2) and e) PLA sample. Scale bar is 500 µm.

In particular, Figure 48a refers to the device containing only PCL, characterized by a homogenous pores size distribution. Figure 48b shows the laminate LAM_0.5 characterized by a PLA-based core layer (500 µm thick), evidenced by the red lines and a PCL-based shell. Figure 48c reports the laminate developed by assembling 1 mm of PCL (top), 1 mm of PLA (core) and 1 mm of PCL (bottom) (LAM_1). Figure 48d shows the morphology of the LAM_2, the multilayer with the highest volumetric fraction of PLA, while the Figure 48e shows the device composed entirely of PLA.

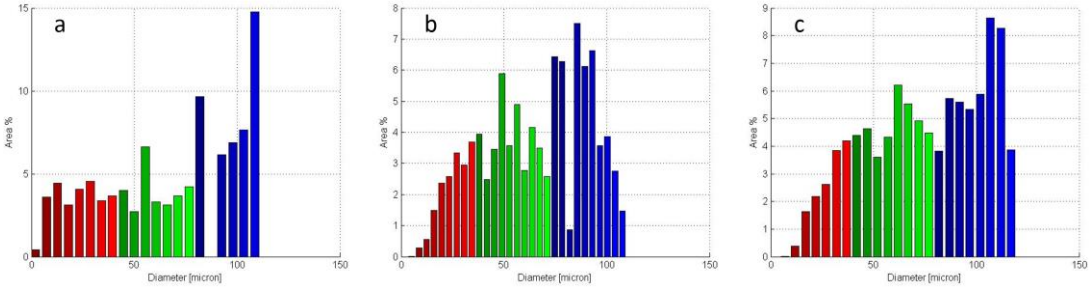

Figure 49 - Histograms representing the PAD of a) PCL sample; b) PCL laminate with PLA core 1 mm thick (LAM_1); c) PLA sample. PAD of LAM_0.5 and LAM_2 not shown for sake of brevity.

These pictures suggest that the macro-pore architecture (about 100 µm) of the laminates is not dependent on the kind of material but only on the granulometry of the sieved NaCl filled during the melt mixing process, that was in the range of 90-110 µm. Indeed, the morphology of the multi-phasic laminates, reported in Figure 48b-c, is very similar to those of the monophasic devices (Figure 48a,e), as further confirmed by the pore area distribution (PAD) calculated by image processing and reported inFigure 49a-c. The histograms put into evidence that all the laminates present a similar PAD

with a concentration of pores within the range 90-110 µm, the same as the sieved salt particles, thus confirming that the macropores network can be controlled, tuned and predicted by the granulometry of the salt filled in the polymer matrix.

Moreover, by comparing the morphologies of PCL (Figure 49Figure 50a) and PLA (Figure 49c), it is possible to detect a higher amount of pores around 10 µm for PCL sample.

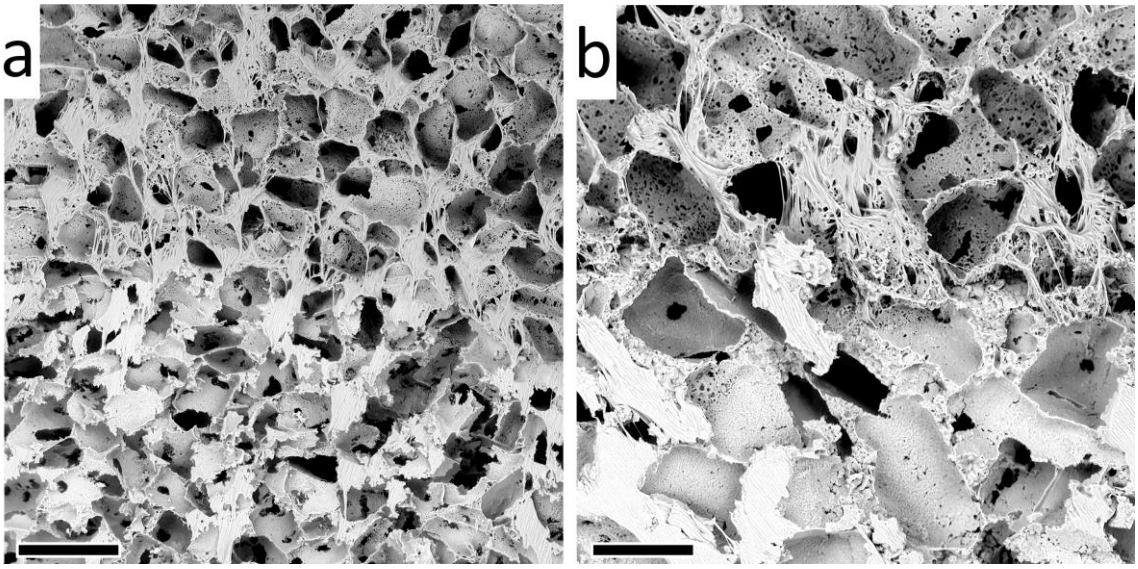

Figure 50 - SEM images of the interface region between the PCL (top) and PLA (bottom) layer of the sample C. a) Scale bar is 200 µm b) Scale bar is 100 µm.

In fact, SEM analysis carried out at higher magnification showed that the two phases exhibit slight differences in the pores architecture. Figure 50a,b reports the micrographs taken at the interface region between the PCL (top) and the PLA (bottom) layer of the LAM_1, chosen as representative multi-phasic laminate for sake of brevity. Figure 50a confirms that the macropore structure of the two layers is very similar but the PCL phase is characterized by a continuous network of micro-pores (about 5 µm), likely due to the solvation of the PEG phase [46], clearly visible at higher magnification (see Figure 50b). Even the PLA region presents a microporous network due to the PEG solvation [19] but, owing to the higher solubility of PEG in PLA, the concentration of micro-pores is significantly lower than those observed within PCL layers. Moreover, PAD analysis carried out by image processing strongly confirm this hypothesis. (Figure 49c).

Figure 51 - Digital photo of sections of the multi-phasic laminates with the PLA core layer green colored. a) PCL laminate with PLA core 0.5 mm thick (LAM_0.5); b) PCL laminate with PLA core 1 mm thick (LAM_1); c) PCL laminate with PLA core 2 mm thick (LAM_2). Scale bar is 1 mm.

The presence of the microporous network in the PCL phase allowed us to better distinguish each layer during SEM observations; however, one of the polymeric phases (PLA) was colored with a green pigment in order to better identify each polymer, thus providing further confirmation that each relative layer thickness was effectively developed according to the previous design. Figure 51a-c show the digital pictures of LAM_0.5, LAM_1 and LAM_2 sections. The images confirmed that the method here presented allowed achieving the full control of the thickness for each layer composing the laminate. In fact, the whole sample is 3 mm high in all the cases, the thickness of green stained PLA layer is about equal to 500 µm (Figure 51a), 1000 µm (Figure 51b) and 2000 µm (Figure 51c), in compliance with the planned design.

Another important morphological analysis regarded the interface between each layer of the composite. In Figure 48b-d it can be observed that the entire device does not present any internal cleavages; moreover, no discontinuity can be distinguished in the interlayer region. The high adhesion is clearly visible even in Figure 50a,b and furtherly confirmed by tensile tests, as will be better discussed below.

Porosity, connectivity and water uptake analysis

Table 16 summarizes theoretical porosity (%), porosity (%), connectivity (%) and water uptake (%) for each different laminate. In this work, the formulation of the mixture was designed in order to obtain scaffolds with a theoretical porosity of 70.8%. The porosity, calculated by Eqn 11, is very close to that theoretically predicted for all the laminates, hence suggesting that all the porogen agents were extracted from devices within the leaching step [19,46]. The data collected about the connectivity, calculated according to Eqn 12 and resulted higher than 99 % for all the samples, strongly confirm this hypothesis. The laminates showed a water uptake ranging within 220 % (for neat PCL) and 290 % (for neat PLA) likely due to the different wettability

of the polymers. Consequently, the multi-phasic samples displayed a water uptake dependent on the content of PLA. The higher the PLA amount the higher the water uptake.

Table 16 - Theoretical porosity (%), porosity (%), connectivity (%), water uptake (%) as a function of the type of laminate.

Sample code	Theoretical	Porosity	Connectivity	Water Uptake (%)
PCL	70.84	70.18 ± 0.55	99.45 ± 0.15	220.2 ± 11.4
LAM_0.5	70.84	69.84 ± 0.42	99.32 ± 0.14	270.3 ± 14.7
LAM_1	70.84	69.97 ± 0.47	99.54 ± 0.22	280.8 ± 7.1
LAM_2	70.84	69.55 ± 0.72	99.60 ± 0.20	285.5 ± 13.3
PLA	70.84	70.25 ± 0.42	99.50 ± 0.22	290.5 ± 10.2

Laminates tensile mechanical behavior

Figure 52 reports the experimental and theoretical (iso-stress model prediction) data carried out from tensile tests.

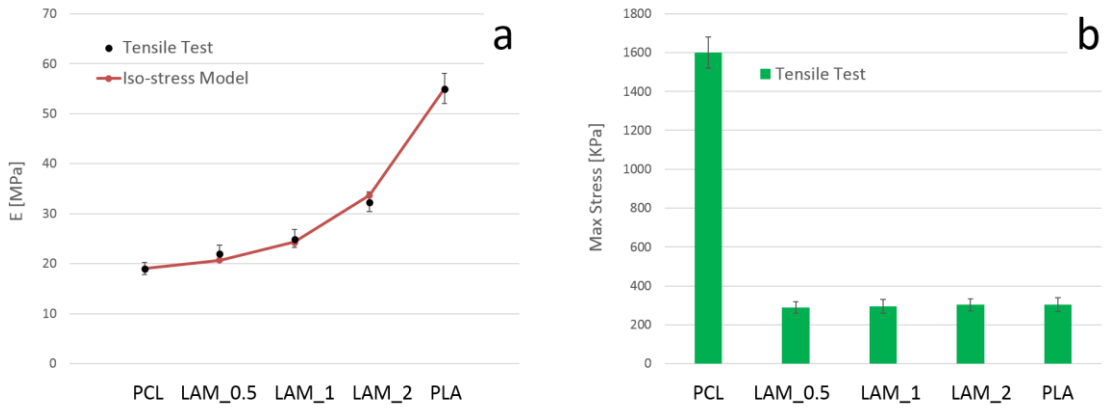

Figure 52 - a) E modulus and iso-stress model of the tensile mechanical test for the different laminates; b) Tensile stress for the different laminates

In particular, Young's modulus, reported in Figure 52a, was found to strongly depend on the relative thickness of the different layers, i.e. the larger the PLA layer the higher the E value. Furthermore, the iso-stress model, which is valid if each layer of the composite is ideally subjected at the same stress, fits very well the experimental

data collected; that is reasonably due to the high adhesion strength between the different layers of the laminates.

The high adhesion strength is confirmed by the maximum stress values plotted in Figure 52b. Tensile strength is 1.6 MPa for the porous PCL and 360 kPa for PLA. The multi-phasic laminates showed a tensile strength comparable with the PLA laminate and the fracture always occurred in the PLA region, as highlighted in Figure 53a-d, and never at the interface. This feature demonstrates that the adhesion strength is higher than the ultimate resistance of the PLA layer.

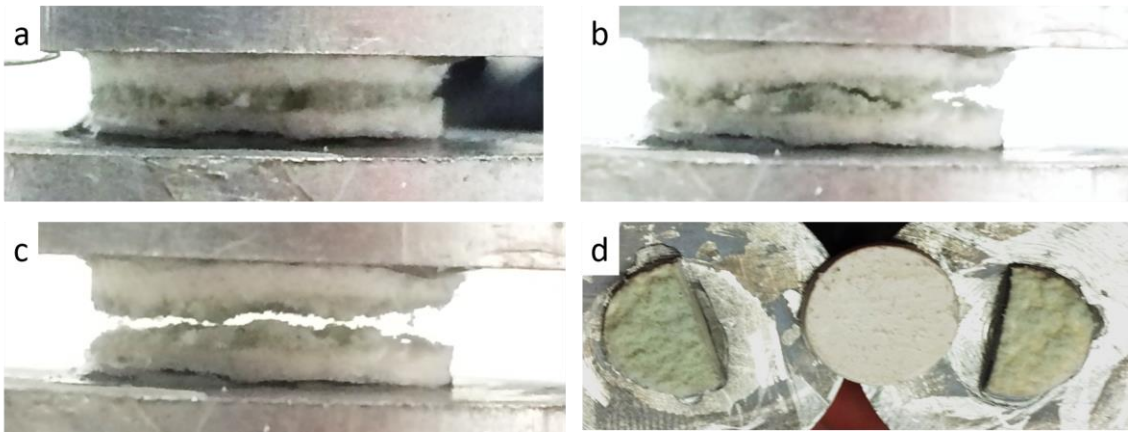

Figure 53 - Digital photo of the LAM_1 tensile test at different deformation. a) not deformed; b) the crack start in the PLA layer (green); c) complete fracture; d) surface fracture of the sample is green, the white laminate in the center is to see better the col

In order to ensure that the fracture of the device occurred in the PLA layer, ATR analysis were carried out on both the fracture surfaces. The spectra, reported in Figure 54a,b, show the typical peaks of the PLA, as listed in Table 17, thus ensuring that the fracture occurred within the PLA layer for all the multi-phasic laminates investigated [272].

Table 17 – Peak band assignment for PLA [272]

Peak number	***Assignment***	***Wavenumber cm^{-1}***
1	-CH- stretch	3000 (asym.),
2	-C=O carbonyl stretch	2948 (sym.),
3	-CH_3 bending	1747
4	-CH- asymmetric; symmetric deformation	1456
5	-CH- bending	1382; 1360
6	-C-O- stretching	1315-1300
7	-C=O bending	1265
8,9,10	-C-O- stretching	1211
11	-OH bending	1180, 1129, 1083
12	-CH_3 rocking mode	955, 916
13	-C-C- stretching crystalline phase	869
14	Amorphous phase	755

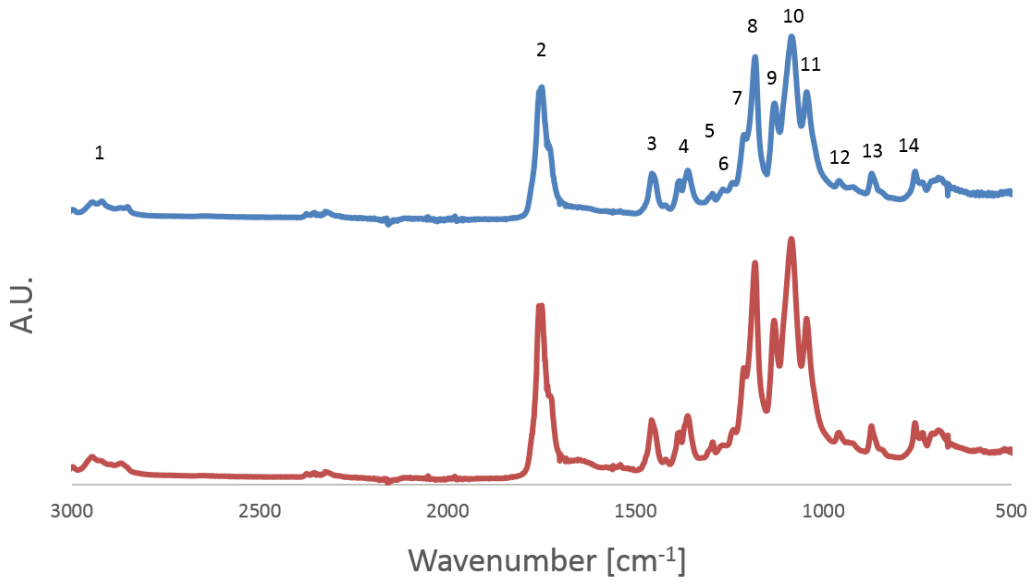

Figure 54 - ATR-FTIR of both the fractured surfaces of the LAM_1 sample. It present the typical peaks of the PLA for both the fractured surfaces.

Laminates compressive mechanical behavior

Figure 55a,b reports the mechanical behavior under compression and the corresponding iso-stress model predictions for all the samples. The elastic modulus (Figure 55a), in this case, was practically constant and equal to about 7 MPa.

Getting into the details, one may notice that the compressive modulus was found to depend only on the weakest layer (PCL), regardless of PLA thickness [19,46]. For this reason, the iso-stress model was unable to predict the experimental data (Figure 55a).

These results can be likely explained by considering that the aspect ratio of the cell ribs, characterized by a very low thickness in comparison with their height (i.e. pore diameter), makes them prone to elastic buckling [25]. This phenomenon, occurring only under compression, mainly affects the softest layer. Likely due to this feature, the experimental data for the multi-phasic structures remain practically constant and close to that of PCL.

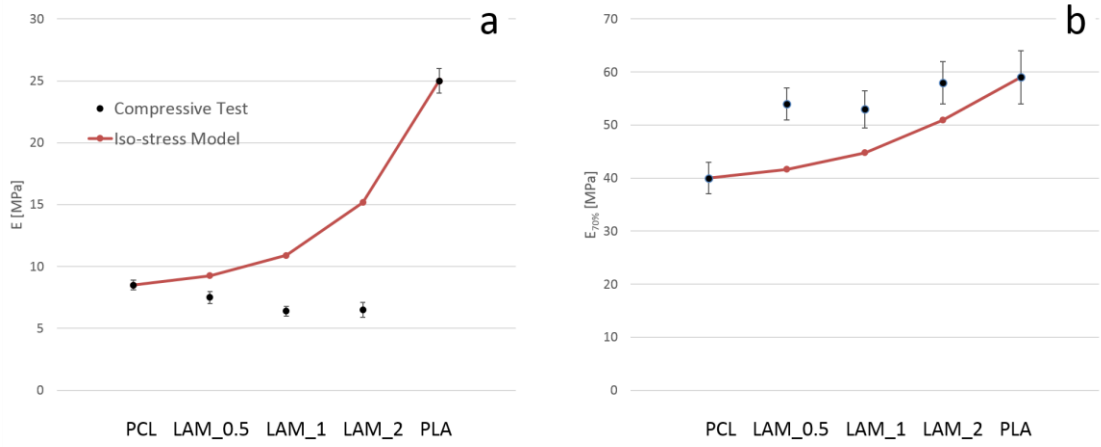

Figure 55 - a) E modulus and iso-stress model of the compressive mechanical test for the different laminates; b) E¬¬D measured in the linear densification region and iso-stress prediction.

In the last region of the stress-strain curves, σ was found to linearly increase as a function of the strain. This feature can be ascribed to the densification phenomena occurring since the pore walls collapsed thus filling the voids. The slope of this linear zone (E_D) was then measured and plotted in Figure 55b as a function of the PLA thickness.

Except for the PCL, this property levels off, remaining equal to that of PLA, i.e. around 55MPa. Even in this case, the iso-stress model is unable to fit the experimental data. Interestingly, E_D seems to be totally controlled by the PLA layer.

Conclusions

In this work, porous PCL/PLA multi-phasic laminates were prepared by combining melt mixing, compression molding and selective leaching. The devices showed highly interconnected porous structure with a porosity of 70%. This eco-friendly technique ensures achieving high predictability of both pore size and porosity, by simply tuning the amount and the granulometry of NaCl, respectively as confirmed by SEM, image processing and gravimetric analyses.

Morphological and mechanical analyses highlighted that three-layered laminates are characterized by well joint regions without loss of adhesion or interface fracture.

Tensile mechanical tests showed the strong correlation between E value and the relative thickness of the layers composing the laminates, with a trend that strongly follows the iso-stress model predictions. Compressive mechanical tests showed that the E value is controlled by the weakest layer composing the multi-phasic laminates i.e. the PCL.

In conclusion, this approach permits to design multi-phasic porous devices with a high control of both morphological and mechanical characteristics.

Bilayer Heterogenous Scaffold Presenting Pore Size Gradient

In this section it will be discussed the preparation and characterization of a bi-layered scaffolds (BLS) composed by PLA with pores in the range of 90–110 μm and PCL with pores ranging from 5 to 40 μm.

The different chemo-physical properties of the two biopolymers combined with the tunable pore architecture permitted to realize a monolithic BLS engineered to be potentially used for interface tissue regenerations.

BLS morphology was investigated by SEM. The compressive mechanical behavior of the scaffolds was evaluated both in air and under immersion in PBS solution at 37 °C, in order to simulate the physiological environment. Furthermore, tensile tests were also performed in order to investigate the interfacial adhesion strength between PCL and PLA layers. Biological tests were carried out in culture and co-culture of osteoblast seeded in the PLA layer and fibroblast seeded in the PCL layer. These cell

lines were chosen as models due to their different sizes, with the aim to investigate the influences of the chosen different pore size on their migration and proliferation inside the BLS.

Morphological analysis

Figure 56A is a SEM image of the entire BLS that shows a well interconnected porous structure with a strong difference between the PLA pore architecture and the PCL layer.

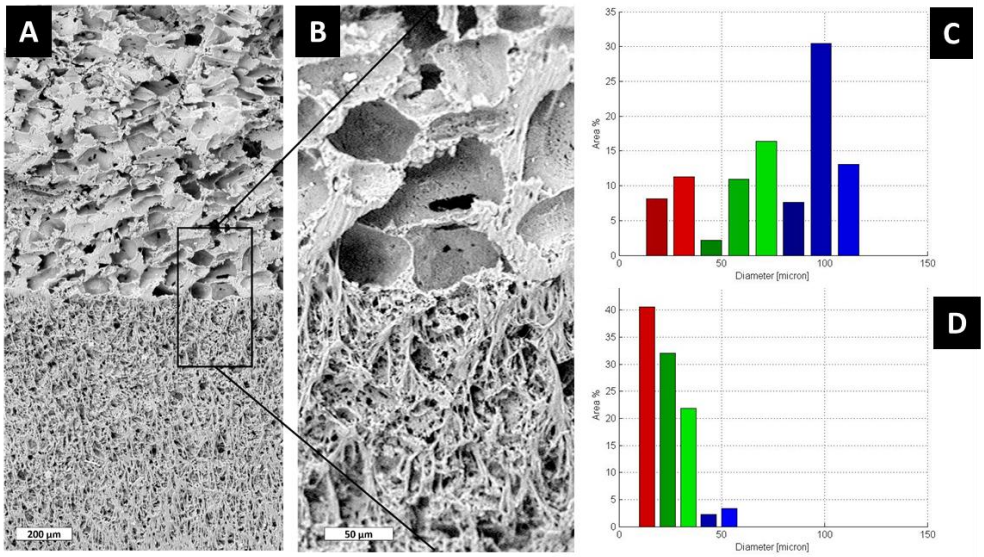

Figure 56 - A) SEM image of the entire BLS; top half refers to the PLA layer with pores smaller than 110 µm; bottom half refers to the PCL layer with pores smaller than 40 µm. B) Higher magnification of the interface region; (C,D) Histograms representing the PAD of (C) PLA layer; (D) PCL layer.

The interface region between PLA and PCL of the device do not present internal cleavages nor matrix discontinuity as better shown in the magnification in Figure 56B. More in detail, the pore size analysis of the PLA layer, showed in Figure 56C, reported a three-modal pore distribution with roughly cubic macropores with main size in the range of 30 µm, 70 µm and 100 µm and a micropores network due to the solvation of the PEG phase, better visible in Figure 56B. The walls around the macropores are 5 µm deep and fully covered by the micropores network. On the other hand, the PCL layer is characterized by a high density of well-interconnected pores ranging from 5 to 40 µm (Figure 56D).

Porosity, connectivity and water uptake analysis

In Table 18, there are summarized theoretical porosity (%), porosity (%), connectivity (%), water uptake (%) for the single layers and for BLS.

Table 18 - Theoretical porosity (%), porosity (%), connectivity (%), water uptake (%) as a function of the type of scaffold

Scaffold code	Theoretical Porosity (%)	Porosity (%)	Connectivity (%)	Water Uptake (%)
PLA	70,84	70,18 ± 0,55 [a]	99,45 ± 0,15 [a]	290,2 ± 11,4[a]
BLS	70,84	69,84 ± 0,42 [a]	99,32 ± 0,14 [a]	240,3 ± 14,7[b]
PCL	70,84	69,97 ± 0,47 [a]	99,54 ± 0,22 [a]	218,4 ± 7,1[c]

Values are given as means ± SD. Different letters in the same column indicate significant differences ($p < 0.05$) when analyzed by Tukey's multiple comparisons tests.

In this work, the composition of the mixture was designed to obtain scaffolds with theoretical porosity of 70.8%. Actually, the porosity calculated according to Eqn 11, is very close to the theoretical one for all the scaffolds and then it is possible to conclude that all the porogen agents were extracted from the scaffolds during the leaching step. This hypothesis is confirmed by the value of connectivity higher than 99% for all the materials, calculated using Eqn 12. The water uptake calculated using Eqn 13, slightly changes for the different layer and it is lower for the PCL.

Mechanical properties

The histogram in Figure 57a reports the compression elastic moduli evaluated in air and in PBS for the PCL and PLA monolayers and for BLS. As expected, the modulus of PLA is sharply higher than that of PCL while BLS did not show significant difference if compared with the elastic performance of the PCL. The presence of PBS affected the E of PLA; in particular, it decreased of the 12%. On the contrary, the E value of the PCL and BLS measured in wet condition did not significantly change in comparison with the dry mode.

Figure 57b,c, show the experimental data obtained by tensile tests carried out in dry and PBS environment. In particular, Young's moduli, reported in Figure 57b, were found to be dependent on the kind of scaffold. More in detail, the modulus of PLA was

more than two times higher than that of PCL while the BLS elastic modulus showed an intermediate value.

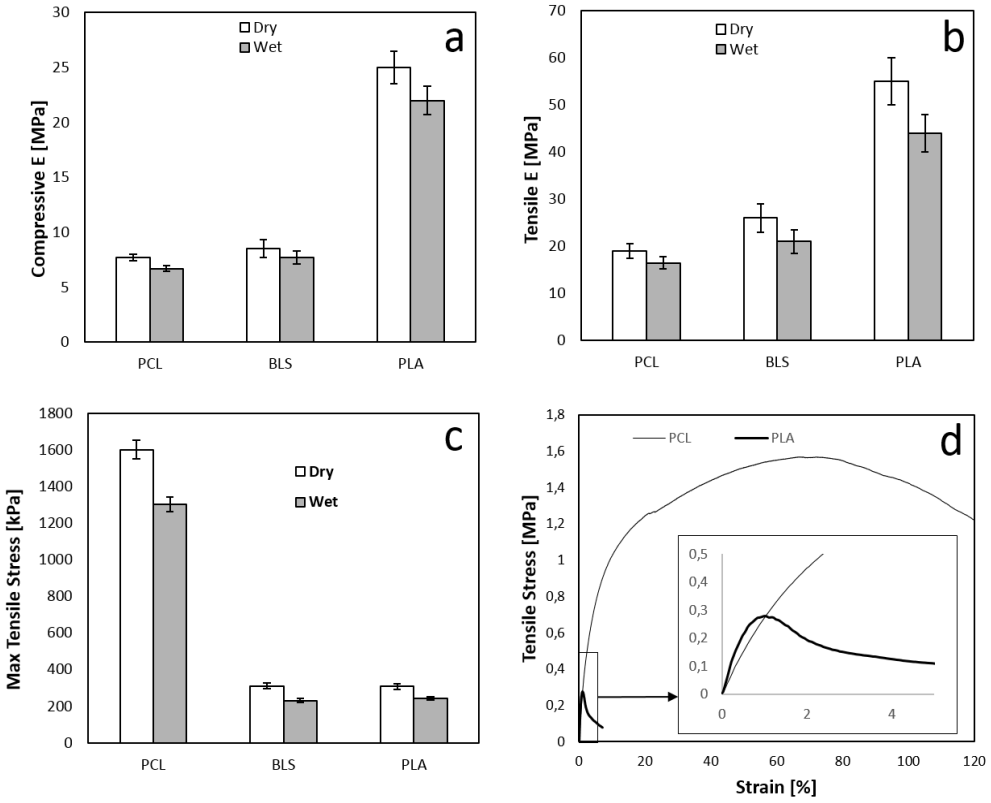

*Figure 57 - a) Compressive elastic moduli in dry and wet environment of PCL, BLS and PLA scaffolds. b) Tensile elastic moduli in dry and wet environment of PCL, BLS and PLA scaffolds. c) Tensile strength in dry and wet environment of PCL, BLS and PLA scaffolds. d) Stress-strain curves of PLA (dark line) and PCL (light line) scaffolds measured in tensile mode. Values are given as means ± SD. * indicates statistically significant differences ($p < 0.05$) when analyzed by Tukey's multiple comparisons tests.*

Similarly, to the tests carried out in compression mode, the E value of the PCL and BLS measured in wet condition did not significantly change in comparison with the dry condition while the only system affected is the PLA that reduced its E value of 20%. On the other hand, the tensile strength (**TS**) of the PCL scaffold is higher if compared with that of PLA. In fact, PCL is characterized by the typical stress-strain curve of a ductile polymer with high elongation at break while PLA showed a fragile behavior (Figure 57d). The tensile strength of BLS is comparable with that of the PLA layer and the fracture always occurred in the PLA region that is the more fragile of the entre device, as highlighted in Figure 58a,b, and never at the interface. This feature

was confirmed by SEM analysis carried out on BLS after fracture in tensile mode Figure 58C.

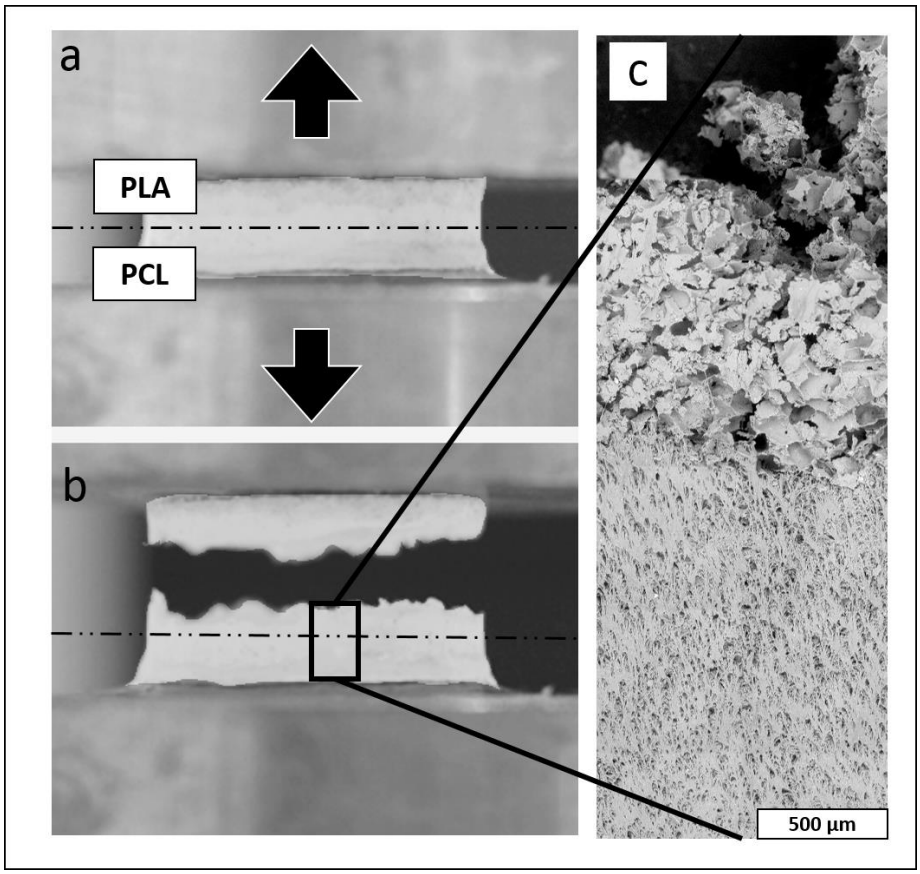

Figure 58 - a) Picture of the BLS glued on the custom-designed interfacial strength test equipment. b) Picture of the fractured samples after tensile test. The line represents the interface between PCL and PLA layer. c) SEM image of the BLS after tensile fracture.

The image clearly reveals that the fracture occurs in the middle of the PLA layer of BLS while the interface region remained well joint even after the mechanical tests. The presence of PBS during the tensile tests slightly affected the TS of all the tested samples even if the higher difference can be attributed to the PLA system.

Cells morphology and migration

As it is possible to observe in Figure 59a-d, the two different seeded cell line showed a different way of proliferation on the scaffold surfaces. In the fluorescence microscopy images, the blue dots represent NIH3T3 fibroblastic nuclei stained with DAPI and they grew on PCL surface respectively for 1 day (Figure 59a) and 6 days (Figure 59b). Figure 59c,d show MC3T3-E1 osteoblastic cells stained with CSFE (green cytoplasm) and grew on PLA surface respectively for 1 day (Figure 59c) and

6 days (Figure 59d). In particular, by fluorescence microscopy assay it was possible to observe NIH3T3 fibroblastic cells, grew both on PCL scaffold surface and, at the same time, migrated inside. As matter of fact, in Figure 59b it was possible to observe a lower number of NIH3T3 cells on surface likely due to a penetration inside the porous support. On the contrary, on the PLA side, MC3T3-E1 osteoblastic cells, continued to grow on the PLA surface up to 6 days without further penetrating (Figure 59c).

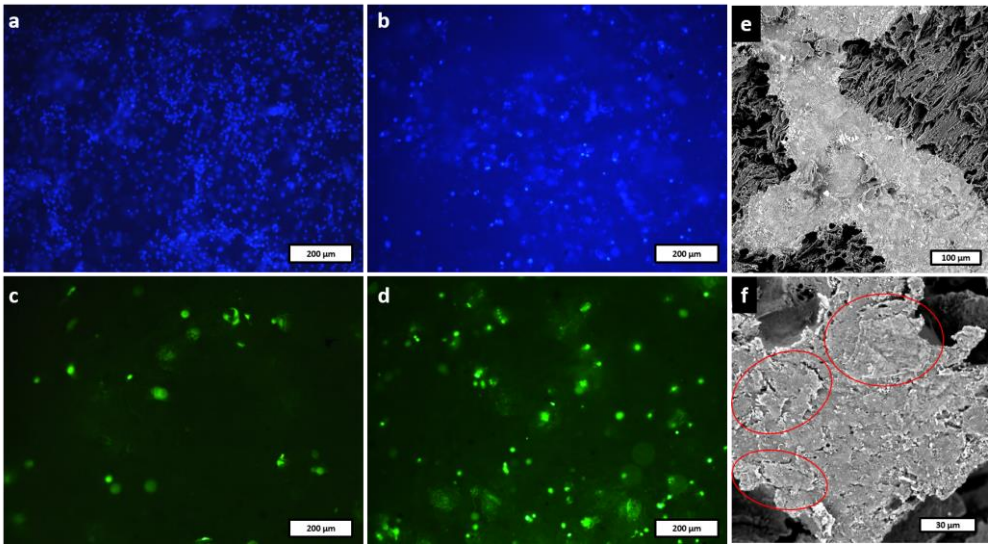

Figure 59 - Fluorescence microscopy images of: a,b) NIH3T3 fibroblastic cell growth on PCL surface respectively for 1 (a) and (b) 6 days. The blue dots were cell nuclei stained with DAPI; c,d) MC3T3-E1 osteoblastic cell, growth on PLA surface respectively for 1 (a) and (b) 6 days. Cells were stained with CSFE (green cytoplasm). e,f) SEM images of NIH3T3 fibroblastic cells (e) and MC3T3-E1 osteoblastic cells (f) growth on PCL surface.

The morphology of the cells on both BLS surfaces were observed by SEM (Figure 59e,f). Fibroblasts, showed in Figure 59e, generated a biofilm on the PCL side constituted by several cells. On the other hand, osteoblasts on the PLA side appeared to be well spread but more isolated at the same time (Figure 59f). In order to investigate the degree of penetration of the different cell lines inside their respective layers, the cross sections of the BLS was analyzed with both SEM and fluorescence microscopy (Figure 60a-d). The analyses of seven different cross sections of the devices allowed quantifying the degree of cell penetration. Figure 60e reports the length of cell penetration (considering zero the seeding surface) and the corresponding percentage of layer infiltration (based on the layer thickness) as a function of time after seeding. The analyses revealed that the NIH3T3 cells, after a quick adhesion on the surface, tended to penetrate inside of the scaffold.

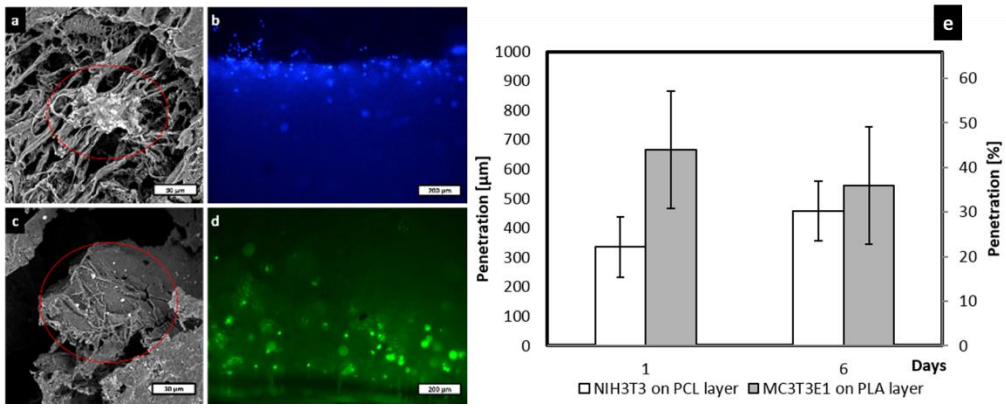

*Figure 60 - Transverse sections of bilayer PCL-PLA scaffold in which there are evidence of cell penetrations inside the scaffold. a,b) NIH3T3 fibroblastic cells from mouse, growth inside PCL layer. a) SEM micrograph; b) cell nuclei stained with DAPI (blue dot). c,d) MC3T3-E1 osteoblastic cells from mouse calvaria, growth on PLA layer. c) SEM micrograph; d) cell stained before seeding with CFSE (green cytoplasm); e) Penetration rate from the seeding surface of the different cell line in co-culture as a function of time expressed in µm (left axes) and as percentage of infiltration (right axes); b) Cell number quantification in the BLS as a function of the culture days. Values are given as means ± SD. * indicates statistically significant differences ($p < 0.05$) when analyzed by Tukey's multiple comparisons tests.*

Their degree of penetration is about 20% after 1 day after sowing, and infiltrated to about 36% of the PCL layer on the sixth day. The osteoblasts penetrated rather quickly to about 40% after 1 day but the infiltration leveled off in the following days. The cells continued to proliferate abundantly on the surface of the porous support. The quantitative analysis (Figure 60e) confirmed that, on the third day of culture, the two cell lines acquired a very different trend. Osteoblasts, seeded on PLA layer, significantly increased their number only in the sixth day if culture, while the fibroblasts seeded on PCL layer, showed a rapid increase that lasts up to six days of culture.

Discussion

This study focused on the preparation and the characterization of a bi-phasic functional scaffold designed to be potentially used for interface tissue engineering. In particular, the monolithic-graded scaffold was composed by a rigid PLA layer presenting pores smaller than 110 µm and a soft layer in PCL with pores ranging from 5 to 40 µm. It is well known that both the chemical composition and the mechanical behavior as well as the pore shape and size of scaffold can tune the efficiency of tissue regeneration [19,41,47,157,273–275]. For instance, PLA was deeply investigated as material for the bone regeneration, considering its high rigidity and degradation rate.

On the contrary, PCL is preferred for soft-tissue repair [276]. The BLS here developed were designed to exhibit both these features in a single heterogeneous scaffold [277].

The morphological analysis showed that the BLS presented a well joint interface region and different pore size distributions. This feature is likely able to permit a differential permeation of cell lines presenting different size such as osteoblasts and fibroblasts, as previously shown in our other works [19,46]. NaCl was chosen as water soluble porogen agent and since it acts as a template, the pore structure strongly depend on its size and morphology. Furthermore, the presence of an organic water-soluble porogen phase (PEG), partially miscible in PLA and PCL, create a microporous network able to enhance pores interconnection. This feature was confirmed by the value of the connectivity higher than 99% for all the materials as calculated by calculated using Eqn 12. Moreover, the real porosity of the scaffolds is very close to theoretical one (70.8%) thus confirming that all the porogen agents were removed during leaching. The differences in the water uptake can be explained considering the different water affinity of PCL ad PLA, previously investigated in the scientific literature [278].

The compressive mechanical behavior of BLS was compared with each single layer both in dry and wet environment. The results showed that the elastic behavior of BLS depends only on the weakest layer i.e. PCL in both cases. This result can be likely explained considering that the aspect ratio of the cell ribs, characterized by a very low thickness in comparison with their height (i.e. pore diameter), makes them prone to elastic buckling [276]. This phenomenon, occurring only under compression, mainly affects the softest layer and likely, for this reason, the E value of the bi-phasic structures is very close to that of PCL [167].

One of the most complex problems to overcome in the production of multi-layered devices is avoiding any kind of detachment or cleavage between one layer and another [19,55]. SEM analysis qualitatively proved the strong adhesion between the layers composing BLS. Furthermore, the tensile mechanical tests quantitatively demonstrated that the TS of the BLS is the same of that of PLA i.e. the most fragile layer. Moreover, the fracture of BLS under tensile mechanical test always occurred in the middle of the PLA layer, as confirmed by the pictures and SEM analysis showed

in Figure 58a-c, and never at the interface. All these features indicated that the adhesion strength between PCL and PLA is higher than the TS of the BLS.

Since the structural characteristics of BLS were designed for applications in interface tissue regeneration, cultures and co-cultures of two different cell populations were tested in order to evaluate their proliferation and migration in the two different layers. The rigid PLA layer, presenting an average pore size of 100 μm, was designed to permit the proliferation of osteoblastic mouse cells (MC3T3-E1). On the other hand, PCL layer, softer than PLA and with smaller pores, was designed to permit the proliferation of fibroblastic mouse cells (NIH3T3) and to avoid the infiltration of the osteoblastic cell line as demonstrated in previously [19,46].

As expected, these preliminary investigations showed that the two different cell lines have a different proliferation path on their respective scaffold surfaces. In particular, NIH3T3 grew abundantly on PCL surface and, at the same time, migrated inside it, as indicated by quantitative analysis. On the contrary, the rather quickly penetration of MC3T3-E1 was probably due to a larger pore size in the PLA layer. The osteoblastic cells were found to proliferate abundantly on the surface of the scaffold during the first day not showing further penetration in the following. This feature was likely due to the presence of collagen that promotes a fast adhesion of the cells that quickly take contact with the scaffold surface, anchor themselves and proliferate on its surface forming an uniform layer.

Actually, one of the main reasons to choose the pore size of the PCL layer was to avoid cell trespassing from one layer to another. As matter of fact, in the performed biological tests, the osteoblast seeded in the presented device are unable to pass through the entire PLA layer and so the ability to prevent the migration of osteoblastic cells from the PLA layer to the PCL one cannot be evaluated. However, the presented method permit to prepare scaffold of any thickness as demonstrated in our previous work [167]. A thinner PLA layer (i.e. 600 μm) would be completely crossed by osteoblasts and the PCL pore size distribution would be able to avoid the osteoblastic cell infiltration as discussed in our previous work [46].

Moreover, the cell migration can be enhanced by modifying other characteristics of the device such as the architecture of the pore interconnections. In fact, even if the connectivity was found to be higher than 99% for all the samples, it could be not

adequate from a topological point of view. In particular, if the channels that connect one pore to another are too small, they could prevent the transport of metabolites within the pores creating a bad conductive environment, that negatively affect the cell proliferation. This hypothesis will be evaluated by further studies and, if confirmed, it can be easily faced by changing the pore size distribution of the device or the cultivation method from static to dynamic by inserting the scaffold in a perfusion system [279].

Conclusions

In this work, PCL/PLA bi-layered multiphasic scaffolds designed for interface tissue engineering were fabricated by combining melt mixing, compression molding and particulate leaching. The devices showed highly interconnected pore structure with a porosity of 70% and high predictability of pore size of each layer by controlling the granulometry of NaCl during the melt mixing step, as confirmed by SEM and image processing analyses. Morphological analysis and tensile mechanical test showed that scaffold is characterized by a well joint interface region with an interface adhesion strength higher than the tensile strength of the device. Compressive mechanical tests showed the strong correlation between E value of the device and the elastic behavior of the PCL layer i.e. its weakest layer. The characteristics of the scaffold and biological responses suggest that the designed device could have major applications in the field of interface tissue regeneration.

4.6 Effect of Adding GO-g-PEG on Electrospun PCL Mats

In this study, the effect of different GO-g-PEG concentrations on the mechanical properties of PCL electrospun scaffolds was studied, making a comparison with PCL/GO nanofiber mats in the same loading range. The composite nanofibers were characterized using SEM, DSC, WCA and tensile measurements both in dry and wet mode in order to imitate the physiological environment. Furthermore, in order to evaluate the capability of MC3T3-E1 osteoblastic cells to proliferate on the surfaces of PCL and PCL/GO-g-PEG nanocomposite scaffolds, preliminary proliferation rate assays on were investigated.

Structure of the electrospun nanofibers

The SEM images of GO nanosheets and of GO-g-PEG are shown in Figure 61a and Figure 61b respectively. As clearly visible from Figure 61a the GO lamellae were found to be remarkably wrinkled and crumpled. After PEGylation, the structure become deeply different, as the lamellae appear well stretched, totally wrinkle-free and apparently forming a 3D porous network (Figure 61b).

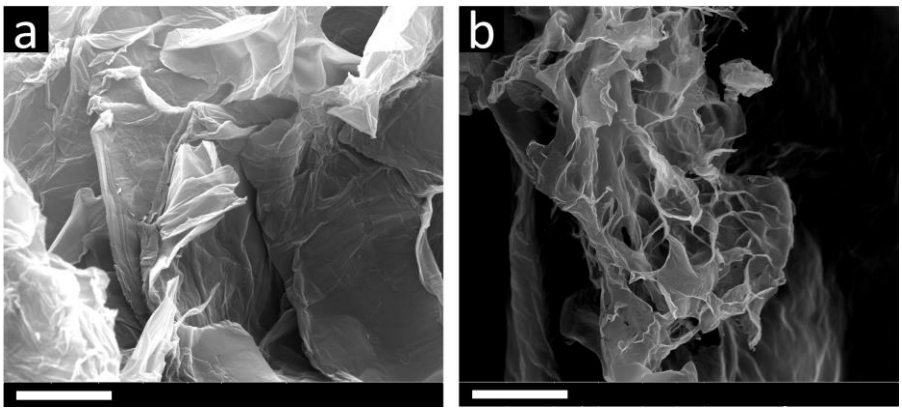

Figure 61 - a) SEM image of GO nanosheets; b) SEM image of GO-g-PEG nanosheets. Scale bars are 5 μm

The SEM images of the electrospun PCL, PCL/GO, and PCL/GO-g-PEG composite nanofibers are presented in Figure 62a-g. The figures show that all the fibers are in nanoscale and randomly distributed.

Both nanoparticles are well dispersed in the polymeric matrix especially at low concentrations. In fact, the fibers morphology is generally smooth and regular and some irregular fiber due to the presence of the filler is visible only at high concentration

in Figure 62g for the PCL/GO-g-PEG 1 wt% and in Figure 62d for the PCL/GO 1 wt% mats.

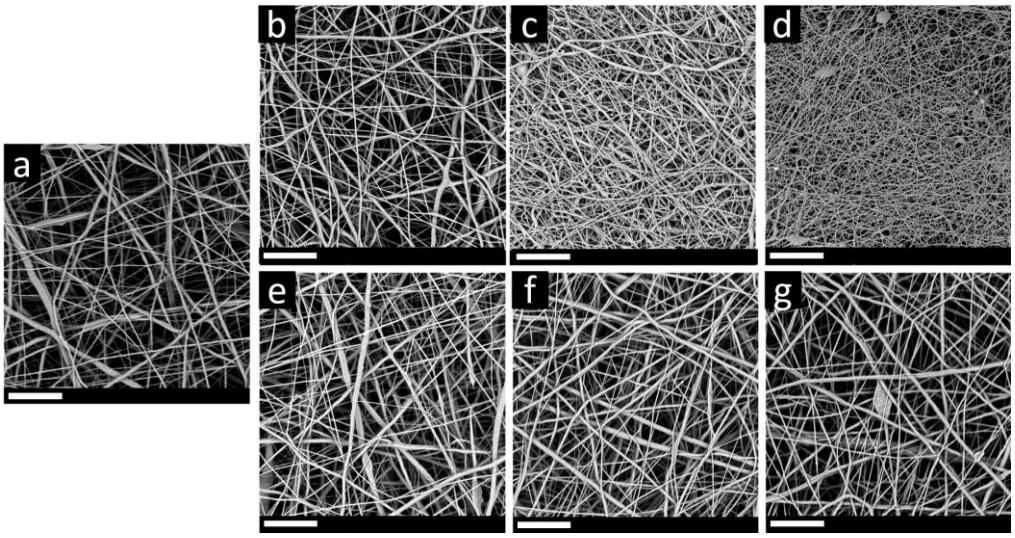

Figure 62 - SEM image of electrospun: a) PCL; b) PCL/GO 0.25 wt%; c) PCL/GO 0.5 wt%; d) PCL/GO 1.0 wt%; e) PCL/GO-g-PEG 0.25 wt%; f) PCL/GO-g-PEG 0.5 wt%; g) PCL/GO-g-PEG 1.0 wt%; h) Magnification of GO-g-PEG nanosheets incorporated in PCL/GO-g-PEG 1.0 wt% nanofiber. Scale bars are 20 µm.

XRD analysis was performed and shown in Figure 63. GO sheets display a characteristic peak at 9.8°. However, PCL/GO and PCL/GO-g-PEG systems showed no peaks in the range 5° - 10°, maintaining the same pattern as that of neat PCL. This feature could be attributed to the relatively low contents of GO and GO-g-PEG. SEM micrographs display how the kind and the amount of nanoparticles affected the morphology of the devices. Compared with electrospun PCL (Figure 62a), PCL/GO (Figure 62b-d) nanofibers exhibited smaller diameters with increasing amount of GO. On the contrary, increasing the amount of GO-g-PEG (Figure 62e-g) induced a little increase of the nanofiber diameters. The diameter range distribution was quantitatively analyzed by using an ImageJ plugin [245].

Table 19 - Electrospun PCL, PCL/GO, and PCL/GO-g-PEG fibers diameters and crystallinity %. Average diameters are given as means ± Standard Deviation.

Samples	Average Diameter (nm)	χ_c (%)
PCL	515 ± 259	59.1
PCL/GO 0.25%	460 ± 164	58.3
PCL/GO 0.5%	446 ± 188	75.0
PCL/GO 1%	379 ± 137	74.6
PCL/GO-g-PEG 0.25%	548 ± 302	54.8
PCL/GO-g-PEG 0.5%	624 ± 331	62.3
PCL/GO-g-PEG 1%	677 ± 358	64.9

The diameter distribution of the electrospun nanofibers are shown if Figure 64 as a function of GO and GO-g-PEG concentrations, while the calculated average diameters of as-spun fibers are displayed in Table 19.

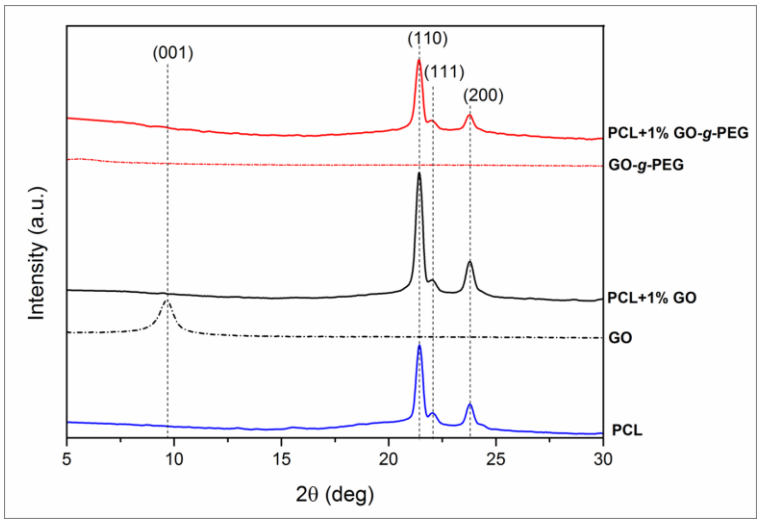

Figure 63 - XRD patterns of GO, GO-g-PEG and electrospun PCL, PCL/GO (1 wt%), PCL/GO-g- PEG (1 wt%).

PCL showed an average fiber diameter of 515 µm; the presence of GO reduced this value from 460 µm of the PCL/GO 0.25% sample, to the 379 µm of the PCL/GO 1%.

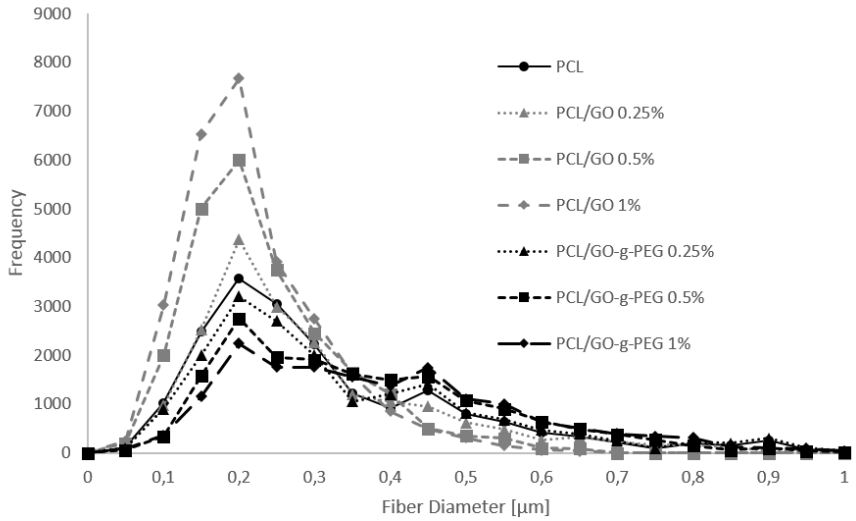

Figure 64 - Diameter distribution for electrospun PCL, PCL/GO and PCL/GO-g-PEG nanocomposites obtained with ImageJ.

On the contrary, the presence of GO-g-PEG induced an increase of the diameter (677 µm for the PCL/GO-g-PEG 1 wt%). In Figure 64 it is also possible to note that for the PCL/GO-g-PEG systems, the diameter distribution is more heterogeneous, in

particular for the highest GO-g-PEG concentration, as confirmed from the high value of the mean diameter standard deviations in Table 19.

It is well known that generally, an increase in the solution viscosity tends to produce fibers with larger average diameters [10]. In order to evaluate the correlation between the viscosity and the fiber diameter of electrospun mats, the complex viscosity of PCL solution, as well as PCL/GO and PCL/GO-g-PEG suspensions were measured and are presented in Figure 65. As expected and coherently with the fiber diameter analysis, PCL/GO-g-PEG suspensions showed a higher viscosity if compared with neat PCL solution in the whole range of investigated frequencies and it increased upon increasing GO-g-PEG amount. Furthermore, the suspension with the highest filler loading showed a sharp increase of the viscosity in the low frequency range thus exhibiting a more pronounced non-Newtonian behavior if compared with the other systems.

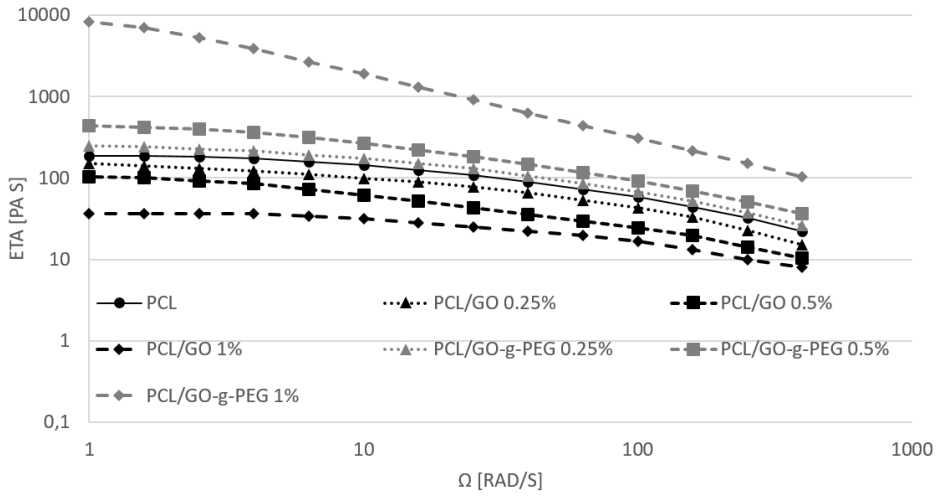

Figure 65 - Complex viscosity of the PCL solution, PCL/GO and PCL/GO-g-PEG suspensions

On the other hand, the rheological tests revealed that the viscosity of all the materials containing GO is lower than the viscosity exhibited by the pure matrix and in agreement with the fiber diameter analysis it decreased upon increasing the content of incorporated GO. Usually, the presence of nanoparticles increase the complex viscosity of polymeric melts or solution [280,281], except that for nanoparticles with plasticizer [125] or pro-degradative effects [3,282] on the polymeric matrix. In order to verify the pro-degradative effect of GO nanoparticles in the PCL matrix, pH

measurement of GO water suspensions (0.5 mg ml^{-1}) was carried out thus showing a pH of 2.9. For this reason, the reduction of viscosity in the presence of GO can be likely associated to the pro-degradative effect induced by the active moieties on the GO surface. Indeed, the oxygenated functional groups of GO can interact with the PCL chains activating their hydrolytic scission acting as a pro-degradative agent, such as recently demonstrated for poly(butylene-succinate)/GO nanocomposites [40]. On the other hand, pH measurement of GO-g-PEG aqueous suspension (0.5 mg ml^{-1}) revealed a higher pH value (6.3) that can be attributed to the presence of PEG covalently bonded to the oxygen moieties of GO. Probably, the grafting was able to reduce the acid behavior of GO-g-PEG thus avoiding their pro-degradative interactions with PCL in agreement with aforementioned rheological results.

Wettability

The water contact angle (WCA) of the electrospun nanofiber mats was measured and reported in Figure 66. WCA analyses were carried out in order to evaluate the effect of the different kind of fillers and their amount on the wettability of the electrospun mats. In fact, PCL shows an intrinsic poor hydrophilicity and, consequently, a relative low cellular affinity that can be improved by enhancing its hydrophilicity [177]. As GO surface is fully covered by oxygenated moieties and PEG is water soluble, it was expected that the addition of GO and GO-g-PEG would improve the hydrophilicity of the electrospun nanofibers. As displayed in Figure 66, the WCA of PCL was 118.3°, while PCL/GO composite nanofiber mats showed a slight WCA decrease with the addition of GO at 0.125 wt% (112.1°). WCA remained almost constant up to 0.75 wt% GO content and decreased again when PCL was filled with 1 wt% of GO (105.5°). As expected, GO-g-PEG induced a higher wettability effect on PCL if compared with GO. In fact, WCA decreased upon increasing GO-g-PEG up to 0.5 wt% (104.7°), remained constant for PCL/GO-g-PEG 0.75 wt% mats and decreased again for PCL/GO-g-PEG 1 wt% that exhibited the highest wettability performance (102.3°).

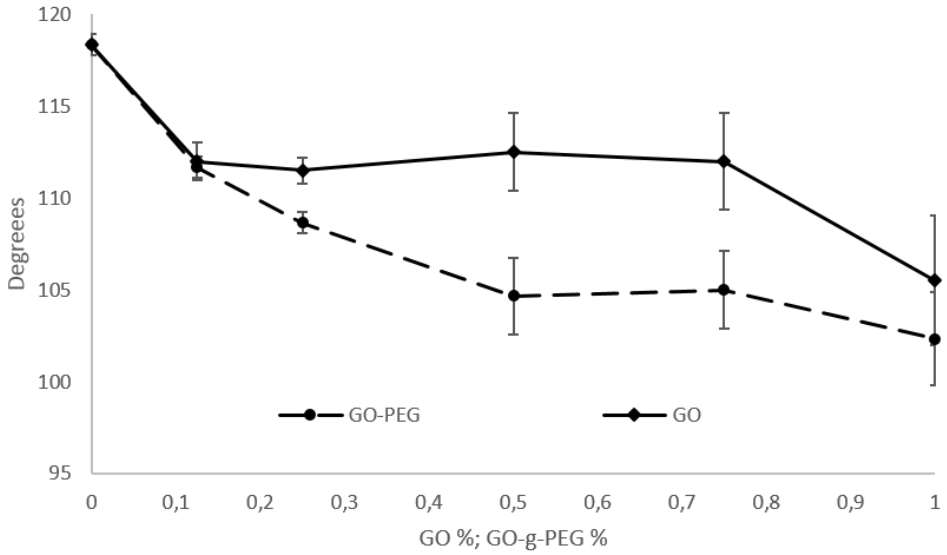

Figure 66 - Water contact angles of the electrospun nanofiber mats.

Mechanical properties

Figure 67a-c display the Young moduli (E) (Figure 67a), maximum tensile stress (TS) (Figure 67b) and elongation-at-break (EB) (Figure 67c) of the electrospun mats as a function of GO or GO-g-PEG concentration.

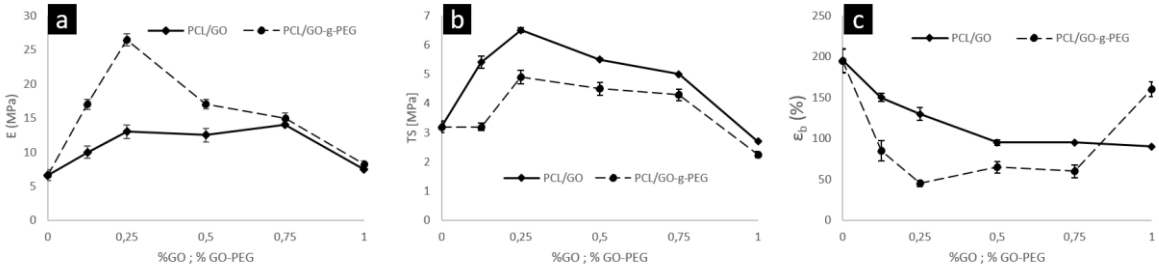

Figure 67 - a) Young modulus of the electrospun nanofiber mats; b) Tensile strength of the electrospun nanofiber mats; c) Elongation at break of the electrospun nanofiber mats. The values are given as means ± Standard Deviation.

The strength of polymeric materials can be enhanced with the addition of rigid fillers, but this is always accompanied by a compromise in ductility. The results indicate that the addition of GO and GO-g-PEG caused an improvement in tensile stress (Figure 67a,b). However, the presence of nanofillers resulted in a significant decrease in ductility with a lower elongation-at-break, as visible from Figure 67c.

In particular, the elastic modulus (E) of the scaffolds, Figure 67a, increased at low amount of fillers and then decreased, returning almost to the same value of

electrospun PCL. More in detail, the highest increase of E (around 400% if compared with electrospun PCL), was found in PCL/GO-g-PEG 0.25 wt%. At the same concentrations, showed a lower increment of the modulus (around 200%) that remain almost constant up to 0.75 wt% of GO. The higher elastic moduli of the PCL/GO-g-PEG systems can be likely attributed to the grafting of PEG onto the GO, which enabled good dispersion of the filler in the PCL matrix thus maximizing the filler/matrix interface area. At higher concentrations, the nanoparticles tend progressively to aggregate thus reducing the E value for both the kind of nanocomposites.

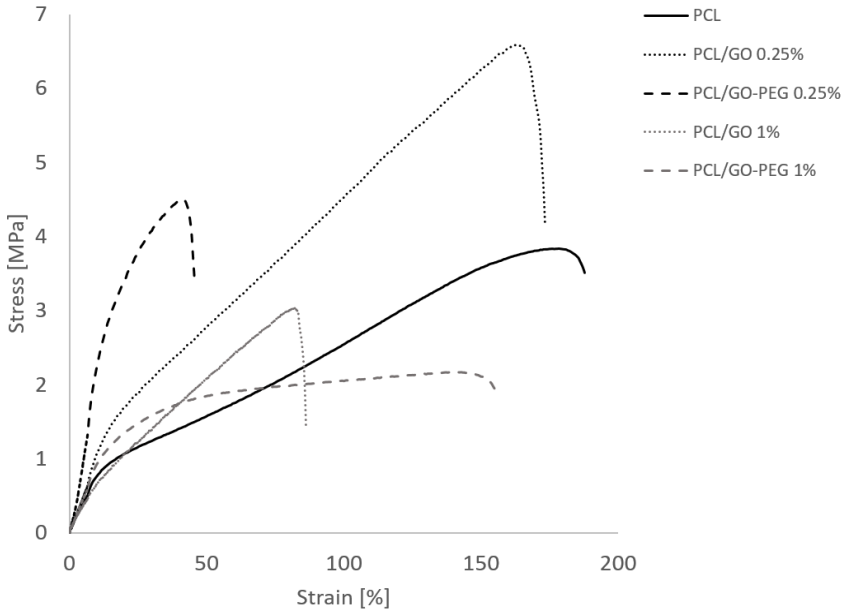

Figure 68 - Stress-strain curves of PCL, PCL/GO-g-PEG and PCL/GO at 0.25 and 1 wt%

A different trend can be observed for TS that is higher for PCL/GO than for PCL/GO-g-PEG in all the compositions investigated. The higher TS of the PCL/GO system can be explained by observing the stress-strain curves in Figure 68 here reported only for PCL and for the nanocomposites containing 0.25 and 1 wt% of nanofillers for sake of brevity (all the other nanocomposites displayed a behavior similar to those containing 0.25 wt%)**.** Figure 68 shows that the PCL/GO-g-PEG nanocomposite at 0.25 wt% is more rigid than the respective PCL/GO system but less deformable i.e. the failure occurred prematurely for the PCL/GO-g-PEG thus showing smaller TS values [1]. These results were indicative of the stronger reinforcing effect of GO-g-PEG as compared to GO in particular at low concentration.

Furthermore, it can be noticed from Figure 68c and Figure 69 that at 1 wt% the EB of the PCL/GO-g-PEG system, increases up to 160% that is two-fold of PCL/GO nanocomposite at the same GO content. This behavior can be likely due to the plasticizer PEG effect on the PCL matrix that becomes notable for concentration higher than a certain threshold, as already observed in a similar system [184].

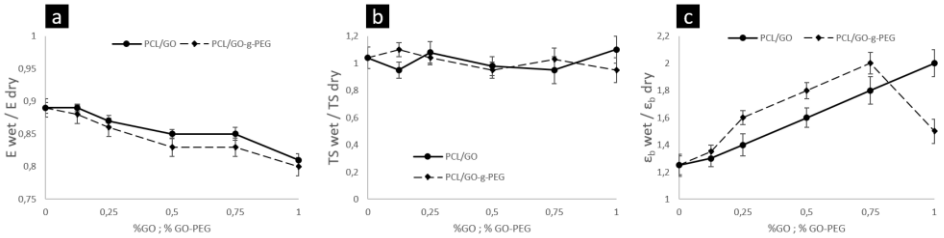

Figure 69 - a) E wet / E dry of the electrospun nanofiber mats; b) TS wet / TS dry of the electrospun nanofiber mats; c) EB wet / EB dry of the electrospun nanofiber mats. The values are given as means ± Standard Deviation.

In order to analyze the effect of the wet environment (PBS at 37 °C) on the mechanical performances, the ratios between the wet and dry properties, i.e. E, TS and EB, were reported in Figure 69a-c. The tests revealed that the presence of PBS during the tensile tests slightly reduced the Young's modulus and increased the EB of all the tested samples, while the TS seems unaffected by the testing mode as visible from Figure 69b. In particular, Figure 69a clearly reveals that immersing the PCL samples in PBS caused a reduction of E of about 10%. E wet/E dry ratio slight decreased upon increasing the amount of GO and GO-g-PEG, with a maximum decrease of 20% when PCL is filled with 1% of nanoparticles. The wet environment seems to affect a little bit more the systems filled with GO-g-PEG than that filled with GO. This trend can be likely associated to the different wettability of the device i.e. the more the wettability, the more the influence of the wet environment on the final mechanical performance of the devices. The wettability seems to control even more the gap among the EB evaluated in wet environment (EB wet) and the EB obtained in dry condition (EB dry) as shown in Figure 69c. In particular, the wet environment caused an increase of the EB for all the nanocomposites that is more evident on increasing the amount fillers in PCL, except that for the PCL/GO-g-PEG 1 wt%. In fact, the PCL/GO nanocomposites showed a linear increase of EB wet / EB dry ratio, from 1.2 to 2 while the EB wet of PCL/GO-g-PEG doubled the value of the corresponding EB dry at 0.75 wt% of GO-g-PEG but, taking into account the higher composition (1 wt%), the increment assessed

around 50%. This discontinuity in the trend can be explained considering that PCL/GO-g-PEG 1 wt% showed a relative high EB dry (160%), likely due plasticizer PEG effect on the PCL, as previously discussed.

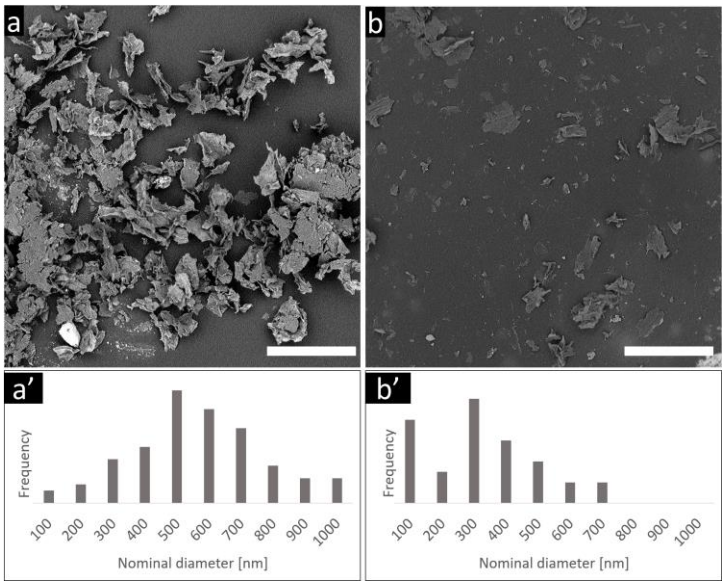

Figure 70 - SEM images and size distribution of a,a') GO and b,b') GO-g-PEG extracted from the nanocomposites loaded with 0.25 wt% (scale bars are 1μm)

In order to perform a closer investigation of interphase and dispersion, the samples were dissolved in DCM to extract free polymer chains, while the insoluble fraction of each sample was collected and analyzed via SEM, according to a previous work [283]. Figure 70a-b reports the micrographs of interphase extracted from PCL+0.25% GO and PCL+0.25% GO-g-PEG, while the size distribution of lamellae is provided in Figure 70a'-b'. As one can see, extracted GO lamellae were found to be more aggregated and to contain residual PCL chains, likely reacted with graphene oxide, thus confirming that the fillers show a good affinity towards the matrix, despite their poor dispersion. On the other hand, the extracted GO-g-PEG sheets generally display a lower lateral size and no aggregative phenomena were recognized, presumably owing to the PEG grafted onto lamellae.

Based on these observation, one can suppose that, despite its good wettability, GO presents a certain tendency to self-aggregate.

DSC analyses were carried out in order to evaluate the influence of crystallinity on the mechanical behavior of the electrospun nanofibers. The DSC tests revealed that the PCL crystallinity (Table 20) remained almost constant at low GO content (0.25

wt%) and increased for higher GO content. On the other hand, GO-g-PEG at low concentration (0.25 wt%) caused a smaller χ_c if compared with neat PCL mats, while higher concentration induced a slight increment of χ_c.

Table 20 - Electrospun PCL, PCL/GO, and PCL/GO-g-PEG fibers diameters and crystallinity %. Average diameters are given as means ± Standard Deviation.

Samples	Average Diameter (nm)	χ_c (%)
PCL	515 ± 259	59.1
PCL/GO 0.25%	460 ± 164	58.3
PCL/GO 0.5%	446 ± 188	75.0
PCL/GO 1%	379 ± 137	74.6
PCL/GO-g-PEG0.25%	548 ± 302	54.8
PCL/GO-g-PEG 0.5%	624 ± 331	62.3
PCL/GO-g-PEG 1%	677 ± 358	64.9

In fact, it is well known that nanofillers can act as nucleating agent thus inducing a heterogeneous crystallization of PCL [284]. In particular, the heterogeneous crystallization ability of the PCL matrix is related to the PCL chains capacity to interact with the nanofillers [284]. Indeed, as previously discussed, while GO offers an easy attachable surface for the PCL chains, the PEG chains grafted on GO-g-PEG could prevent the interaction between the matrix and the filler thus decreasing the heterogeneous crystallization ability of the PCL. In fact, even if the PCL chains are attached on the GO-g-PEG, the flexible PEG chains might hinder the PCL ability to form ordinate structures.

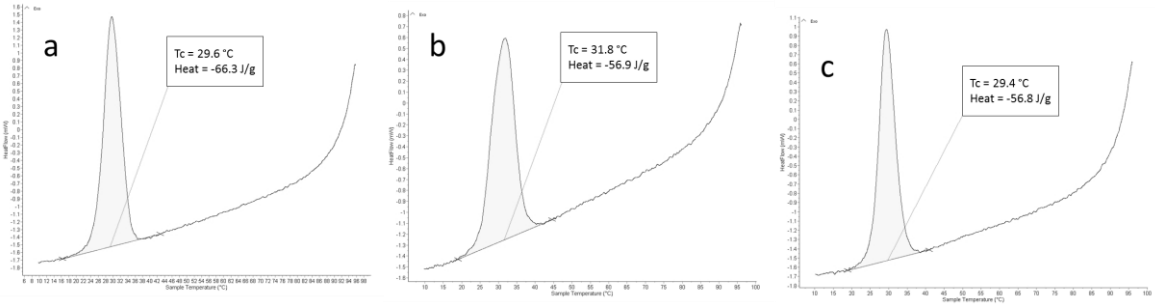

Figure 71 - DSC cooling curves of electrospun a) PCL; b) PCL/GO-g-PEG 0.25 wt%; c) PCL/GO 0.25 wt%

These hypotheses are confirmed by DSC cooling curves showed and by Tc in Figure 71. If compared with that of PCL, the T_c values of PCL/GO (0.25 wt%) increased about 2.3 °C while remained almost constant for the PCL/GO-g-PEG sample thus demonstrating the different nucleating effect of the two different nanofillers [285].

As matter of fact, these results indicate that the high mechanical performance of the PCL/GO-g-PEG (0.25 wt%) system can be ascribed to the good dispersion of GO-g-PEG in the PCL matrix likely able to overlook the negative effect of its relative low crystallinity.

Cells morphology and migration

In order to assess the potential applications of the electrospun nanofibers in tissue engineering, MC3T3-E1 cells were cultured on selected nanofiber mats up to 9 days to evaluate the preliminary proliferation rate on these materials. PCL and PCL/GO-g-PEG (0.25 wt%) were chosen in order to make a comparison between the pristine electrospun material and the one that exhibited the best mechanical performance. Figure 72a-d,a'-d' show fluorescence images of the live cells on the scaffolds after 1, 3, 7 and 9 days of culture.

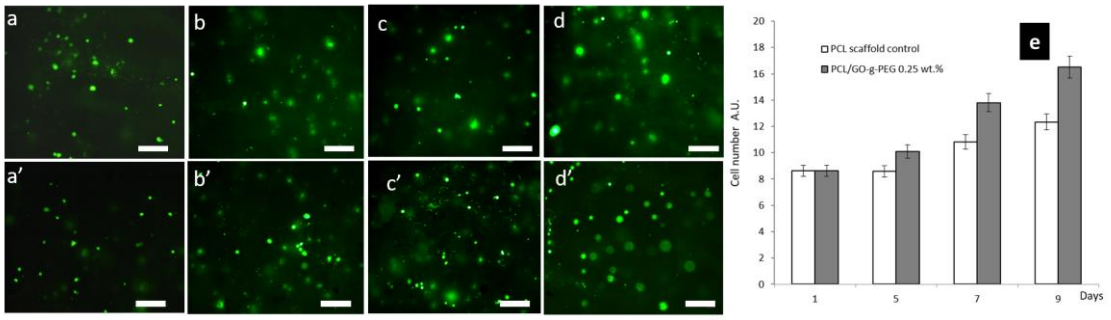

Figure 72 – Electrospun PCL (a,b,c,d) and PCL/GO-g-PEG (0.25 wt%) (a',b',c',d') scaffolds, seeded with MC3T3-E1 osteoblastic cells, cultured on the scaffold surface respectively for 1 (a,a'); 5 (b,b'); 7 (c,c'); 9 (d,d') days. Scale bars are 200μm; (e) Cell counts of MC3T3-E1 osteoblastic cells seeded on PCL and PCL/GO-g-PEG (0.25 wt%) mats as a function of time; (e) .

The images show that the cells grown on the surface of PCL/GO-g-PEG scaffolds (Figure 72a'-d'), revealing more affinity for it than for the PCL electrospun control. As a result, the addition of GO-g-PEG, even at low concentration, promotes cellular adhesion by increasing the proliferation degree, as evident from the Figure 72e.The SEM images of the fixed cells on the scaffolds taken at day 1 and day 9 are presented in Figure 72a-d.

The Figure 73a,c reveal that the cells spread out on the PCL/GO-g-PEG scaffolds rapidly if compared with the electrospun PCL. Furthermore from Figure 73b,d obtained after 9 days of culture, it can be observed that the cells aggregated more abundantly onto

PCL/GO-g-PEG scaffold if compared with PCL control that showed only isolate cells or little cell aggregations.

All these data, suggest that the PCL/GO-g-PEG (0.25 wt%) provided a favorable environment for the cells proliferation, increasing the hydrophilicity and therefore the degree of cell affinity for the substrate, if compared with the electrospun PCL scaffold.

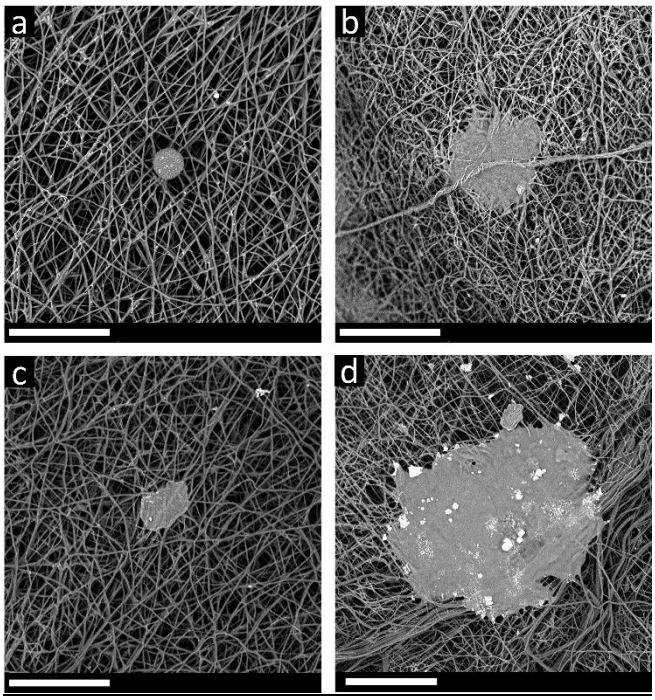

Figure 73 - SEM images of MC3T3-E1 osteoblastic cells cultured on PCL (a,b) and PCL/GO-g-PEG (0.25 wt%) (c,d), respectively for 1 (a,c) and 9 days (b,d). Scale bars are 80 µm.

Conclusions

In this work, GO and GO-g-PEG were incorporated in electrospun PCL in order to make a comparative study on their structural and reinforcing effect. The increase in complex viscosity of PCL/GO-g-PEG suspensions caused an increase in the average fiber diameter if compared with PCL mats. On the contrary, the complex viscosity of the PCL/GO suspensions is lower if compared with that of the PCL solution thus causing a reduction of PCL/GO nanofiber diameters. WCA measurements showed that both PCL/GO and PCL/GO-g-PEG composite fiber improved the PCL wettability, but PCL/GO-g-PEG exhibited better performance with lower water contact angles than PCL and PCL/GO. Tensile tests showed that the addition of GO and GO-g-PEG in PCL achieved significantly improved tensile

properties while reducing the EB. However, GO-g-PEG was more effective in reinforcing PLA than GO, in particular at low concentration, likely due to the grafted PEG chains, which improved the filler dispersion. Moreover, preliminary biological assay demonstrated that PCL/GO-g-PEG enhanced the capability of supporting cell attachment and growth. The PCL/GO-g-PEG scaffold with enhanced mechanical strength and good cytocompatibility showed to be promising for its potential use in tissue engineering.

4.7 Plasma Effect on Wettability and Morphology of PLA Electrospun Mats

In this study, PLA and PLA-plasma membranes were prepared and used for carrying out immobilized-cell cultivations of *S. coelicolor*. In particular, the membranes, that reproduces the conditions of mycelial growth on an organic substrate, have been used in order to evaluate a correlation between their structure and/or plasma modification and a corresponding physiological response in terms of total protein and of ACT yields of the immobilized-cells.

Structure of PLA and PLA-plasma membranes

Preliminarily, the effect of the plasma treatment on the PLA nanofiber morphology was investigated. SEM images of the electrospun PLA and PLA-plasma nanofiber mats are presented in Figure 74a,b highlighting that all the fibers are in the nanoscale and randomly distributed.

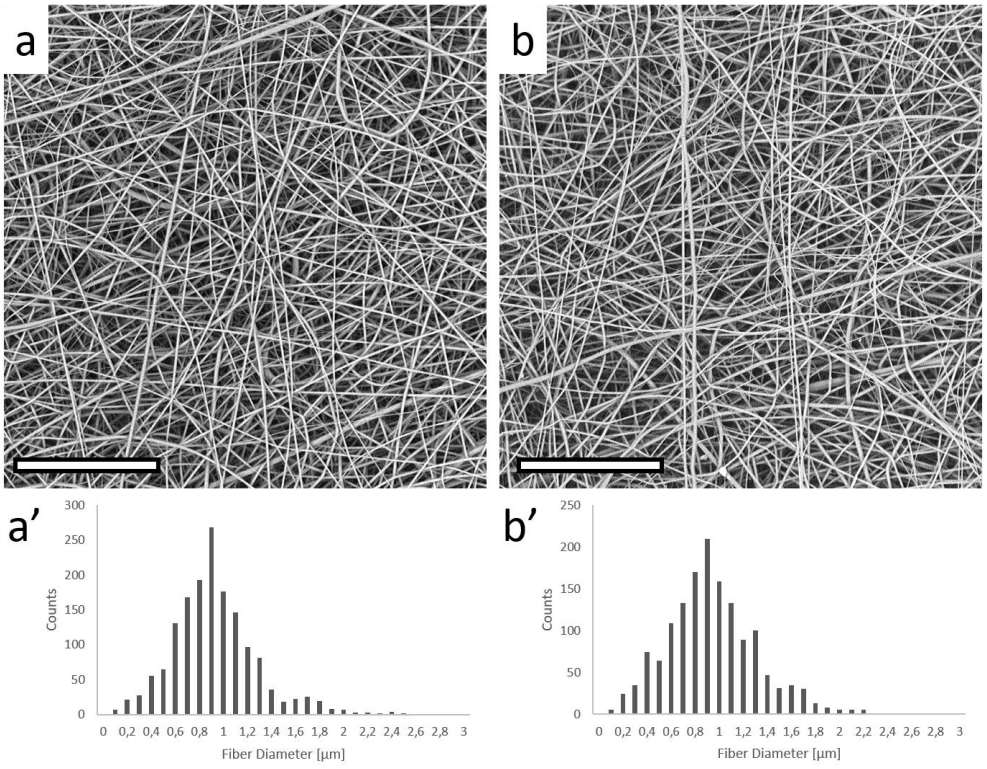

Figure 74 - SEM images of a) PLA and b) PLA plasma membranes. Scale bars are 80 µm. Diameter size distribution of a') PLA and b') PLA-plasma membranes.

From image processing analysis, a similar narrow distribution of fiber diameters was observed for both the systems, as reported in Figure 74a',b' thus demonstrating

that, in the selected conditions, plasma treatment did not induce significant changes in the PLA nanofiber morphology.

Wettability

Generally, plasma modification acts on polymeric substrates by excitation, deionization and dissociation events through free radical species that insert, generate or remove functional groups at the surface. The expected effect of the oxygen plasma treatment for the electrospun PLA is a combined process of modification and etching through reactions with oxygen radicals. Wettability analysis (Table 21) were carried out on PLA and PLA-plasma film obtained by solvent casting in order to evaluate SE that is an intrinsic property of the material. On the other hand, the same analysis were carried out on electrospun PLA and PLA-plasma in order to evaluate the effect of the nanostructure on the wettability behavior of the membrane that are directly exposed with the cells.

Water (θ_W) and diiodomethane (θ_D) contact angles of unmodified PLA film are about 67° and 40° respectively. As expected, plasma surface modification of PLA decreased θ_W to about 49 and increased the θ_D value to about 52°. The results of SE calculation are reported in the same Table 21. Plasma treatment resulted in a significant increase in the value of SE that was 4.4 mJ/m^2 for neat PLA film and 20.4 mJ/m^2 for PLA-plasma film.

Table 21 - Contact angles of water and diiodomethane on casted PLA and electrospun PLA with and without plasma treatment; γSp, γSd and ES of casted PLA with and without plasma treatment

Sample	θ_W	θ_D	γ_S^p [mJ/m^2]	γ_S^d [mJ/m^2]	γ_S [mJ/m^2]
Film-PLA	67.1 ± 0.4	40.0 ± 1.1	3.78	0.72	4.40
Film-PLA-plasma	48.7 ± 0.7	51.7 ± 0.5	12.43	7.96	20.39
PLA	115.9 ± 1.1	0	-	-	-
PLA-plasma	41.3 ± 1.7	0	-	-	-

Surface contact angle or wettability is dependent on surface chemical functional groups and on surface roughness that can be altered by plasma treatment [286]. It is well known [287] that increasing roughness leads to increase the contact angle of non wetting liquids and to decrease the contact angle of wetting liquids. However, morphological analysis of PLA films treated with plasma at the chosen condition (not

showed for sake of brevity) present a roughness comparable to that of neat PLA films so that the decrease of θ_W values that occurs during plasma modification of PLA film can be almost exclusively attributed to changes in the surface chemical composition of PLA. In fact, when samples are modified under oxygen atmosphere, oxygenated moieties are likely formed. These groups strongly interact with water molecules resulting in increased surface wettability of PLA.

The effect of plasma treatment was observed even more in the electrospun mats. In fact, electrospun PLA showed a θ_W of about 116°, more than 70° higher if compared with cast PLA film. This phenomenon can be reasonably ascribed to the high porosity of the device that is able to entrap air when the surface is immersed in water, thus enhancing the hydrophobicity of the neat material [288]. However, plasma treatment induced a significant decrease of θ_W to about 41°. θ_D evaluated for both electrospun mats is zero due to the low ES of the fluid and demonstrating the relative good affinity of diiodomethane with PLA.

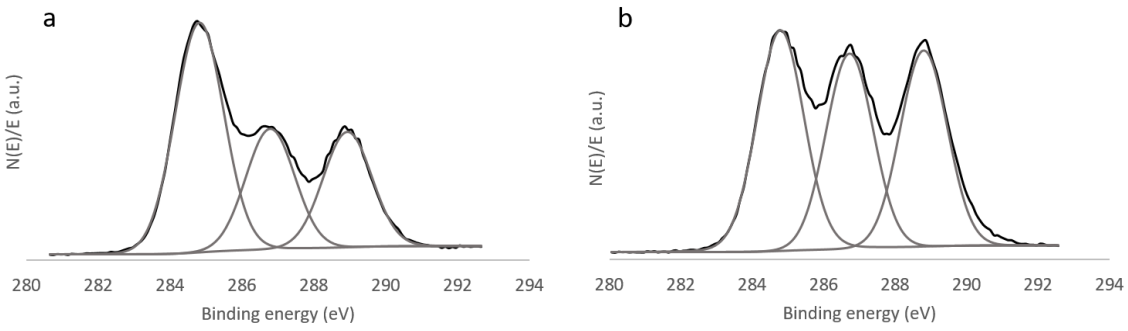

Figure 75 - C 1s core-level spectra of PLA and PLA-plasma electrospun membranes.

In order to analyze the chemical composition of PLA, XPS studies were carried out. Table 22 shows the atomic percentages determined from the areas of the C 1s and O 1s peaks and the fraction of carbon functional groups from high resolution C 1s XPS peaks. The results show that the oxygen plasma treatment increases the overall oxygen content at the surface by approximately 4 atomic% units thus increasing the O/C ration from 0.52 to 0.63. The major changes occurring in C 1s peaks due to the plasma treatment are highlighted by the spectra in Figure 75. In particular, the saturated hydrocarbon C–C C 1s peak decreased after plasma treatment, with concomitant increase in the intensities of the C–O (from 25.65% to 30.72%) and O=C–O (from

24.70% to 30.90%) peaks, which can be attributed to the introduction of oxygen functionalities and the increase in carboxyl groups on the surface.

Table 22 - Surface elemental composition from wide-scan and fraction of carbon functional groups from high resolution C1s XPS peaks of electrospun PLA and PLA-plasma

	Atomic percentage [a] [%]			C-C (%)	C-O (%)	O=C-O (%)
Sample	**C 1s (%)**	**O 1s (%)**	**O/C**	**~285 eV**	**~285 eV**	**~288.9 eV**
Pristine PLA	65.58	34.42	0.52	49.65	25.65	24.70
PLA-plasma	61.25	38.75	0.63	38.38	30.72	30.90

[a] The elemental percentages are deduced from the relative areas of the C 1s and O 1s peaks for the pristine and plasma treated electrospun material.

4.8 Bacterial Bioprocess Intensification

Intensification of Actinorhodin Production

3D Porous PCL/PEG Structures

In this study three PCL/PEG pores structures having different pore sizes were prepared and used for carrying out immobilized-mycelium cultivations of S. coelicolor in order to find a correlation between membrane morphology and a corresponding bioprocess response. More in detail, in Table 23 are reported the mixing composition and the NaCl granulometry chosen for this work.

Table 23 - Sample Codes and System Characteristics

Sample code	PCL (%wt)	PEG (%wt)	NaCl (%wt)	NaCl Granulometry (µm)
M 500	11	7	82	400-600
M 100	11	7	82	75-125
M 50	11	7	82	< 65

PCL/PEG 3D membrane morphology

3D membrane were prepared by using 3 different NaCl granulometries in order to control the pore size distribution as well as the pore architecture of the devices. The influence of pores structure on the metabolic activity of the cells was reported in several studies [11,14,43,46,117].

SEM images (Figure 76) revealed a strong influence of NaCl granulometry on the pores architecture of the membranes. In Figure 76a it is shown a micrograph of the PCL-PEG membrane obtained by melt mixing PCL/PEG and NaCl ranging from 400 to 600 µm (M 500). The porous structure is characterized by well interconnected pores with a multimodal distribution: macropores from 400 to 600 µm and a micropores around 20 µm due both to crystal particles fractured into small particles during melt mixing process and to partial PEG leaching [13,19,43].

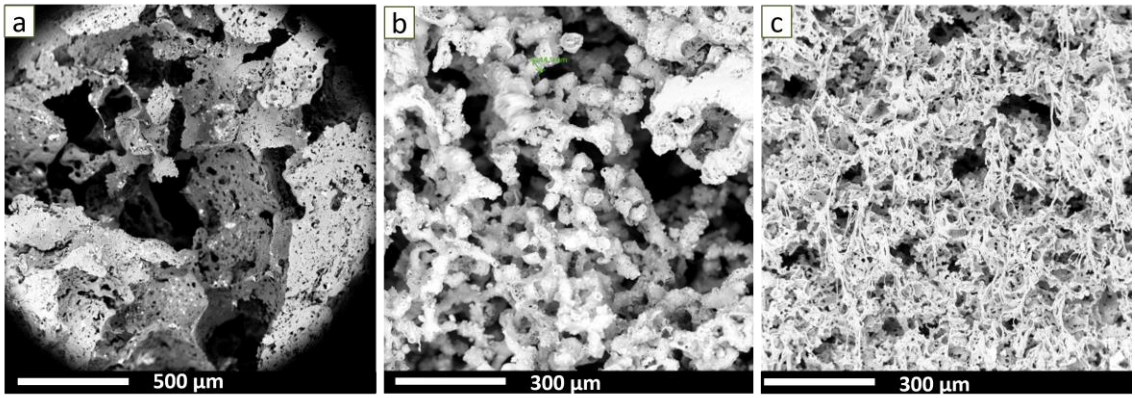

Figure 76 - SEM images of membranes developed by leaching materials filled with different NaCl particle size: M 500 (a), M 100 (b) and M 50 (c).

When the membrane is prepared with NaCl ranging from 75 to 125 µm (M 100 in Figure 76b) the pore structure changes drastically. In fact, it can be observed the presence of beams with an average diameter of 45 µm and the pores appear highly interconnected. Every beam is strewed by pores ranging from 2 to 5 µm due to the solvation of PEG phase, partially miscible in PCL [13,19,43].

The third morphology obtained with NaCl grains smaller than 65 µm (M 50 in Figure 76c) is characterized by large amount of pores around 40 µm of diameter, surrounded by very thin walls. Each wall presented several micropores from 2 to 5 µm reasonable due to the PEG phase solvation.

Porosity determination.

Porosity and connectivity are important parameters to distinguish 3D membrane. The first feature refers to the volume that could be potentially filled by fluids, the second issue influences the degree of interconnection between pores by assuming that the porogen agents (NaCl and PEG) are removed by the fluid phase (Water) during the leaching step.

The membranes were designed with a volumetric porosity of 82% evaluated by calculated using Eqn 10 and by assuming a theoretical complete extraction of porogen agents. The measurement of the real porosity of membranes, calculated according to calculated using Eqn 11, are reported in Table 24. In some cases porosity was found to be higher than the theoretical one, presumably due to the loss of low amounts of PCL during process or to some inhomogeneity of the leachable phase into the matrix.

Table 24 - Blend compositions and NaCl granulometry of the three 3D membrane produced.

Sample Designation	Theoretical Porosity (%)	Real Porosity (%)	Connectivity
M 500	82	81,9 ± 0.5	99,2 ± 0,5
M 100	82	82.9 ± 0.3	99,6 ± 0,3
M 50	82	83.5 ± 0.4	99,6 ± 0,2

The value of the real porosity did not significantly change as a function of the pore size distribution because in much more influenced by the amount of porogen agent filled into the polymer matrix in melt mixing preparation.

The value of the connectivity measured according to calculated using Eqn 12 was higher than 99% for all materials, indicating that most of porogen agent was removed during leaching process, in agreement with real porosity value very close to the theoretical one.

Streptomyces coelicolor M145 immobilization on PCL/PEG porous membranes

PCL/PEG membranes having 100 μm pore sizes were used to test the mycelium ability to adhere, penetrate and grow. Cultivations were carried out using the rich growth medium R2YE, which is suitable for ACT production [229], and 96 well microtiter plates containing per well one PCL membrane and 108/ml S. coelicolor M145 spores.

The experiment was performed by setting different procedures for bacterial inoculation. In particular: i) 10 μl of spore suspension in an aqueous glycerol solution (20% v/v) were inoculated by direct placement on the apical portion of PCL/PEG membranes already placed in microtiter wells containing 250 μl of R2YE medium; ii) 50 μl of spore suspension were prepared using three different aqueous solutions of glycerol 4% (v/v), glycerol 20% (v/v), and glycerol (4% v/v) and polypropylene glycol (0.02% v/v), respectively, and then placed at the bottom of microtiter wells containing the PCL/PEG membranes only. In all the cases, the inoculated microplates were firstly kept under static conditions for 3 h to allow the spores entry; in the case (ii) 250 μl R2YE medium was then added into each well. Finally, all the microtiter plates were incubated on orbital shaking (200 rpm) for five days at 30°C.

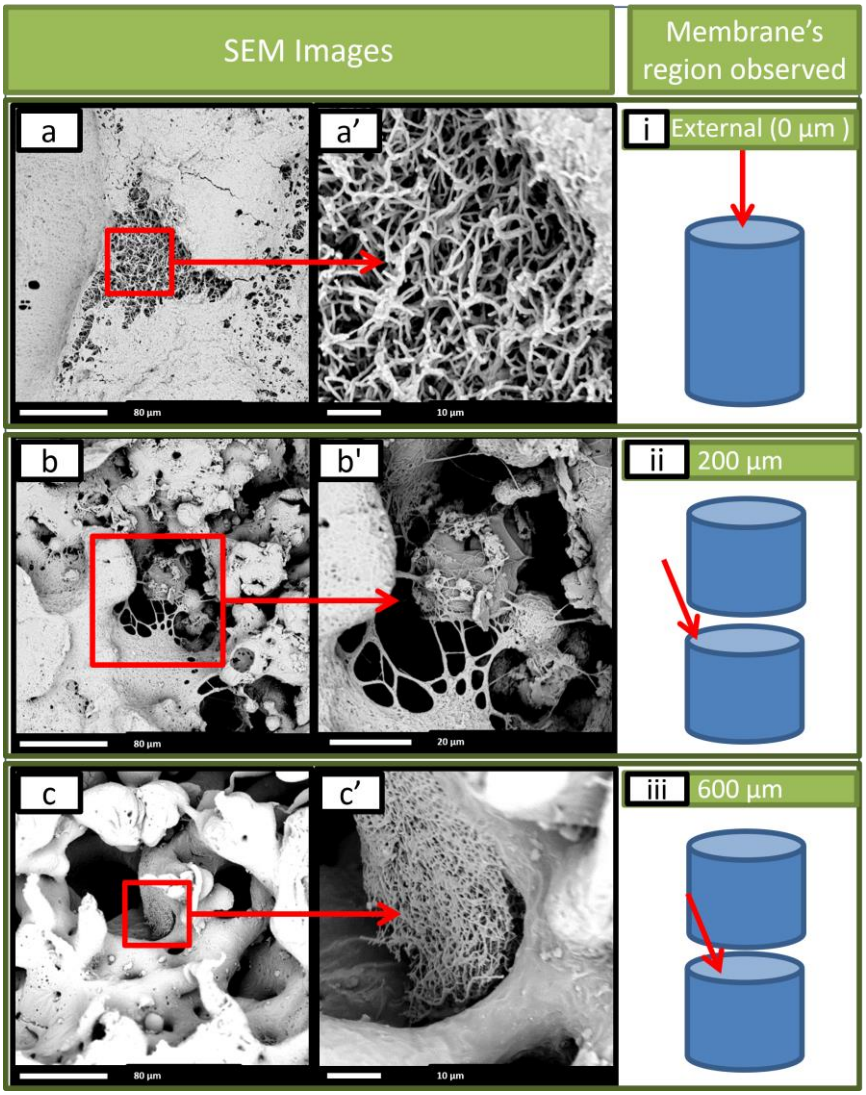

Figure 77 - SEM images of S. coelicolor on and inside the membrane M 100. (a,a') are images obtained, at different magnification, in the external surface of M 100; b,b' mycelial cells observed at 200 µm deep from the external surface of M 100; c,c' mycelial cells observed in the bulk of the membrane at 600 µm deep from the external surface; i, ii, iii schematic representation of membrane's region observed with SEM.

After 3, 4 and 5 days of incubation both the external and internal portion of PCL/PEG membranes were observed by SEM. In particular, S. coelicolor mycelium resulted immobilized on the pores of external surface forming a dense cell-layer (Figure 77a,a'). The bacterial mycelium penetrated inside the PCL/PEG membranes for about 200 µm (Figure 77b,b'); with some rare exception which was observed in the bulk at 600 µm from the membrane surface (Figure 77c,c').

SEM observation did not show any differences in mycelium immobilization with respect to the different inoculation procedures but the apical placement of spore

suspension resulted in a restricted localization of mycelium distribution on the PCL/PEG membranes coinciding with the inoculation place.

Therefore, the subsequent cultivations, aimed to study the effect of immobilization on bacterial biomass and secondary metabolite production yield, were performed by placing the PCL/PEG membranes into the microtiter wells containing 10 µl of spores (108/ml) in an aqueous glycerol solution (20% v/v) and 240 µl R2YE medium.

Effect of PCL/PEG membranes in ACT production and protein biosynthesis

S. coelicolor M145 was incubated in 96 well microtiter plates as above described using three PCL/PEG membranes having 50, 100 and 500 µm pore sizes, respectively, as support to perform immobilized-mycelium cultivations. The effect of immobilization and of different pore sizes was monitored on protein and ACT production yield using S. coelicolor M145 parallel cultivations performed without PCL membranes.

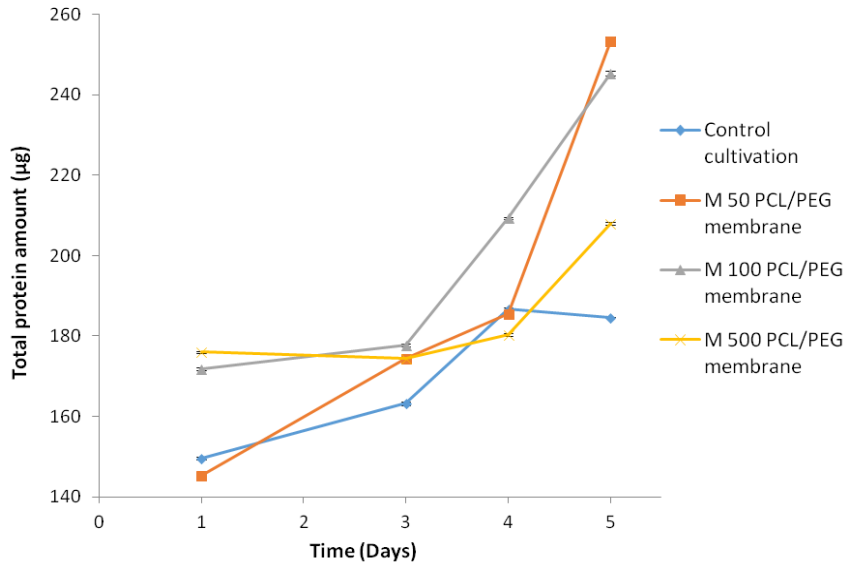

Figure 78 - S. coelicolor growth kinetics in immobilized-mycelium cultivations. Total protein content was extracted from PCL/PEG-immobilized mycelium of each microtiter well containing M 50, M 100 and M 500 respectively, at different growth times. Parallel cultivations without the presence of PCL/PEG membranes were used as control condition. Values are reported as mean of three cultivations; standard deviation is also reported as vertical bars.

The bacterial growth was measured by determining the total protein content extracted from free and PCL/PEG-immobilized mycelium grown in each microtiter well (Figure 78). Similar protein accumulation kinetics were revealed up to 3-4 days of growth. After 4 days of growth the immobilized-mycelium cultivations showed a

still increasing protein content while the control cultivation shows a constant amount. In particular, at 5 days of growth a protein content increment of about 1.4 fold was revealed in the mycelium immobilized on the membrane having 50 and 100 µm pore size compared to the control cultivation, thus revealing that mycelium-immobilization results in an improved protein biosynthesis capability.

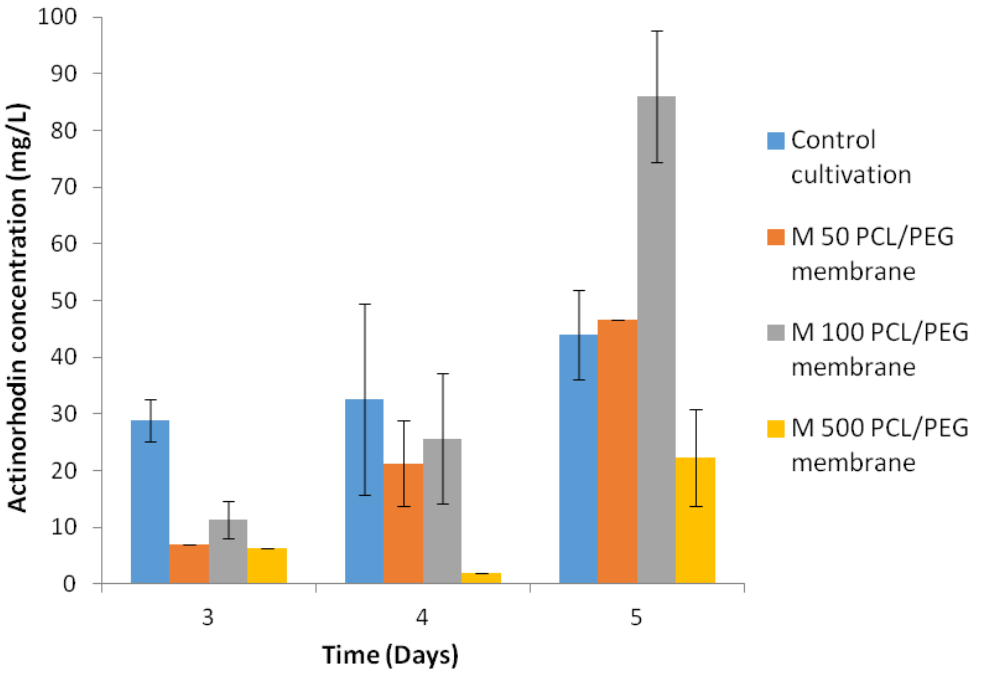

Figure 79 - Production of ACT, extracted from PCL/PEG immobilized mycelium cultivations in microtiter wells containing M 50, M 100 and M 500 respectively. Parallel cultivations without the presence of PCL/PEG membranes were used as control condition. Values are reported as mean of three independent measurements; standard deviation is also reported as vertical bars

Concerning secondary metabolism production, total amount of ACT antibiotic was calculated from free and PCL/PEG-immobilized mycelium cultivations in each microtiter well. During the observation time, the maximum ACT yield was obtained after five days of growth performed using M 100. In this case about two fold increased ACT content was measured compared to the control cultivation. On the contrary, the lower production yield was obtained using 500 µm pores size membrane (Figure 79).

Based on these data, bacterial growth was scaled up to 1 ml of R2YE medium in tester tubes and carried out using membranes with pores size of either 50 or 100 µm as support for mycelium immobilization. In particular, S. coelicolor spores were inoculated at the final concentration of 108/ml and three membranes were used for 1 ml of R2YE. Cultivations performed in parallel with the exception of PCL/PEG

membranes addition were used as control. The tester tubes were incubated at 30°C at 200 rpm and after three and five days of growth the assay for ACT production was carried out on the spent medium. In agreement with microtiter cultivation trials, an increased production was observed only when PCL/PEG membranes with pores size of 100 μm were used for S. coelicolor mycelium immobilization (Figure 80).

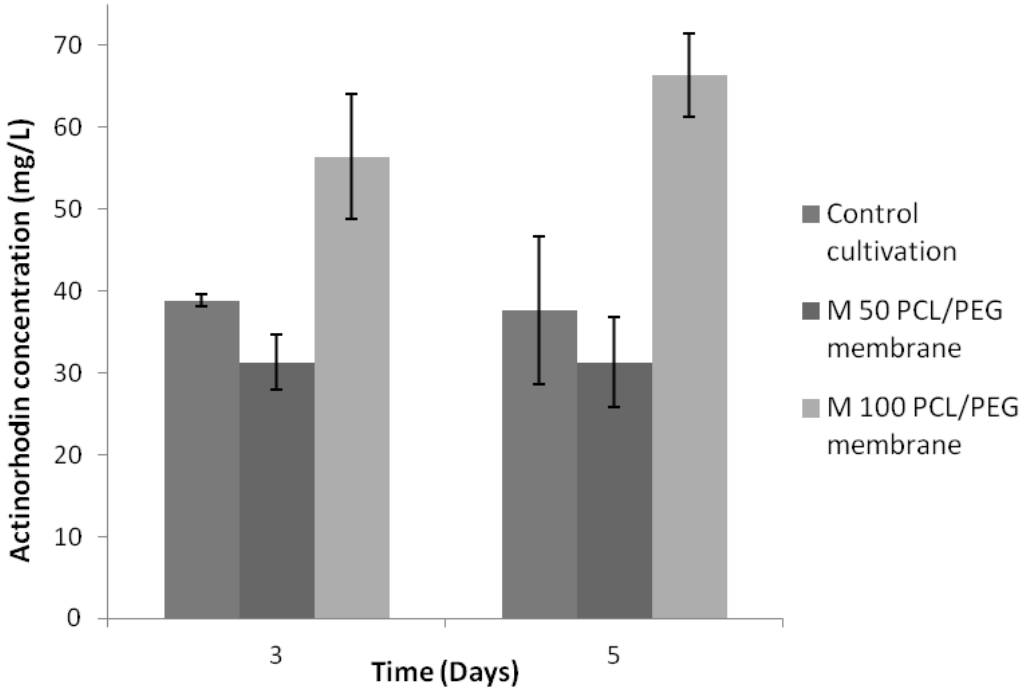

Figure 80 -Production of ACT, released in the spent medium from of PCL/PEG immobilized mycelium cultivations in tester tubes containing either M 50 or M 100. Parallel cultivations without the presence of PCL/PEG membranes were used as control condition. Values are reported as mean of three independent cultivations; standard deviation is also reported as vertical bars.

In particular, an increment of 1.5 and 1.7 was showed in presence of 100 μm pore size PCL/PEG membranes with respect to control cultivations after 3 and 5 days of growth, respectively. On the contrary, the use of 50 μm pore size PCL/PEG membranes resulted in an ACT production yield similar to that of control cultivations.

Conclusions

Actinomycete fermentation processes based on submerged cultivations are valuable means for producing natural products having biological activity of industrial and commercial interests such as antibiotic compounds [78,289]. However, submerged cultivations revealed some limitations mainly due to the fact that in their natural environments actinomycetes usually grow in the presence of a substrate for mycelium

adhesion and development [229,290]. In the absence of a substrate, these filamentous bacteria are prone to grow in a pellet-shape way which negatively affects production yield [84]. This work originally highlights the possible use of microporous PCL/PEG membranes as support for mycelium adhesion in actinomycete fermentations reporting data concerning S. coelicolor, the model strain of study for this family of bacteria.

The PCL/PEG membranes were designed for microtiter cultivations and indeed their shape and morphology were demonstrated suitable for bacterial immobilization by adhesion. In particular, the spores inoculated in the medium were able to germinate, adhere and penetrate the membrane throughout the pore lumen developing a dense mycelium network as revealed by SEM observations on cross sections of inoculated PCL/PEG membranes. The *S. coelicolor* immobilized mycelium, incubated in submerged microvolumetric cultivations, showed an improved capability to produce biomass (measured as total protein content) and secondary metabolites (measured as ACT amount) with respect to free mycelium submerged cultivations in agreement with Ndlovu et al. [14]. In addition, this work originally revealed a bioproduction capability which is affected in a pore size dependent manner revealing the fundamental importance in controlling production process parameters to obtain porous membranes possessing a specific microstructure. The possibility to adapt the microporous PCL/PEG membranes to conventional fermentation was tested by scaling up the cultivation volume using canonical test tubes where an improved ACT release in the medium was revealed in presence of 100 μm pore size PCL/PEG membranes, thus confirming the results obtained in microtiter cultivations.

Therefore, this study encourages the use of microporous PCL/PEG membranes as support for the development of actinomycete fermentation-based bioreactors and further encourage studies for process scale-up. In addition, microporous PCL/PEG membranes, proven as an easy-to-be-handle from a microbiological laboratory perspective, could be a useful tool for investigating at the molecular level the biochemical and metabolic events which lead to the improvement of bioproductivity in immobilized bacterial mycelium with respect to free mycelium in submerged cultivations thus possibly addressing the need from both academy and bioproduction industry of an improved understanding of actinomycete physiology.

S. coelicolor immobilized-cells cultivation on Electrospun PLA membranes

In this study, PLA and PLA-plasma membranes were prepared and used for carrying out immobilized-cell cultivations of *S. coelicolor*. In particular, the membranes, that reproduces the conditions of mycelial growth on an organic substrate, have been used in order to evaluate a correlation between their structure and/or plasma modification and a corresponding physiological response in terms of total protein and of ACT yields of the immobilized-cells.

Streptomyces coelicolor A3(2) immobilization on PLA and PLA-plasma membranes

PLA and PLA-plasma membranes were used to test the ability of *S. coelicolor* mycelium to adhere, penetrate and grow on their surface starting from spore inoculum. Therefore, after 3, 5, and 7 days of incubation, both the external and internal portions of each kind of PLA membranes were observed by SEM. The Figure 81a,d show several PLA and PLA-plasma fibers are visible under the biofilm thus demonstrating that after 3 days the biofilm is not able to cover the whole surface of the membranes. Otherwise, after 5 days (Figure 81b,e) the biofilm become more compact but only after 7 days the membrane appears completely covered by the mycelial biofilm as highlighted in Figure 81c,f. Furthermore, from Figure 81c,f it can be also observed that after 7 days, *S. coelicolor* biofilm is more compact on PLA-plasma membrane while on the PLA membrane some fibers can be observed under the biofilm. The possible relationships between biological effects of mycelium immobilization and the different chemical modification of PLA and PLA-plasma membranes were monitored on the biosynthetic capability in terms of total protein and ACT production yield using as control condition S. coelicolor) free-cell cultivations. All these analyses were conducted at 3, 5 and 7 day of cultivation. In particular, concerning total protein content, despite SEM observations, which revealed a different and progressive increment of mycelial cells on the surface of each kind of PLA membranes, a similar protein accumulation profile were revealed for both PLA and PLA-plasma immobilized-cell cultivations.

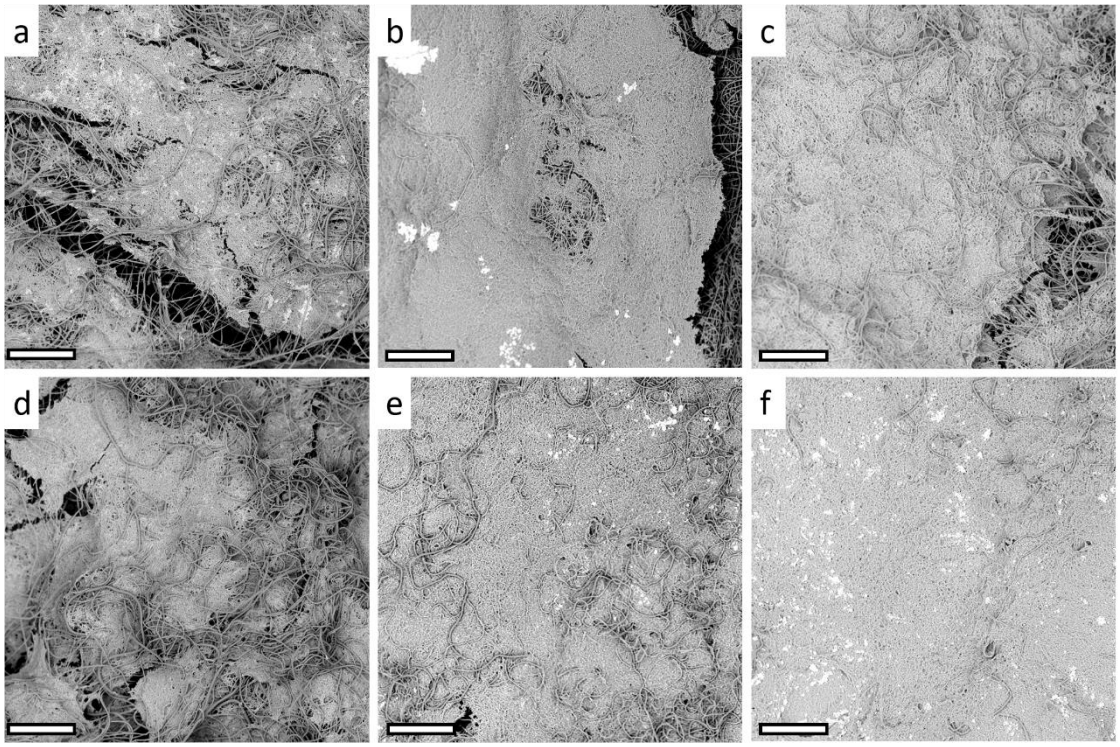

Figure 81 - SEM images of S. coelicolor adhered on PLA electrospun membranes after 3 (a), 5 (b) and 7 (c) days and on PLA-plasma electrospun membranes after 3 (d), 5 (e) and 7 (f) days. Scale bars are 100 µm.

S. coelicolor protein biosynthesis and ACT production in PLA and PLA-plasma immobilized-cell cultivations

In particular, the maximal protein amount, reached after 3 days and maintained at similar values thereafter, was about 2-fold increase in comparison to the control cultivation (Figure 82). Thus, this analysis revealed that cell immobilization on PLA and PLA-plasma membranes resulted in an improved protein biosynthesis capability in agreement with previous studies performed using PCL-based membranes [13]. Concerning antibiotic production, both PLA and PLA-plasma immobilized-cell cultivations produced a higher amount of ACT in the respect of free-cell cultivations used as control condition (Figure 83). Interestingly, it was estimated that about 80% of the total ACT produced is embedded in the membranes. In particular, the maximal ACT yield was obtained after 3 and 5 days of growth using PLA and PLA-plasma membranes, respectively, with the amounts of ACT remaining essentially the same thereafter.

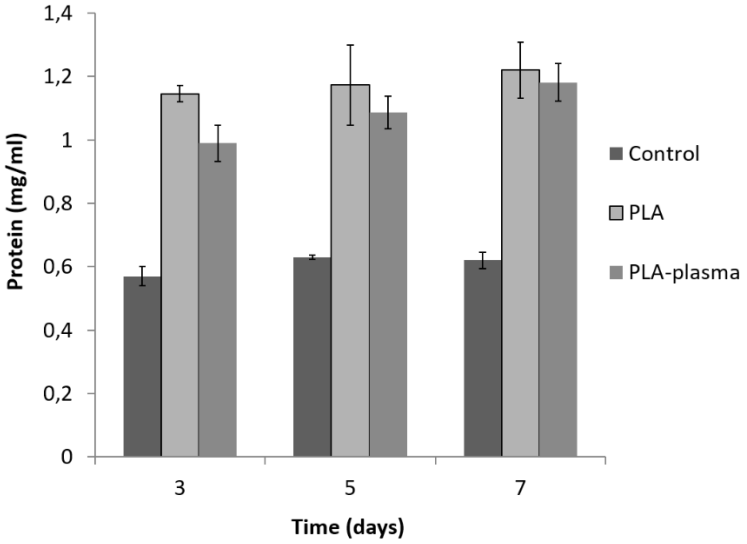

Figure 82 - Accumulation profiles of S. coelicolor total protein content extracted from free- and PLA and PLA-plasma membrane immobilized-cell cultivations. Values are reported as mean of three biological replicas; standard deviation is also reported as vertical bars.

Beside the difference in the ACT production kinetics, it is noteworthy that the maximal amount of ACT was about five and ten fold in the respect of control condition using PLA and PLA-plasma, respectively.

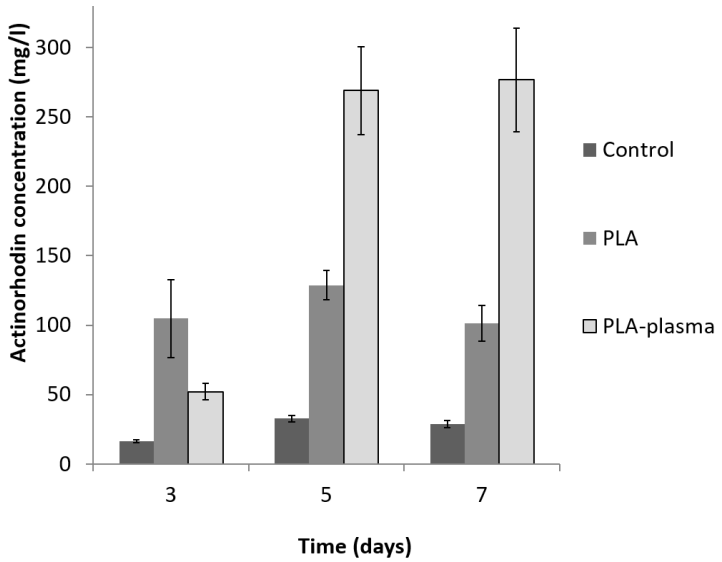

Figure 83 - Accumulation profiles of total ACT obtained from free- and PLA and PLA-plasma membrane immobilized-cell cultivations. Values are reported as mean of three biological replicas; standard deviation is also reported as vertical bars

Conclusion

In this work, electrospun PLA-based membranes subjected or not to O_2-plasma treatment, were used as support for adhesion *S. coelicolor* mycelium cells during submerged fermentation. Contact angles measurements revealed that the O_2-plasma treatment enhanced wettability of PLA electrospun membranes increasing the ES. XPS analysis confirmed that the increased wettability of PLA-plasma can be ascribed to the introduction of oxygen functionalities and the increase in carboxyl groups on the surface. SEM analysis highlighted that *S. coelicolor* spores inoculated in the growth medium were able to germinate and adhere both PLA and PLA-plasma membranes creating a dense mycelium network more effectively in PLA-plasma system. The *S. coelicolor* immobilized-cell cultivations showed superior performance in terms of protein and biologically active metabolite bioproduction of *S. coelicolor* mycelium immobilised on PLA-based membranes in the respect to free-cell cultivations. More in detail, although a similar amount of proteins was measured in both kinds of immobilized-cell cultivations, *S. coelicolor* immobilized-cells in PLA and PLA-plasma membranes produced an ACT amounts about five and ten fold increased, respectively, thus showing a specific positive influence of O_2-plasma treatment in the respect of biologically active metabolite production. Therefore, from one hand, this study encourages the use of nanofibrous PLA-based membranes as support for the development of actinomycete-fermentation bioreactors and further encourages studies for process scale-up. On the other hand, it would be of scientific interest to elucidate the deterministic correlation between O_2-plasma treatment and the increment of ACT production. In addition and more in general, an improved understanding of actinomycete physiology would be gained by investigating the biochemical and metabolic events at the molecular level which leads to the improvement of bio-productivity in immobilized-cells in comparison to free-cells in submerged cultivations. In this regard, preliminary investigations of monodimensional protein patterns of free- and PLA or PLA-plasma membrane immobilized-cells, obtained by SDS-PAGE analysis, revealed a set of differentially abundant protein bands which may suggest a differential regulation of cellular functions (data not shown) and which could be highlighted in the next feature by a comparative proteomic approach [291].

Intensification of Bacterial-Degradation of Oily Pollutants

After 48h of the incubation at 30°C in oil-degrader bacterial cultures, the porous 3D PCL based scaffolds were observed using SEM. The images confirmed the high capacity of adhesion and proliferation of bacterial cells within the 3D structure. Both the external and internal portions of scaffolds have shown a significant bacterial density due to a biofilm formation (Figure 84A-D).

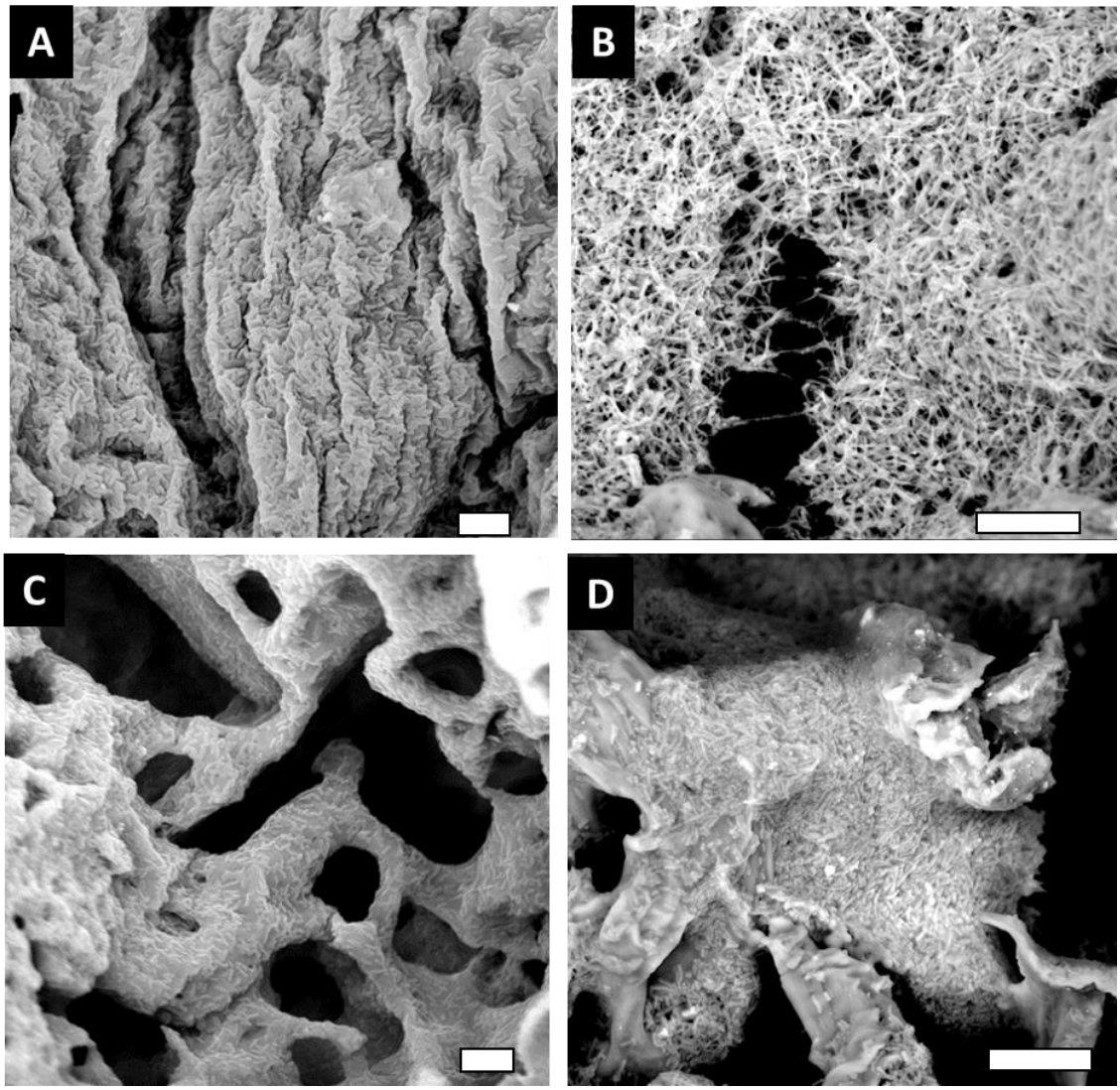

Figure 84 - SEM images of the bacterial biofilm formed on the scaffold by Nocardia SoB on the Scaffold surface (A) and in the porous structure (C) and Alcanivorax SK2 on the Scaffold surface (B) and in the porous structure (D).

No differences can be observed for the internal or external parts of the scaffold, which showed the same cell adhesion. Moreover both bacterial strains have showed

the same colonization and biofilm formation capacity. The ability to form biofilm on various surfaces is advantageous for the microorganisms, cells in biofilm have better chance of survival and adaptability and the biofilm ensured higher bioavailability of contaminants. Several studies reported that biofilm formation was a promoting factor for biodegradation respect to planktonic cells.

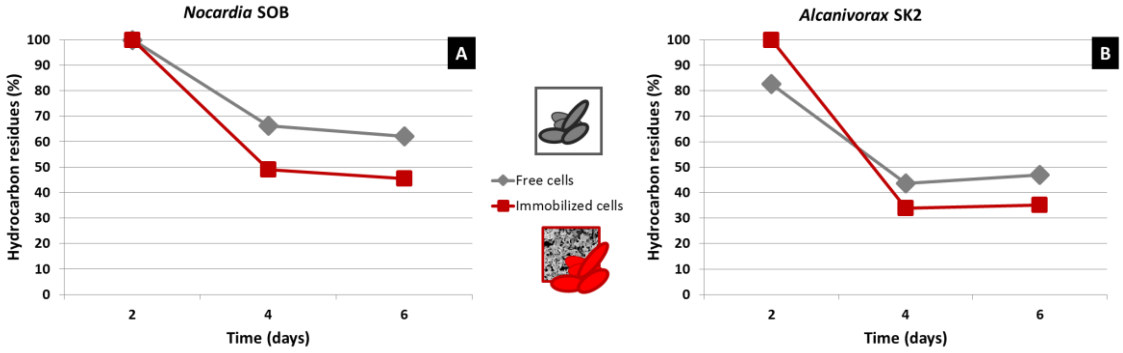

Figure 85 - Degradation efficiency of free cells and immobilized cells hydrocarbons-degrading bacteria Nocardia sp. SoB and Alcanivorax SK2.

More than 50% and 70% of oil hydrocarbons were removed by Nocardia SoB and Alcanivorax SK2 biofilm respectively, about 15% more in respect to the free cells (Figure 85). Biodegradation of 90% (Nocardia SoB) and 60% (Alcanivorax SK2) was observed for n-alkanes after the same incubation period (data not shown).

4.9 Synthesis and Self-Assembly of GO-g-PEG Aerogel

The strategy followed to synthesize GO-PEG Aerogel (GPA) is illustrated in Figure 86.

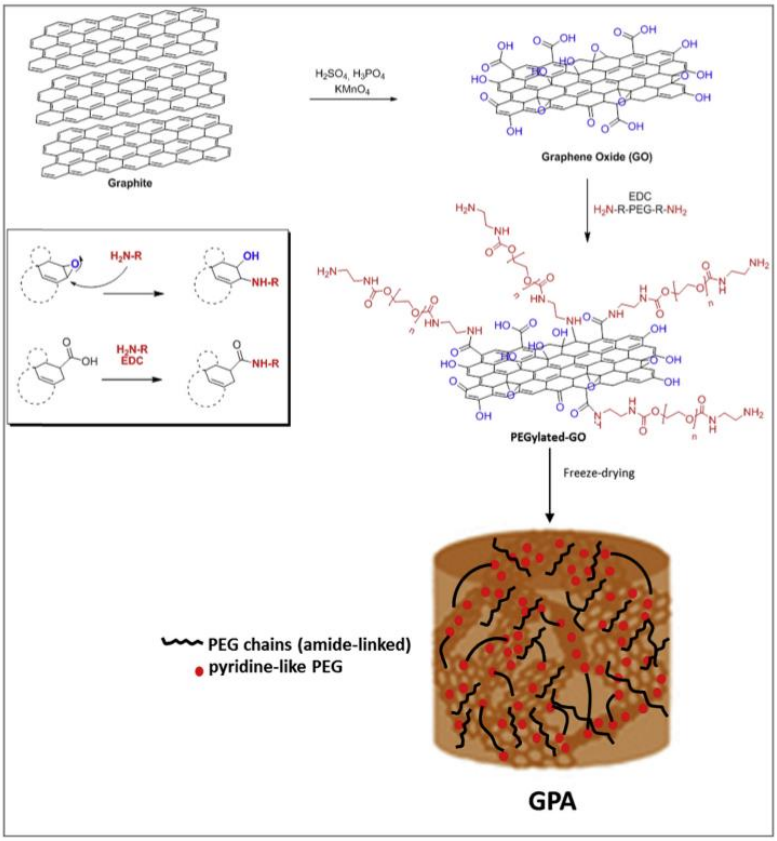

Figure 86 – Schematics of the pathway followed to synthesize GO-PEG aerogel (GPA).

More in detail, the GO used in the frame of this work was an ultra-oxygenated sample achieved by oxidizing neat graphite by using a quite common method, as described in the experimental part, while the diffusive phenomena regulating the formation of oxygen moieties were controlled by monitoring stirring speed and, as a consequence, the shear viscosity of the melt. The aged GO (i.e. stored for 200 days under acidic conditions) had an extremely high oxygen content (C/O ratio = 1.1, measured by XPS elemental analysis), especially if compared to that achieved in the same way but immediately purified (C/O ratio = 1.9).

Amino-terminated PEG was prepared at room temperature in two steps (see inset in Figure 86). At first PEG-OH was prepared by mixing PEG200 and CDI in anhydrous chloroform with the aim to obtain an intermediate capable to react with an

amino terminated chain. Indeed, by reaction with ethylenediamine, it was obtained the desired bis-amino terminated PEG, that was then used for the coupling with GO.

In fact, the amino groups of the PEG-NH_2 obtained act as nucleophile agents and are extremely reactive both towards carboxylic groups of the GO (properly activated with carbodiimide), and towards epoxy rings present onto the surface of GO sheets. The result was a GO sheet decorated with PEG tails, as represented in Figure 86.

The PEGylated-GO sheets were well dispersed in water to form a stable dark brown colloidal dispersion, by exploiting their reciprocal electrostatic repulsion resulting from the ionized carboxyl groups. After freeze-drying, the GPA appeared brown composed by eye-visible flakes.

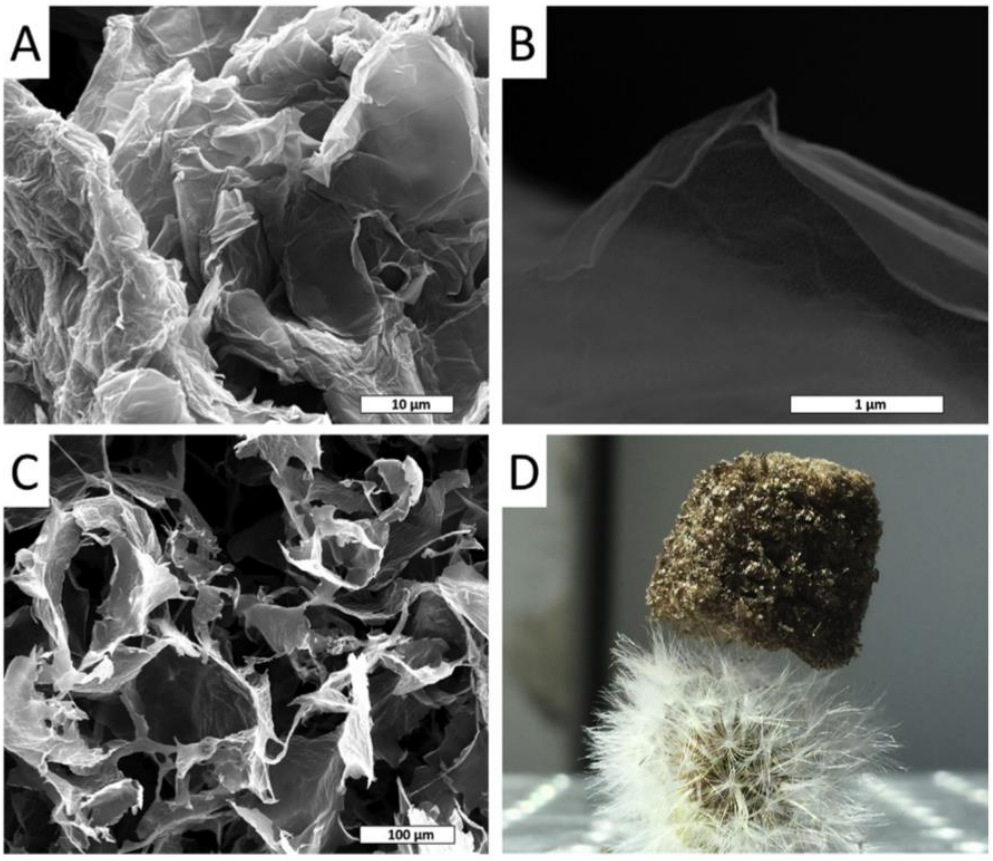

Figure 87 - Morphological analysis of GO-based structures: (A) SEM micrograph of as synthesized GO, (B–C): SEM micrographs of GO-PEG aerogel (GPA) at different magnifications, (D) digital photograph of a GPA monolith standing on Taraxacum officinalis.

SEM gives insight concerning the microstructure of GPA. As a result of chemical modification induced by the high content of oxygenated moieties, the GO lamellae

were found to be remarkably wrinkled and crumpled, as clearly visible in Figure 87A. After PEGylation, the structure become deeply different, as the lamellae appear well stretched and totally wrinkle-free (Figure 87B). Furthermore, the freeze-dried GPA possesses GO-PEG walls 1–2 nm thick, assembled in a 3D porous network, characterized by interconnected macropores, ranging from one hundred to three hundreds micrometers (Figure 87C).Due to its high porosity (99.7%), GPA is extremely ultralight, as evidenced by Figure 87D, where GPA is light enough to preserve the structure of Taraxacum officinalis.

Several spectroscopic measurements were carried out to demonstrate the covalent binding of PEG chains onto GO lamellae, thus providing further information about the chemical structure of the nanohybrid.

In order to demonstrate the successful amino-functionalization of PEG and the subsequent conjugation with GO, FTIR/ATR spectra of PEG-OH, PEG-NH_2, GO and GPA were collected within the range 4000–400 cm^{-1} and reported in Figure 88.

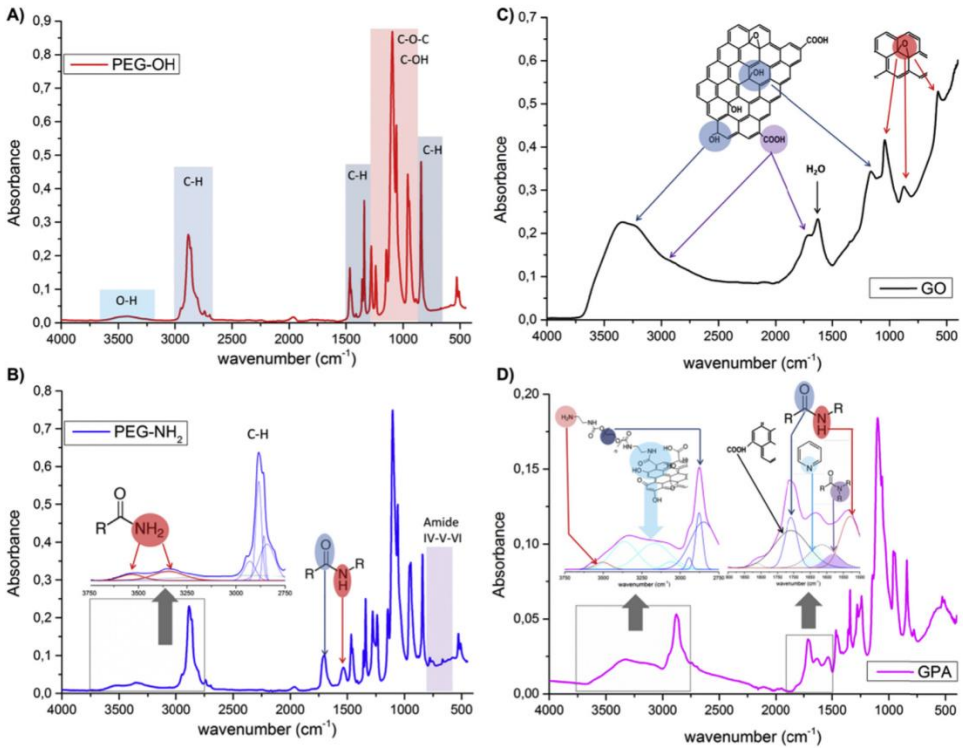

Figure 88 - FTIR/ATR spectra of: A) PEG-OH; B) PEG-NH_2 with magnification of multi-peak fitted curve in the range 3750–2750 cm^{-1}; C) GO and D) GO-PEG aerogel (GPA) with magnification of multi-peak fitted curve in the ranges 3750–2750 cm^{-1} and 1900–1500 cm^{-1}.

The spectrum of PEG-OH displays the characteristic bands attributable to CH bonds (stretching at 2750–3000 cm^{-1}, bending and rocking within1500–1350 cm^{-1},

770 cm^{-1}), and to C-O-C/C-OH bonds within the range 1200–900 cm^{-1} (see evidenced zones in the plot). Furthermore, the broad band centered at around 3400 cm^{-1} is assigned to OH stretching. After modification of PEG with amino-groups, the most significant differences (see evidenced zones in the plot) refer to three spectral ranges, i.e. 4000–2500 cm^{-1}, 1800–1500 cm^{-1}, 750–600 cm^{-1}. More in detail, the signal assigned to the OH stretching disappears, while it is clearly visible the insurgence of new bands, centered at 3525 cm^{-1} and 3300 cm^{-1}, respectively attributable to NH_2 asymmetric and symmetric stretching (see inset in Figure 88B). A shoulder located at 3235 cm^{-1} can be likely assigned to amide stretching of carbamate groups. In the spectral region 1900–1500 cm^{-1}, it is possible to observe that after amino-functionalization, PEG-NH_2 displays two bands, located at 1535 cm^{-1} and 1700 cm^{-1}, respectively assigned to amide and carbonyl moieties introduced after the covalent attachment of EDA.

Moreover, at lower wavenumbers (750–600 cm^{-1}) the rising of three features can be ascribed to the spatial conformation of amidic linkages. More in detail, amide V mode refers to out-of-plane bending of NH groups, whereas amide IV and amide VI modes are attributable to in-plane and out-of-plane bending of CO, respectively [292].

FTIR spectrum of GO is consistent with known data [293]**.** Although the end-groups refer substantially to OH, C-O-C and COOH, the presence of a highly aromatic and variegated environment surrounding oxygen moieties determines the coexistence of phenols, epoxy, ethers, lactols, lactones, aldehydes, ketones, aromatic acids, and many other functionalities, besides water molecules adsorbed. Due to these features, GO was found to absorb practically within the entire spectral range, especially at lower wavenumbers. Nevertheless, the broad absorption band in the 3750–2300 cm^{-1} region can be assigned to OH stretching due to phenols, carboxyls and water. Two well recognizable bands are centered at around 1720 cm^{-1} and 1624 cm^{-1}, with the former being undoubtedly assigned to carbonyls while the latter presumably originating by bending modes of water molecules integrated into GO structure [**28**]. At wavenumbers below 1250 cm^{-1}, a bunch of overlapping signals was proposed to be due to C-O-C and COH features, under the form of either epoxy, cyclic ethers and organic alcohols.

After the covalent functionalization of GO with PEG-NH_2, it is possible to observe the disappearance of the peak assigned to epoxy moieties of GO, thus confirming that

epoxy rings reacted with amino-moieties of the polymer. Furthermore, GPA displays the characteristic absorption peaks of PEG-NH_2, although the overlapping and broadening of the signals make very difficult to clearly identify each band. It is worth noting that the weakening and broadening of some bands attributed to PEG-NH_2 and GO could be due to the formation of a nanohybrid, highly resonant structure. Aiming to perform a deeper investigation, the two most variegated spectral ranges were fitted by means of Gaussian curves and provided in two insets in Figure 88D. In the spectral range within 3750–2750 cm^{-1}, GPA displays the bands associated to CH stretching (alkanes and alkenes) of the polymer. The signals characteristic of amide are still present, although the bands are broad, due to the overlapping with those related to GO oxygen-moieties. In the spectral region within 1900–1500 cm^{-1}, it can be observed that GPA spectrum retains the features ascribed to amide and carbonyl moieties, respectively centered at 1535 cm^{-1} and 1700 cm^{-1}, whereas the appearance of at least other three spectral components at around 1600 cm^{-1} (see inset in Figure 88D) can be reasonably attributable to carbonyl stretching of carbamate moiety of secondary and tertiary amides, in fully agreement with the results above described. The signals attributable to amide groups become stronger than those referred to free amines, as a result of the crosslinking between PEG and GO. Moreover, the presence of pyridine-like structures could be suggested by the increase of optical density in the 1650–1500 cm^{-1} range, although it is extremely difficult to get conclusive information.

Raman spectroscopy is widely considered among the most powerful tools for probing carbonaceous compounds such as graphene-based materials due to its high sensitivity to graphene crystals domains and defects.

For the Micro-Raman analysis a Bruker SENTERRA instrument, with diode laser excitation at 532 nm and spectral resolution 9–15 cm^{-1}, has been used. The laser power was fixed at 0.2 mW to avoid sample modifications; furthermore, measurements in three different sample positions have been repeated for each treatment to check the homogeneity of the sample. Analysis of the spectra has been done after subtraction of a linear baseline in the range 1200–1800 cm^{-1}, for the D and G bands and another linear baseline in the range 2500–3500 cm^{-1}, for the 2D region. The spectra have been successively normalized to the G band and to the central feature of the 2D region at ~2960 cm^{-1}, respectively.

Figure 89A,B show the micro-Raman spectra of GO and GPA focused on two spectral ranges of particular concern, respectively referred to first-order (1000–1900 cm^{-1}) and second-order (2500–3500 cm^{-1}) Raman scattering.

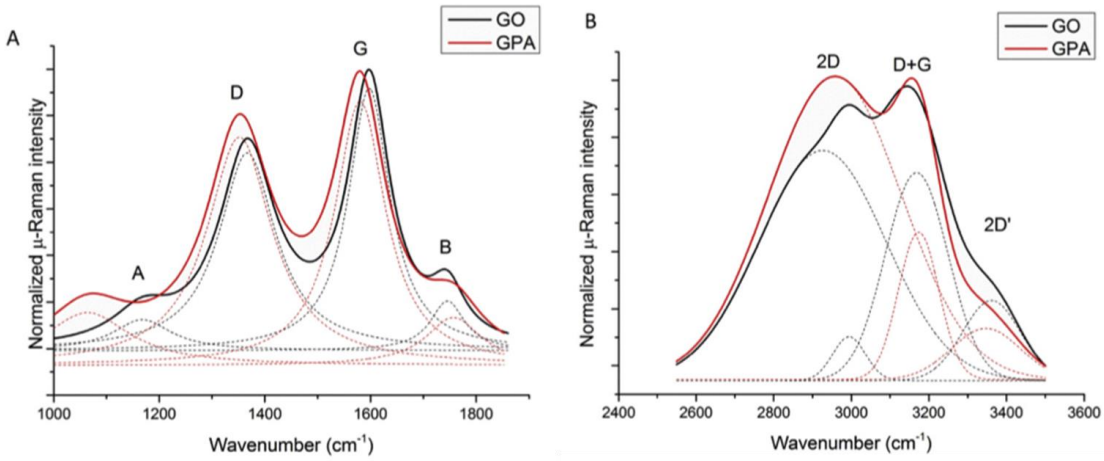

Figure 89 - Multi-peak fitted μ-Raman spectra of GO and GO-PEG aerogel (GPA) collected in the spectral ranges of first-order (A) and second-order (B) scattering.

The results put into evidence that the typical Raman modes of the graphenic materials are still present after PEGylation. Nevertheless, the functionalization introduces relevant changes in D and G bands, traditionally ascribed to sp^3 and sp^2 hybridized carbons, as well as in the modes resulting from their combination and overtone (2D, D + G, 2D′).

In particular, the covalent binding of PEG-NH_2 to GO induces a broadening of both D and G modes, which were found even slightly shifted. These findings could be ascribed to the overlapping of the other signals coming from amides, alkyl-amides and aromatic amides. As a consequence, the ID/IG ratio is found to increase, although the size of crystal graphene domains should remain constant in GPA. However, the most interesting feature is, in our opinion, the disappearance of the A mode, related to CH vibrations of rings and edges of GO [294], and the insurgence of a new band, located at around 1060 cm^{-1}, that can be ascribed to amide bonds [295].

Furthermore, the 2D contribution at 2680 cm^{-1} increases, while the 2D′ contribution at about 3150 cm^{-1} decreases with respect to the amplitude of the D + G component at 2950 cm^{-1}. The observed features are in good agreement with the FTIR data, suggesting that PEGylation, as clear, induces modifications of the GO.

XPS characterization was performed to get further confirmation about the presence of PEG-NH_2, easily detectable by monitoring N1s signal, Figure 90, since this latter was obviously not present in GO. The analysis of N1s spectra, fitted by means of Gaussian curves, revealed that nitrogen is mainly present both as amides (BE = 399.7 eV) and pyridine-like compounds (EB = 398.3 eV). This feature, in fully agreement with the outcomes of FTIR/ATR and Raman spectroscopy, suggests that the coupling between GO and PEG-NH_2 was ensured by the formation of covalent bonds between NH_2 functional groups of the polymer and the epoxy and carboxyl groups of GO, to give tertiary and secondary amides, respectively, whereas the reaction between PEG-NH_2 and the epoxy rings in the proximity of aromatic domains, presumably led to the formation of pyridine-like structures, due to the re-arrangement of PEG, as reported for similar systems [296]. Finally, these findings confirm those obtained by FTIR and Raman spectroscopy.

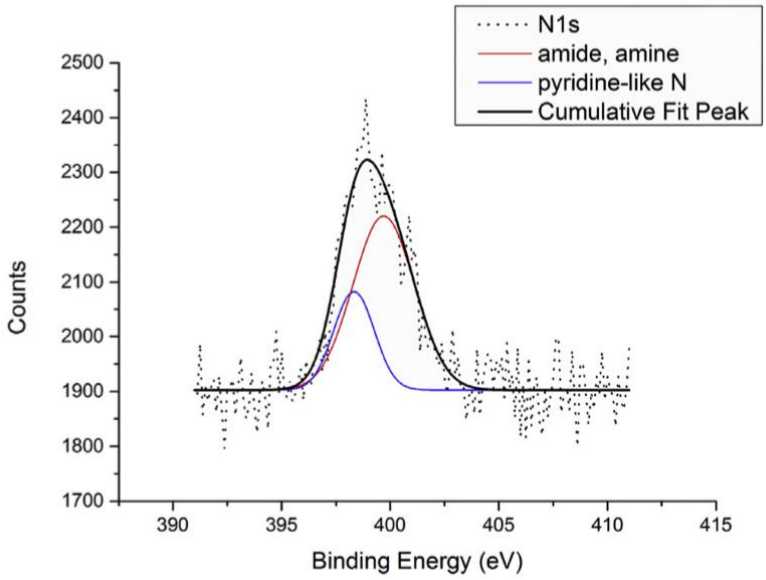

Figure 90 - XPS results: N1s spectrum of GO-PEG Aerogel (GPA).

XRD patterns, Figure 91, highlighted that interlayer spacing of GO lamellae increased from 9 Å to 16 Å after PEGylation and this aspect can be explained by considering that PEG coupling could have increased the interlayer distance, thus permitting to obtain very thin layers of exfoliated graphene with polymeric layers adhered onto sheets. Moreover, the re-arrangement of PEG into pyridine-like

structures in the basal planes may also contribute to a significantly increased interlamellar distance. As a consequence, no characteristic peaks of PEG was detected.

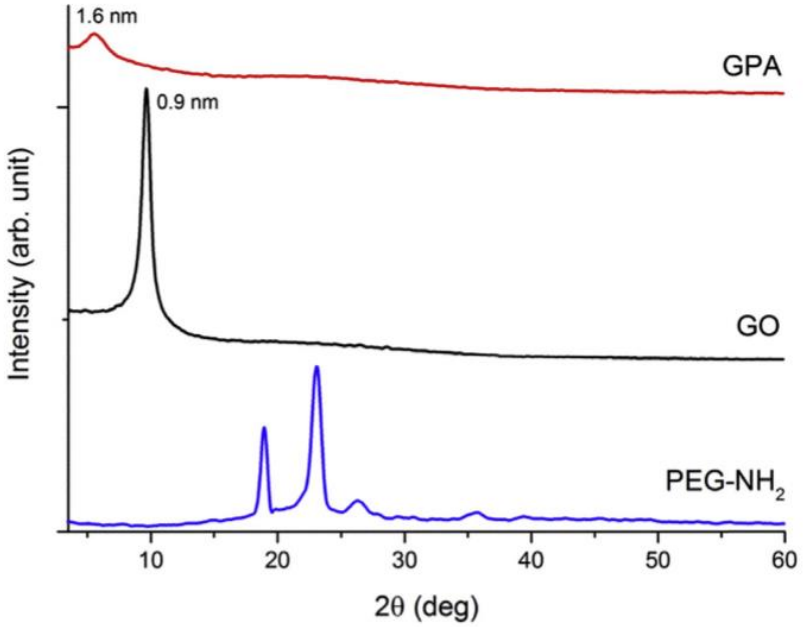

Figure 91 - XRD patterns of PEG-NH_2, GO and GO-PEG Aerogel (GPA).

BET results of GPA are shown in Figure 92. The BET adsorption/desorption isotherm of GPA shows a hysteresis loop at high relative pressure, indicating the existence of mesopores (in addition to the macropores easily detected by SEM analysis) in the aerogel. The PSD, provided in the inset of Figure 92, confirms the presence of pores within the range 2–60 nm. The total pores volume is equal to 0.37 cm^3/g. The specific surface measured is 226.6 m^2/g, slightly higher than those measured for graphene-based aerogels prepared by freeze-drying [297]. Despite its extremely high porosity and extraordinary lightness, GPA possesses even interesting mechanical properties. Figure 93 reports a representative stress-strain curve obtained during compressive tests. The plot put into evidence that GPA shows the typical behavior of graphene-based aerogels under compression tests.

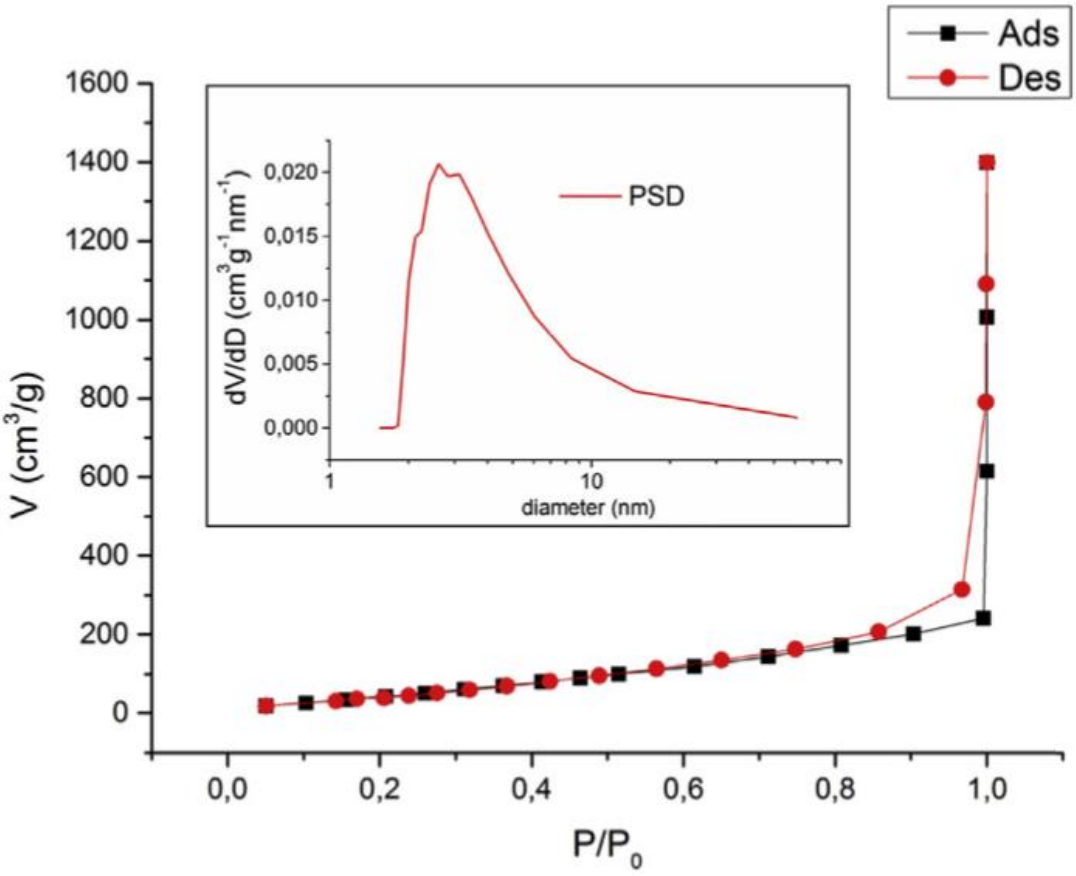

Figure 92 - Nitrogen adsorption (square) and desorption (circle) isotherms of GPA (inset: pore size distribution).

The sample displays an initial linear-elastic behavior associated with the progressive bending of the pores walls. The compression elastic modulus (E1), determined as the slope within this linear region of the stress-strain curve, was found to be slightly higher than those reported for other graphene-based aerogels [298]. The behavior of the curves seems to reveal a multi-step densification, followed by a plateau, symptomatic of a transition attributable to the beginning of the plastic deformation. Thereafter, a ductile-brittle transition is observed and within the last region of the plot, the stress varies linearly with the strain and the slope of the curve dramatically increases, due to the more prominent densification phenomena occurring since the pore walls collapsed thus filling the voids. Therefore, a steep increasing in stress is measured.

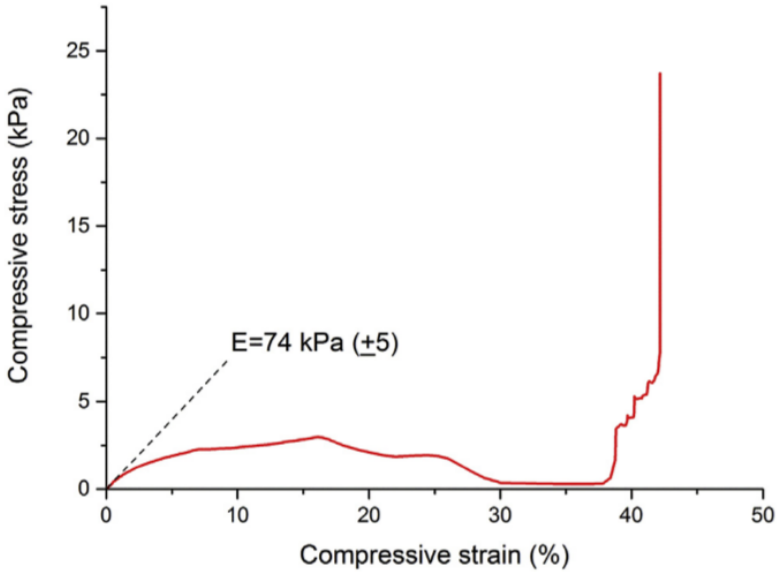

Figure 93 - Representative stress-strain curve of GO-PEG aerogel (GPA) during compressive tests.

Finally, GPA recovers its original height and shape after compression release. Presumably, this behavior is explainable by taking into consideration the aforementioned strong electrostatic interaction between the free terminations of PEG-NH_2 chains and the adjacent moieties of the GO lamellae, as confirmed by XRD patterns discussed above.

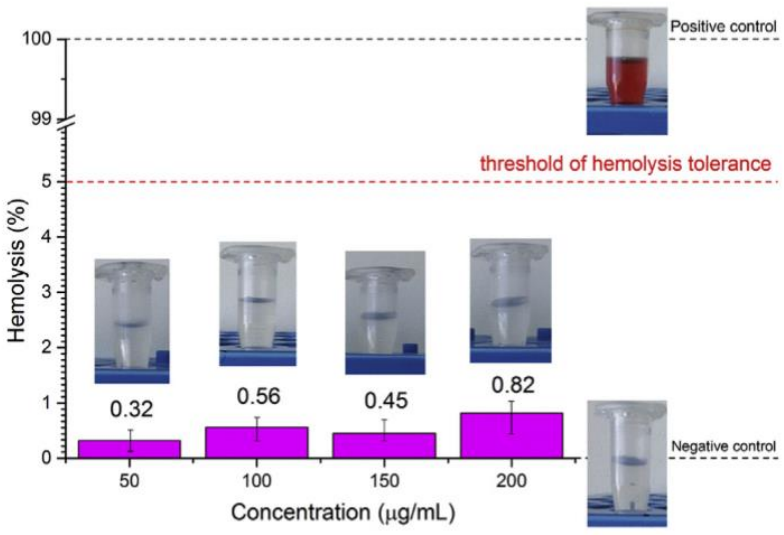

Figure 94 - Percentage of hemolysis of erythrocytes plotted as a function of GO-PEG concentration.

Safety evaluation of new products or ingredients destined for human use is crucial prior to exposure. One important factor in the development of novel systems for parenteral administration is to determine their ability to cause hemolysis by interaction

with cell membranes. Therefore, we examined this interaction by using erythrocytes as a model biological membrane system, since they are commonly adopted as a suitable model for studying the interaction of amphiphiles and other molecules with biological membranes [299,300]. The percentage of erythrocytes lysis is plotted as a function of nanohybrid concentration and provided in Figure 94, together with the digital photographs of each dispersion after centrifugation. The extent of hemolysis was found to range from 0.3% to 0.8%, upon increasing the GPA concentration, i.e. practically constant (and within the experimental noise). For all the concentrations assayed, the percentage of hemolysis was extremely lower than the permissible level of 5% [299] and, more interestingly, remarkably lower than those exhibited by other GO-based materials [300]. Furthermore, after incubation with GPA no erythrocyte aggregation was detected. Hence, under these conditions, GPA showed no significant hemolytic effects, indicating no detectable interaction with red blood cell membranes. These findings suggest that PEGylated GO can be considered quite biocompatible and this feature opens new scenarios for the use of this class of biocompatible aerogel materials for biomedical applications, such as tissue engineering and drug delivery.

Conclusion

In the present work, starting from commercial samples of graphite and PEG, we prepared a PEGylated-GO aerogel, with the aim to enhance its biocompatibility and to achieve a very low density porous structure with high mechanical properties. All the synthetic steps were confirmed by spectroscopic analysis, the morphology and the structure, together with the ultimate properties of the aerogel were deeply investigated. Furthermore, cytocompatibility and hemolysis essays certified that GO covered with biocompatible polymers such as PEG exhibits no toxicity in vitro at the tested doses. Due to all these features, GPA makes promises to be suitable for a large variety of applications.

5 Concluding remarks

In the present PhD work, biopolymeric porous structures for advanced applications were prepared and characterized. The procedures adopted were optimized in order to achieve the best performance on the basis of the final application involved for each device. In particular, we successfully developed 3D functionally graded porous scaffold for tissue engineering. Furthermore, appropriately modified nanoparticles were used in order to improve the mechanical and wettability properties of an electrospun mats designed for tissue engineering.

3D and 2D membranes were successfully prepared and optimized in terms of pore size distribution and wettability for the bioprocess intensification. More in detail, the *S. coelicolor* immobilized-cell cultivations showed superior performance in terms of protein and biologically active metabolite bioproduction of *S. coelicolor* mycelium immobilised on the biopolymeric porous structures if compared with free- cell cultivations.

Finally, we demonstrated the possibility to prepare biopolymeric porous sponges able to selectively absorb oil from water with high oil uptake. Furthermore, these devices are able also to support the growth of oil-degradator cells thus giving important further effort in bioremediation applications.

6 Future Perspectives

This PhD thesis focused on some of the most important techniques for developing porous biopolymeric structures i.e. particulate leaching, electrospinning and freeze-drying. In future, the systematic approach herein adopted to correlate structure-processing-properties relationships could be adopted with other different techniques such as 3D printing or gas foaming. Furthermore, the possibility to create super hydrophobic surfaces by means of chemical functionalization could represent another important feature for the oil/water separation. Furthermore, the degradation rate of functionally graded scaffold will be evaluated by taking into account several parameters such as the chemical composition of the matrix and its molecular weight, the effect of pro/anti degradative additives and/or the process parameters. A further investigation related to the mechanism involved in the bioprocess intensification, could lead to find innovative solution to further boost the bioactivity of industrial microbial cells.

Acknowledgements

I want to thank Prof. Giulio Ghersi and Dott. Silvia Rigogliuso of the department of *Scienze e Tecnologie Biologiche Chimiche e Farmaceutiche* (STEBICEF) for the fundamental biological essays conducted on the biopolymeric scaffold designed for tissue engineering applications.

I want to thank Prof. Anna Maria Puglia, Dott. Giuseppe Gallo and Alberto Sutera of the department of *Scienze e Tecnologie Biologiche Chimiche e Farmaceutiche* (STEBICEF) for the help and the invaluable suggestions about the study on the effects of biopolymeric porous devices on bioprocess intensification.

Finally, I want to sincerely thank Dott. Paola Quatrini and Valentina Catania of the department of *Scienze e Tecnologie Biologiche Chimiche e Farmaceutiche* (STEBICEF) for the help and invaluable suggestions about the study on the effects of biopolymeric porous devices on bioremediation.

References

[1] V. Fiore, L. Botta, R. Scaffaro, A. Valenza, A. Pirrotta, PLA based biocomposites reinforced with Arundo donax fillers, Compos. Sci. Technol. 105 (2014) 110–117. doi:10.1016/j.compscitech.2014.10.005.

[2] R. Scaffaro, L. Botta, M. Sanfilippo, G. Gallo, G. Palazzolo, A.M. Puglia, Combining in the melt physical and biological properties of poly(caprolactone) and chlorhexidine to obtain antimicrobial surgical monofilaments, Appl. Microbiol. Biotechnol. 97 (2013) 99–109. doi:10.1007/s00253-012-4283-x.

[3] R. Scaffaro, L. Botta, E. Passaglia, W. Oberhauser, M. Frediani, L. Di Landro, Comparison of different processing methods to prepare poly(lactid acid)-hydrotalcite composites, Polym. Eng. Sci. 54 (2014) 1804–1810. doi:10.1002/pen.23724.

[4] R. Scaffaro, L. Botta, G. Gallo, A.M. Puglia, Influence of Drawing on the Antimicrobial and Physical Properties of Chlorhexidine-Compounded Poly(caprolactone) Monofilaments, Macromol. Mater. Eng. 12 (2015) 1268–1277. doi:10.1002/mame.201500121.

[5] M. Ho, K. Lau, H. Wang, D. Hui, Improvement on the properties of polylactic acid (PLA) using bamboo charcoal particles, Compos. Part B Eng. 81 (2015) 14–25. doi:10.1016/j.compositesb.2015.05.048.

[6] M. Morreale, R. Scaffaro, A. Maio, F.P. La Mantia, Mechanical behaviour of Mater-Bi/wood flour composites: A statistical approach, Compos. Part A Appl. Sci. Manuf. 39 (2008) 1537–1546. doi:10.1016/j.compositesa.2008.05.015.

[7] M.P. Arrieta, E. Fortunati, F. Dominici, E. Rayón, J. López, J.M. Kenny, PLA-PHB/cellulose based films: Mechanical, barrier and disintegration properties, Polym. Degrad. Stab. 107 (2014) 139–149. doi:10.1016/j.polymdegradstab.2014.05.010.

[8] G. Siqueira, J. Bras, A. Dufresne, New process of chemical grafting of cellulose nanoparticles with a long chain isocyanate, Langmuir. 26 (2010) 402–411. doi:10.1021/la9028595.

[9] Z. Song, H. Xiao, Y. Zhao, Hydrophobic-modified nano-cellulose fiber/PLA biodegradable composites for lowering water vapor transmission rate (WVTR) of paper, Carbohydr. Polym. 111 (2014) 442–448. doi:10.1016/j.carbpol.2014.04.049.

[10] C. Zhou, Q. Shi, W. Guo, L. Terrell, A.T. Qureshi, D.J. Hayes, et al., Electrospun bio-nanocomposite scaffolds for bone tissue engineering by cellulose nanocrystals reinforcing maleic anhydride grafted PLA, ACS Appl. Mater. Interfaces. 5 (2013) 3847–3854. doi:10.1021/am4005072.

[11] R. Scaffaro, F. Lopresti, L. Botta, S. Rigogliuso, G. Ghersi, Integration of PCL and PLA in a monolithic porous scaffold for interface tissue engineering, J. Mech. Behav. Biomed. Mater. 63 (2016) 303–313. doi:10.1016/j.jmbbm.2016.06.021.

[12] J.S. Son, S.G. Kim, J.S. Oh, M. Appleford, S. Oh, J.L. Ong, et al., Hydroxyapatite/polylactide biphasic combination scaffold loaded with dexamethasone for bone regeneration, J. Biomed. Mater. Res. - Part A. 99 A (2011) 638–647. doi:10.1002/jbm.a.33223.

[13] R. Scaffaro, F. Lopresti, A. Sutera, L. Botta, R.M. Fontana, A.M. Puglia, et al., Effect of PCL/PEG-Based Membranes on Actinorhodin Production in Streptomyces coelicolor Cultivations, Macromol. Biosci. 16 (2016) 686–693. doi:10.1002/mabi.201500391.

[14] T.M. Ndlovu, A.C. Ward, J. Glassey, J. Eskildsen, G. Akay, Bioprocess intensification of antibiotic production by Streptomyces coelicolor A3(2) in micro-porous culture., Mater. Sci. Eng. C. Mater. Biol. Appl. 49 (2015) 799–806. doi:10.1016/j.msec.2015.01.052.

[15] J. Feng, S.T. Nguyen, Z. Fan, H.M. Duong, Advanced fabrication and oil absorption properties of super-hydrophobic recycled cellulose aerogels, Chem. Eng. J. 270 (2015) 168–175. doi:10.1016/j.cej.2015.02.034.

[16] R. Scaffaro, F. Lopresti, A. Maio, L. Botta, S. Rigogliuso, G. Ghersi, Electrospun PCL/GO-g-PEG structures: Processing-morphology-properties relationships, Compos. Part A Appl. Sci. Manuf. 92 (2016) 97–107. doi:10.1016/j.compositesa.2016.11.005.

[17] S. Surucu, K. Masur, H.T. Sasmazel, T. Von Woedtke, K.D. Weltmann, Atmospheric plasma surface modifications of

electrospun PCL/chitosan/PCL hybrid scaffolds by nozzle type plasma jets for usage of cell cultivation, Appl. Surf. Sci. 385 (2016) 400–409.

[18] G.G. Niederauer, M.A. Slivka, N.C. Leatherbury, D.L. Korvick, H.H. Harroff, W.C. Ehler, et al., Evaluation of multiphase implants for repair of focal osteochondral defects in goats., Biomaterials. 21 (2000) 2561–2574. doi:10.1016/S0142-9612(00)00124-1.

[19] R. Scaffaro, F. Lopresti, L. Botta, S. Rigogliuso, G. Ghersi, Preparation of three-layered porous PLA/PEG scaffold : relationship between morphology , mechanical behavior and cell permeability, J. Mech. Behav. Biomed. Mater. 54 (2016) 8–20. doi:10.1016/j.jmbbm.2015.08.033.

[20] M. Alhag, E. Farrell, M. Toner, T.C. Lee, F.J. O'Brien, N. Claffey, Evaluation of the ability of collagen-glycosaminoglycan scaffolds with or without mesenchymal stem cells to heal bone defects in Wistar rats., Oral Maxillofac. Surg. 16 (2012) 47–55. doi:10.1007/s10006-011-0299-0.

[21] G.P. Duffy, E.M. Byrne, T.M. McFadden, E.M. Farrel, F.J. O'Brien, In vitro vascularisation of collagen-gag scaffolds using mesenchymal stem cells, in: Eur. Cells Mater., 2009: p. 16. http://www.scopus.com/inward/record.url?eid=2-s2.0-84860361279&partnerID=tZOtx3y1.

[22] A. Matsiko, T.J. Levingstone, J.P. Gleeson, F.J. O'Brien, Incorporation of TGF-Beta 3 within Collagen-Hyaluronic Acid Scaffolds Improves their Chondrogenic Potential., Adv. Healthc. Mater. 4 (2015) 1175–9. doi:10.1002/adhm.201500053.

[23] Chitosan for gene delivery and orthopedic tissue engineering applications., Molecules. 18 (2013) 5611–47. http://www.scopus.com/inward/record.url?eid=2-s2.0-84878288360&partnerID=tZOtx3y1 (accessed June 15, 2015).

[24] N.G. Mehr, C.D. Hoemann, B.D. Favis, Chitosan Surface Modification of Fully Interconnected 3D Porous Poly(ε-caprolactone) by the LbL Approach, Polymer (Guildf). 64 (2015) 112–121. doi:10.1016/j.polymer.2015.03.025.

[25] X.-Y. Wang, Z.-H. Jin, B.-W. Gan, S.-W. Lv, M. Xie, W.-H. Huang, Engineering interconnected 3D vascular networks in hydrogels using molded sodium alginate lattice as the sacrificial template, Lab Chip. 14 (2014) 2709–2716. doi:10.1039/C4LC00069B.

[26] D. Algul, H. Sipahi, A. Aydin, F. Kelleci, S. Ozdatli, F.G. Yener, Biocompatibility of biomimetic multilayered alginate–chitosan/β-TCP scaffold for osteochondral tissue, Int. J. Biol. Macromol. 79 (2015) 363–369. doi:10.1016/j.ijbiomac.2015.05.005.

[27] L. Coluccino, P. Stagnaro, M. Vassalli, S. Scaglione, Bioactive TGF-β1/HA alginate-based scaffolds for osteochondral tissue repair: Design, realization and multilevel characterization, J. Appl. Biomater. Funct. Mater. 14 (2016) e42–e52. doi:10.5301/jabfm.5000249.

[28] T. Hodgkinson, A. Bayat, In vitro and ex vivo analysis of hyaluronan supplementation of integra® dermal template on human dermal fibroblasts and keratinocytes, J. Appl. Biomater. Funct. Mater. 14 (2016) e9–e18. doi:10.5301/jabfm.5000259.

[29] P. Gupta, K.K. Nayak, Compatibility study of alginate/keratin blend for biopolymer development, J. Appl. Biomater. Funct. Mater. 13 (2015) E332–E339. doi:10.5301/jabfm.5000242.

[30] E. Martín-López, M. Nieto-Díaz, M. Nieto-Sampedro, Influence of Chitosan concentration on cell viability and proliferation in vitro by changing film topography, J. Appl. Biomater. Funct. Mater. 11 (2013) 151–158. doi:10.5301/JABFM.2012.10449.

[31] Z. Zhang, G. Sèbe, D. Rentsch, T. Zimmermann, P. Tingaut, Ultralightweight and flexible silylated nanocellulose sponges for the selective removal of oil from water, Chem. Mater. 26 (2014) 2659–2668. doi:10.1021/cm5004164.

[32] N. Chitpong, S.M. Husson, Polyacid functionalized cellulose nanofiber membranes for removal of heavy metals from impaired waters, J. Memb. Sci. 523 (2017) 418–429. doi:10.1016/j.memsci.2016.10.020.

[33] K. Bazaka, M. V. Jacob, R.J. Crawford, E.P. Ivanova, Plasma-assisted surface modification of organic biopolymers to prevent bacterial attachment, Acta Biomater. 7 (2011) 2015–2028. doi:10.1016/j.actbio.2010.12.024.

[34] C. Zandén, M. Voinova, J. Gold, D. Mörsdorf, I. Bernhardt, J. Liu, Surface characterisation of oxygen plasma treated electrospun polyurethane fibres and their interaction with red blood cells, Eur. Polym. J. 48 (2012) 472–482. doi:10.1016/j.eurpolymj.2012.01.004.

[35] K. Moraczewski, M. Stepczyńska, R. Malinowski, P. Rytlewski, B. Jagodziński, M. Zenkiewicz, Stability studies of plasma

modification effects of polylactide and polycaprolactone surface layers, Appl. Surf. Sci. 377 (2016) 228–237. doi:10.1016/j.apsusc.2016.03.171.

[36] A. Maio, L. Botta, A.C. Tito, L. Pellegrino, M. Daghetta, R. Scaffaro, Statistical study of the influence of CNTs purification and plasma functionalization on the properties of polycarbonate-CNTs nanocomposites, Plasma Process. Polym. 11 (2014) 664–677. doi:10.1002/ppap.201400008.

[37] Z. Wang, J.P. Barford, C.W. Hui, G. McKay, Kinetic and equilibrium studies of hydrophilic and hydrophobic rice husk cellulosic fibers used as oil spill sorbents, Chem. Eng. J. 281 (2015) 961–969. doi:10.1016/j.cej.2015.07.002.

[38] Y. Mi, W. Zhou, Q. Li, F. Gong, R. Zhang, G. Ma, et al., Preparation of water-in-oil emulsions using a hydrophobic polymer membrane with 3D bicontinuous skeleton structure, J. Memb. Sci. 490 (2015) 113–119. doi:10.1016/j.memsci.2015.04.054.

[39] S.M. Sidik, A.A. Jalil, S. Triwahyono, S.H. Adam, M.A.H. Satar, B.H. Hameed, Modified oil palm leaves adsorbent with enhanced hydrophobicity for crude oil removal, Chem. Eng. J. 203 (2012) 9–18. doi:10.1016/j.cej.2012.06.132.

[40] K.C. Payne, C.D. Jackson, C.E. Aizpurua, O.J. Rojas, M.A. Hubbe, Oil spills abatement: factors affecting oil uptake by cellulosic fibers., Environ. Sci. Technol. 46 (2012) 7725–30. doi:10.1021/es3015524.

[41] A.-M. Yousefi, M.E. Hoque, R.G.S. V. Prasad, N. Uth, Current strategies in multiphasic scaffold design for osteochondral tissue engineering: A review, J. Biomed. Mater. Res. Part A. 103 (2015) 2460–2481. doi:10.1002/jbm.a.35356.

[42] S.J. Hollister, Porous scaffold design for tissue engineering., Nat. Mater. 4 (2005) 518–24. doi:10.1038/nmat1421.

[43] G. Lo Re, F. Lopresti, G. Petrucci, R. Scaffaro, A facile method to determine pore size distribution in porous scaffold by using image processing, Micron. 76 (2015) 37–45. doi:10.1016/j.micron.2015.05.001.

[44] T. Nie, L. Xue, M. Ge, H. Ma, J. Zhang, Fabrication of poly(L-lactic acid) tissue engineering scaffolds with precisely controlled gradient structure, Mater. Lett. 176 (2016) 25–28. doi:10.1016/j.matlet.2016.04.078.

[45] R. Scaffaro, F. Lopresti, L. Botta, S. Rigogliuso, G. Ghersi, Preparation of three-layered porous PLA / PEG scaffold : relationship between morphology , mechanical behavior and cell permeability, J. Mech. Behav. Biomed. Mater. 54 (2016) 8–20. doi:10.1016/j.jmbbm.2015.08.033.

[46] R. Scaffaro, F. Lopresti, L. Botta, S. Rigogliuso, G. Ghersi, Melt Processed PCL/PEG Scaffold With Discrete Pore Size Gradient for Selective Cellular Infiltration, Macromol. Mater. Eng. 301 (2016) 182–190. doi:10.1002/mame.201500289.

[47] S.H. Oh, I.K. Park, J.M. Kim, J.H. Lee, In vitro and in vivo characteristics of PCL scaffolds with pore size gradient fabricated by a centrifugation method, Biomaterials. 28 (2007) 1664–1671. doi:10.1016/j.biomaterials.2006.11.024.

[48] Y. Wang, R. Xu, G. Luo, Q. Lei, Q. Shu, Z. Yao, et al., Biomimetic fibroblast-loaded artificial dermis with “sandwich” structure and designed gradient pore sizes promotes wound healing by favoring granulation tissue formation and wound re-epithelialization, Acta Biomater. 30 (2016) 246–257. doi:10.1016/j.actbio.2015.11.035.

[49] G. Tang, H. Zhang, Y. Zhao, Y. Zhang, X. Li, X. Yuan, Preparation of PLGA Scaffolds with Graded Pores by Using a Gelatin-Microsphere Template as Porogen., J. Biomater. Sci. Polym. Ed. 23 (2011) 2241–2257. doi:10.1163/156856211X614185.

[50] M. Sadat-Shojai, M.T. Khorasani, A. Jamshidi, A new strategy for fabrication of bone scaffolds using electrospun nano-HAp/PHB fibers and protein hydrogels, Chem. Eng. J. 289 (2016) 38–47. doi:10.1016/j.cej.2015.12.079.

[51] Y. Zhu, H. Wu, S. Sun, T. Zhou, J. Wu, Y. Wan, Designed composites for mimicking compressive mechanical properties of articular cartilage matrix, J. Mech. Behav. Biomed. Mater. 36 (2014) 32–46. doi:10.1016/j.jmbbm.2014.04.003.

[52] H.M. Aydin, A three-layered osteochondral plug: Structural, mechanical, and in vitro biocompatibility analysis, Adv. Eng. Mater. 13 (2011) 511–517. doi:10.1002/adem.201180005.

[53] P. Yusong, S. Qianqian, P. Chengling, W. Jing, Prediction of mechanical properties of multilayer gradient hydroxyapatite reinforced poly(vinyl alcohol) gel biomaterial, J. Biomed. Mater. Res. - Part B Appl. Biomater. 101 B (2013) 729–735. doi:10.1002/jbm.b.32875.

[54] E. Kon, M. Delcogliano, G. Filardo, M. Fini, G. Giavaresi, S. Francioli, et al., Orderly osteochondral regeneration in a sheep model using a novel nano-composite multilayered biomaterial, J. Orthop. Res. 28 (2010) 116–124. doi:10.1002/jor.20958.

[55] T.J. Levingstone, A. Matsiko, G.R. Dickson, F.J. O’Brien, J.P. Gleeson, A biomimetic multi-layered collagen-based scaffold for osteochondral repair, Acta Biomater. 10 (2014) 1996–2004. doi:10.1016/j.actbio.2014.01.005.

[56] B.S. Kim, E.J. Kim, J.S. Choi, J.H. Jeong, C.H. Jo, Y.W. Cho, Human collagen-based multilayer scaffolds for tendon-to-

bone interface tissue engineering, J. Biomed. Mater. Res. - Part A. 102 (2014) 4044–4054. doi:10.1002/jbm.a.35057.

[57] A. Tampieri, M. Sandri, E. Landi, D. Pressato, S. Francioli, R. Quarto, et al., Design of graded biomimetic osteochondral composite scaffolds, Biomaterials. 29 (2008) 3539–3546. doi:10.1016/j.biomaterials.2008.05.008.

[58] F.J. Bye, J. Bissoli, L. Black, A.J. Bullock, S. Puwanun, K. Moharamzadeh, et al., Development of bilayer and trilayer nanofibrous/microfibrous scaffolds for regenerative medicine, Biomater. Sci. 1 (2013) 942. doi:10.1039/c3bm60074b.

[59] S. Ding, L. Li, X. Liu, G. Yang, G. Zhou, S. Zhou, A nano-micro alternating multilayer scaffold loading with rBMSCs and BMP-2 for bone tissue engineering, Colloids Surfaces B Biointerfaces. 133 (2015) 286–295. doi:10.1016/j.colsurfb.2015.06.015.

[60] S.M. Lien, C.H. Chien, T.J. Huang, A novel osteochondral scaffold of ceramic-gelatin assembly for articular cartilage repair, Mater. Sci. Eng. C. 29 (2009) 315–321. doi:10.1016/j.msec.2008.07.017.

[61] Y.F. Wang, H.F. Guo, D.J. Ying, Multilayer scaffold of electrospun PLA-PCL-collagen nanofibers as a dural substitute, J. Biomed. Mater. Res. - Part B Appl. Biomater. 101 (2013) 1359–1366. doi:10.1002/jbm.b.32953.

[62] H.-Y. Mi, X. Jing, E. Yu, J. McNulty, X.-F. Peng, L.-S. Turng, Fabrication of triple-layered vascular scaffolds by combining electrospinning, braiding, and thermally induced phase separation, Mater. Lett. 161 (2015) 305–308.

[63] C. Liu, Z. Han, J.T. Czernuszka, Gradient collagen / nanohydroxyapatite composite scaffold : Development and characterization, Acta Biomater. 5 (2009) 661–669. doi:10.1016/j.actbio.2008.09.022.

[64] N.H. Dormer, C.J. Berkland, M.S. Detamore, Emerging techniques in stratified designs and continuous gradients for tissue engineering of interfaces, Ann. Biomed. Eng. 38 (2010) 2121–2141. doi:10.1007/s10439-010-0033-3.

[65] Y. Wang, H. Tian, L. Zhang, Role of starch nanocrystals and cellulose whiskers in synergistic reinforcement of waterborne polyurethane, Carbohydr. Polym. 80 (2010) 665–671. doi:http://dx.doi.org/10.1016/j.carbpol.2009.10.043.

[66] H. Bai, D. Wang, B. Delattre, W. Gao, J. De Coninck, S. Li, et al., Biomimetic gradient scaffold from ice-templating for self-seeding of cells with capillary effect, Acta Biomater. 20 (2015) 113–119. doi:10.1016/j.actbio.2015.04.007.

[67] J.M. Oliveira, M.T. Rodrigues, S.S. Silva, P.B. Malafaya, M.E. Gomes, C.A. Viegas, et al., Novel hydroxyapatite/chitosan bilayered scaffold for osteochondral tissue-engineering applications: Scaffold design and its performance when seeded with goat bone marrow stromal cells, Biomaterials. 27 (2006) 6123–6137. doi:10.1016/j.biomaterials.2006.07.034.

[68] A. Seidi, M. Ramalingam, Protocols for Biomaterial Scaffold Fabrication, in: Integr. Biomater. Tissue Eng., 2012: pp. 1–23. doi:10.1002/9781118371183.ch1.

[69] R.J. McCoy, C. Jungreuthmayer, F.J. O'Brien, Influence of flow rate and scaffold pore size on cell behavior during mechanical stimulation in a flow perfusion bioreactor., Biotechnol. Bioeng. 109 (2012) 1583–94. doi:10.1002/bit.24424.

[70] C. Lloyd-Griffith, G.P. Duffy, F.J. O'Brien, Investigating the effect of hypoxic culture on the endothelial differentiation of human amniotic fluid-derived stem cells., J. Anat. (2015). doi:10.1111/joa.12283.

[71] H. V Almeida, Y. Liu, G.M. Cunniffe, K.J. Mulhall, A. Matsiko, C.T. Buckley, et al., Controlled release of transforming growth factor-β3 from cartilage-extra-cellular-matrix-derived scaffolds to promote chondrogenesis of human-joint-tissue-derived stem cells., Acta Biomater. 10 (2014) 4400–9. doi:10.1016/j.actbio.2014.05.030.

[72] K. Atesok, M.N. Doral, J. Karlsson, K.A. Egol, L.M. Jazrawi, P.G. Coelho, et al., Multilayer scaffolds in orthopaedic tissue engineering, Knee Surgery, Sport. Traumatol. Arthrosc. (2014). doi:10.1007/s00167-014-3453-z.

[73] A.D. Rouillard, J.W. Holmes, Mechanical boundary conditions bias fibroblast invasion in a collagen-fibrin wound model, Biophys. J. 106 (2014) 932–943. doi:10.1016/j.bpj.2013.12.002.

[74] J. Chen, Z. Liu, M. Chen, H. Zhang, X. Li, Electrospun Gelatin Fibers with a Multiple Release of Antibiotics Accelerate Dermal Regeneration in Infected Deep Burns, Macromol. Biosci. (2016) 1368–1380. doi:10.1002/mabi.201600108.

[75] A. Di Martino, M. Sittinger, M. V. Risbud, Chitosan: A versatile biopolymer for orthopaedic tissue-engineering, Biomaterials. 26 (2005) 5983–5990. doi:10.1016/j.biomaterials.2005.03.016.

[76] D. Algul, H. Sipahi, A. Aydin, F. Kelleci, S. Ozdatli, F.G. Yener, Biocompatibility of biomimetic multilayered alginate–chitosan/β-TCP scaffold for osteochondral tissue, Int. J. Biol. Macromol. 79 (2015) 363–369. doi:10.1016/j.ijbiomac.2015.05.005.

[77] O. Bas, E.M. De-Juan-Pardo, M. Chhaya, F.M. Wunner, J. Jeon, T. Klein, et al., Enhancing structural integrity of hydrogels by using highly organised melt electrospun fibre constructs, Eur. Polym. J. (2015). doi:10.1016/j.eurpolymj.2015.07.034.

[78] S. Donadio, S. Maffioli, P. Monciardini, M. Sosio, D. Jabes, Antibiotic discovery in the twenty-first century: current trends and future perspectives, J. Antibiot. (Tokyo). 63 (2010) 423–430. doi:10.1038/ja.2010.62.

[79] D. Prakash, N. Nawani, M. Prakash, M. Bodas, A. Mandal, M. Khetmalas, et al., Actinomycetes: A repertory of green catalysts with a potential revenue resource, Biomed Res. Int. 2013 (2013).

[80] E. Palazzotto, G. Gallo, G. Renzone, A. Giardina, A. Sutera, J. Silva, et al., TrpM, a Small Protein Modulating Tryptophan Biosynthesis and Morpho-Physiological Differentiation in Streptomyces coelicolor A3 (2), PLoS One. 11 (2016) e0163422.

[81] S.D. Bentley, K.F. Chater, A.-M. Cerdeño-Tárraga, G.L. Challis, N.R. Thomson, K.D. James, et al., Complete genome sequence of the model actinomycete Streptomyces coelicolor A3(2)., Nature. 417 (2002) 141–7. doi:10.1038/417141a.

[82] K.F. Chater, S. Biró, K.J. Lee, T. Palmer, H. Schrempf, The complex extracellular biology of Streptomyces, FEMS Microbiol. Rev. 34 (2010) 171–198.

[83] K.P. Singh, P.P. Wangikar, S. Jadhav, Correlation between pellet morphology and glycopeptide antibiotic balhimycin production by Amycolatopsis balhimycina DSM 5908., J. Ind. Microbiol. Biotechnol. 39 (2012) 27–35. doi:10.1007/s10295-011-0995-7.

[84] D. van Dissel, D. Claessen, G.P. van Wezel, Morphogenesis of Streptomyces in submerged cultures., Adv. Appl. Microbiol. 89 (2014) 1–45. doi:10.1016/B978-0-12-800259-9.00001-9.

[85] M.T. López-Garcìa, B. Rioseras, P. Yagüe, J.R. Álvarez, Á. Manteca, Cell immobilization of Streptomyces coelicolor: effect on differentiation and actinorhodin production, Int. Microbiol. Off. J. Spanish Soc. Microbiol. 17 (2014) 75.

[86] S.S. Yang, C.Y. Yueh, Oxytetracycline production by immobilized Streptomyces rimosus, J. Microbiol. Immunol. Infect. 34 (2001) 235–242. http://www.scopus.com/inward/record.url?eid=2-s2.0-0035682441&partnerID=tZOtx3y1.

[87] H. Zhu, W. Wang, J. Liu, Q. Caiyin, J. Qiao, Immobilization of Streptomyces thermotolerans 11432 on polyurethane foam to improve production of acetylisovaleryltylosin., J. Ind. Microbiol. Biotechnol. 42 (2015) 105–11. doi:10.1007/s10295-014-1545-x.

[88] S. Devi, P. Sridhar, Production of cephamycin C in repeated batch operations from immobilized Streptomyces clavuligerus, Process Biochem. 36 (2000) 225–231.

[89] C.J. Kim, Y.K. Chang, G.-T. Chun, Y.-H. Jeong, S.J. Lee, Continuous culture of immobilized Streptomyces cells for kasugamycin production, Biotechnol. Prog. 17 (2001) 453–461.

[90] I.-C. Kim, C.-H. Kim, S.-I. Hong, S.-W. Kim, Fed-batch cultivation for the production of clavulanic acid by an immobilized Streptomyces clavuligerus mutant, World J. Microbiol. Biotechnol. 17 (2001) 869–872.

[91] S. Anisuddin, N. Al Hashar, S. Tasheen, Prevention of oil spill pollution in seawater using locally available materials, Arab. J. Sci. Eng. 30 (2005) 143–152.

[92] M.A. Hubbe, O.J. Rojas, M. Fingas, B.S. Gupta, Cellulosic substrates for removal of pollutants from aqueous systems: A Review. 3. Spilled oil and emulsified organic liquids, BioResources. 8 (2013) 3038–3097.

[93] N.E. Kinner, L. Belden, P. Kinner, Unexpected sink for Deepwater Horizon oil may influence future spill response, Eos, Trans. Am. Geophys. Union. 95 (2014) 176.

[94] D.P. Prendergast, P.M. Gschwend, Assessing the performance and cost of oil spill remediation technologies, J. Clean. Prod. 78 (2014) 233–242.

[95] A.A. Al-Majed, A.R. Adebayo, M.E. Hossain, A sustainable approach to controlling oil spills, J. Environ. Manage. 113 (2012) 213–227.

[96] A.K. Bledzki, J. Gassan, Composites reinforced with cellulose based fibres, Prog. Polym. Sci. 24 (1999) 221–274. doi:10.1016/S0079-6700(98)00018-5.

[97] H.M. Choi, R.M. Cloud, Natural sorbents in oil spill cleanup, Environ. Sci. Technol. 26 (1992) 772–776. doi:10.1021/es00028a016.

[98] G. Deschamps, H. Caruel, M.E. Borredon, C. Albasi, J.P. Riba, C. Bonnin, et al., Oil Removal from Water by Sorption on Hydrophobic Cotton Fibers. 2. Study of Sorption Properties in Dynamic Mode, Environ. Sci. Technol. 37 (2003) 5034–5039. doi:10.1021/es020249b.

[99] C. Teas, S. Kalligeros, F. Zanikos, S. Stournas, E. Lois, G. Anastopoulos, Investigation of the effectiveness of absorbent materials in oil spills clean up, Desalination. 140 (2001) 259–264. doi:10.1016/S0011-9164(01)00375-7.

[100] T.T. Lim, X. Huang, Evaluation of kapok (Ceiba pentandra (L.) Gaertn.) as a natural hollow hydrophobic-oleophilic fibrous sorbent for oil spill cleanup, Chemosphere. 66 (2007) 955–963. doi:10.1016/j.chemosphere.2006.05.062.

[101] Q.F. Wei, R.R. Mather, A.F. Fotheringham, R.D. Yang, Evaluation of nonwoven polypropylene oil sorbents in marine oil-spill recovery, Mar. Pollut. Bull. 46 (2003) 780–783. doi:10.1016/S0025-326X(03)00042-0.

[102] X.-F. Sun, R. Sun, J.-X. Sun, Acetylation of rice straw with or without catalysts and its characterization as a natural sorbent in oil spill cleanup, J. Agric. Food Chem. 50 (2002) 6428–6433.

[103] M.D. Teli, S.P. Valia, Acetylation of banana fibre to improve oil absorbency, Carbohydr. Polym. 92 (2013) 328–333. doi:10.1016/j.carbpol.2012.09.019.

[104] P. Zhang, R. Tian, R. Lv, B. Na, Q. Liu, Water-permeable polylactide blend membranes for hydrophilicity-based separation, Chem. Eng. J. 269 (2015) 180–185. doi:10.1016/j.cej.2015.01.111.

[105] C.D. Scott, Immobilized cells: a review of recent literature, Enzyme Microb. Technol. 9 (1987) 66–72.

[106] M.B. Cassidy, H. Lee, J.T. Trevors, Environmental applications of immobilized microbial cells: a review, J. Ind. Microbiol. 16 (1996) 79–101.

[107] C. Elliott, Z. Ye, S.C. Mojumdar, M.T. Saleh, A potential bacterial carrier for bioremediation, J. Therm. Anal. Calorim. 90 (2007) 707–711.

[108] Y.-S. Oh, J. Maeng, S.-J. Kim, Use of microorganism-immobilized polyurethane foams to absorb and degrade oil on water surface, Appl. Microbiol. Biotechnol. 54 (2000) 418–423.

[109] M.P. Diaz, K.G. Boyd, S.J.W. Grigson, J.G. Burgess, Biodegradation of crude oil across a wide range of salinities by an extremely halotolerant bacterial consortium MPD-M, immobilized onto polypropylene fibers, Biotechnol. Bioeng. 79 (2002) 145–153.

[110] C.O. Obuekwe, E.M. Al-Muttawa, Self-immobilized bacterial cultures with potential for application as ready-to-use seeds for petroleum bioremediation, Biotechnol. Lett. 23 (2001) 1025–1032.

[111] E. Quek, Y.-P. Ting, H.M. Tan, Rhodococcus sp. F92 immobilized on polyurethane foam shows ability to degrade various petroleum products, Bioresour. Technol. 97 (2006) 32–38.

[112] K.T. O'reilly, R.L. Crawford, Degradation of pentachlorophenol by polyurethane-immobilized Flavobacterium cells., Appl. Environ. Microbiol. 55 (1989) 2113–2118.

[113] J.A. Resnick, Degradation of petroleum hydrocarbons with organisms encapsulated in wax, (1998).

[114] W. Jianlong, Q. Yi, Microbial degradation of 4-chlorophenol by microorganisms entrapped in carrageenan-chitosan gels, Chemosphere. 38 (1999) 3109–3117.

[115] P. Kilonzo, A. Margaritis, M. Bergougnou, Effects of surface treatment and process parameters on immobilization of recombinant yeast cells by adsorption to fibrous matrices, Bioresour. Technol. 102 (2011) 3662–3672. doi:10.1016/j.biortech.2010.11.055.

[116] D. Hou, X. Shen, Q. Luo, Y. He, Q. Wang, Q. Liu, Enhancement of the diesel oil degradation ability of a marine bacterial strain by immobilization on a novel compound carrier material, Mar. Pollut. Bull. 67 (2013) 146–151. doi:10.1016/j.marpolbul.2012.11.021.

[117] R. Scaffaro, F. Lopresti, L. Botta, A. Maio, F. Sutera, M.C. Mistretta, et al., A Facile and Eco-friendly Route to Fabricate Poly(Lactic Acid) Scaffolds with Graded Pore Size, J. Vis. Exp. (2016) 1–8. doi:10.3791/54595.

[118] S.H. Oh, S.G. Kang, E.S. Kim, S.H. Cho, J.H. Lee, Fabrication and characterization of hydrophilic poly (lactic-co-glycolic acid)/poly (vinyl alcohol) blend cell scaffolds by melt-molding particulate-leaching method, Biomaterials. 24 (2003) 4011–4021.

[119] J. Reignier, M.A. Huneault, Preparation of interconnected poly(ε-caprolactone) porous scaffolds by a combination of polymer and salt particulate leaching, Polymer (Guildf). 47 (2006) 4703–4717.

[120] C.-J. Liao, C.-F. Chen, J.-H. Chen, S.-F. Chiang, Y.-J. Lin, K.-Y. Chang, Fabrication of porous biodegradable polymer scaffolds using a solvent merging/particulate leaching method, J. Biomed. Mater. Res. 59 (2002) 676–681.

[121] L. Wu, D. Jing, J. Ding, A "room-temperature" injection molding/particulate leaching approach for fabrication of biodegradable three-dimensional porous scaffolds, Biomaterials. 27 (2006) 185–191.

[122] D. Sin, X. Miao, G. Liu, F. Wei, G. Chadwick, C. Yan, et al., Polyurethane (PU) scaffolds prepared by solvent

casting/particulate leaching (SCPL) combined with centrifugation, Mater. Sci. Eng. C. 30 (2010) 78–85. doi:http://dx.doi.org/10.1016/j.msec.2009.09.002.

[123] Q. Hou, D.W. Grijpma, J. Feijen, Porous polymeric structures for tissue engineering prepared by a coagulation, compression moulding and salt leaching technique, Biomaterials. 24 (2003) 1937–1947. doi:http://dx.doi.org/10.1016/S0142-9612(02)00562-8.

[124] K. Makaya, S. Terada, K. Ohgo, T. Asakura, Comparative study of silk fibroin porous scaffolds derived from salt/water and sucrose/hexafluoroisopropanol in cartilage formation, J. Biosci. Bioeng. 108 (2009) 68–75.

[125] C. Zhang, L. Wang, T. Zhai, X. Wang, Y. Dan, L.-S. Turng, The surface grafting of graphene oxide with poly(ethylene glycol) as a reinforcement for poly(lactic acid) nanocomposite scaffolds for potential tissue engineering applications, J. Mech. Behav. Biomed. Mater. 53 (2016) 403–413. doi:http://dx.doi.org/10.1016/j.jmbbm.2015.08.043.

[126] L.R. Rad, A. Momeni, B.F. Ghazani, M. Irani, M. Mahmoudi, B. Noghreh, Removal of Ni2+ and Cd2+ ions from aqueous solutions using electrospun PVA/zeolite nanofibrous adsorbent, Chem. Eng. J. 256 (2014) 119–127. doi:10.1016/j.cej.2014.06.066.

[127] J. Chen, Z. Liu, M. Chen, H. Zhang, X. Li, Electrospun Gelatin Fibers with a Multiple Release of Antibiotics Accelerate Dermal Regeneration in Infected Deep Burns, Macromol. Biosci. (2016). doi:10.1002/mabi.201600108.

[128] J.H. Wendorff, S. Agarwal, A. Greiner, Nanofiber Properties, in: Electrospinning, 2012: pp. 69–104. doi:10.1002/9783527647705.ch3.

[129] Q. Shi, C. Zhou, Y. Yue, W. Guo, Y. Wu, Q. Wu, Mechanical properties and in vitro degradation of electrospun bio-nanocomposite mats from PLA and cellulose nanocrystals, Carbohydr. Polym. 90 (2012) 301–308. doi:10.1016/j.carbpol.2012.05.042.

[130] Y. Ding, J.A. Roether, A.R. Boccaccini, D.W. Schubert, Fabrication of electrospun poly (3-hydroxybutyrate)/poly (ε-caprolactone)/silica hybrid fibermats with and without calcium addition, Eur. Polym. J. 55 (2014) 222–234. doi:10.1016/j.eurpolymj.2014.03.020.

[131] Y. Yao, H. Wei, J. Wang, H. Lu, J. Leng, D. Hui, Fabrication of hybrid membrane of electrospun polycaprolactone and polyethylene oxide with shape memory property, Compos. Part B Eng. 83 (2015) 264–269. doi:10.1016/j.compositesb.2015.08.060.

[132] S.I. Jeong, S.Y. Kim, S.K. Cho, M.S. Chong, K.S. Kim, H. Kim, et al., Tissue-engineered vascular grafts composed of marine collagen and {PLGA} fibers using pulsatile perfusion bioreactors, Biomaterials. 28 (2007) 1115–1122. doi:http://dx.doi.org/10.1016/j.biomaterials.2006.10.025.

[133] H. Liu, X. Li, G. Zhou, H. Fan, Y. Fan, Electrospun sulfated silk fibroin nanofibrous scaffolds for vascular tissue engineering, Biomaterials. 32 (2011) 3784–3793. doi:http://dx.doi.org/10.1016/j.biomaterials.2011.02.002.

[134] H.G. Sundararaghavan, J. a. Burdick, Gradients with depth in electrospun fibrous scaffolds for directed cell behavior, Biomacromolecules. 12 (2011) 2344–2350. doi:10.1021/bm200415g.

[135] E. Sachlos, D.A. Wahl, J.T. Triffitt, J.T. Czernuszka, The impact of critical point drying with liquid carbon dioxide on collagen-hydroxyapatite composite scaffolds, Acta Biomater. 4 (2008) 1322–1331.

[136] Y. Ikada, Tissue engineering: fundamentals and applications, Academic Press, 2011.

[137] Y.S. Nam, T.G. Park, Porous biodegradable polymeric scaffolds prepared by thermally induced phase separation, J. Biomed. Mater. Res. 47 (1999) 8–17.

[138] F.J. Hua, G.E. Kim, J.D. Lee, Y.K. Son, D.S. Lee, Macroporous poly (L-lactide) scaffold 1. Preparation of a macroporous scaffold by liquid-liquid phase separation of a PLLA-dioxane-water system, J. Biomed. Mater. Res. 63 (2002) 161–167.

[139] G.A. Mannella, G. Conoscenti, F.C. Pavia, V. La Carrubba, V. Brucato, Preparation of polymeric foams with a pore size gradient via Thermally Induced Phase Separation (TIPS), Mater. Lett. 160 (2015) 31–33. doi:10.1016/j.matlet.2015.07.055.

[140] M.G. Haugh, C.M. Murphy, F.J. O'Brien, Novel freeze-drying methods to produce a range of collagen-glycosaminoglycan scaffolds with tailored mean pore sizes., Tissue Eng. Part C. Methods. 16 (2010) 887–94. doi:10.1089/ten.TEC.2009.0422.

[141] F. O'Brien, Influence of freezing rate on pore structure in freeze-dried collagen-GAG scaffolds, Biomaterials. 25 (2004) 1077–1086. doi:10.1016/S0142-9612(03)00630-6.

[142] B.B. Mandal, S.C. Kundu, Osteogenic and adipogenic differentiation of rat bone marrow cells on non-mulberry and

mulberry silk gland fibroin 3D scaffolds, Biomaterials. 30 (2009) 5019–5030.

[143] C. Vepari, D.L. Kaplan, Silk as a biomaterial, Prog. Polym. Sci. 32 (2007) 991–1007.

[144] X. Niu, X. Li, H. Liu, G. Zhou, Q. Feng, F. Cui, et al., Homogeneous chitosan/poly (L-lactide) composite scaffolds prepared by emulsion freeze-drying, J. Biomater. Sci. Polym. Ed. 23 (2012) 391–404.

[145] S. Lee, P. Yuan, M.R. Robinson, Encyclopedia of biomaterials and biomedical engineering, Taylor & Francis, 2004.

[146] A.K.M. Khoda, I.T. Ozbolat, B. Koc, Designing heterogeneous porous tissue scaffolds for additive manufacturing processes, CAD Comput. Aided Des. 45 (2013) 1507–1523. doi:10.1016/j.cad.2013.07.003.

[147] N. Sudarmadji, J.Y. Tan, K.F. Leong, C.K. Chua, Y.T. Loh, Investigation of the mechanical properties and porosity relationships in selective laser-sintered polyhedral for functionally graded scaffolds., Acta Biomater. 7 (2011) 530–7. doi:10.1016/j.actbio.2010.09.024.

[148] J.M. Sobral, S.G. Caridade, R.A. Sousa, J.F. Mano, R.L. Reis, Three-dimensional plotted scaffolds with controlled pore size gradients: Effect of scaffold geometry on mechanical performance and cell seeding efficiency, Acta Biomater. 7 (2011) 1009–1018. doi:10.1016/j.actbio.2010.11.003.

[149] C. Fritzmann, M. Wiese, T. Melin, M. Wessling, Helically microstructured spacers improve mass transfer and fractionation selectivity in ultrafiltration, J. Memb. Sci. 463 (2014) 41–48. doi:10.1016/j.memsci.2014.03.059.

[150] K.F. Leong, C.K. Chua, N. Sudarmadji, W.Y. Yeong, Engineering functionally graded tissue engineering scaffolds, J. Mech. Behav. Biomed. Mater. 1 (2008) 140–152. doi:http://dx.doi.org/10.1016/j.jmbbm.2007.11.002.

[151] M.B. Ghandashtani, F.Z. Ashtiani, M. Karimi, A. Fouladitajar, A novel approach to fabricate high performance nano-SiO 2 embedded PES membranes for microfiltration of oil-in-water emulsion, Appl. Surf. Sci. 349 (2015) 393–402.

[152] F. Zhang, S. Gao, Y. Zhu, J. Jin, Alkaline-induced superhydrophilic/underwater superoleophobic polyacrylonitrile membranes with ultralow oil-adhesion for high-efficient oil/water separation, J. Memb. Sci. 513 (2016) 67–73.

[153] J.-H. Kim, K.-H. Lee, Effect of PEG additive on membrane formation by phase inversion, J. Memb. Sci. 138 (1998) 153–163.

[154] C. Wang, C. Xiao, Q. Huang, J. Pan, A study on structure and properties of poly (p-phenylene terephthamide) hybrid porous membranes, J. Memb. Sci. 474 (2015) 132–139.

[155] Y. Peng, Z. Guo, Recent advances in biomimetic thin membranes applied in emulsified oil/water separation, J. Mater. Chem. A. 4 (2016) 15749–15770.

[156] W. Zhang, Z. Shi, F. Zhang, X. Liu, J. Jin, L. Jiang, Superhydrophobic and superoleophilic PVDF membranes for effective separation of water-in-oil emulsions with high flux, Adv. Mater. 25 (2013) 2071–2076.

[157] A. Seidi, M. Ramalingam, I. Elloumi-Hannachi, S. Ostrovidov, A. Khademhosseini, Gradient biomaterials for soft-to-hard interface tissue engineering, Acta Biomater. 7 (2011) 1441–1451. doi:10.1016/j.actbio.2011.01.011.

[158] C.M. Murphy, M.G. Haugh, F.J. O'Brien, The effect of mean pore size on cell attachment, proliferation and migration in collagen-glycosaminoglycan scaffolds for bone tissue engineering., Biomaterials. 31 (2010) 461–6. doi:10.1016/j.biomaterials.2009.09.063.

[159] C. Jelen, G. Mattei, F. Montemurro, C. De Maria, M. Mattioli-Belmonte, G. Vozzi, Bone scaffolds with homogeneous and discrete gradient mechanical properties., Mater. Sci. Eng. C. Mater. Biol. Appl. 33 (2013) 28–36. doi:10.1016/j.msec.2012.07.046.

[160] B.A. Harley, A.K. Lynn, Z. Wissner-Gross, W. Bonfield, I. V Yannas, L.J. Gibson, Design of a multiphase osteochondral scaffold. II. Fabrication of a mineralized collagen--glycosaminoglycan scaffold, J. Biomed. Mater. Res. Part A. 92 (2010) 1066–1077.

[161] W. Swieszkowski, B.H.S. Tuan, K.J. Kurzydlowski, D.W. Hutmacher, Repair and regeneration of osteochondral defects in the articular joints, Biomol. Eng. 24 (2007) 489–495.

[162] N.E. Fedorovich, W. Schuurman, H.M. Wijnberg, H.-J. Prins, P.R. van Weeren, J. Malda, et al., Biofabrication of osteochondral tissue equivalents by printing topologically defined, cell-laden hydrogel scaffolds., Tissue Eng. Part C. Methods. 18 (2012) 33–44. doi:10.1089/ten.TEC.2011.0060.

[163] C.P. Laurent, D. Durville, D. Mainard, J.F. Ganghoffer, R. Rahouadj, A multilayer braided scaffold for Anterior Cruciate Ligament: Mechanical modeling at the fiber scale, J. Mech. Behav. Biomed. Mater. 12 (2012) 184–196.

doi:10.1016/j.jmbbm.2012.03.005.

[164] M. Lee, B.M. Wu, Recent advances in 3D printing of tissue engineering scaffolds, Methods Mol. Biol. 868 (2012) 257–267. doi:10.1007/978-1-61779-764-4_15.

[165] Y. Luo, A.R. Akkineni, M. Gelinsky, Three-dimensional plotting is a versatile rapid prototyping method for the customized manufacturing of complex scaffolds and tissue engineering constructs., Zhongguo Xiu Fu Chong Jian Wai Ke Za Zhi. 28 (2014) 279–85. doi:10.7507/1002-1892.20140064.

[166] J.-H. Shim, J.-S. Lee, J.Y. Kim, D.-W. Cho, Bioprinting of a mechanically enhanced three-dimensional dual cell-laden construct for osteochondral tissue engineering using a multi-head tissue/organ building system, J. Micromechanics Microengineering. 22 (2012) 85014. doi:10.1088/0960-1317/22/8/085014.

[167] R. Scaffaro, F. Lopresti, L. Botta, A. Maio, Mechanical behavior of Polylactic acid/Polycaprolactone porous layered functional composites, Compos. Part B Eng. 98 (2016) 70–77. doi:10.1016/j.compositesb.2016.05.023.

[168] X. Wang, E. Wenk, X. Zhang, L. Meinel, G. Vunjak-novakovic, D.L. Kaplan, Growth factor gradients via microsphere delivery in biopolymer scaffolds for osteochondral tissue engineering, J. Control. Release. 134 (2009) 81–90. doi:10.1016/j.jconrel.2008.10.021.

[169] H. Bai, X. Zan, J. Juay, D.D. Sun, Hierarchical heteroarchitectures functionalized membrane for high efficient water purification, J. Memb. Sci. 475 (2015) 245–251. doi:10.1016/j.memsci.2014.10.036.

[170] B.A. Harley, A.K. Lynn, Z. Wissner-Gross, W. Bonfield, I. V Yannas, L.J. Gibson, Design of a multiphase osteochondral scaffold III: Fabrication of layered scaffolds with continuous interfaces, J. Biomed. Mater. Res. Part A. 92 (2010) 1078–1093.

[171] B.M. Bailey, L.N. Nail, M.A. Grunlan, Acta Biomaterialia Continuous gradient scaffolds for rapid screening of cell – material interactions and interfacial tissue regeneration, Acta Biomater. 9 (2013) 8254–8261. doi:10.1016/j.actbio.2013.05.012.

[172] Y. Qi, Y. Du, W. Li, X. Dai, T. Zhao, W. Yan, Cartilage repair using mesenchymal stem cell (MSC) sheet and MSCs-loaded bilayer PLGA scaffold in a rabbit model, Knee Surgery, Sport. Traumatol. Arthrosc. 22 (2014) 1424–1433. doi:10.1007/s00167-012-2256-3.

[173] P. Duan, Z. Pan, L. Cao, Y. He, H. Wang, Z. Qu, et al., The effects of pore size in bilayered poly(lactide-co-glycolide) scaffolds on restoring osteochondral defects in rabbits, J. Biomed. Mater. Res. - Part A. 102 (2014) 180–192. doi:10.1002/jbm.a.34683.

[174] G. Chen, T. Sato, J. Tanaka, T. Tateishi, Preparation of a biphasic scaffold for osteochondral tissue engineering, Mater. Sci. Eng. C. 26 (2006) 118–123. doi:10.1016/j.msec.2005.07.024.

[175] P. Giannoni, E. Lazzarini, L. Ceseracciu, A.C. Barone, R. Quarto, S. Scaglione, Design and characterization of a tissue-engineered bilayer scaffold for osteochondral tissue repair, J. Tissue Eng. Regen. Med. 9 (2015) 1182–1192.

[176] D. Algul, H. Sipahi, A. Aydin, F. Kelleci, S. Ozdatli, F.G. Yener, Biocompatibility of biomimetic multilayered alginate–chitosan/β-TCP scaffold for osteochondral tissue, Int. J. Biol. Macromol. 79 (2015) 363–369. doi:10.1016/j.ijbiomac.2015.05.005.

[177] J. Song, H. Gao, G. Zhu, X. Cao, X. Shi, Y. Wang, The preparation and characterization of polycaprolactone/graphene oxide biocomposite nanofiber scaffolds and their application for directing cell behaviors, Carbon N. Y. 95 (2015) 1039–1050. doi:10.1016/j.carbon.2015.09.011.

[178] A.J. Bauer, Y. Wu, B. Li, Electrospun Poly (ε-caprolactone)/Polyhedral Oligomeric Silsesquioxane-Based Copolymer Blends: Evolution of Fiber Internal Structures., Macromol. Biosci. (2016).

[179] F.M. Ghorbani, B. Kaffashi, P. Shokrollahi, E. Seyedjafari, A. Ardeshirylajimi, PCL/chitosan/Zn-doped nHA electrospun nanocomposite scaffold promotes adipose derived stem cells adhesion and proliferation., Carbohydr. Polym. 118 (2015) 133–42. doi:10.1016/j.carbpol.2014.10.071.

[180] G.-Y. Liao, X.-P. Zhou, L. Chen, X.-Y. Zeng, X.-L. Xie, Y.-W. Mai, Electrospun aligned PLLA/PCL/functionalised multiwalled carbon nanotube composite fibrous membranes and their bio/mechanical properties, Compos. Sci. Technol. 72 (2012) 248–255. doi:10.1016/j.compscitech.2011.11.009.

[181] W. Zhu, F. Masood, J. O'Brien, L.G. Zhang, Highly aligned nanocomposite scaffolds by electrospinning and electrospraying

for neural tissue regeneration, Nanomedicine Nanotechnology, Biol. Med. 11 (2015) 693–704.

[182] G. Nitya, G.T. Nair, U. Mony, K.P. Chennazhi, S. V Nair, In vitro evaluation of electrospun PCL/nanoclay composite scaffold for bone tissue engineering, J. Mater. Sci. Mater. Med. 23 (2012) 1749–1761.

[183] R. Asmatulu, S. Patrick, M. Ceylan, I. Ahmed, S.-Y. Yang, N. Nuraje, Antibacterial Polycaprolactone/Natural Hydroxyapatite Nanocomposite Fibers for Bone Scaffoldings, J. Bionanoscience. 9 (2015) 120–126.

[184] C. Zhang, L. Wang, T. Zhai, X. Wang, Y. Dan, L.-S. Turng, The surface grafting of graphene oxide with poly(ethylene glycol) as a reinforcement for poly(lactic acid) nanocomposite scaffolds for potential tissue engineering applications, J. Mech. Behav. Biomed. Mater. 53 (2016) 403–413. doi:10.1016/j.jmbbm.2015.08.043.

[185] A. Maio, R. Fucarino, R. Khatibi, S. Rosselli, M. Bruno, R. Scaffaro, A novel approach to prevent graphene oxide re-aggregation during the melt compounding with polymers, Compos. Sci. Technol. 119 (2015) 131–137. doi:http://dx.doi.org/10.1016/j.compscitech.2015.10.006.

[186] R. Scaffaro, A. Maio, F. Lopresti, D. Giallombardo, L. Botta, M.L. Bondì, et al., Synthesis and self-assembly of a PEGylated-graphene aerogel, Compos. Sci. Technol. 128 (2016) 193–200. doi:10.1016/j.compscitech.2016.03.030.

[187] M. Antunes, G. Gedler, H. Abbasi, J.I. Velasco, Graphene Nanoplatelets as a Multifunctional Filler for Polymer Foams, Mater. Today Proc. 3 (2016) S233–S239. doi:10.1016/j.matpr.2016.02.039.

[188] K.S. Novoselov, A.K. Geim, S. V Morozov, D. Jiang, Y. Zhang, S. V Dubonos, et al., Electric field effect in atomically thin carbon films, Science (80-.). 306 (2004) 666–669.

[189] C. Lee, X. Wei, J.W. Kysar, J. Hone, Measurement of the elastic properties and intrinsic strength of monolayer graphene, Science (80-.). 321 (2008) 385–388.

[190] A. Maio, D. Giallombardo, R. Scaffaro, A.P. Piccionello, I. Pibiri, Synthesis of a fluorinated graphene oxide-silica nanohybrid: improving oxygen affinity, RSC Adv. 6 (2016) 46037–46047. doi:10.1039/C6RA02585D.

[191] A. Maio, S. Agnello, R. Khatibi, L. Botta, A. Alessi, A. Piazza, et al., A rapid and eco-friendly route to synthesize graphene-doped silica nanohybrids, J. Alloys Compd. 664 (2016) 428–438.

[192] G. Gedler, M. Antunes, J.I. Velasco, Viscoelastic properties of polycarbonate-graphene nanoplatelets nanocomposite foams, Compos. Part B Eng. 93 (2016) 143–152. doi:10.1016/j.compositesb.2016.03.032.

[193] H. Shin, S. Jo, A.G. Mikos, Biomimetic materials for tissue engineering, Biomaterials. 24 (2003) 4353–4364.

[194] P. Balasubramanian, J.A. Roether, D.W. Schubert, J.P. Beier, A.R. Boccaccini, Bi-layered porous constructs of PCL-coated 45S5 bioactive glass and electrospun collagen-PCL fibers, J. Porous Mater. 22 (2015) 1215–1226. doi:10.1007/s10934-015-9998-5.

[195] Y.-P. Jiao, F.-Z. Cui, Surface modification of polyester biomaterials for tissue engineering, Biomed. Mater. 2 (2007) R24.

[196] Y. Cao, W. Liu, G. Zhou, L. Cui, Tissue engineering and tissue repair in immunocompetent animals: tissue construction and repair, Handchirurgie{·} Mikrochirurgie{·} Plast. Chir. 39 (2007) 156–160.

[197] M.S.K. Chong, C.N. Lee, S.H. Teoh, Characterization of smooth muscle cells on poly (-caprolactone) films, Mater. Sci. Eng. C. 27 (2007) 309–312.

[198] C.S.N. Choong, D.W. Hutmacher, J.T. Triffitt, Co-culture of bone marrow fibroblasts and endothelial cells on modified polycaprolactone substrates for enhanced potentials in bone tissue engineering, Tissue Eng. 12 (2006) 2521–2531.

[199] Q. Zhu, Q. Pan, F. Liu, Facile removal and collection of oils from water surfaces through superhydrophobic and superoleophilic sponges, J. Phys. Chem. C. 115 (2011) 17464–17470.

[200] D.D. Nguyen, N.-H. Tai, S.-B. Lee, W.-S. Kuo, Superhydrophobic and superoleophilic properties of graphene-based sponges fabricated using a facile dip coating method, Energy Environ. Sci. 5 (2012) 7908–7912.

[201] X. Zhou, Z. Zhang, X. Xu, X. Men, X. Zhu, Facile fabrication of superhydrophobic sponge with selective absorption and collection of oil from water, Ind. Eng. Chem. Res. 52 (2013) 9411–9416.

[202] Y. Liu, J. Ma, T. Wu, X. Wang, G. Huang, Y. Liu, et al., Cost-effective reduced graphene oxide-coated polyurethane sponge as a highly efficient and reusable oil-absorbent, ACS Appl. Mater. Interfaces. 5 (2013) 10018–10026.

[203] Q. Zhu, Y. Chu, Z. Wang, N. Chen, L. Lin, F. Liu, et al., Robust superhydrophobic polyurethane sponge as a highly reusable oil-absorption material, J. Mater. Chem. A. 1 (2013) 5386–5393.

[204] N. Chen, Q. Pan, Versatile fabrication of ultralight magnetic foams and application for oil--water separation, ACS Nano. 7

(2013) 6875–6883.

[205] H. Sun, A. Li, Z. Zhu, W. Liang, X. Zhao, P. La, et al., Superhydrophobic Activated Carbon-Coated Sponges for Separation and Absorption, ChemSusChem. 6 (2013) 1057–1062.

[206] C.-F. Wang, S.-J. Lin, Robust superhydrophobic/superoleophilic sponge for effective continuous absorption and expulsion of oil pollutants from water, ACS Appl. Mater. Interfaces. 5 (2013) 8861–8864.

[207] S.M. Desai, R.P. Singh, Surface modification of polyethylene, in: Long Term Prop. Polyolefins, Springer, 2004: pp. 231–294.

[208] S.D. Perincek, K. Duran, A.E. Koerlue, M.I. Bahtiyari, Ultraviolet technology, Tekst. ve Konfeksiyon. 17 (2007) 219–223.

[209] J. Guan, C. Gao, L. Feng, J. Shen, Surface modification of polyurethane for promotion of cell adhesion and growth 1: Surface photo-grafting with N, N-dimethylaminoethyl methacrylate and cytocompatibility of the modified surface, J. Mater. Sci. Mater. Med. 12 (2001) 447–452.

[210] M.J. Walzak, S. Flynn, R. Foerch, J.M. Hill, E. Karbashewski, A. Lin, et al., UV and ozone treatment of polypropylene and poly (ethylene terephthalate), J. Adhes. Sci. Technol. 9 (1995) 1229–1248.

[211] I. Mathieson, R.H. Bradley, Improved adhesion to polymers by UV/ozone surface oxidation, Int. J. Adhes. Adhes. 16 (1996) 29–31.

[212] M.R. Davidson, S.A. Mitchell, R.H. Bradley, Surface studies of low molecular weight photolysis products from UV-ozone oxidised polystyrene, Surf. Sci. 581 (2005) 169–177.

[213] T. Jacobs, R. Morent, N. De Geyter, P. Dubruel, C. Leys, Plasma surface modification of biomedical polymers: influence on cell-material interaction, Plasma Chem. Plasma Process. 32 (2012) 1039–1073.

[214] B. Singh, N. Sharma, Mechanistic implications of plastic degradation, Polym. Degrad. Stab. 93 (2008) 561–584.

[215] K. Kato, E. Uchida, E.-T. Kang, Y. Uyama, Y. Ikada, Polymer surface with graft chains, Prog. Polym. Sci. 28 (2003) 209–259.

[216] J. Deng, L. Wang, L. Liu, W. Yang, Developments and new applications of UV-induced surface graft polymerizations, Prog. Polym. Sci. 34 (2009) 156–193.

[217] H.-Y. Yu, J.-M. He, L.-Q. Liu, X.-C. He, J.-S. Gu, X.-W. Wei, Photoinduced graft polymerization to improve antifouling characteristics of an SMBR, J. Memb. Sci. 302 (2007) 235–242.

[218] R.L. Clough, High-energy radiation and polymers: a review of commercial processes and emerging applications, Nucl. Instruments Methods Phys. Res. Sect. B Beam Interact. with Mater. Atoms. 185 (2001) 8–33.

[219] A. Södergård, Perspectives on modification of aliphatic polyesters by radiation processing, J. Bioact. Compat. Polym. 19 (2004) 511–525.

[220] U. Edlund, M. Källrot, A.-C. Albertsson, Single-step covalent functionalization of polylactide surfaces, J. Am. Chem. Soc. 127 (2005) 8865–8871.

[221] M.C. Gupta, V.G. Deshmukh, Radiation effects on poly (lactic acid), Polymer (Guildf). 24 (1983) 827–830.

[222] S.C.J. Loo, C.P. Ooi, Y.C.F. Boey, Radiation effects on poly (lactide-co-glycolide)(PLGA) and poly (L-lactide)(PLLA), Polym. Degrad. Stab. 83 (2004) 259–265.

[223] I. Djordjevic, L.G. Britcher, S. Kumar, Morphological and surface compositional changes in poly (lactide-co-glycolide) tissue engineering scaffolds upon radio frequency glow discharge plasma treatment, Appl. Surf. Sci. 254 (2008) 1929–1935.

[224] S.-D. Lee, G.-H. Hsiue, C.-Y. Kao, P.C.-T. Chang, Artificial cornea: surface modification of silicone rubber membrane by graft polymerization of pHEMA via glow discharge, Biomaterials. 17 (1996) 587–595.

[225] G.H. Ryu, W.-S. Yang, H.-W. Roh, I.-S. Lee, J.K. Kim, G.H. Lee, et al., Plasma surface modification of poly (D, L-lactic-co-glycolic acid)(65/35) film for tissue engineering, Surf. Coatings Technol. 193 (2005) 60–64.

[226] E. Stoffels, I.E. Kieft, R.E.J. Sladek, Superficial treatment of mammalian cells using plasma needle, J. Phys. D. Appl. Phys. 36 (2003) 2908.

[227] M. Araya, T. Yuji, T. Watanabe, J. Kashihara, Y. Sumida, Application to cleaning of waste plastic surfaces using atmospheric non-thermal plasma jets, Thin Solid Films. 515 (2007) 4301–4307.

[228] E. Ranucci, P. Ferruti, a New Synthetic Method for Amino-Terminated Poly(Ethyleneglycol) Derivatives, Synth. Commun. 20 (1990) 2951–2957. doi:10.1080/00397919008051511.

[229] T. Kieser, Practical streptomyces genetics, John Innes Foundation, 2000.

[230] P. Quatrini, G. Scaglione, C. De Pasquale, S. Riela, A.M. Puglia, Isolation of Gram-positive n-alkane degraders from a hydrocarbon-contaminated Mediterranean shoreline, J. Appl. Microbiol. 104 (2008) 251–259.

[231] W.-R. Abraham, H. Meyer, M. Yakimov, Novel glycine containing glucolipids from the alkane using bacterium Alcanivorax borkumensis, Biochim. Biophys. Acta - Lipids Lipid Metab. 1393 (1998) 57–62. doi:http://dx.doi.org/10.1016/S0005-2760(98)00058-7.

[232] R.K. Roy, A primer on the Taguchi method, Society of Manufacturing Engineers, 2010.

[233] A. Awada, B. Wegmann, I. Viering, A. Klein, Optimizing the Radio Network Parameters of the Long Term Evolution System Using Taguchi ' s Method, 60 (2011) 3825–3839.

[234] P.J.P.J. Ross, Taguchi techniques for quality engineering: loss function, orthogonal experiments, parameter and tolerance design, 1996.

[235] B.M. Gopalsamy, B. Mondal, S. Ghosh, Taguchi method and anova: An approach for process parameters optimization of hard machining while machining hardened steel, J. Sci. Ind. Res. (India). 68 (2009) 686–695.

[236] Y. Hu, D.W. Grainger, S.R. Winn, J.O. Hollinger, Fabrication of poly ($α$-hydroxy acid) foam scaffolds using multiple solvent systems, J. Biomed. Mater. Res. 59 (2002) 563–572.

[237] F.A. Maspero, K. Ruffieux, B. Müller, E. Wintermantel, Resorbable defect analog PLGA scaffolds using CO2 as solvent: structural characterization, J. Biomed. Mater. Res. 62 (2002) 89–98.

[238] S.T. Ho, D.W. Hutmacher, A comparison of micro CT with other techniques used in the characterization of scaffolds, Biomaterials. 27 (2006) 1362–1376.

[239] R. Nazarov, H.-J. Jin, D.L. Kaplan, Porous 3-D scaffolds from regenerated silk fibroin, Biomacromolecules. 5 (2004) 718–726.

[240] G. Bodner, P. Scholl, H.-P. Kaul, Field quantification of wetting--drying cycles to predict temporal changes of soil pore size distribution, Soil Tillage Res. 133 (2013) 1–9.

[241] H.J. Vogel, A. Kretzschmar, Topological characterization of pore space in soil—sample preparation and digital image-processing, Geoderma. 73 (1996) 23–38.

[242] E.N. Codaro, R.Z. Nakazato, A.L. Horovistiz, L.M.F. Ribeiro, R.B. Ribeiro, L.R. de O. Hein, An image processing method for morphology characterization and pitting corrosion evaluation, Mater. Sci. Eng. A. 334 (2002) 298–306.

[243] H. Khayyeri, S. Checa, M. Tägil, F.J. O'Brien, P.J. Prendergast, Tissue differentiation in an in vivo bioreactor: in silico investigations of scaffold stiffness., J. Mater. Sci. Mater. Med. 21 (2010) 2331–2336. http://www.scopus.com/inward/record.url?eid=2-s2.0-79952112305&partnerID=tZOtx3y1.

[244] A.A. Al-Munajjed, N.A. Plunkett, J.P. Gleeson, T. Weber, C. Jungreuthmayer, T. Levingstone, et al., Development of a biomimetic collagen-hydroxyapatite scaffold for bone tissue engineering using a SBF immersion technique., J. Biomed. Mater. Res. B. Appl. Biomater. 90 (2009) 584–91. doi:10.1002/jbm.b.31320.

[245] N.A. Hotaling, K. Bharti, H. Kriel, C.G. Simon, DiameterJ: A validated open source nanofiber diameter measurement tool., Biomaterials. 61 (2015) 327–38. doi:10.1016/j.biomaterials.2015.05.015.

[246] D. Dollimore, G.R. Heal, Pore size distribution in a system considered as an ordered packing of spherical particles, J. Colloid Interface Sci. 42 (1973) 233–249.

[247] H. Kweon, M.K. Yoo, I.K. Park, T.H. Kim, H.C. Lee, H.S. Lee, et al., A novel degradable polycaprolactone networks for tissue engineering, Biomaterials. 24 (2003) 801–808. doi:10.1016/S0142-9612(02)00370-8.

[248] J.H. Clint, Adhesion and components of solid surface energies, Curr. Opin. Colloid Interface Sci. 6 (2001) 28–33. doi:10.1016/S1359-0294(00)00084-4.

[249] A.M. Puglia, J. Vohradsky, C.J. Thompson, Developmental control of the heat-shock stress regulon in Streptomyces coelicolor, Mol. Microbiol. 17 (1995) 737–746. doi:10.1111/j.1365-2958.1995.mmi_17040737.x.

[250] M.M. Bradford, A rapid and sensitive method for the quantitation of microgram quantities of protein utilizing the principle of protein-dye binding, Anal. Biochem. 72 (1976) 248–254. doi:10.1016/0003-2697(76)90527-3.

[251] W.K. Pratt, Image enhancement, Digit. Image Process. PIKS Sci. Insid. Fourth Ed. (2001) 247–305.

[252] R.C. Gonzalez, R.E. Woods, S.L. Eddins, Digital Image Data Processing Using Matlab, (2004).

[253] R. Scaffaro, F. Lopresti, A. Maio, F. Sutera, L. Botta, Development of polymeric functionally graded scaffold: a brief review, J. Appl. Biomater. Funct. Mater. In Press (2016). doi:10.5301/jabfm.5000252.

[254] W.T. Su, Y.T. Wang, C.M. Chou, Optimal fluid flow enhanced mineralization of MG-63 cells in porous chitosan scaffold, J. Taiwan Inst. Chem. Eng. 45 (2014) 1111–1118. doi:10.1016/j.jtice.2013.10.016.

[255] J.T. Podichetty, S. V Madihally, Modeling of porous scaffold deformation induced by medium perfusion, J. Biomed. Mater. Res. Part B Appl. Biomater. 102 (2014) 737–748.

[256] S.M. Giannitelli, F. Basoli, P. Mozetic, P. Piva, F.N. Bartuli, F. Luciani, et al., Graded porous polyurethane foam: A potential scaffold for oro-maxillary bone regeneration, Mater. Sci. Eng. C. 51 (2015) 329–335. doi:10.1016/j.msec.2015.03.002.

[257] R. Scaffaro, G. Lo Re, S. Rigogliuso, G. Ghersi, 3D polylactide-based scaffolds for studying human hepatocarcinoma processes in vitro, Sci. Technol. Adv. Mater. 13 (2012) 45003. doi:10.1088/1468-6996/13/4/045003.

[258] T. Serra, M. Ortiz-Hernandez, E. Engel, J.A. Planell, M. Navarro, Relevance of PEG in PLA-based blends for tissue engineering 3D-printed scaffolds, Mater. Sci. Eng. C. 38 (2014) 55–62.

[259] M. Fan, G. Guo, S. Shi, X. Wang, S. Fu, X. Li, et al., Preparation and Characterization of Porous Scaffold Based on Poly (Lactic Acid) and Poly (Ethylene Glycol) by Phase Separation Method, Adv. Sci. Lett. 11 (2012) 80–85.

[260] X. Gong, C.Y. Tang, Y. Zhang, C.T. Wong, S. Wu, J. Liu, Fabrication of graded macroporous poly (lactic acid) scaffold by a progressive solvent casting/porogen leaching approach, J. Appl. Polym. Sci. 125 (2012) 571–577.

[261] C. Bordes, V. Fréville, E. Ruffin, P. Marote, J.Y. Gauvrit, S. Briançon, et al., Determination of poly(ε-caprolactone) solubility parameters: Application to solvent substitution in a microencapsulation process, Int. J. Pharm. 383 (2010) 236–243. doi:10.1016/j.ijpharm.2009.09.023.

[262] V.M. Correlo, L.F. Boesel, E. Pinho, A.R. Costa-Pinto, M.L. Alves da Silva, M. Bhattacharya, et al., Melt-based compression-molded scaffolds from chitosan-polyester blends and composites: Morphology and mechanical properties., J. Biomed. Mater. Res. A. 91 (2009) 489–504. doi:10.1002/jbm.a.32221.

[263] J.-E. Park, M. Todo, Development and characterization of reinforced poly(L-lactide) scaffolds for bone tissue engineering., J. Mater. Sci. Mater. Med. 22 (2011) 1171–1182. doi:10.1007/s10856-011-4289-4.

[264] R.M. Allaf, I. V. Rivero, N. Abidi, I.N. Ivanov, Porous poly(ε-caprolactone) scaffolds for load-bearing tissue regeneration: Solventless fabrication and characterization, J. Biomed. Mater. Res. - Part B Appl. Biomater. 101 B (2013) 1050–1060. doi:10.1002/jbm.b.32915.

[265] T.J. Levingstone, A. Matsiko, G.R. Dickson, F.J. O'Brien, J.P. Gleeson, A biomimetic multi-layered collagen-based scaffold for osteochondral repair, Acta Biomater. 10 (2014) 1996–2004. doi:10.1016/j.actbio.2014.01.005.

[266] C.M. Murphy, A. Schindeler, J.P. Gleeson, N.Y.C. Yu, L.C. Cantrill, K. Mikulec, et al., A collagen-hydroxyapatite scaffold allows for binding and co-delivery of recombinant bone morphogenetic proteins and bisphosphonates., Acta Biomater. 10 (2014) 2250–8. doi:10.1016/j.actbio.2014.01.016.

[267] C.M. Murphy, A. Matsiko, M.G. Haugh, J.P. Gleeson, F.J. O'Brien, Mesenchymal stem cell fate is regulated by the composition and mechanical properties of collagen-glycosaminoglycan scaffolds., J. Mech. Behav. Biomed. Mater. 11 (2012) 53–62. doi:10.1016/j.jmbbm.2011.11.009.

[268] E. Fournier, C. Passirani, C.N. Montero-Menei, J.P. Benoit, Biocompatibility of implantable synthetic polymeric drug carriers: focus on brain biocompatibility, Biomaterials. 24 (2003) 3311–3331. doi:10.1016/S0142-9612(03)00161-3.

[269] H. Chen, L. Yuan, W. Song, Z. Wu, D. Li, Biocompatible polymer materials: Role of protein–surface interactions, Prog. Polym. Sci. 33 (2008) 1059–1087. doi:10.1016/j.progpolymsci.2008.07.006.

[270] E. Tziampazis, J. Kohn, P. V. Moghe, PEG-variant biomaterials as selectively adhesive protein templates: model surfaces for controlled cell adhesion and migration, Biomaterials. 21 (2000) 511–520. doi:10.1016/S0142-9612(99)00212-4.

[271] I. Batalov, A.W. Feinberg, Differentiation of cardiomyocytes from human pluripotent stem cells using monolayer culture, Biomark. Insights. 10 (2015) 71–76. doi:10.4137/BMIMI.S20050.

[272] B. Şengül, N. Dilsiz, Barrier properties of polylactic acid/layered silicate nanocomposites for food contact applications, Polym. Sci. Ser. A. 56 (2014) 896–906. doi:10.1134/S0965545X14060194.

[273] C.M. Murphy, M.G. Haugh, F.J. O'Brien, The effect of mean pore size on cell attachment, proliferation and migration in collagen-glycosaminoglycan scaffolds for bone tissue engineering., Biomaterials. 31 (2010) 461–6.

doi:10.1016/j.biomaterials.2009.09.063.

[274] A. Matsiko, J.P. Gleeson, F.J. O'Brien, Scaffold mean pore size influences mesenchymal stem cell chondrogenic differentiation and matrix deposition., Tissue Eng. Part A. 21 (2015) 486–97. doi:10.1089/ten.TEA.2013.0545.

[275] S.M. Lien, L.Y. Ko, T.J. Huang, Effect of pore size on ECM secretion and cell growth in gelatin scaffold for articular cartilage tissue engineering, Acta Biomater. 5 (2009) 670–679. doi:10.1016/j.actbio.2008.09.020.

[276] D.W. Hutmacher, Scaffolds in tissue engineering bone and cartilage, Biomaterials. 21 (2000) 2529–2543. doi:10.1016/S0142-9612(00)00121-6.

[277] P. Nooeaid, V. Salih, J.P. Beier, A.R. Boccaccini, Osteochondral tissue engineering: Scaffolds, stem cells and applications, J. Cell. Mol. Med. 16 (2012) 2247–2270. doi:10.1111/j.1582-4934.2012.01571.x.

[278] D. Wu, D. Lin, J. Zhang, W. Zhou, M. Zhang, Y. Zhang, et al., Selective Localization of Nanofillers: Effect on Morphology and Crystallization of PLA/PCL Blends, Macromol. Chem. Phys. 212 (2011) 613–626. doi:10.1002/macp.201000579.

[279] A.B. Yeatts, J.P. Fisher, Bone tissue engineering bioreactors: dynamic culture and the influence of shear stress, Bone. 48 (2011) 171–181.

[280] L. Botta, F.P. La Mantia, N.T. Dintcheva, R. Scaffaro, Rheological response of polyethylene/clay nanocomposites to annealing treatment, Macromol. Chem. Phys. 208 (2007) 2533–2541. doi:10.1002/macp.200700241.

[281] X. Chen, J. Gug, M.J. Sobkowicz, Role of polymer/filler interactions in the linear viscoelasticity of poly(butylene succinate)/fumed silica nanocomposite, Compos. Sci. Technol. 95 (2014) 8–15. doi:http://dx.doi.org/10.1016/j.compscitech.2014.01.025.

[282] X. Du, X. Xu, X. Liu, J. Yang, Y. Wang, X. Gao, Graphene oxide induced crystallization and hydrolytic degradation of poly (butylene succinate), Polym. Degrad. Stab. 123 (2016) 94–104.

[283] R. Scaffaro, A. Maio, A green method to prepare nanosilica modified graphene oxide to inhibit nanoparticles re-aggregation during melt processing, Chem. Eng. J. 308 (2017) 1034–1047. doi:http://dx.doi.org/10.1016/j.cej.2016.09.131.

[284] E. Zhuravlev, A. Wurm, P. Pötschke, R. Androsch, J.W.P. Schmelzer, C. Schick, Kinetics of nucleation and crystallization of poly(ε-caprolactone) - Multiwalled carbon nanotube composites, Eur. Polym. J. 52 (2014) 1–11. doi:10.1016/j.eurpolymj.2013.12.015.

[285] C. Guo, L. Zhou, J. Lv, Effects of expandable graphite and modified ammonium polyphosphate on the flame-retardant and mechanical properties of wood flour-polypropylene composites, Polym. Polym. Compos. 21 (2013) 449–456. doi:10.1002/app.

[286] S.J. Hitchcock, N.T. Carroll, M.G. Nicholas, Some effects of substrate roughness on wettability, J. Mater. Sci. 16 (1981) 714–732.

[287] C. Wang, X. He, Polypropylene surface modification model in atmospheric pressure dielectric barrier discharge, Surf. Coatings Technol. 201 (2006) 3377–3384. doi:http://dx.doi.org/10.1016/j.surfcoat.2006.07.205.

[288] M.A. Samaha, H.V. Tafreshi, M. Gad-el-Hak, Superhydrophobic surfaces: From the lotus leaf to the submarine, Comptes Rendus - Mec. 340 (2012) 18–34. doi:10.1016/j.crme.2011.11.002.

[289] A.L. Demain, Pharmaceutically active secondary metabolites of microorganisms, Appl. Microbiol. Biotechnol. 52 (1999) 455–463. doi:10.1007/s002530051546.

[290] E.R. Angert, Alternatives to binary fission in bacteria, Nat. Rev. Microbiol. 3 (2005) 214–224. doi:10.1038/nrmicro1096.

[291] G. Gallo, G. Renzone, E. Palazzotto, P. Monciardini, S. Arena, T. Faddetta, et al., Elucidating the molecular physiology of lantibiotic NAI-107 production in Microbispora ATCC-PTA-5024, BMC Genomics. 17 (2016) 1.

[292] T.C. Cheam, S. Krimm, Infrared intensities of amide modes in N-methylacetamide and poly(glycine I) from abinitio calculations of dipole moment derivatives of N-methylacetamide, J. Chem. Phys. 82 (1985) 1631–1641.

[293] D.C. Marcano, D.V. Kosynkin, J.M. Berlin, A. Sinitskii, Z.Z. Sun, A. Slesarev, et al., Improved Synthesis of Graphene Oxide, ACS Nano. 4 (2010) 4806–4814. doi:10.1021/nn1006368.

[294] X. Diez-Betriu, S. Álvarez-Garcia, C. Botas, P. Álvarez, J. Sánchez-Marcos, C. Prieto, et al., Raman spectroscopy for the study of reduction mechanisms and optimization of conductivity in graphene oxide thin films, J. Mater. Chem. C. 1 (2013) 6905–6912.

[295] W. Sun, Q. Zhao, M. Zhao, B. Yang, C. Cui, J. Ren, Structural evaluation of myofibrillar proteins during processing of

Cantonese sausage by Raman spectroscopy, J. Agric. Food Chem. 59 (2011) 11070–11077.

[296] H. Hu, Z. Zhao, W. Wan, Y. Gogotsi, J. Qiu, Ultralight and highly compressible graphene aerogels, Adv. Mater. 25 (2013) 2219–2223.

[297] Z. Xu, Y. Zhang, P. Li, C. Gao, Strong, conductive, lightweight, neat graphene aerogel fibers with aligned pores, ACS Nano. 6 (2012) 7103–7113. doi:10.1021/nn3021772.

[298] Y. Wu, N. Yi, L. Huang, T. Zhang, S. Fang, H. Chang, et al., Three-dimensionally bonded spongy graphene material with super compressive elasticity and near-zero Poisson's ratio, Nat. Commun. 6 (2015).

[299] M.C. Morán, T. Tozar, A. Simon, A. Dinache, A. Smarandache, I.R. Andrei, et al., Toxicity study in blood and tumor cells of laser produced medicines for application in fabrics, Colloids Surfaces B Biointerfaces. 137 (2016) 91–103.

[300] K.-H. Liao, Y.-S. Lin, C.W. Macosko, C.L. Haynes, Cytotoxicity of graphene oxide and graphene in human erythrocytes and skin fibroblasts, ACS Appl. Mater. Interfaces. 3 (2011) 2607–2615.

Pubblications

1. Lo Re, G., **Lopresti, F.**, Petrucci, G. & Scaffaro, R. A facile method to determine pore size distribution in porous scaffold by using image processing. *Micron* 76, 37–45 (2015).

2. Scaffaro, R., **Lopresti, F.**, Botta, L., Rigogliuso, S. & Ghersi, G. Integration of PCL and PLA in a monolithic porous scaffold for interface tissue engineering. *J. Mech. Behav. Biomed. Mater.* **63,** 303–313 (2016).

3. Scaffaro, R., **Lopresti, F.**, Botta, L., Rigogliuso, S. & Ghersi, G. Preparation of three-layered porous PLA / PEG scaffold : relationship between morphology, mechanical behavior and cell permeability. *J. Mech. Behav. Biomed. Mater.* **54,** 8–20 (2016).

4. Scaffaro, R., **Lopresti, F.**, *et al.* Electrospun PCL/GO-g-PEG structures: Processing-morphology-properties relationships. *Compos. Part A Appl. Sci. Manuf.* **92,** 97–107 (2016).

5. Scaffaro, R., **Lopresti, F.**, Botta, L., Rigogliuso, S. & Ghersi, G. Melt Processed PCL/PEG Scaffold With Discrete Pore Size Gradient for Selective Cellular Infiltration. *Macromol. Mater. Eng.* **301,** 182–190 (2016).

6. Scaffaro, R., **Lopresti, F.**, Botta, L. & Maio, A. Mechanical behavior of Polylactic acid/Polycaprolactone porous layered functional composites. *Compos. Part B Eng.* **98,** 70–77 (2016).

7. Scaffaro, R., **Lopresti, F.**, *et al.* Synthesis and self-assembly of a PEGylated-graphene aerogel. *Compos. Sci. Technol.* **128,** 193–200 (2016).

8. Scaffaro, R., **Lopresti, F.,** *et al.* A Facile and Eco-friendly Route to Fabricate Poly(Lactic Acid) Scaffolds with Graded Pore Size. *J. Vis. Exp.* 1–8 (2016). doi:10.3791/54595

9. Scaffaro, R., **Lopresti, F.,** *et al.* Effect of PCL/PEG-Based Membranes on Actinorhodin Production in Streptomyces coelicolor Cultivations. *Macromol. Biosci.* **16,** 686–693 (2016).

10. Scaffaro, R., Botta, L., **Lopresti, F.**, Maio, A. & Sutera, F. Polysaccharide nanocrystals as fillers for PLA based nanocomposites: a review. *Cellulose*, *Accepted*, **In Press,** (2016).

11. Scaffaro, R., **Lopresti, F.**, Maio, A., Sutera, F. & Botta, L. Development of polymeric functionally graded scaffold: a brief review. *J. Appl. Biomater. Funct. Mater.* Accepted, **In Press,** (2016).

Book Chapter

- Scaffaro, R., Botta, L., **Lopresti, F.,** et al. "Green nanocomposites based on PLA and natural organic fillers", 21th Chapter in: Handbook of composites from renewable materials. Published by Wiley-Scrivener, **In Press,** (2016)

International Conference Proceedings

1. **F. Lopresti,** L. Botta, R. Scaffaro "Preparation and characterization of PCL/GO-g-PEG biocomposite nanofiber scaffolds". XXXII LIAC Meeting on Vascular Research. Ustica (PA) 14 – 17 Settembre 2016. Oral Communication.

2. A. Maio, **F. Lopresti,** D. Giallombardo, L. Botta, R. Scaffaro. "Synthesis of a biocompatible aerogel based on graphene oxide and a modified polyethylene glycol". ICNN4 - 4th International Conference on Nanomechanics and Nanocomposites. Vicenza, 14-17 September 2016.

3. **F. Lopresti,** A. Maio, L. Botta, R. Scaffaro. "Preparation and mechanical characterization of polycaprolactone/graphene oxide biocomposite nanofibers". VIII International Conference on "Times of Polymers and Composites", Ischia, 19-23 June 2016. ISBN 978-0-7354-1390-0

National Conference Proceedings

1. Sutera, R. M. Fontana, **F. Lopresti**, L. Botta, A. M. Puglia, R. Scaffaro, G. Gallo "PCL/PEG based membranes for bacterial cells immobilization stimulate actinorhodin antibiotic production in S. coelicolor". 3° Meeting Biotecnologie. Palermo 17-18 Dicembre 2015

2. V. Catania, **F. Lopresti**, P. Quatrini, S. Santisi, S. Cappello and R. Scaffaro "A new scaffold-bacteria-based system for bioremediation of oil-contaminated water" 31° Meeting Società Italiana di Microbiologia Generale e Biotecnologie Microbiche (SIMGBM). Ravenna 23-26 Settembre 2015

3. R. Scaffaro, **F. Lopresti**. "Three-layered porous device in PCL/PEG blend for interface tissue engineering" INSTM CONFERENCE, Favignana (TP), 28th June – 1st July 2015.

4. **F. Lopresti**, D. Giallombardo, R. Scaffaro. "Bio-polymeric based sponges for oily waste recovery" INSTM CONFERENCE, Favignana (TP), 28th June – 1st July 2015.

5. R. Scaffaro, F. P. La Mantia, F. Sutera, **F. Lopresti** "Parameters optimization in porous scaffold fabrication process based on Taguchi method and ANOVA". INSTM CONFERENCE, Favignana (TP), 28th June – 1st July 2015.

6. M. L. Bondì, C. Botto, E. Amore, V. Vincenti, A. Maio, D. Giallombardo**, F. Lopresti** and R. Scaffaro. "Pegylated-graphene oxide (GO-PEG) as new carrier for chemotherapeutic agent delivery" INSTM CONFERENCE, Favignana (TP), 28th June – 1st July 2015.

7. A. Maio, R. Scaffaro, **F. Lopresti**, L. Botta, S. Rosselli, M. Bruno, S. P. Agnello, M. L. Bondì, A. Mezzi. "Rapid and eco-friendly synthesis of graphene oxide-silica nanohybrids". I materiali biocompatibili per la medicina. Convegno nazionale della Società Italiana Biomateriali. Palermo, 2-4 Luglio 2014.

8. R. Scaffaro, **F. Lopresti**, A. Maio, L. Botta, G. Ghersi, S Rigogliuso "Pore size graded scaffold for selective cellular permeation". I materiali biocompatibili per la medicina. Convegno nazionale della Società Italiana Biomateriali. Palermo, 2-4 Luglio 2014.

9. L. Botta, R. Scaffaro, **F. Lopresti** "Preparation and characterization of multilayer porous PLA scaffolds". IX Convegno Nazionale INSTM sulla Scienza e Tecnologia dei Materiali. Bari 30 Giugno – 3 Luglio, 2013.

Educational Activities

Attended courses

- **Tecnologia dei polimeri** – Prof F.P. La Mantia
- **Packaging dei prodotti alimentari** – Ing. Luigi Botta

Attended PhD Schools

- **Partecipazione alla XX Scuola AIMAT/SIB 2015** Rivestimenti e trattamenti

funzionali Ischia Porto (NA), 18 - 22 Luglio 2015

- **Partecipazione alla XVIII Scuola INSTM 2014** Carbon based nano-structured materials: graphene as a new player. Technologies, characterization, applications. Ischia Porto (NA), 16 - 20 Luglio 2014

Attended Conferences

- **Partecipazione al "XXXII LIAC Meeting on Vascular Research"** Ustica (PA), 14 – 17 Stemmebre 2016

- **Partecipazione al Congresso Nazionale Biomateriali 2014** Hotel Piazza Borsa, Via dei Cartari, 18, 2 – 4 Luglio Palermo

- **Partecipazione al X Convegno Nazionale INSTM** sulla Scienza e Tecnologia dei Materiali 28 Giugno – 1 Luglio, 2015 – Tonnara Florio, Favignana (TP)

PhD Seminar and Courses

- **Partecipazione al corso di formazione Comunicazione in pubblico** (Ciclo di eventi "Formazione per la Ricerca") Palermo 7-8 Aprile 2014

- **Partecipazione al corso di formazione** Occasioni di finanziamento della ricerca e della mobilità in ambito europeo: Le Marie Sklodowska-Curie Actions (MSCA) e l'ERC in Horizon 2020. (Ciclo di eventi "Formazione per la Ricerca") Palermo 20-21 Febbraio 2014

- **Partecipazione al corso di formazione** Inside the Review Process (Ciclo di eventi "Formazione per la Ricerca") Palermo, 27-28 Ottobre 2015

- **Partecipazione al corso di formazione** Corso pratico introduttivo a LabVIEW. Organizzato dalla National Intrument a Palermo, il 20 Marzo 2014.

- **Partecipazione al corso di formazione** Trasferimetno tecnologico e progetti di ricerca applicata (Ciclo di eventi "Formazione per la Ricerca") Palermo, 18 Giugno 2014

- **Partecipazione al seminario** "New trends and research perspectives towards a more sustainable environment" (Ciclo di eventi "Formazione per la Ricerca") Palermo, 14 Marzo 2014

- **Partecipazione al seminario** "Indici bibliometrici: come valutare la propria attività scientifica" (Ciclo di eventi "Formazione per la Ricerca") Palermo, 20 Maggio 2014

- **Partecipazione al seminario** "La sicurezza sociale dei giovani ricercatori: situazione pensionistica e accesso al credito" (Ciclo di eventi "Formazione per la Ricerca") Palermo, 4 Febbraio 2014

- **Partecipazione al seminario** "La tutela giuridica della innovazione tecnologica" (Ciclo di eventi "Formazione per la Ricerca") Palermo, 3 Aprile 2014

- **Partecipazione al seminario** "La tutela della proprietà intellettuale e concorrenza" (Ciclo di eventi "Formazione per la Ricerca") Palermo, 11 Maggio 2015

- **Partecipazione al seminario** "Spin-off accademico: fare impresa all'Università di Palermo" (Ciclo di eventi "Formazione per la Ricerca") Palermo, 30 Settembre 2015

- **Partecipazione al seminario** "Software per la presentazione di contributi scientifici" (Ciclo di eventi "Formazione per la Ricerca") Palermo, 16 Marzo 2015

- **Partecipazione al seminario** "Author workshop: How to write a paper" (Ciclo di eventi "Formazione per la Ricerca") Palermo, 23 Marzo 2015